

UNDERSTANDING EFFECTS OF TAPERING CANTILEVERED PIEZOELECTRIC  
BIMORPHS FOR ENERGY HARVESTING FROM VIBRATIONS

by

Naved Ahmed Siddiqui

A dissertation submitted to the Graduate Faculty of  
Auburn University  
in partial fulfillment of the  
requirements for the Degree of  
Doctor of Philosophy

Auburn, AL  
December 13, 2014

Keywords: Piezoelectric Energy Harvesting, Tapering, Resonance, Electromechanical Coupling  
Coefficient, Impedance Spectroscopy, Damping,

Approved by:

Barton C. Prorok, Chair, Professor of Materials Engineering  
Jeffrey W. Fergus, Professor of Materials Engineering  
Dong-Joo Kim, Professor of Materials Engineering  
Robert L. Jackson, Associate Professor of Mechanical Engineering  
Ruel A. Overfelt, Professor of Materials Engineering

## Abstract

Piezoelectric energy harvesting from vibrations is a field that has gathered much attention over the past decade. The purpose of this application is to realize ambient sources of kinetic energy such as vibrations, and turn them into useful electrical energy for powering low powered sensor nodes. The most typical form of piezoelectric energy harvesting comes from cantilevered bimorphs. These bimorph structures are typically rectangular in shape with a tip mass, resonating in the fundamental mode of vibration. This creates a stress concentration near the fixed end of the cantilever, which linearly decreases towards the free end, hence creating an inefficient system. In order to improve this scenario by achieving a constant axial strain profile through the length of the geometry, tapered cantilevered bimorphs have been proposed in literature. However, an exhaustive set of experimental data and proper characterization, with appropriate constraints such as matching resonance frequency to prove this concept is elusive.

In this dissertation, the effect of changing the geometry from rectangular cantilevered bimorphs into triangular ones with matching resonance frequency and volumes is presented. It is shown that for tapered geometry with matching volume and resonance frequencies, triangular bimorphs operate at lower maximum stresses, and provide enhanced electromechanical coupling coefficients. With enhanced electromechanical coupling coefficients, the impedance at resonance is lower, providing a smaller optimal load resistance value from which power can be extracted at lower currents. The absolute values of peak capacitance are also enhanced, with larger positive capacitance peaks and smaller negative capacitance peaks for triangular cantilevers as compared to rectangular counterparts. Studies for damping ratios as a function of load resistance also show damping ratios at optimal load resistance values indicate optimal damping ratios for power generation exist for high coupling systems. With increased electromechanical coupling and damping, triangular bimorphs provide higher electromechanical coupling figure of merits, when they can be compared with matching size, proof mass, and frequencies.

## Acknowledgements

As I arrive towards the culmination of this document, several thoughts race through my head. I am thankful to a number of people who have helped me through the course of my Ph.D. However, the first people that I have to acknowledge are my parents, Mohammed Fareed and Fahmida Siddiqui. Without their prayers, and unconditional love and support from a distance, this Ph.D would simply not have been possible. Words are not enough to describe the gratitude I have for them. I would also like to acknowledge my siblings Sabah, Sarah, and Ahmed as well for the same.

From a professional front, I would first like to thank Dr. Prorok, and Dr. Overfelt, both for their support, during the course of my Ph.D. The training I received developed my aptitude in critical thinking, which will be a lifelong tool that will allow me to take on scientific research and engineering problems in a much more thoughtful manner. This will be invaluable for the rest of my life.

I would like to thank Dr. Dong-Joo Kim, for his support with the project, serving on the committee, and especially for allowing me to use his laboratory equipment, without which this project would simply not be possible.

I would like to thank Dr. Fergus, who has become a role model for me; and someone who mentored me, and allowed me in his office at any time, without any hesitation. I am also truly thankful for the impromptu tutoring multiple times during the time I was preparing for my qualifying exams. I am truly thankful to him, and honored to have him on my committee.

I would also like to thank Dr. Jackson for serving on my committee, and for his helpful suggestions with this dissertation. The multi-physics modeling course I took under him turned out to be invaluable for my career.

I would like to thank Dr. Ahmed for serving as my external reader for this dissertation, and also for the mentorship and support, which greatly helped me through this Ph.D.

Finally, I would like to acknowledge several friendships I made during my time here at Auburn. Patrick Bass and MariAnne Sullivan, who have become close friends, deserve a very

special mention. A special mention also goes out to Sachin Jambovane, Nitilaksh Hiremath, and Victor Agubra. I would also like to acknowledge my current and former lab-mates: Yan Chen, Brandon Frye, Kevin Schweiker, Daniel Slater, Shakib Morshed, Zhan Xu. I would also like to thank other group members: Ricky Lance Haney, Stanley Chou, Mobbassar Hassan Sk, Amy Buck, Amanda Neer, John Andress, and Bethany Brooks. Matthew Roberts deserves a very special mention for his help with developing the MATLAB code that I used for my damping ratio calculations in this dissertation.

I would also like to mention all the other fellow graduate students that I went through this program with (in no particular order): Yating Chai, Shin Horikawa, Kanchana Weerakoon, Sadhwi Ravichandran, Zhizhi Sheng, Honglong Wang, Tong Yang, Wei Wang, Yu Zhao, Hyejin Park, Yoonsung Chung, Seon-Bae Kim. I will have fond memories with each of them. I hope I am not making the inevitable mistake of inadvertently forgetting anyone here.

Special thanks are also due to Steve Moore, who also became a very special friend. Michael Crumpler, Steve Best, Clyde Wikle, Dr. Martin Baltazar-Lopez and L.C. Mathison (deceased). I will cherish all the light hearted moments with each of you.

I also want to acknowledge my best friend Andrew Roszak, who has been a big part of my life. I also want to thank Mr. Rakesh Ahuja and Dr. Philip Oldiges at IBM; thank you for the incredible opportunity with the summer internship.

Once again, thank you everyone. I do not have enough words to express the gratitude that I have for each of you.

Finally, above all, I have to thank the Almighty for his blessings

## Table of Contents

Abstract .....	ii
Acknowledgements.....	iii
List of Figures .....	vii
List of Tables .....	xv
CHAPTER 1: INTRODUCTION .....	1
CHAPTER 2: LITERATURE REVIEW .....	6
2.1 Brief introduction to piezoelectricity and piezoelectric bimorphs .....	6
2.2 Literature Review on Piezoelectric Generators.....	12
2.2.1 Impact Coupled Devices .....	12
2.3 Human Powered Piezoelectric Generation.....	12
2.4 Energy Harvesting from constant base excitations .....	14
2.4 Energy Harvesting from Vibrations using piezoelectric cantilever devices .....	17
2.5 Distributed Parameters Models .....	21
2.6 Shape Optimization of single cantilever beams .....	23
2.7 Optimization of cantilever beams with zigzag structures .....	36
2.8 Optimized shape with variable thickness .....	38
2.9 Torsional system for $d_{15}$ and $d_{36}$ modes .....	39
2.10: Studies on parameter identification and optimization.....	41
CHAPTER 3: METHODOLOGY .....	44
3.1 Numerical Modeling.....	44
3.2 Experimental Procedure .....	49
3.2.1 Sample Preparation.....	49
3.2.2 Experimental Setup for Energy Harvesting.....	50
3.2.4 Impedance Analyzer Measurements .....	53
CHAPTER 4: PRELIMINARY NUMERICAL ANALYSIS .....	55
4.1 Quasi-static numerical analysis for various shaped cantilevers .....	55

4.2	Effect of shape change on resonance frequency .....	60
4.2.2	Constant resonance frequency and volumes .....	62
4.2.3	Triangles with L=30.5mm and changing base widths.....	64
CHAPTER 5: EXPERIMENTAL RESULTS .....		65
5.1	Introduction to a single experimental run.....	65
5.2:	Experimental Results with no proof mass .....	75
5.2.1:	70 mm <sup>3</sup> samples .....	75
5.2.2	104 mm <sup>3</sup> samples.....	87
5.2.3	140 mm <sup>3</sup> samples.....	94
5.2.4	Summary for no proof-mass samples .....	101
5.3	Studies with 2 gram Proof Mass Samples .....	106
5.3.1	RT70-1M .....	106
5.3.2	RT104-1M .....	118
5.3.3	RT140-1M .....	126
5.3.4	Summary for devices with 2 grams proof mass .....	134
5.4	Increased Proof Masses .....	141
5.4.1:	70 mm <sup>3</sup> devices with 4 grams proof mass .....	141
5.4.2:	Summary on 70 mm <sup>3</sup> devices as a function of proof mass .....	149
5.5:	Comparison with Triangles with L=21.5 mm .....	154
5.5.1:	R70-1M vs. T35-1M .....	154
5.5.2:	R140-1M vs. T70-1M .....	164
5.5.3	Summary on constrained length devices .....	173
5.6	Damping Ratio as a function of load resistance .....	174
CHAPTER 6: CONCLUSIONS & FUTURE WORK .....		177
BIBLIOGRAPHY.....		179
APPENDIX A: Coupled-Field Numerical Simulations.....		183

## List of Figures

Figure 1: Comparison of three electromechanical transduction mechanisms [9].....	3
Figure 2: Power Density estimates versus operation voltages for various sources of energy [7] ..	3
Figure 3: Perovskite Structure in PZT [19].....	6
Figure 4: Cartesian Coordinate System for Piezoelectric Materials [22] .....	8
Figure 5: Series and Parallel poling in piezoelectric bimorphs [26].....	11
Figure 6: Electrical representation of (a) Series, (b) Parallel poled piezoelectric bimorphs [26]	11
Figure 7: Impact on a piezoelectric bulk generator [27].....	12
Figure 8: Shoe insert power generator [10] .....	13
Figure 9: An internal generator representing an energy scavenging system from vibrations [13]	14
Figure 10: Equivalent Circuit Model for Piezoelectric Bimorph with a Resistive Load [5] .....	17
Figure 11: Vibrating Piezoelectric generator with attached proof mass [1] .....	19
Figure 12: Measured output power versus resistive load [1] .....	19
Figure 13: Design optimization for piezoelectric bender [6].....	20
Figure 14: Quick Pack actuator for vibration energy harvesting [28] .....	20
Figure 15: Effect of shape change on the transversal stress along the length of a cantilever [18]	23
Figure 16: Development of MEMS scale PZT harvester with a tapered piezoelectric patch [34]	24
Figure 17: Cross-sections of a) Homogeneous, b) symmetric heterogeneous and c) asymmetric heterogeneous cantilevers [36] .....	25
Figure 18: Mean curvature for rectangular, trapezoidal and triangular beam for various tip mass- to beam mass ratio [37].....	29
Figure 19: Mode shapes for triangular beam with no tip mass [37] .....	29
Figure 20: Normalized power for various shapes based on truncation ratio's for different tip masses [37].....	29
Figure 21: Maximum achievable excitation amplitude based for different shapes [37].....	29
Figure 22: Three geometries showing Rectangular, Tapered and Reverse-Tapered bimorphs ....	30
Figure 23: a) Mode shapes for the three geometries b) 2 <sup>nd</sup> spatial derivative of mode shape .....	30

Figure 24: a) Strain distribution along the length over the surface of the beam, and b) weighted strain distribution due to tapering through the length of the beam .....	31
Figure 25: Geometries showing a) optimal linear, and b) optimal curved profile.....	32
Figure 26: Non-linear optimized geometry.....	32
Figure 27: Effect of geometry on a) strain distribution, and b) weighted strain, when the structures are under maximum allowable excitation amplitudes.....	33
Figure 28: Trapezoidal and Reverse Trapezoidal geometries [39].....	34
Figure 29: Reverse Trapezoidal geometry with a proof mass [14].....	34
Figure 30: FEM results from scavenger shapes of equal maximum transversal widths.....	34
Figure 31: Optimal shapes: Maximum average power [15] .....	35
Figure 32: Single and Meandered cantilever device [16] .....	36
Figure 33: Zigzag cantilever device for piezoelectric energy harvesting [17] .....	37
Figure 34: Tapered cantilevered piezoelectric bimorph [18].....	38
Figure 35: Operating principle of a shear mode piezoceramic. $E_1$ is the electric field developed, and P is the poling direction [19].....	39
Figure 36: Poling and harvesting directions for the $d_{15}$ shear mode harvester [19] .....	40
Figure 37: Poling and harvesting direction for the $d_{36}$ mode energy harvester [19].....	40
Figure 38: SOLID186 and SOLID226 element shapes .....	45
Figure 39: CIRCU98 Elements in ANSYS.....	45
Figure 40: Example of a developed FEM model in ANSYS for a piezoelectric unimorph [51]..	48
Figure 41: Abrasive Slurry Saw – Model 850, South Bay Technology .....	50
Figure 42: Schematic of energy harvesting experimental setup [22] .....	51
Figure 43: Energy Harvesting Experimental Setup in Laboratory [55].....	52
Figure 44: Piezoelectric voltage response to an impulse wave [5].....	53
Figure 45: Geometric considerations for cantilevered devices.....	56
Figure 46: Deflection Contours of cantilevered devices.....	57
Figure 47: Deflection along mid-span of cantilevered devices .....	57
Figure 48: Axial Stress Contours on cantilevered devices .....	59
Figure 49: Axial Stresses along the length over the mid-span of the cantilevered devices.....	59
Figure 50: Resonance Frequency of Rectangular cantilevered bimorph structures with $L=21.5\text{mm}$ , $t=0.51\text{mm}$ and varying widths .....	61

Figure 51: Resonance Frequency of Triangular Cantilevers with $L=21.5\text{mm}$ , $t=0.51\text{mm}$ and varying widths.....	62
Figure 52: Effect of length on resonance frequency for triangles $70\text{ mm}^3$ in volume.....	63
Figure 53: Effect of base angle on triangles $70\text{ mm}^3$ in volume.....	63
Figure 54: Resonance Frequency for triangular cantilevers with varying clamping widths .....	64
Figure 55: Resonance frequency as a function of load resistance for the $70\text{ mm}^3$ rectangular bimorph.....	66
Figure 56: Normalized Resonance Frequency illustrating the electromechanical coupling in the system .....	67
Figure 57: RMS voltage generated from the piezoelectric bimorph into various load resistors at resonance.....	68
Figure 58: Power generated by the piezoelectric bimorph as a function of load resistance, each at their corresponding resonance frequency .....	69
Figure 59: Power Density of $70\text{ mm}^3$ device without a proof mass .....	70
Figure 60: Impedance analyzer measurement for the $70\text{ mm}^3$ rectangular bimorph with $100\text{ mV}$ oscillations as a function of frequency.....	71
Figure 61: Capacitance and Dissipation factor for $70\text{ mm}^3$ rectangular bimorph with $100\text{ mV}$ oscillations as a function of frequency.....	72
Figure 62: Damped voltage response to an impulse wave from the cantilevered bimorph.....	73
Figure 63: Calculation of damping ratio for $70\text{ mm}^3$ Rectangle under Open Circuit Conditions	74
Figure 64: Schematics for $70\text{ mm}^3$ devices without a proof mass.....	75
Figure 65: Resonance frequency as a function of load resistance for $70\text{ mm}^3$ samples without a proof mass.....	76
Figure 66: Normalized resonance frequency for $70\text{ mm}^3$ samples without a proof mass .....	77
Figure 67: Power Generated from $70\text{ mm}^3$ geometries without a proof mass.....	78
Figure 68: Deflection for $70\text{ mm}^3$ Rectangular Cantilevered bimorph structure (non-piezoelectric) at resonance.....	80
Figure 69: Deflection for $70\text{ mm}^3$ Triangular Cantilevered bimorph structure (non-piezoelectric) at resonance.....	80
Figure 70: Axial Stress for $70\text{ mm}^3$ Rectangular Cantilevered bimorph structure (non-piezoelectric) at resonance.....	81

Figure 71: Axial Stress for 70 mm <sup>3</sup> Rectangular Cantilevered bimorph structure (non-piezoelectric) at resonance .....	81
Figure 72: Deflection of the 70 mm <sup>3</sup> cantilevers along the beam mid-span.....	82
Figure 73: Axial stress per unit width along the beam midspan for 70 mm <sup>3</sup> cantilevers .....	82
Figure 74: Impedance and Phase angle for R70-0M .....	84
Figure 75: Impedance and Phase angle for T70-0M.....	84
Figure 76: Capacitance and Dissipation factor for R70-0M.....	86
Figure 77: Capacitance and Dissipation factor for T70-0M .....	86
Figure 78: Schematic for 104 mm <sup>3</sup> devices with no proof mass .....	87
Figure 79: Resonance Frequency for 104 mm <sup>3</sup> devices.....	88
Figure 80: Normalized resonance frequency for the 104 mm <sup>3</sup> samples .....	88
Figure 81: Power generated from 104 mm <sup>3</sup> samples without a proof mass .....	89
Figure 82: Deflection of 104 mm <sup>3</sup> cantilevers without a proof mass .....	90
Figure 83: Axial Stress for 104 mm <sup>3</sup> samples .....	90
Figure 84: Impedance-Phase Angle for R104-0M.....	92
Figure 85: Impedance-Phase Angle for T104-0M .....	92
Figure 86: Capacitance-Dissipation factor for R104-0M .....	93
Figure 87: Capacitance-Dissipation Factor for T104-0M.....	93
Figure 88: Schematics for 140 mm <sup>3</sup> devices without a proof mass.....	94
Figure 89: Resonance frequency for 140 mm <sup>3</sup> cantilevered bimorphs without proof mass.....	95
Figure 90: Normalized Resonance frequency for 140 mm <sup>3</sup> cantilevers without proof mass .....	95
Figure 91: Power generated from 140 mm <sup>3</sup> cantilevered bimorphs without proof mass .....	96
Figure 92: Deflection along the mid-span for the 140 mm <sup>3</sup> cantilevered bimorphs without proof mass.....	97
Figure 93: Axial Stress for 140 mm <sup>3</sup> cantilevered bimorphs without proof mass.....	97
Figure 94: Impedance-Phase Angle for R140-0M.....	99
Figure 95: Impedance-Phase Angle for T140-0M .....	99
Figure 96: Equivalent Parallel Capacitance-Dissipation Factor for R140-0M.....	100
Figure 97: Equivalent Parallel Capacitance-Dissipation Factor for T140-0M .....	100
Figure 98: Power density for rectangular cantilevered bimorphs without proof mass .....	102
Figure 99: Power density for triangular cantilevered bimorphs without proof mass .....	102

Figure 100: Effect of changing geometry on the electromechanical coupling coefficient for cantilevered piezoelectric bimorphs without a proof mass.....	103
Figure 101: Damping Ratio in open circuit conditions for cantilevered piezoelectric bimorphs without a proof mass.....	103
Figure 102: Electromechanical Coupling figure of merit for cantilevered bimorphs without proof mass.....	104
Figure 103: Maximum and Minimum Impedance values for cantilevered piezoelectric bimorphs with no proof mass.....	105
Figure 104: Maximum and Minimum Equivalent Parallel Capacitance for piezoelectric bimorphs with no proof mass.....	105
Figure 105: Schematic for R70-1M and T70-1M.....	107
Figure 106: Resonance frequency as a function of load resistance for R70-1M and T70-1M...	108
Figure 107: Normalized resonance frequencies as a function of load resistance for R70-1M and T70-1M.....	109
Figure 108: Power generated by R70-1M and T70-1M into various load resistors .....	110
Figure 109: Deflection for 70 mm <sup>3</sup> bimorphs with a 2 gram proof mass.....	112
Figure 110: Axial Stress along the length over the surface for 70mm <sup>3</sup> bimorphs with a 2 gram proof mass.....	112
Figure 111: Impedance-Phase Angle for R70-1M.....	114
Figure 112: Impedance-Phase Angle for T70-1M.....	114
Figure 113: Impedance-Phase Angle for T70-1M-P .....	115
Figure 114: Capacitance-Dissipation Factor for R70-1M .....	116
Figure 115: Capacitance-Dissipation factor for T70-0M.....	116
Figure 116: Capacitance-Dissipation Factor for T70-1M-P.....	117
Figure 117: 104 mm <sup>3</sup> devices with a 2 gram proof mass.....	118
Figure 118: Resonance frequency of the 104 mm <sup>3</sup> devices with a 2 gram proof mass as a function of load resistance.....	119
Figure 119: Short circuit normalized resonance frequency for 104 mm <sup>3</sup> devices as a function of load resistance.....	119
Figure 120: Power generated by the 104 mm <sup>3</sup> devices with a 2 gram proof mass into various load resistors .....	121

Figure 121: Deflection for 104 mm <sup>3</sup> devices with a 2 gram proof mass .....	122
Figure 122: Axial stress along the mid-span length over the surface for the 104 mm <sup>3</sup> devices with a 2 gram proof mass .....	122
Figure 123: Impedance - Phase Angle for R104-1M.....	124
Figure 124: Impedance – Phase Angle for T104-1M .....	124
Figure 125: Capacitance – Dissipation Factor for R104-1M.....	125
Figure 126: Capacitance – Dissipation Factor for T104-1M .....	125
Figure 127: 140 mm <sup>3</sup> devices with a 2 gram proof mass.....	126
Figure 128: Resonance frequency for 140 mm <sup>3</sup> devices with a 2 gram proof mass with varying load resistance.....	127
Figure 129: Short circuit normalized resonance frequency for 140 mm <sup>3</sup> devices with a 2 gram proof mass.....	127
Figure 130: Power generated by 140 mm <sup>3</sup> devices with a 2 gram proof mass into various load resistors .....	129
Figure 131: Deflection for the 140 mm <sup>3</sup> devices with a 2 gram proof mass at resonance .....	130
Figure 132: Axial stress along the mid-span length over the surface for the 104 mm <sup>3</sup> devices with a 2 gram proof mass .....	130
Figure 133: Impedance – Phase Angle for R140-1M.....	132
Figure 134: Impedance – Phase Angle for T140-1M .....	132
Figure 135: Capacitance – Dissipation Factor for R140-1M.....	133
Figure 136: Capacitance – Dissipation Factor for T140-1M .....	133
Figure 137: Power Density for 2 gram proof mass rectangular bimorphs as a function of load resistance.....	136
Figure 138: Power Density for 2 gram proof mass triangular bimorphs as a function of load resistance.....	136
Figure 139: Maximum tip deflection for 2 gram proof mass bimorphs .....	137
Figure 140: Electromechanical Coupling Coefficient for devices with 2 gram proof mass.....	137
Figure 141: Damping Ratio for 2 gram proof mass devices .....	138
Figure 142: Coupling Figure of Merit for 2 gram proof mass devices .....	138
Figure 143: Minimum Impedance for 2 gram proof mass devices .....	139
Figure 144: Maximum Impedance for devices with 2 gram proof mass .....	139

Figure 145: Capacitance peaks for 2 gram proof mass devices .....	140
Figure 146: Schematic for R70-2M and T70-2M .....	141
Figure 147: Resonance frequencies as a function of load resistance for 70 mm <sup>3</sup> devices with 4 grams proof mass .....	142
Figure 148: Short circuit resonance frequency normalized resonance frequencies as a function of load resistance for 70 mm <sup>3</sup> devices with 4 grams proof mass .....	142
Figure 149: Power generated by 70 mm <sup>3</sup> samples with 4 grams proof mass as a function of load resistance.....	144
Figure 150: Deflection at resonance for R70-2M and T70-2M.....	145
Figure 151: Axial stress along the mid-span length for R70-2M and T70-2M .....	145
Figure 152: Impedance – Phase Angle for R70-2M .....	147
Figure 153: Impedance – Phase Angle for T70-2M .....	147
Figure 154: Capacitance – Dissipation Factor for T70-2M.....	148
Figure 155: Capacitance – Dissipation factor for T70-2M.....	148
Figure 156: Electromechanical coupling coefficient for 70 mm <sup>3</sup> devices as a function of proof mass.....	150
Figure 157: Open Circuit Damping Ratio for 70 mm <sup>3</sup> devices as a function of proof mass .....	150
Figure 158: Electromechanical coupling figure of merit for 70 mm <sup>3</sup> devices as a function of proof mass.....	151
Figure 159: Minimum Impedance peaks for 70 mm <sup>3</sup> devices as a function of proof mass.....	152
Figure 160: Maximum Impedance peaks for 70 mm <sup>3</sup> devices as a function of proof mass .....	152
Figure 161: Capacitance measurements for 70 mm <sup>3</sup> devices as a function of proof mass.....	153
Figure 162: R70-1M and T35-1M .....	155
Figure 163: Resonance frequency for R70-1M and T35-1M as a function of load resistance...	156
Figure 164: Short Circuit normalized Resonance frequency for R70-1M and T35-1M as a function of load resistance .....	156
Figure 165: Power generated by R70-1M and T35-1M-L into various load resistors.....	158
Figure 166: Power density for R70-1M and T35-1M into various load resistors.....	158
Figure 167: Longitudinal deflection along the mid-span for R70-1M and T35-1M-L .....	160
Figure 168: Axial Stress over the midspan for R70-1M and T35-1M.....	160
Figure 169: Impedance – Phase Angle for R70-1M ( <i>same as Figure 111</i> ).....	162

Figure 170: Impedance – Phase Angle for T35-1M-L.....	162
Figure 171: Capacitance – Dissipation Factor for R70-1M ( <i>same as Figure 114</i> ) .....	163
Figure 172: Capacitance – Dissipation factor for T35-1M-L .....	163
Figure 173: Schematic for T140-1M and T70-1M-L .....	164
Figure 174: Resonance frequency vs. load resistance for R140-1M and T70-1M-L .....	165
Figure 175: Short circuit normalized Resonance frequency vs. load resistance for R140-1M and T70-1M-L .....	165
Figure 176: Power generated by R140-1M and T70-1M-L as a function of load resistance .....	167
Figure 177: Power density for R140-1M and T70-1M-L as a function of load resistance.....	167
Figure 178: Longitudinal Deflection for R140-1M and T70-1M-L at resonance .....	169
Figure 179: Axial Stress along the mid-span for R140-1M and T70-1M-L.....	169
Figure 180: Impedance – Phase angle for R140-1M .....	171
Figure 181: Impedance – Phase Angle for T70-1M-L.....	171
Figure 182: Capacitance – Dissipation for R140-1M.....	172
Figure 183: Capacitance – Dissipation Factor for T70-1M-L .....	172
Figure 184: Damping ratio as a function of load resistance for 104 mm <sup>3</sup> devices with 2 grams proof mass.....	176
Figure 185: Damping ratio as a function of load resistance for 70 mm <sup>3</sup> devices with 4 grams proof mass.....	176
Figure 186: Real part of tip displacement for R70-0M at various load resistances.....	184
Figure 187: Imaginary part of tip displacement for R70-0M at various load resistances.....	184
Figure 188: Real part of electric potential for R70-0M at various load resistances .....	185
Figure 189: Imaginary part of electric potential for R70-0M at various load resistances .....	185

## List of Tables

Table 1: Coefficients of common piezoelectric materials [6, 14].....	9
Table 2: Piezoelectric Bimorphs dimensions as available from Piezo Systems, Inc.....	49
Table 3: Power output at optimal load resistance values for 70 mm <sup>3</sup> samples without proof mass .....	78
Table 4: Impedance characteristics for 70 mm <sup>3</sup> devices with no proof mass .....	83
Table 5: Capacitance characteristics for 70 mm <sup>3</sup> devices with no proof mass.....	85
Table 6: Power output at optimal load resistance values for 104 mm <sup>3</sup> samples without proof mass .....	89
Table 7: Impedance measurements for 104 mm <sup>3</sup> devices with no proof mass.....	91
Table 8: Capacitance measurements for 104 mm <sup>3</sup> devices with no proof mass.....	91
Table 9: Power output at optimal load resistance's for 140 mm <sup>3</sup> devices without proof mass ....	96
Table 10: Impedance measurements for 140 mm <sup>3</sup> samples with no proof mass .....	98
Table 11: Capacitance measurements for 140 mm <sup>3</sup> samples with no proof mass .....	98
Table 12: Summary of Power generated from 70mm <sup>3</sup> bimorphs with a 2 gram proof mass .....	110
Table 13: Summary of impedance analysis for 70 mm <sup>3</sup> devices with a 2 gram proof mass .....	113
Table 14: Capacitance measurements for 70 mm <sup>3</sup> devices with 2 gram proof mass.....	115
Table 15: Power generated at optimal load resistance values for the 104 mm <sup>3</sup> devices with a 2 gram proof mass.....	120
Table 16: Impedance characteristics for 104 mm <sup>3</sup> devices with a 2 gram proof mass.....	123
Table 17: Equivalent Parallel Capacitance for 104 mm <sup>3</sup> devices with a 2 gram proof mass .....	123
Table 18: Power generated at optimal load resistance values for the 140 mm <sup>3</sup> devices with a 2 gram proof mass.....	128
Table 19: Impedance – Phase Angle for 140 mm <sup>3</sup> devices with a 2 gram proof mass .....	131
Table 20: Capacitance – Dissipation Factor for 140 mm <sup>3</sup> devices with a 2 gram proof mass ...	131
Table 21: Power generated at optimal load resistance values for 70 mm <sup>3</sup> devices with 4 grams proof mass.....	143

Table 22: Impedance – Phase Angle for 70 mm <sup>3</sup> devices with 4 grams proof mass .....	146
Table 23: Capacitance – Dissipation Factor for 70 mm <sup>3</sup> devices with 4 grams proof mass.....	146
Table 24: Power generated by R70-1M and T35-1M at optimal load resistances.....	159
Table 25: Impedance measurements for T70-1M and T35-1M.....	161
Table 26: Capacitance peaks for R70-1M and T35-1M-L.....	161
Table 27: Power at optimal load resistance for R140-1M and T70-1M.....	166
Table 28: Impedance Analysis for R140-1M and T70-1M-L.....	170
Table 29: Capacitance peaks for R140-1M and T70-1M-L.....	170

## CHAPTER 1: INTRODUCTION

With the developments and incredible advancements in silicon technology, and developments of devices such as MEMS or NEMS (micro or nano- electro mechanical systems), electronic devices are seeing very high levels of integration. [1, 2]. Examples of these very highly integrated devices include multigate transistors such as FinFETs. With such high levels of integration and complexity, electronic devices are comprised of a vast number of individual sensor nodes [1] that are connected to larger wireless networks. These sensor nodes individually require low levels of power for operation, which fall in the micro- to milli-watt range. In order to power these nodes, traditional solutions have utilized electrochemical batteries, which can be tedious and expensive to replace, and in some cases impractical, especially when sensors are placed in remote locations [3]. A scenario such as this could be presented when sensors for detection of harmful gases such as CO, CO<sub>2</sub>, ozone, tri-cresyl-phosphate (TCP) are placed on board an airliner in the passenger cabin, or in the bleed air system of the aircraft, which would be a highly inaccessible location [4]. In such cases, it would be very desirable to power up sensors, or other such devices requiring low levels of power using a method alternative to batteries.

Some alternative solutions to batteries that have been presented, as reviewed by Roundy et al [5, 6] and Cook-Chennault [7] include micro-batteries, micro-fuel cells, micro-turbine generators, micro-heat engines; but these may require a source for fuel. In certain cases, they might not have the desired efficiency, or may be expensive and cumbersome to integrate into low powered sensor nodes. Truly renewable sources of energy that are completely regenerative would utilize sources that are present within the sensors vicinity such as light, thermal or kinetic energy in the environment. Photovoltaics for solar panels, and thermoelectric motors could provide solutions, but the sources of energy required for their operation are insufficient in indoor applications. Other sources of energy to consider could be kinetic energy in the environment; such as ambient vibrations. [6, 7].

Vibrations are ubiquitous in the environment in the form of noise from various machines such as microwave ovens, HVAC ducts, or on mobile structures such as automobile engines or

airplanes. Such ambient noise sources typically vibrate from 60 Hz for HVAC ducts to 240 Hz for a refrigerator, with peak acceleration amplitudes ranging from  $0.1 \text{ ms}^{-2}$  for a refrigerator to  $10 \text{ ms}^{-2}$  for the base of a 5 horsepower 3-axis machine tool [6]. A publication depicting a study for identification of vibration from various objects and instruments is provided in [8], and also mentioned in [1, 6], which have been characterized in [9]. Such vibrations can also be harnessed from human motion such as walking [10], or even heartbeats as well [11], which are characterized by low frequency, high amplitude displacements. Therefore, there is a great opportunity to harness these vibrations, which are forms of ambient kinetic energy in the mechanical form, and convert them into usable electric energy for powering a sensor node.

The conversion of mechanical to electrical energy requires an electro-mechanical transduction mechanism. Vibration energy is suitable in cases where an inertial frame is attached to a vibrating host or generator, which acts as a fixed reference. This vibrating fixed reference can transmit vibrations to a suspended inertial mass producing a relative displacement between them. Such a system would possess a characteristic resonance frequency, which when matched would amplify the relative displacement of the system [12]. Williams and Yates [13] identified the use of three different transduction mechanisms in the form of these inertial generators, which include electromagnetic, electrostatic, and piezoelectric devices. These transduction mechanisms are described individually in [6], and have been compared by Priya [9] in Figure 1. Even though electrostatic devices offer easy integration into microelectronics such as CMOS devices, they suffer from high impedance, and require mechanical stops. Figure 2 [7], which illustrates voltages versus power density for various devices, does not feature electrostatic devices due to their high voltages. Electromagnetic devices tend to be somewhat bulky, and require multistage post-processing to reach desired levels of voltages [14]. Piezoelectric devices however are less bulky, and theoretically provide the largest energy density per volume when compared to other inertial generators. They also have a direct voltage output, inherent to the material. Figure 2 [7] depicts them as the most versatile in terms of output voltages, and fairly high power densities compared to other sources of energy.



Therefore, piezoelectric materials are prime candidates for vibration energy harvesting, and the publication of a number of review articles [2, 9, 12, 15-17] within the last 10 years bears testament to this exploding area of research. Piezoelectric energy harvesting is usually carried out using cantilevered bimorphs, which are heterogeneous structures consisting of two piezoceramic layers sandwiching a metallic layer. These devices are attached on a vibrating host generating a dynamic strain in the beam, resulting in an alternating voltage across their electrodes. This is an inherent property of piezoelectric devices, which is described in the following section.

Cantilevered piezoelectric bimorphs have been widely explored and studied in the past decade for energy harvesting from vibrations. In this field, the  $d_{31}$  mode of operation is exploited, where the cantilevered bimorph is attached on a vibrating host structure causing longitudinal deflections in the bimorph, when resonating in the fundamental mode. This vibration causes axial stresses over the surfaces of the bimorphs, while generating charge in the longitudinal direction. Most commonly, these axial stresses are concentrated near the fixed end of the beam, and linearly decrease towards the free end of the beam. This results in inefficiencies in the cantilevered piezoelectric bimorphs wherein only a small portion of the device is engaged in generating power. In order to circumvent this inefficiency, the geometry of the cantilevered bimorph can be altered. Changing the geometry from a rectangular to triangular bimorph, where the wide end of the isosceles triangle is clamped, can result in a linear stress profile [18].

This concept of tapering geometry and even shape optimization to obtain greater amounts of power from a cantilevered device has been presented in a few studies, which are reviewed in the following section. However, changing the geometry usually affects the resonance frequency of the device, yielding results that are difficult to compare with rectangular counterparts. Moreover, the effect of changing geometry on various important parameters such as electromechanical coupling coefficients, impedance, capacitance, and damping ratios are elusive in literature. Therefore, in this dissertation, various sets of rectangular and triangular cantilevered piezoelectric bimorphs with matching volumes and resonance frequencies are found and experimentally characterized for these parameters. The tests are conducted with piezoelectric bimorphs with varying degrees of proof masses into varying load resistances. It is shown that triangular devices with the given constraints of matching volume and resonance frequency operate with lower values of maximum stress, resulting in larger electromechanical coupling

coefficients ( $k_{31}$ ), and larger electromechanical coupling figure of merits ( $k^2Q_m$ ). It is also shown that with these larger coupling coefficients, the triangular devices are more electrically compliant, since they provide lower impedance values at resonance, and larger impedance values at anti-resonance. The capacitance characteristics in the frequency domain are also measured, indicating larger absolute values of positive and negative capacitance peaks in the case of triangular bimorphs, compared to their rectangular counterparts. Therefore, the dissertation reports an exhaustive electronic characterization of these materials, which so far have only been partly reported in literature, mostly by means of numerical studies, showcasing the effects of electronic parameters such as  $k_{31}$  and  $Q_m$  from a hypothetical point of view.

## CHAPTER 2: LITERATURE REVIEW

### 2.1 Brief introduction to piezoelectricity and piezoelectric bimorphs

The phenomenon of piezoelectricity was famously found by the Curie family in 1880. This effect occurs in a special class of crystal structures, which is among the 21 non centrosymmetric point groups. In these materials, when the crystal is strained, it becomes electrically polarized, and the degree of polarization is proportional to the applied strain [7, 12]. This behavior is seen in single crystal materials such as Quartz and Rochelle salt. Engineering materials that have a perovskite crystal structure, as shown in Figure 3 gives rise to strong levels of piezoelectricity below the Curie temperature, where they maintain non-centrosymmetry. The most common examples of materials that possess the perovskite structure include Barium Titanate (BTO) and Lead Zirconate Titanate (PZT), which contain two cations and an oxygen atom acting as the anion per unit cell. The most commonly used material in the field of piezoelectric energy harvesting are versions of PZT materials – namely PZT-5A and PZT-5H.

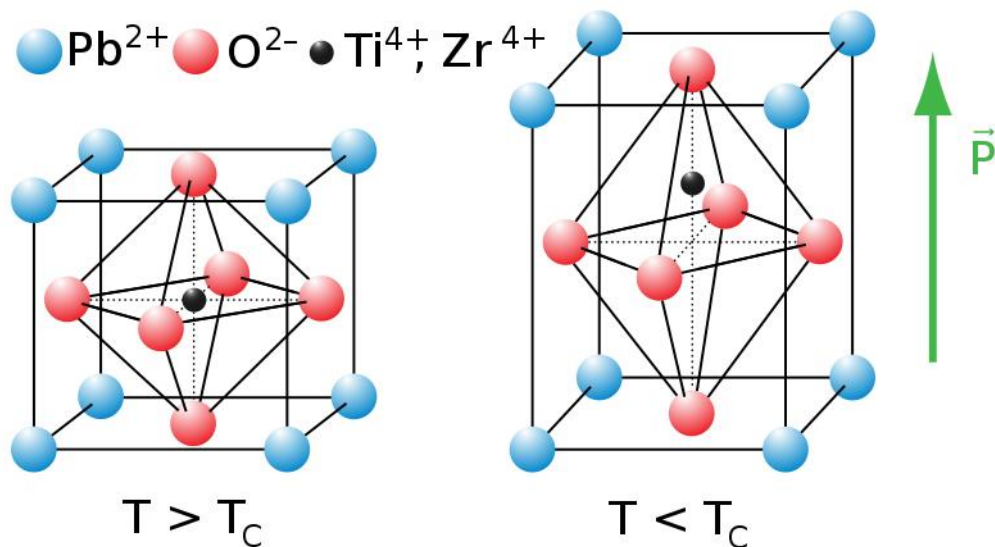


Figure 3: Perovskite Structure in PZT [19]

Due to the mentioned non-centrosymmetry, piezoelectric materials exhibit anisotropic characteristics in terms of stress, strain, compliance, stiffness, permittivity and piezoelectric coefficients. These are related to the orientation of the ceramic material and the direction of measurements and applied stresses/forces. Therefore, these properties are reported in tensor forms. The constitutive equations [20, 21] that describe the piezoelectric effect are as follows:

$$S_{ij} = s_{ijkl}^E T_{kl} + d_{kij} E_k \quad (1)$$

$$D_i = d_{ikl} T_{kl} + \varepsilon_{ik}^T E_k \quad (2)$$

where,

$S_{ij}$  is strain,

$s_{ijkl}^E$  is elastic compliance at constant electric field,

$T_{kl}$  is stress,

$E_k$  is the electric field,

$D_i$  is dielectric displacement component,

and  $\varepsilon_{ik}^T$  is the permittivity of the material at constant stress.

The subscripts indicate the tensor notation.

$d_{kij}$ , the piezoelectric coefficient is one of the most important properties, which is a third rank tensor. This property is a representation of the charge developed based on the applied stress, or the strain developed based on the applied electric field. Hence, it can be represented as [12]:

$$d = \frac{\text{short circuit charge density}}{\text{applied stress}} C/N \quad (3)$$

$$d = \frac{\text{strain developed}}{\text{applied field}} m/V \quad (4)$$

The reduced piezoelectric coefficient is represented as  $d_{ij}$ , where i is the direction of poling, and j is the direction of stress. Since the magnitude of stress/strain defines how much charge can be extracted from a piezoelectric material, the mode of operation is based on the direction of stress. These directions are based on the Cartesian coordinate system as represented in Figure 4. There are three major modes of operation:  $d_{31}$ ,  $d_{33}$  and  $d_{15}$ , which are based on an indicial Cartesian system, as shown in Figure 4. Therefore, it can be observed that the  $d_{31}$  mode is one where the voltage acts in the 3 direction, which is considered as the longitudinal direction that is parallel to the applied electric field or voltage; and the resulting stresses act in the 1 direction, which is the axial direction. The  $d_{33}$  mode is such that the stress and voltage both act in

the same longitudinal direction. The  $d_{15}$  mode is a shear mode, where the voltage acts in the 1 direction, while the material is sheared in the 5 direction. Piezoelectric coefficients for commonly used piezoelectric materials are represented in Table 1.

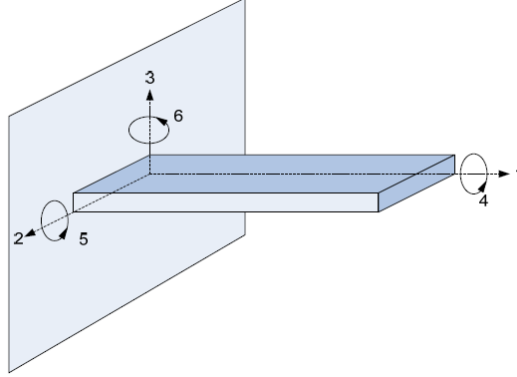


Figure 4: Cartesian Coordinate System for Piezoelectric Materials [22]

Typically, for commonly used PZT materials such as PZT-5A and PZT-5H,  $d_{15} > d_{33} > d_{31}$ . However, the shear mode is very difficult to realize in brittle ceramics such as PZT. The  $d_{33}$  mode is realized by the use of interdigitated electrodes. The most commonly used mode of operation is the  $d_{31}$  mode due to its ease of application while utilizing a piezoelectric cantilevered device. The  $d_{31}$  mode of operation is the main focus of this research. The reduced constitutive equations for this mode of operation are given as follows [23]:

$$S_1 = s_{11}^E T_1 + d_{31} E_3 \quad (5)$$

$$D_3 = d_{31} T_1 + \varepsilon_3^T E_3 \quad (6)$$

Another important property of piezoelectric materials that is not included in the constitutive equations is its electro-mechanical coupling coefficient, which for piezoelectric materials is a third rank tensor. By definition, the coupling coefficient relates the total energy put into a system to the amount of energy that is converted by the transducer. It is similar to the efficiency of the material in context, and therefore, describes how efficiently the input mechanical energy is converted into electrical energy. In the absence of a load such as a resistor on the output of the transducer, the ratio of the input to the output energy is equal to the square of the coupling coefficient [24]. Therefore, it can be mathematically represented as [12]:

$$k_{ij}^2 = \frac{W_i^e}{W_j^m}$$

where  $W_i^e$  is the electrical energy stored at the output port of the transducer in the  $i$  axis, and  $W_j^m$  is the mechanical energy input into the system in the  $j$  axis. Typical  $k_{33}$  and  $k_{31}$  values for common piezoelectric materials are also included in Table 1.

Table 1: Coefficients of common piezoelectric materials [6, 14]

Property	PZT-5H	PZT-5A	BaTiO <sub>3</sub>	PVDF
$d_{33}$ ( $10^{-12}$ C/N)	593	374	149	-33
$d_{31}$ ( $10^{-12}$ C/N)	-274	-171	75	23
$k_{33}$	0.75	0.71	0.48	0.15
$k_{31}$	0.39	0.31	0.21	0.12
Relative Permittivity ( $\epsilon/\epsilon_0$ )	3400	1700	1700	12

The electromechanical coupling coefficient reported in Table 1 however is based on unconstrained conditions, such as a freestanding beam, or a bar-like shaped bulk material where the resonance frequency of the device is very high. In conditions where the boundary conditions can cause the resonance frequency of the device to be closer to the frequency of operation, the electromechanical coupling coefficient is greatly affected, and deviates from theoretical, or manufacturer furnished values. In such cases, the electromechanical coupling coefficient can be calculated based on the resonance and anti-resonance frequency of the device, or the open-circuit and short-circuit resonance frequency of the device, given as [25]:

$$k^2 = 1 - \left(\frac{f_r}{f_a}\right)^2 \quad (8)$$

where  $f_r$  is the resonance frequency of the device, and  $f_a$  is the anti-resonance frequency of the device. These values can be obtained from impedance spectroscopy, which are explained in the methodology section.

In a similar fashion, the electromechanical coupling coefficient can also be calculated from the open circuit and short circuit resonance frequencies as [6]:

$$k^2 = \frac{\omega_{OC}^2 - \omega_{SC}^2}{\omega_{OC}^2} \quad (9)$$

where,  $\omega_{OC}$  is the resonance frequency of the device in open-circuit conditions, and  $\omega_{SC}$  is the resonance frequency of the device under short circuit conditions.

Therefore, as mentioned earlier, the piezoelectric coefficients in the  $d_{33}$  mode are higher than in  $d_{31}$  mode, and the higher coupling coefficients also illustrate that the longitudinal mode is theoretically more efficient. However, this mode is more difficult to realize since piezoelectric materials such as PZT are brittle, and under compression they can crack when mechanically strained beyond certain limits. The  $d_{31}$  mode is realized in the form of cantilevered devices, where the material is displaced in the direction of poling, and the charge is generated as a function of strain in the material, and the cantilevered boundary condition allows for the maximum possible strain on a beam or a plate like structure.

The most commonly used structures for cantilevered piezoelectric energy harvesters are piezoelectric bimorphs, which contain two layers of PZT materials that sandwich a metallic shim, which is used for structural compliance. The two piezoelectric layers can be poled in opposite directions; which is called series poling, or they can be poled in the same direction, which is called parallel poling. An illustration for the two poling cases is shown in Figure 5 [26].

In order to understand the operation of these piezoelectric bimorphs, an electrical representation is convenient, as shown in Figure 6 [26]. Each piezoelectric layer is represented as a current generating source in parallel with an inherent capacitor. As the cantilevered piezoelectric bimorph is bent, the stresses in the surface under tension have a positive sign, and the stresses in compression have a negative sign. Therefore, in the case of series poled bimorphs, with opposite signs of stress, the voltages generated across the two surfaces have the same sign due to opposite polarities, and hence they add together. In the case of parallel poled bimorphs, with the stresses having the opposite signs, but with the shim layer being grounded (hence requiring an extra electrical connection), the voltages are halved, but the currents add together. Regardless of the configurations, the power generated remains the same.

Due to the simplicity of the series poling in terms of the electrical connections required, and the fact that it is associated with higher voltages, series poled bimorphs are chosen for the work in this dissertation.

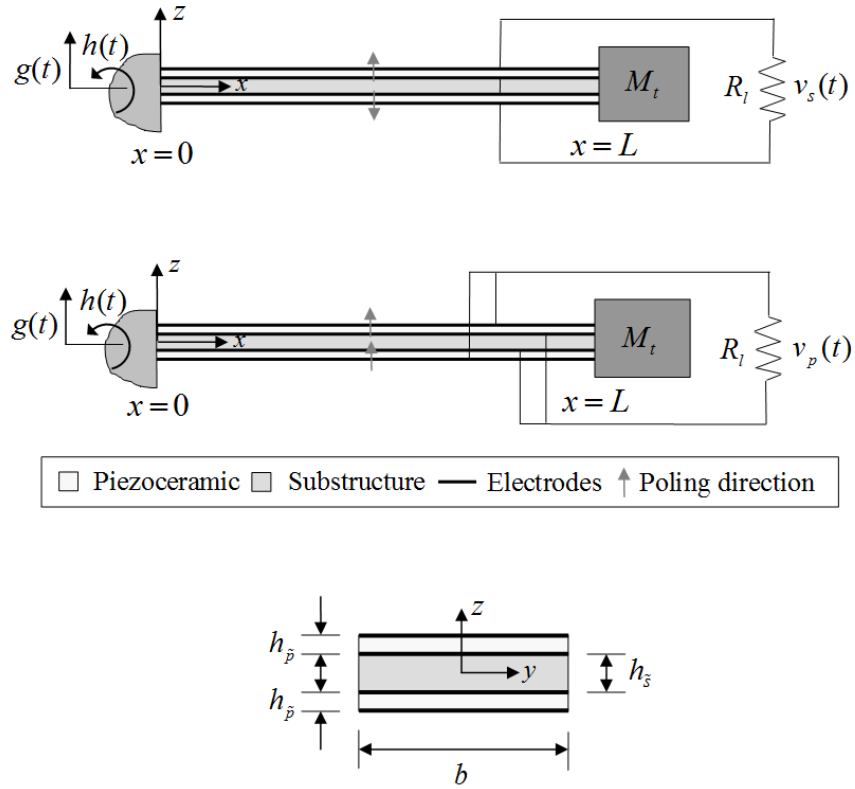


Figure 5: Series and Parallel poling in piezoelectric bimorphs [26]

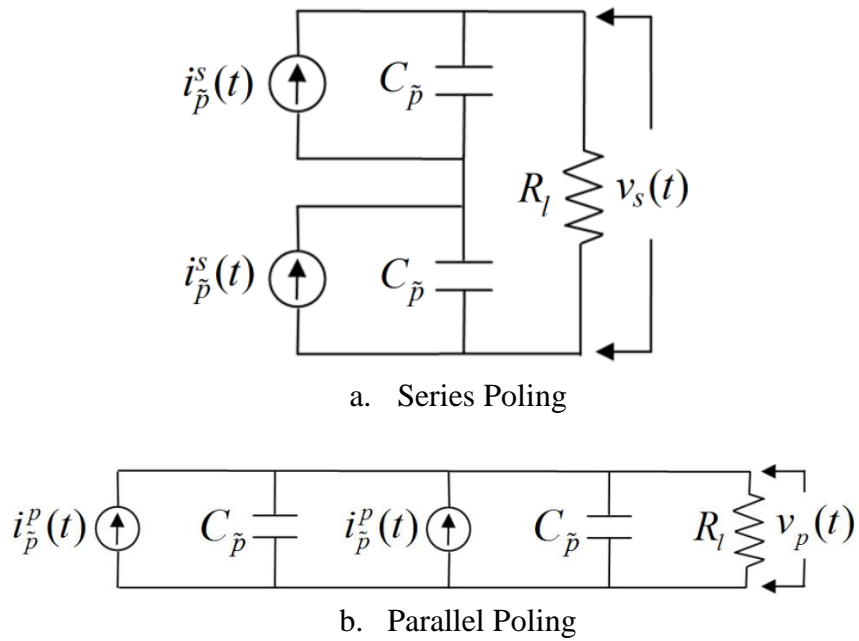


Figure 6: Electrical representation of (a) Series, (b) Parallel poled piezoelectric bimorphs [26]

## 2.2 Literature Review on Piezoelectric Generators

Various types of piezoelectric transduction generators have surfaced in the past few years. Some of the early studies were performed on impact coupled devices, followed by human powered piezoelectric energy harvesting. This was done in order to test the feasibility of piezoelectric devices for power generation, and have been mentioned very briefly.

### 2.2.1 Impact Coupled Devices

The transduction mechanism for piezoelectric devices requires a form kinetic energy, which can be converted into mechanical energy. Some of the early studies that were conducted in this area for consideration and validation of the piezoelectric effect were conducted by Umeda et al [27], where a 5.5 g steel ball was impacted on a piezoelectric 0.25 mm thick generator, while obtaining an efficiency of less than 10% into a resistive load of 10 k $\Omega$ . The low efficiency was attributed to a loss of energy, which was attributed to the bouncing of the ball. Other impact energy experiments that have been conducted have been reviewed in [12].

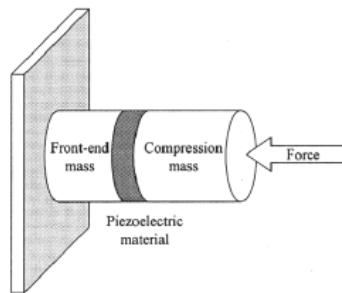


Figure 7: Impact on a piezoelectric bulk generator [27]

## 2.3 Human Powered Piezoelectric Generation

A study on generating power from humans while walking was conducted by Shenck et al [10] which consisted of retrofitting a shoe with piezoelectric devices. The devices were placed below the insole of a shoe, consisting of an 8 layer PVDF stave laminated with electrodes operating under the  $d_{31}$  mode. At walking frequencies of 0.9 Hz, this device produced an average power of 1.3 mW into a 250 k $\Omega$  resistive load. With an added PZT dimorph structure under the heel as shown in Figure 7, the device is capable of generating an alternating voltage with walking, and an average power of 8.4 mW into a 500 k $\Omega$  load.

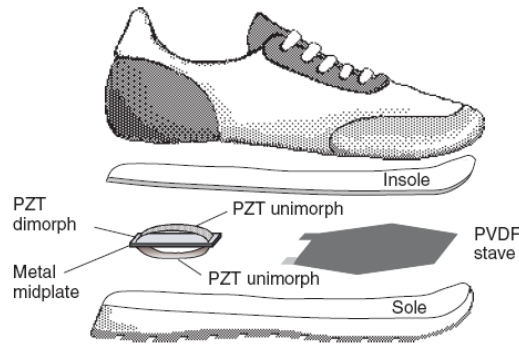


Figure 8: Shoe insert power generator [10]

The above studies are examples of power generated using piezoelectric devices upon impact or human power as a source of energy. Such studies have been further looked into from various authors, as reviewed by Beeby et al [12], which give an illustration of the work done by researchers in using piezoelectric devices for power generation.

## 2.4 Energy Harvesting from constant base excitations

Rather than impact coupled devices as mentioned in the previous section, in recent years, various researchers have developed and explored the use of ambient vibrations as a source of energy for the generation of electricity using piezoelectric devices. The use of an ambient source of kinetic energy such as vibrations to produce power can be depicted by using inertial based generators, such as the one realized by Williams and Yates [13] shown in Figure 9. Such systems consist of a seismic mass  $m$ , on a spring  $k$ . When the inertial frame is sinusoidally excited in the form  $y(t) = Y\sin(\omega t)$ , the seismic mass undergoes a relative displacement  $z(t)$  with respect to the frame. This relative displacement drives a transducer, that is depicted by a damper  $d$ , to generate electrical energy, and also accounts for the parasitic losses encountered by the system based on its damping coefficient.

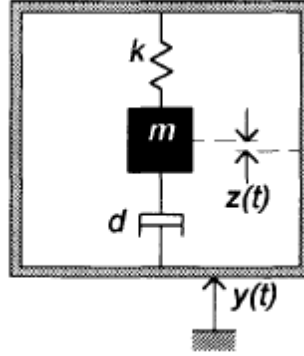


Fig. 1. Schematic diagram of the generator.

Figure 9: An inertial generator representing an energy scavenging system from vibrations [13]

The equation of motion describing the motion of the mass with respect to the frame due to the sinusoidal excitation is given as:

$$m\ddot{z} + d\dot{z} + kz = -m\ddot{y} \quad (10)$$

The steady state solution for the displacement of the mass is given by:

$$z(t) = \frac{\omega^2}{\sqrt{\left(\frac{k}{m} - \omega^2\right)^2 + \left(\frac{d\omega}{m}\right)^2}} Y \sin(\omega t - \phi) \quad (11)$$

where  $\phi$  is the phase angle given by:

$$\phi = \tan^{-1}\left(\frac{d\omega}{k - \omega^2 m}\right) \quad (12)$$

The instantaneous power can be calculated as the product of the force acting on the mass and its velocity, which can be represented as:

$$p(t) = -m\dot{y}[\dot{y}(t) + \dot{z}(t)] \quad (13)$$

Taking Laplace transform for P, we arrive at:

$$P = \frac{m\zeta_T\omega^3 \left(\frac{\omega}{\omega_n}\right)^3 Y^2}{\left(1 - \left(\frac{\omega}{\omega_n}\right)^2\right)^2 + \left(2\zeta_T \frac{\omega}{\omega_n}\right)^2} \quad (14)$$

where

$$\zeta_T = \frac{d}{2m\omega_n} \quad (15)$$

and  $\omega_n$  is the natural frequency of the system

If  $\omega = \omega_n$  then

$$P = \frac{mY^2\omega_n^3}{4\zeta_T} \quad (16)$$

Or,

$$P = \frac{mA^2}{4\omega_n\zeta_T} \quad (17)$$

However, since these are steady state solutions, the maximum power does not tend to infinity as damping tends to zero. In fact, the power available from the vibrating structure is limited by the undesirable parasitic damping  $\zeta_p$  such as air damping. Therefore  $\zeta_T$  is a summation of parasitic damping  $\zeta_p$  and electrical damping  $\zeta_e$ . The expression for power obtained can therefore be attained as

$$P = \frac{mY^2\omega_n^3\zeta_e}{4(\zeta_e + \zeta_p)^2} \quad (18)$$

or in terms of excitation amplitude as

$$P = \frac{mA^2\zeta_e}{4\omega_n(\zeta_e + \zeta_p)^2} \quad (19)$$

The above model has certain restrictions, wherein certain assumptions are to be made in order to apply it to a piezoelectric transducer. One of the major assumptions is that the seismic mass is much larger as compared to the system, and acts as the main driving force for the generator. In addition, the transducer that is represented by the dashpot is assumed to be a linear transducer. These assumptions are a bit crude for a cantilever beam with a small tip mass, but important conclusions can be made based on the model that depicts important behavior for the piezoelectric generator. These conclusions are provided in the following bullets [6, 13]:

- Maximum power is generated at the resonance frequency of the system where the displacement is maximized. Therefore, a system could be designed where  $z(t)$  is maximized within allowable limits.
- Power generated is finite, and reduction in the damping factor results in increased mass displacement.
- However, low damping ratio results in a high peak power concentrated at a particular natural frequency. Therefore, an increased bandwidth for power generation can be obtained with higher damping factors.
- Since power generation is inversely proportional to the resonant frequency at a given acceleration, the system should be designed to operate at the lowest available fundamental frequency.
- The power generated is proportional to the square of the input acceleration amplitude

## 2.4 Energy Harvesting from Vibrations using piezoelectric cantilever devices

The above model is a depiction of a piezoelectric generator in the form of a single degree of freedom lumped parameter model, wherein the power generated is dominated by the seismic mass placed in the system. While this model gives a general idea about the behavior of a piezoelectric generator, it neglects many details of the piezoelectric converter. An analytical model has been developed by Roundy et al in order to account for various factors of the piezoelectric bimorph such as the bending behavior in the  $d_{31}$  mode, and the constitutive equations involved in it. This is done by incorporating the physical characteristics of the bimorph as equivalent electrical components, which make up the mechanical subsystem of the generator. This includes the seismic mass modeled as an inductor  $L$ , the damper is shown as a resistor  $R$ , and the stiffness of the beam is modeled as the capacitor  $C$ . The across variable on the mechanical subsystem is the stress  $\sigma$ , and the through variable is the strain  $\delta$ . The electrical subsystem includes voltage  $V$  as the across variable, and current  $i(t)$  is the through variable. The coupling between the mechanical and electrical subsystems is represented by the number of coils in the transformer represented by  $n$ . The overall equivalent circuit model is shown in Figure 10, which is solved by applying Kirchhoff's current and voltage laws. A complete derivation is provided in the author's publications [5, 6, 23].

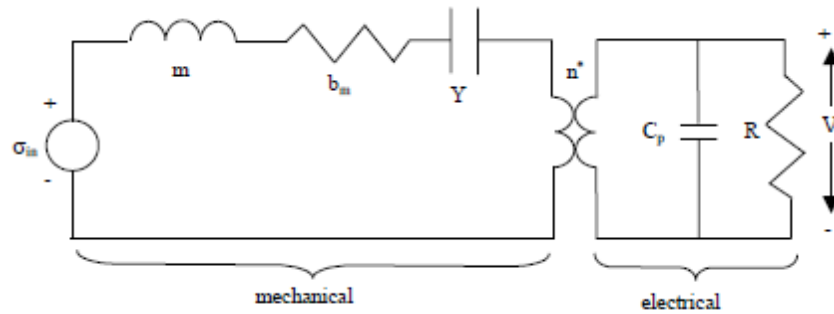


Figure 10: Equivalent Circuit Model for Piezoelectric Bimorph with a Resistive Load [5]

The vibration input is shown as a stress generator ( $\sigma_{in}$ ), which comes from the input acceleration  $\ddot{y}$ . The relationship between the two is

$$\sigma_{in} = \frac{m}{\ddot{b}} \ddot{y} \quad (20)$$

where  $\ddot{b}$  is the geometric constant relating average bending stress to force at the end of the beam:

$$\ddot{b} = \frac{2I}{b(2l_b + l_m - l_e)} \quad (21)$$

The constitutive equations for piezoelectricity are reduced to

$$\sigma = -dYE \quad (22)$$

$$D = -dY\delta \quad (23)$$

Using the above equations, the resulting model is shown as:

$$\ddot{\delta} = \frac{-k_{sp}}{m} \delta - \frac{b_m b^{**}}{m} \dot{\delta} + \frac{k_{sp} d}{m t_c} V + b^* \ddot{y} \quad (24)$$

$$\dot{V} = \frac{-Y d t_c}{\varepsilon} \dot{\delta} \quad (25)$$

Assuming  $\omega = \omega_n$ , the analytical expression for power transferred to the load is shown as:

$$P = \frac{1}{\omega_n^2} \frac{R C_p^2 \left( \frac{Y_c d_{31} t_c b^*}{\varepsilon} \right)^2}{(4\zeta^2 + k_{31}^4)(R C_p \omega)^2 + 4\zeta k_{31}^2 (R C_p \omega) + 2\zeta^2} A_{in}^2 \quad (26)$$

where,

$$b^* = \frac{3b}{l_b^2} \frac{2l_b + l_m - l_c}{2l_b + 1.5l_m} \quad (27)$$

$b$  = distance from center of piezo to center of shim

$l_b$  = length of the beam (not covered with mass)

$l_c$  = length of electrode (in most cases assumed to be  $<$  or  $=$  to  $l_b$ )

$l_m$  = length of the mass

This analytical model that was developed provides further insights into the piezoelectric energy harvesting system from a cantilevered bimorph, that were absent in the Williams and Yates model. The input parameters, driving frequency and acceleration amplitude have profound effects on power generation. In addition, the equation describes the importance of the coupling coefficient, the piezoelectric coefficient, damping ratio, and the geometric constants that are dependent on the beam's and proof mass geometry.

This analytical model was verified by the author on a PZT 5A cantilever beam with a proof mass as shown in Figure 11 [1]. The resonance frequency of the structure was measured, and tuned to a desired driving frequency of 120 Hz, using an attached proof mass, and driven with an acceleration amplitude of  $2.25 \text{ m/s}^2$ , which matches the driving frequency and amplitude of a small microwave oven. The output was measured at different load resistances, and the simulated and experimental power generated is presented in Figure 12, which showed decent validity for the model.

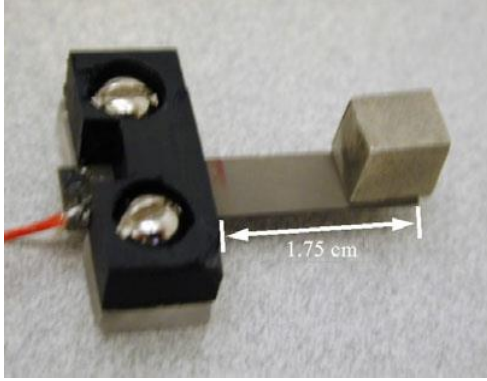


Figure 11: Vibrating Piezoelectric generator with attached proof mass [1]

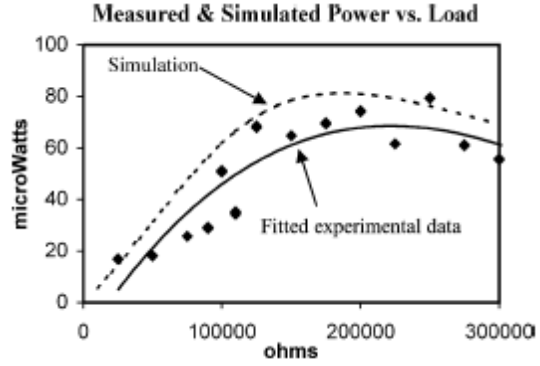


Figure 12: Measured output power versus resistive load [1]

It can be seen that the power dissipated into the load resistor has a maximum value. This occurs when the mechanical damping and electrical damping ratios in the system are matched. This optimal load resistor can be estimated as a function of total damping in the system, and other characteristics of the system. This optimal load resistance can be estimated as:

$$R_{opt} = \frac{1}{\omega C_p} \frac{2\zeta}{\sqrt{4\zeta^2 + k^4}} \quad (28)$$

The optimization of the device to derive the maximum amount of power was also performed by Roundy et al, as illustrated in [6], where the design parameters included the parametric dimensions of the beam, electrode and mass. In general, increasing the mass load on the cantilever device would increase the strain on the material, but then it diminishes the surface of the electrode where the charge is actually generated. Two designs that were optimized are shown in Figure 13, where the constraint was to keep the overall volume of the structure within  $1 \text{ cm}^3$ . Tungsten being one of the most dense structures was utilized as the proof mass, and attached to the surface, and ‘Design 2’ provided a power output of  $375 \mu\text{W}/\text{cm}^3$ . This device was capable of powering a radio transceiver with a capacitor used for energy storage, and achieved a duty cycle of 1.6%.

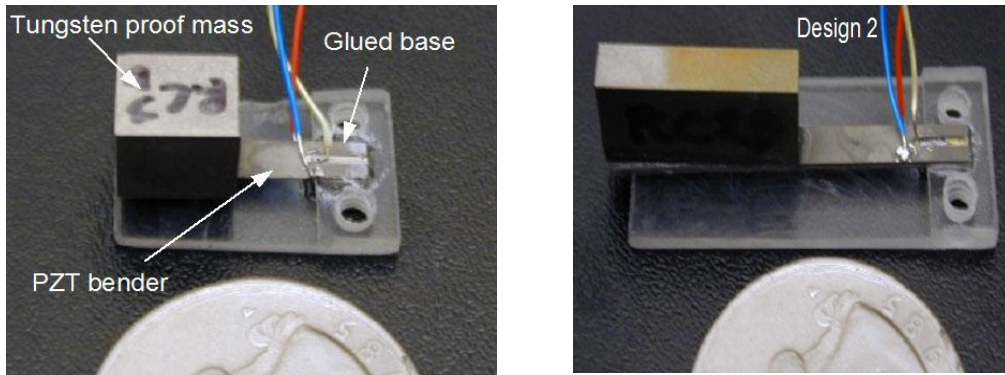


Figure 13: Design optimization for piezoelectric bender [6]

Around the same time, Sodano et al investigated [28] the use of a commercially available actuator, Quick Pack QP40N (Mide Technology Corporation) cantilevered on a mechanical shaker, where the piezoceramic is a composite formed from four piezoceramic elements embedded in a kapton and epoxy matrix. This study honed in on the effect of impedance on damping at various resistive loads. The manufacturer reports that the device with a proof mass would be capable of generating about  $1.7 \mu\text{W}/\text{cm}^3$  power at 113 Hz and 1g acceleration [12].

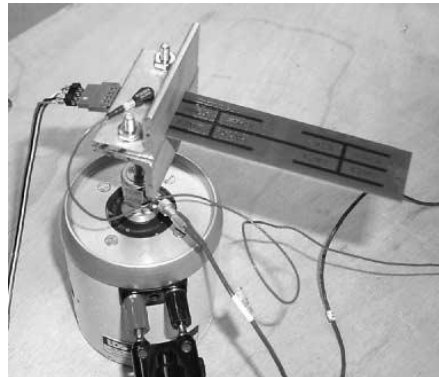


Figure 14: Quick Pack actuator for vibration energy harvesting [28]

## 2.5 Distributed Parameters Models

The lumped parameter models mentioned provide useful insights into the dynamic behavior of piezoelectric bimorphs, but they are reported to be accurate for systems that have large proof masses attached to them. For smaller proof masses, or in the absence of proof masses, various corrections need to be accounted for, which have been realized by Erturk and Inman [14, 29, 30]. This model is based on deflections induced by the bending dynamics of the cantilever, and not on static Euler-Bernoulli assumptions as used by other researchers. The developed general equation of motion based on a continuous system, which is accurate for a cantilever beam is developed using Hamilton's principle and solved using the Rayleigh-Ritz method. The general equation of motion for the coupled cantilevered bimorph device is given as:

$$Y_p I \frac{\partial^4 w_{rel}(x, t)}{\partial x^4} + c_s I \frac{\partial^5 w_{rel}(x, t)}{\partial x^4 \partial t} + c_a \frac{\partial w_{rel}(x, t)}{\partial t} + m \frac{\partial^2 w_{rel}(x, t)}{\partial t^2} + \vartheta V(t) \left[ \frac{d\delta(x)}{dx} - \frac{d\delta(x - l_b)}{dx} \right] = -[m + M\delta(x - l_b)] \frac{\partial^2 y}{\partial t^2} \quad 29$$

where,

$Y_p$  is the Young's modulus of the piezoelectric material

$I$  is the 2<sup>nd</sup> moment of area of the bimorph

$w_{rel}$  is the transverse displacement of the tip relative to the host

$c_s$  is strain rate damping

$c_a$  is damping due to air

$M$  is the proof mass

$\delta(x)$  is the Dirac delta function

$\vartheta$  is the backward coupling term, dependent on material properties and dimensions.

This equation of motion is solved by expanding the relative displacement in the form

$$w_{rel}(x, t) = \sum_{r=1}^{\infty} \varphi_r(x) \eta_r(t) \quad 30$$

where,

$\eta_r(t)$  is the modal coordinate, and

$\varphi_r(x)$  is the mode shape.

Therefore, the dynamics of the mode-shape can be described by the set of coupled equations:

$$\ddot{\eta}_r(t) + 2\zeta_r\omega_r\dot{\eta}_r(t) + \omega_r^2\eta_r(t) + \chi_r V(t) = f_r(t) \quad 31$$

$$\frac{C_p}{2}\dot{V}(t) + \frac{V(t)}{R_L} = i(t) \quad 32$$

where,  $\chi_r$  is the modal coupling term correlated to the mode shape  $\varphi_r$ ,  $\omega_r$  is the resonant frequency,  $f_r(t)$  is the mechanical forcing function and  $C_p$  is the inherent equivalent capacitance of the piezoelectric layer.

Under a pure sinusoidal excitation of the fixed end of the cantilever with a frequency  $\omega_r$ , the electric voltage across the piezoelectric layers in series becomes

$$V = \frac{j2\omega R_L \kappa_r F_r}{(2 + j2\omega R_L C_p)(\omega_r^2 - \omega^2 + j2\zeta_r\omega_r\omega) + j2\omega R_L \kappa_r \chi_r} \quad 33$$

where  $F_r$  is the amplitude of the modal mechanical forcing function, and  $\kappa_r$  is the forward coupling term

Based on a similar approach, with coupled equations of motion, similar to equations 31 and 32, a distributed parameters model for a piezoelectric bimorph with a varying cross-sectional area was presented by Dietl and Garcia [31]. More recently, a similar analysis with expressions for voltage generated by the piezoelectric cantilever have been presented by Rosa and De Marquis Jr. [32]. The expression for voltage generated is given as:

$$\begin{aligned} \frac{V(t)}{a(t)} &= \frac{V(t)}{-\omega^2 Y_0 e^{-j\omega t}} \\ &= j\omega \left( \frac{1}{R} + j\omega C_p \right)^{-1} \Theta^T \times \left[ -\omega^2 \mathbf{M} + j\omega \mathbf{C} + \mathbf{K} + j\omega \left( \frac{1}{R} + j\omega C_p \right)^{-1} \Theta \Theta^T \right] p^* \end{aligned} \quad (34)$$

where,  $\Theta$  is the electromechanical coupling matrix, and the superscript T is for constant stress.  $p^*$  is the input matrix, defined in [32].

It can be noted that due to the changing cross-sectional area, equation (34), and similar equations in [31, 32] for tip displacement or tip velocity are not provided in closed-form. Detailed derivations for these expressions are available in the references mentioned. Hence the terms  $\mathbf{M}$ ,  $\mathbf{C}$ ,  $\mathbf{K}$ , are the mass, damping and stiffness matrices respectively, which are calculated as a function of axial length of the device, where the width varies.

## 2.6 Shape Optimization of single cantilever beams

The piezoelectric power generators tested by Roundy and Sodano as shown in the previous section indicate that the power generation is directly related to the magnitude of the proof mass on the structure. This is also evident in the analytical models developed by William and Yates [13], and Roundy [23] where the input stress from vibrations on the cantilevered structure is due to the force provided by the proof mass. However, the placement of such a proof mass is constrained by the mechanical limits on a cantilevered structure, which should not exceed a maximum stress on a structure. On a rectangular cantilever that is loaded at its free end, the maximum stress is concentrated near the clamped end, which linearly decreases with length. The concentration of maximum stress is generally located over a very small area, and this could greatly diminish the loading that could be applied on a cantilevered bimorph, which being made out of brittle piezoceramics such as PZT would be imperative. This was realized by Roundy et al in [18] where they mention that bulk material properties impose a strain limit of 500 microstrain (one microstrain is the strain producing a deformation of one part per million ( $10^{-6}$ )) on the bimorph to avoid brittle fracture.

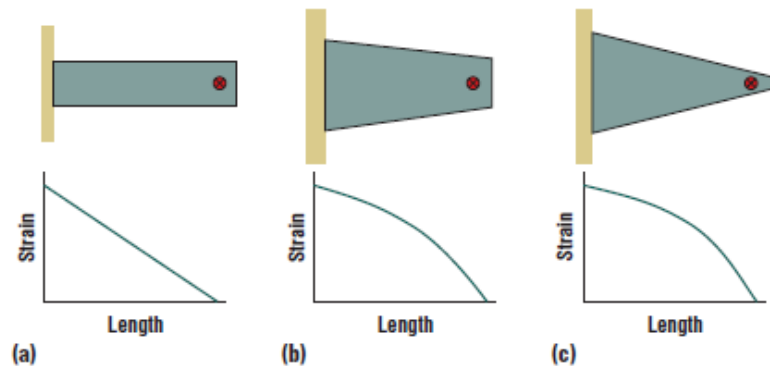


Figure 15: Effect of shape change on the transversal stress along the length of a cantilever [18]

Therefore, in order to mitigate the effects of a large stress concentration near the fixed end of a cantilever beam, which diminishes with a constant slope as shown in Figure 15 [18], there is a motivation to lower the maximum axial stress on the surface in order to make it less susceptible to brittle fracture. Moreover, the decreasing stress distribution along the length of the cantilevered beam also directly translates into inefficient charge generation over the surface. The magnitude of stress at a location dictates the amount of charge being generated at that location, and hence the small stress concentrated area near the clamped end of a beam would generate more charge, while the rest of the cantilever where the stress is decreasing would not be

generating as much charge. Therefore, there is an impetus to find a way of generating equal charge along the length of the beam, while maintaining the maximum stress level below a critical level. Hence, there is a quest to linearize the stress and strain along the length of the beam.

One of the ways to obtain this linearized strain distribution over the surface of the bimorph is by modifying the surface topology of the cantilevered devices. Such modified geometries have been explored by a few researchers. Glynn-Jones et al [33, 34] mentioned a tapered geometry in their early study in the development of thick-film MEMS piezoelectric generator based on PZT5H material, poled for  $d_{31}$  operation. The device geometry, as shown in Figure 16 was tapered such that the piezoelectric patch was an isosceles trapezoid in shape with a base width of 20 mm and a top width of 10 mm, while the PZT layer thickness was 0.07 mm. therefore the PZT patch was  $1.05 \text{ mm}^3$  in volume. This device was able to produce  $3 \mu\text{W}$  of power in to a resistive load of  $333 \text{ k}\Omega$  while resonating at its fundamental frequency of  $80.1 \text{ Hz}$ .

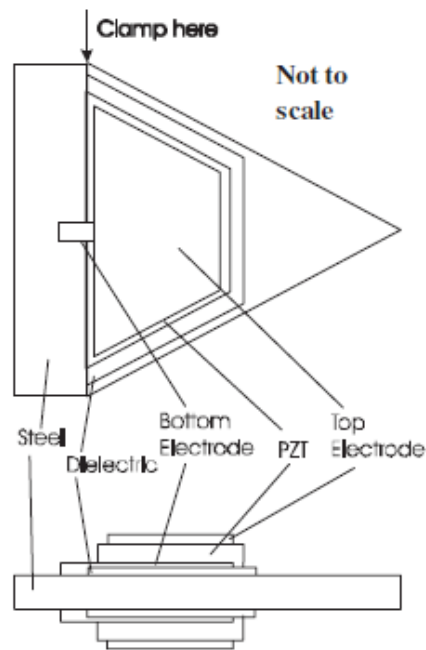


Figure 16: Development of MEMS scale PZT harvester with a tapered piezoelectric patch [34]

In a similar fashion, Friswall and Adhikari [35] studied the effect of four shapes of piezoelectric patches on the surface of a rectangular substrate with fixed dimensions. Based on numerical simulations, it was shown that a triangular patch on the rectangular substrate having a smaller active area produced more power than the fully covered rectangular device. The power generated was into a  $100 \text{ k}\Omega$  load resistor, which may not be the optimal value for both devices. The maximum power generating device from this study was a shorter rectangular patch

on a larger rectangular substrate. Even though the numerical model and example presented was not exhaustive enough to conclude an optimal geometry, the impetus to investigate the effect of changing geometry with changing electromechanical coupling and capacitance was presented.

Mateu and Moll [36] analyzed the tapering effect in homogeneous, symmetric heterogeneous, and asymmetric heterogeneous structures. The homogeneous structures were modeled as two piezoelectric sheets of identical dimensions bonded together, without the presence of a metallic layer. The symmetric heterogeneous structures consisted of two piezoelectric layers sandwiching a metallic layer, and this case is similar to the bimorph as studied in this study. The asymmetric structure can consist of varying numbers piezoelectric and metallic layers, but the study illustrates the use of one piezoelectric layer on a metallic layer, thus representing a unimorph. The cross-sections of these various structures are shown in Figure 17.

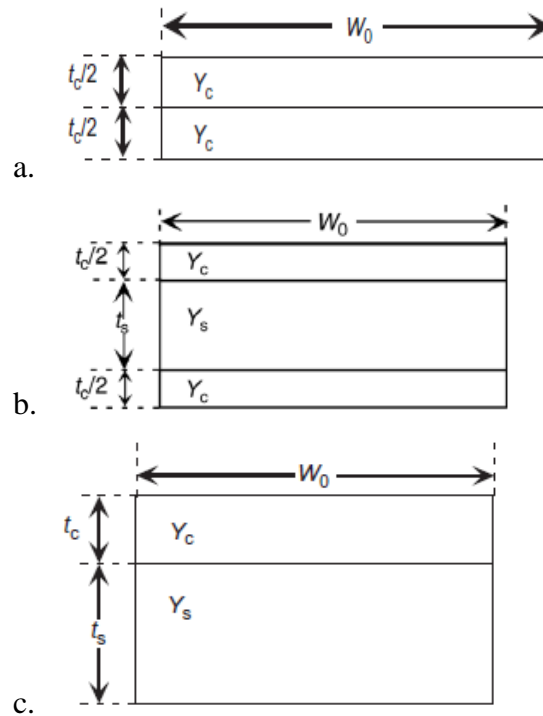


Figure 17: Cross-sections of a) Homogeneous, b) symmetric heterogeneous and c) asymmetric heterogeneous cantilevers [36]

The study focuses on developing mathematical equations for calculating average strain ( $S_{\text{average}}$ ) over the surface of the material for the three structures for the rectangular and triangular shapes. Each of these structures have an overall length  $L$ , which in case of the triangular structure is the altitude. The width  $W_0$  is the base of the rectangle, or the width of the triangle at the base, which linearly decreases with the relation:

$$W(x) = W_0 \left(1 - \frac{x}{L}\right) \quad (35)$$

where  $x$  is any position along the length of the beam.

The average strain for a homogenous structure can be defined as a product of the net strain along the length ( $x$ ) and thickness ( $z$ ) directions as:

$$S_{average} = \frac{1}{t_c/2} \frac{1}{L} \int_0^{t_c/2} \int_0^L \frac{z}{\rho(x)} dz dx \quad (36)$$

where  $t_c$  is the thickness of the piezoelectric layer,  $L$  is the length of the beam,  $z$  is the distance from the neutral axis, which for the homogeneous case is  $t_c/2$ , and  $\rho(x)$  is the radius of curvature of the beam under a concentrated load at the free end of the cantilever.

This results in the following expressions for average strain and maximum deflection for a rectangular homogeneous cantilever:

$$S_x = \frac{3FL}{2Y_c W_0 t_c^2} = \frac{3}{8} \frac{y_{max} t_c}{L^2} \quad (37)$$

$$y_{max} = \frac{4FL^3}{Y_c W_0 t_c^3} \quad (38)$$

And for a triangular homogenous cantilever:

$$S_x = \frac{3FL}{Y_c W_0 t_c^2} = \frac{y_{max} t_c}{2L^2} \quad (39)$$

$$y_{max} = \frac{6FL^3}{Y_c W_0 t_c^3} \quad (40)$$

The above expressions provide very useful insights into behavior of cantilever beams under a point load. For a triangular cantilever, the radius of curvature  $\rho(x)$  is a constant value, and therefore, the strain becomes a constant value through its length. Therefore, for an identical load, the average strain in a rectangular cantilever is 75% of the triangular cantilever as a function of its maximum deflection. In fact in such a case, the maximum deflection of the rectangular cantilever is also seen to be 67% of the triangular cantilever.

The authors in this study also develop similar expressions for the symmetric heterogeneous (bimorph) case. However, here the maximum deflection is restricted by a cavity depth ( $D$ ), and therefore values for absolute maximum deflection and average strain for these cases are not available. However, it may be possible to replace  $D$  with  $y$ -max in these

expressions to obtain absolute deflections. The resulting expressions for triangular homogenous cantilevers are:

$$S_x = \frac{Dt_c}{2L^2} \quad (41)$$

$$y_{max} = \frac{6FL^3}{Y_c W_0 t_c^3} \quad (42)$$

$$z_s = \frac{t_c}{2} \quad (43)$$

And for symmetric heterogeneous triangles, the expressions are given as:

$$S_x = \frac{Dt_c}{2L^2} \left(1 + 2 \frac{t_s}{t_c}\right) \quad (44)$$

$$y_{max} = \frac{6FL^3}{Y_c W_0 t_c^3} \frac{1}{1 + 3(t_s/t_c) + 3(t_s/t_c)^2 + (Y_s/Y_c)(t_s/t_c)^3} \quad (45)$$

$$z_s = \frac{t_c + t_s}{2} \quad (46)$$

Therefore, these expressions can be quite useful in understanding the strain behavior in different types of cantilevers. In the case of homogeneous and symmetric heterogeneous triangular cantilevers, the average strain and maximum deflection are independent of the Young's modulus (which is not the case for asymmetric heterogeneous triangular cantilevers). Also, the average strain in the triangular cantilevers can be increased with increasing thickness ratio of shim thickness to piezoelectric layer thickness. Increasing strain also results in increased charge, which is evident from the constitutive equations, and also equations for harvested power. These equations are elaborated in the reference [36].

In a later study, Goldshmidtboeing and Woias [37] also characterized the differences between rectangular and triangular cantilevers, and also included a truncated rectangle, which was effectively a trapezoidal cantilever. They developed and verified an analytical model, based on which the inferences are made in the study. Unlike the previous study where the cantilevers were characterized for bending behavior using an average stress, this study employed the use of a relative mean curvature  $\kappa'$  in order to characterize the stress homogeneity:

$$\kappa' = \frac{|\kappa_{mean}|}{|\kappa_{max}|} \quad (47)$$

where  $\kappa_{mean}$  refers to the mean curvature of the piezoelectric layer at its surface, and  $\kappa_{max}$  is the maximum absolute value at the surface. Based on the above equation, perfect homogeneity

would occur when  $\kappa'$  is equal to 1; i.e. the radius of curvature would be constant. On the other hand, as  $\kappa'$  goes to zero would imply that the curvature is not defined.

The shapes in this study are classified using a truncation ratio  $r$ , which is a ratio of the base width to the tip width; and hence a rectangle would have an  $r$  value of 1, while a triangle would have a truncation ratio of 0. Figure 18 gives some useful insights into the behavior of three different shapes characterized by the  $r$  values. It can be seen that when the relative mean curvature  $\kappa'$  is plotted as a function of tip mass that is normalized to the mass of the beam, the maximum  $\kappa'$  occurs when the tip mass is 10 times the mass of the beam. For the triangular cantilever, a  $\kappa'$  of 1 is achieved at this loading condition, and hence the radius of curvature, and hence strain can be considered to be constant when the tip mass is 10 times the mass of the beam. The maximum  $\kappa'$  for a trapezoidal beam (with  $r = 0.15$ ) is roughly 0.86, and for the rectangular cantilever is 0.5, indicating that these shapes never obtain constant strain conditions. The first two mode shapes for the triangular cantilever with no tip mass, i.e. when  $\kappa' = 0.61$  from Figure 18 is shown in Figure 19, which clearly shows that the first mode shape has linear bending at a position past  $0.3L$ , where  $L$  is the length of the beam. This happens to be the location of the centroid of a triangular beam, and therefore, a rectangular cantilever without a tip mass has better efficiency since its centroid is located at  $0.5L$ . This effect is further investigated and shown in Figure 20 by simulating values for normalized power for different beam shapes with three cases for mass loading. This figure shows that with changing truncation ratios, i.e. from  $r=0$  (triangle) to  $r=1$  (rectangle), normalized power remains same, which by the authors is explained by opposing mechanisms of mean curvature, which is higher in triangular cantilevers, that is canceled out by the centroid location. However, the maximum mass loading condition in Figure 19 is where the mass of the tip is equal to the mass of the beam, which according to Figure 18 is a condition where the mean curvature is about 0.61, which is well below the desired mean curvature of 1. However, Figure 21 does show an advantage of truncating the shape from a rectangular to a triangular cantilever, as it can be seen that the loading capacity in terms of tolerable acceleration amplitudes is greatly increased for triangular cantilevers.

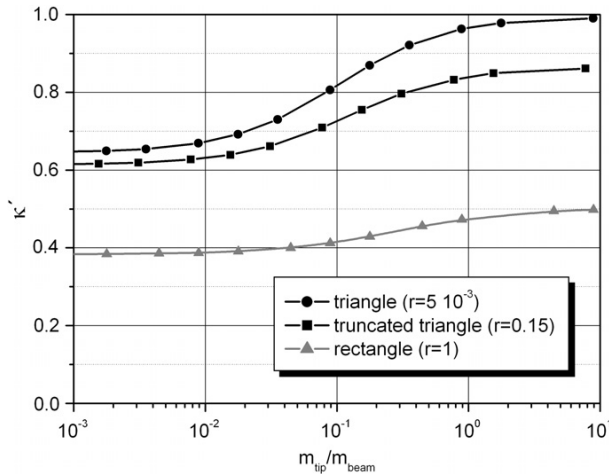


Figure 18: Mean curvature for rectangular, trapezoidal and triangular beam for various tip mass-to beam mass ratio [37]

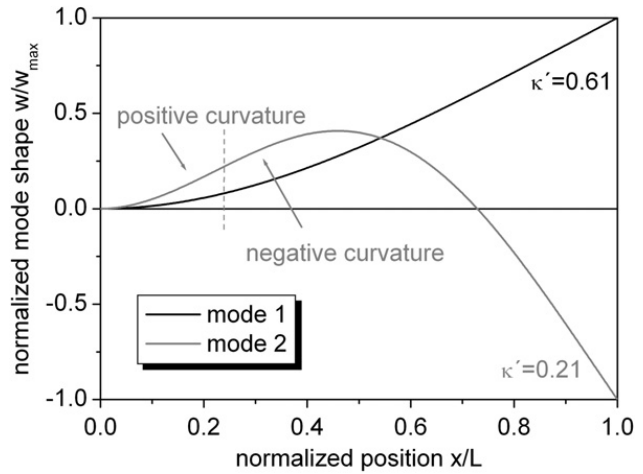


Figure 19: Mode shapes for triangular beam with no tip mass [37]

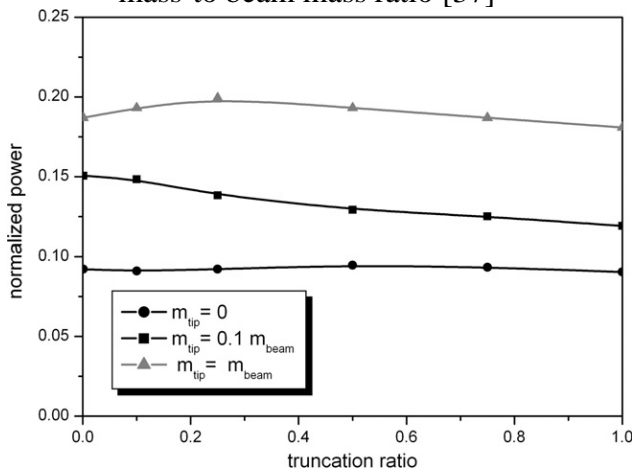


Figure 20: Normalized power for various shapes based on truncation ratio's for different tip masses [37]

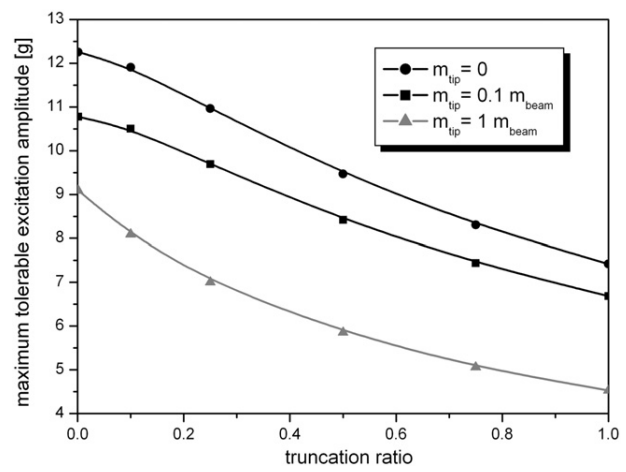


Figure 21: Maximum achievable excitation amplitude based for different shapes [37]

Dietl and Garcia [31] conducted a study for the optimization of beam shapes for power harvesting. They developed a mathematical model using Hamilton's principle, similar to that done by Erturk and Inman [29], but for a varying cross-section, over the surface, and used the Rayleigh-Ritz method to solve the Hamiltonian operators. This method was verified with experimental results first, and then utilized search algorithms in MATLAB for optimization of beam structures. The first exercise conducted was to test three geometries which included a rectangular beam, a tapered beam, and a reverse tapered beam, each of which had a target resonance frequency of 28 Hz, and hence had slightly varying lengths, as shown in Figure 22. These beams were characterized by plotting their mode shapes for each geometry that was

calculated using the analytical model. Figure 23 (a) shows how the amount of deflection in the reverse taper beam, which is the shortest of the three is the highest. More interestingly, they plotted the second derivative of the mode shape, which happens to be the second spatial derivative of the displacement function. This second derivative of the mode shape clearly shows which represents the effect of changing geometry by providing a schematic that is directly proportional to the strain on the surface of the beam, as shown in Figure 23 (b). Therefore, this curve representing the second derivative for each shape (Figure 23 (b)) can be compared to a plot that represents calculated strain distribution along the length of the beam which is shown in Figure 22 (a). However, with tapering geometry over the surface of a beam, the electric field generated at a particular area is not constant due to the changing width, and hence it is weighted with it. This is done by multiplying the strain at a particular transversal location with the width at that point, and dividing that by the mass of the beam at that location. This provides a measure of the effective electric field being generated at each location, as it can be seen in Figure 24 (b).



Figure 22: Three geometries showing Rectangular, Tapered and Reverse-Tapered bimorphs

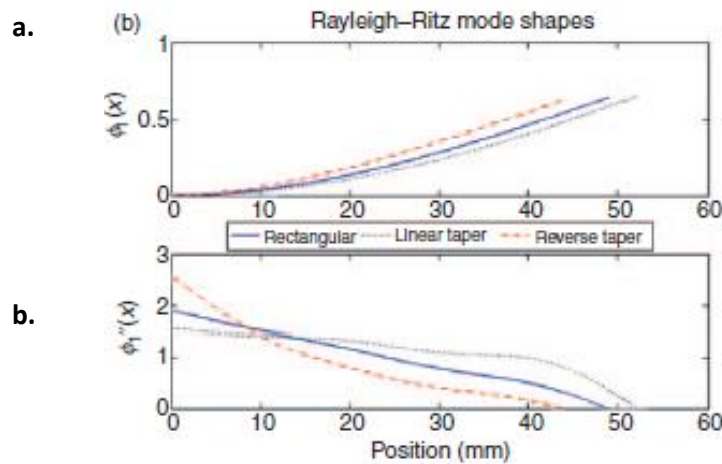


Figure 23: a) Mode shapes for the three geometries b) 2<sup>nd</sup> spatial derivative of mode shape

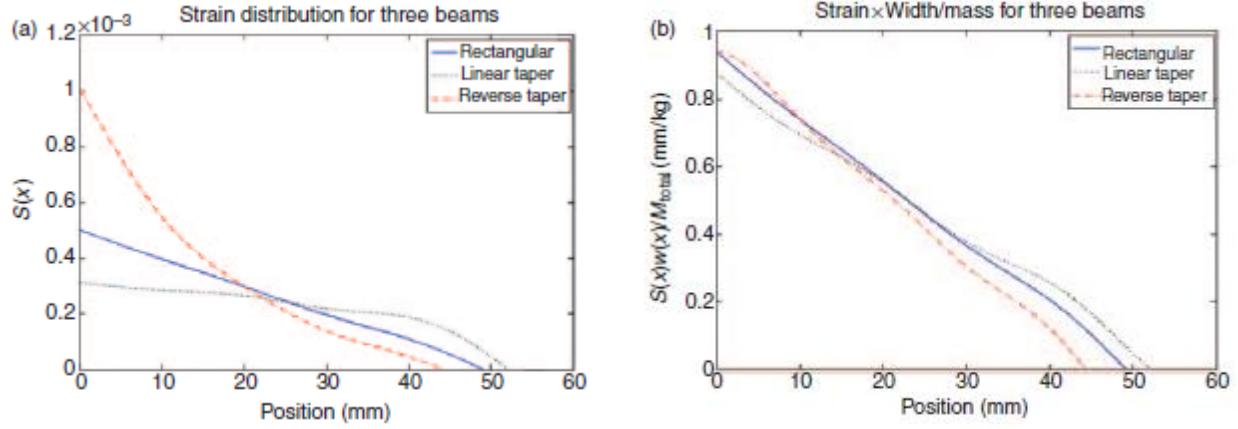


Figure 24: a) Strain distribution along the length over the surface of the beam, and b) weighted strain distribution due to tapering through the length of the beam

Figure 24 (b) provides an important inference. Even though Figure 24 (a) shows that the amount of strain over the surface of the beam drastically changes due to changing geometry, where the tapered beam has a much more linear distribution over its surface, and the reverse tapered is much more skewed, the effect of changing geometry seems to be negated due to the weighting of the strain in those areas, as these plots are more or less linear through the length of the beam. However, as it was pointed out in the last study by Goldshmidtboeing and Woias [37], the fact is that these geometries are not being operated at their limit, and the linear taper has a larger tolerance for acceleration amplitude, which is also conceded by Dietl and Garcia.

Following this, they utilized a method to find an optimal geometry with a linear profile, and also a non-linear profile, by means of calculating an integral where the negative of the average voltage squared that was minimized, as shown in the expression:

$$J = - \lim_{T \rightarrow \infty} \frac{1}{T} \int_0^T V(t, w(x), L)^2 dt \quad (48)$$

where  $T$  is stress,  $V$  is voltage,  $t$  is thickness,  $L$  is length, and the beam shapes are defined using the function  $\tilde{w}(\tilde{x}) = a_0 + a_1\tilde{x} + a_2\tilde{x}^2 + \dots$ . Hence, the linear tapered beams would have no higher order polynomial terms.

Therefore, using this, a linear optimum and curved optimum geometry is shown in Figure 25. Both these geometries had a negligible improvement in performance, and hence results from these are not illustrated here.

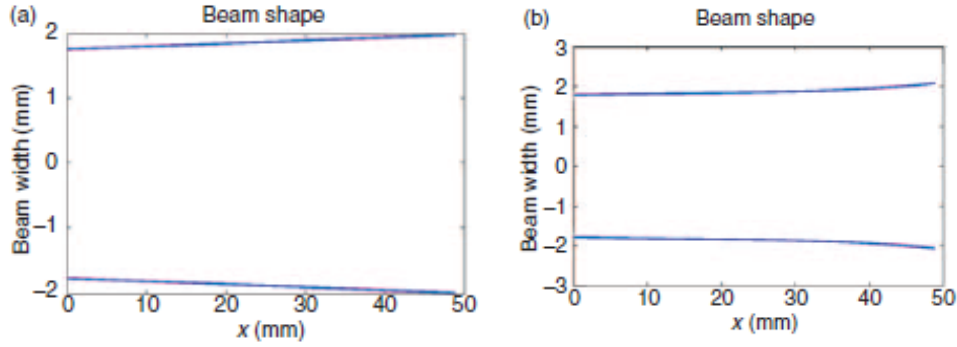


Figure 25: Geometries showing a) optimal linear, and b) optimal curved profile

As mentioned earlier, the beams in Figure 24 and Figure 25 were characterized without taking into account the maximum strain that can be withstood by each of them respectively, and hence the optimization did not show any drastic improvements. Another optimization was thus carried out taking into account the maximum acceleration amplitude that can be tolerated by each of these shapes, and in doing so, another non-linear geometry was explored as well, which is plotted in Figure 26. This geometry has a wider base tip which tapers down, and then curves back out to facilitate the positioning of a large proof mass. The wider base allows a large acceleration amplitude tolerance, and the wider tip perhaps provides greater amount of bending.

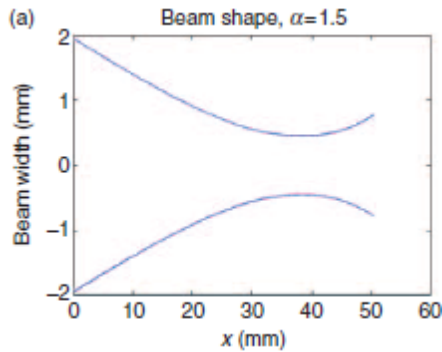


Figure 26: Non-linear optimized geometry

The effect of maximizing the strain for each particular geometry that include the rectangular, linear taper (trapezoidal), reverse taper, and the optimal geometry (Figure 26) can be seen in Figure 27. Figure 27 (a) depicts the strain distribution over the surface, and shows that modifying geometry has a profound effect on each of these structures, where the linear taper has a greater amount of strain compared to the rectangle, and the modified optimal structure is even higher, specially in the areas where the beam is narrow. The weighted strain plot in Figure 27 (b) also shows that when these structures are operated at their maximum strain, the weighted strain

through the length of the beam gives a clear indication of performance of these devices. It can be inferred that the amount of allowable strain in the material can be improved by maxing a wider base, allowing a greater acceleration amplitude, and higher loading. This is evident when noticing the behavior of the reverse tapered beam, which has the lowest strain distribution, and also the lowest weighted strain, which is due to the realization that this configuration is most susceptible to fracture, and has the lowest allowable loading.

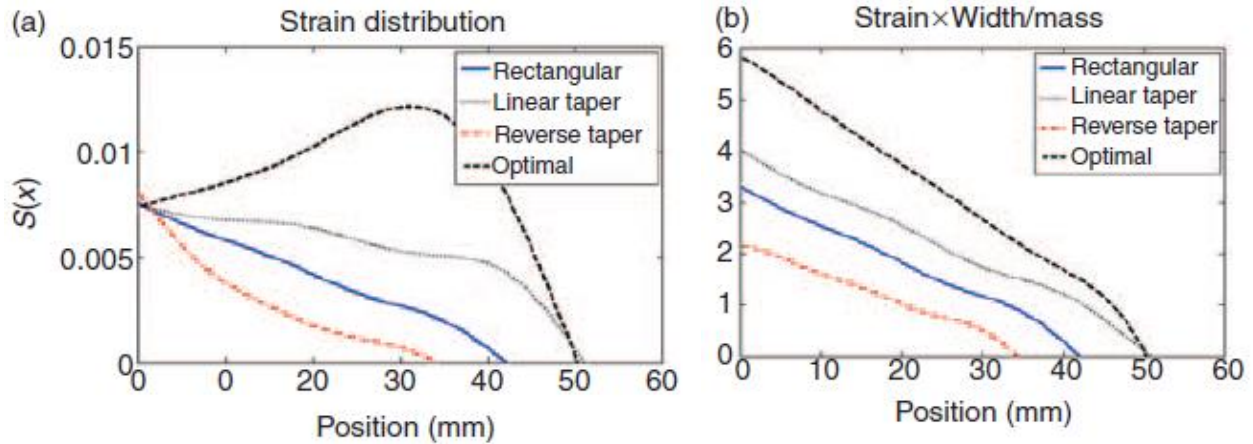


Figure 27: Effect of geometry on a) strain distribution, and b) weighted strain, when the structures are under maximum allowable excitation amplitudes.

A study conducted by Park et al [38] analyzes the stress distribution over the surface of cantilever devices with two geometries – a rectangular cantilever and a trapezoidal one, using fabricated PZT devices. The authors describe that in a rectangular device, the stress is concentrated near the fixed end of a beam, and therefore the area is mainly responsible for the generation of voltage, while the rest of the beam is essentially inactive in power generation. By changing the geometry to a trapezoidal shape, the stress and strain is more evenly distributed through the length of the cantilever, and thus there is a greater power output. Under an acceleration input of  $2.45 \text{ m/s}^2$ , and with a normalized power output based on the real area of the electrodes, this is confirmed in results, where the power output is 39% higher for the trapezoidal cantilever compared to the rectangular cantilever under.

Benasciutti et al [39] looks into the optimization of power output using cantilever beams of optimized shapes as well. The authors realize two types of trapezoidal geometries – the normal trapezoidal and a reverse trapezoidal. In the normal trapezoidal setup, the wide end of the beam is fixed, while in the reverse trapezoidal geometry, the wide end is free, and a proof mass

is attached there. The authors mention that the highest conversion of mechanical energy to electrical energy can be achieved when the material is completely strained. However, in the case of the reversed trapezoidal geometry, since the beam is clamped at the narrow end, it results in a large stress concentration at the fixed end. This however facilitates the positioning of a large proof mass.

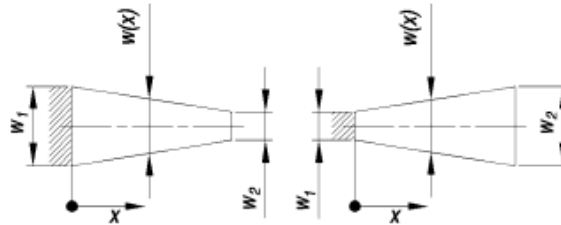


Figure 28: Trapezoidal and Reverse Trapezoidal geometries [39]

The results from this study indicate that the power output from a reversed trapezoidal structure is greater than that of a regular trapezoidal device, and far greater than that of a rectangular geometry. The authors attribute the result to the notion that efficiency of a trapezoidal system are affected by the clamping of the wide end, which causes the voltage levels to drop through the system. This is not convincing enough, since the authors do not indicate that the proof mass situated on both the trapezoidal geometries are identical. They also do not report an effective volume or electrode surface area. In fact, from visual inspection, the proof masses seem to be too large for the structure, and it would be worthwhile reporting a static stress analysis with the described parameters. Other studies have also surfaced, that challenge the optimization of power from tapered piezoelectric bimorphs [40].

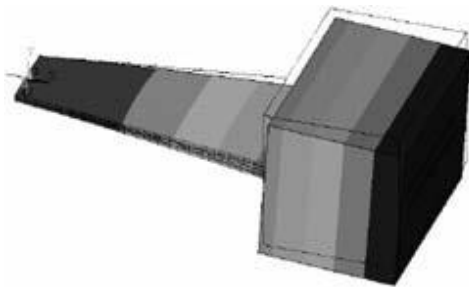


Figure 29: Reverse Trapezoidal geometry with a proof mass [14]

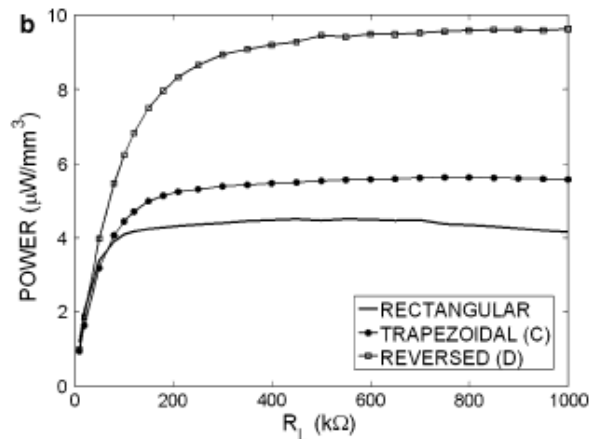


Figure 30: FEM results from scavenger shapes of equal maximum transversal widths

With the outlook for a larger strain through the cantilever device, Park et al [41] explored some innovative designs for piezoelectric energy harvesting. Although, the study is focused towards tip excitations with a fixed amount of displacement amplitude, rather than base excitations with fixed acceleration amplitudes, the authors report resonance frequencies for the devices that vary considerably. However, the authors compare geometries with similar overall areas, and constrain the overall length. In order to design the geometry, the authors chose 4 equally spaced lateral control points referred to as design variables through the length of the beam. A design optimization formulation to maximize power output was solved using the Sequential Quadratic Programming algorithm in MATLAB, and an optimal geometry was found. It is noted, as shown in Figure 31 that with similar areas, as in Design 1, 2, and 4, a wider tip provides increasing amounts of power. Design 3 shows the maximum amount of power, attributed to the largest tip width and the largest area.

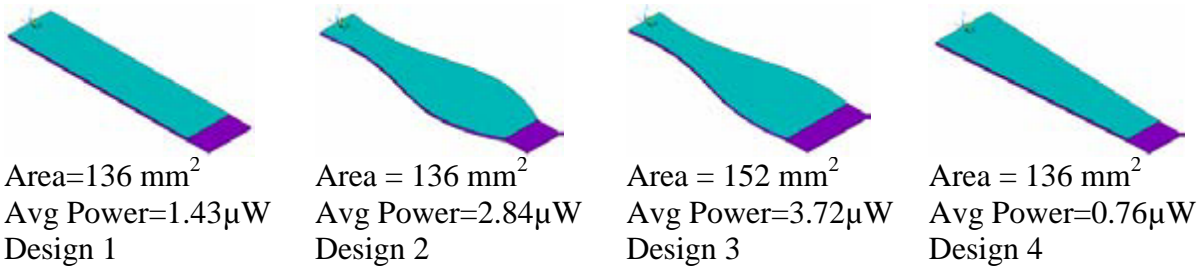


Figure 31: Optimal shapes: Maximum average power [15]

While the authors report that Design 3 generates the largest amount of power with comparable area, the comparison is conducted over varying resonance frequencies. It is interesting to note that the device with the highest power output is the one with the lowest fundamental frequency, around 500 Hz, and the tapered device in Design 4 has the highest fundamental frequency, over 600 Hz.

## 2.7 Optimization of cantilever beams with zigzag structures

A study conducted by Berdy et al [42] demonstrates a novel design of creating a zigzag-like meandered device for power energy harvesting. The main motivation behind this work is to address the issue of charge cancellation; the authors utilize the distribution of strain across the device, by strain-matching two electrodes that are next to each other in the meandered device. It can be seen in Figure 31 (b), that the strain on an electrode (as shown in the light blue color) is a lot lower on the electrode that is next to it (which shows a strain contour). The authors report that there is a significant improvement in the output voltage, by 5 times as compared to the single electrode design. It is true that the charge cancellation is a factor, but an important factor that the authors do not report is the actual distribution of strain throughout the device that most likely provides a much larger average strain when the structure is vibrating, contributing a large power output.

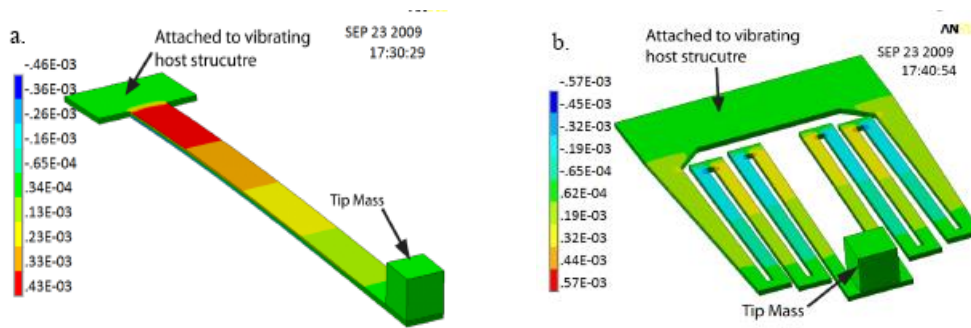


Figure 32: Single and Meandered cantilever device [16]

An in depth study in the numerical modeling of a zigzag geometry has been done by Karami and Inman [43] with the quest of developing a geometry that would resonate at frequencies that are suitable for applications at the MEMS scale. One of the basic parameters identified is the length to thickness ratio, which in a previous study by Lu et al was chosen to be 10:1. This provided resonance frequency to be 3 kHz, which is too large for these applications, and thus the device modeled in this study has a length to thickness ratio of 100:1.

Moreover, the superiority of this type of shape provides a deflection that is 3 times the maximum deflection to that of a simple rectangular beam under the same static load. Therefore, in addition to charge cancellation, the authors do indicate that the larger deflections, resulting in the larger strains do provide much higher output power. An actual prototype has not yet been microfabricated, but a bulk scale device shows good agreement with an analytical model in the

same paper for resonance frequencies and deflections. Also, with the increasing number of members, as shown in Figure 32 the resonance frequency substantially decreases, and with the 11 member structure, the resonance frequency is decreased to 1/17 that of a cantilever beam with the same thickness and beam length.

In addition, this device can also undergo torsional vibrations, i.e. bending at higher frequency modes, which could allow the use of  $d_{15}$  mode from the piezoelectric effect, which allows a much higher piezoelectric coefficient. A recent article [11] by the same authors has proposed the use of such a device for heart pacemakers as an application.

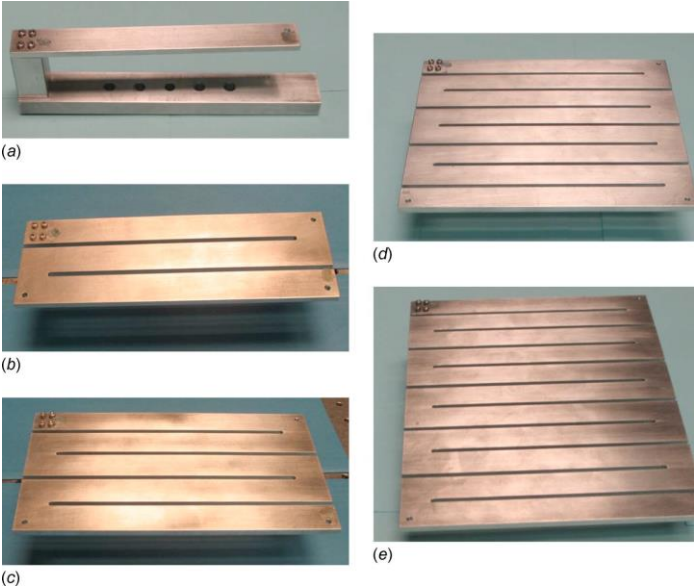


Figure 33: Zigzag cantilever device for piezoelectric energy harvesting [17]

## 2.8 Optimized shape with variable thickness

One design parameter that intuitively comes to mind for design optimization is controlling the thickness of the beam, since it is the greatest contributing factor to the moment of inertia for a beam, and hence the spring constant. In order to obtain a constant strain through the material, this is a design parameter that can be varied. One such study has been reported by Paquin and St-Amant [44], where the authors mathematically model a tapered beam, as shown in Figure 34 and obtain analytical equations for power dissipation for such devices, which have been compared to FEA results. The interesting aspect of this study is that the authors discuss various parameters such as thickness at free end and are able to decouple these by determining a slope angle  $\theta$ , as indicated in Figure 34. They parameterized an optimal slope angle of  $0.94^\circ$ , which increased the power output by 3.6 times when compared to a constant thickness cantilever with similar dimensions. This would effectively be higher, since the volume of the tapered beam would be lower. This device was not microfabricated, but it would be interesting to see if two piezoelectric layers were bonded on a tapered brass shim, and obtain experimental results for such a device.

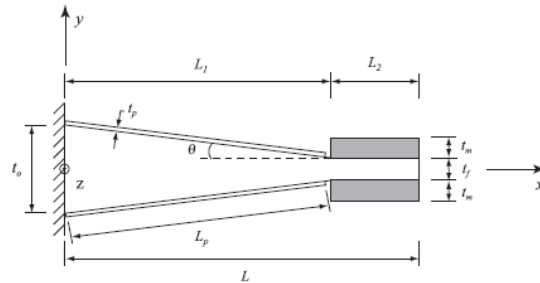


Figure 34: Tapered cantilevered piezoelectric bimorph [18]

## 2.9 Torsional system for $d_{15}$ and $d_{36}$ modes

Most of the literature reported for the optimization of power output by changing geometry, and enhancing strain through the cantilever bimorph device has been reported for the  $d_{31}$  mode, where the voltage generated and applied strain are perpendicular to each other. Thus, mode 1 vibration can be easily applied for this. It has been reported that the  $d_{15}$  mode provides a much higher conversion efficiency, and also larger piezoelectric coefficient. However, this is not as easily extractable, as this requires a shear mode displacement, as illustrated in Figure 34, and with the PZT materials being fairly brittle, there is a chance for fracture. It is also very difficult to apply the right amount of shear on the material to actually access the  $d_{15}$  mode.

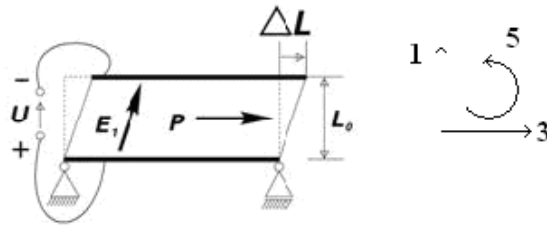


Figure 35: Operating principle of a shear mode piezoceramic.  $E_1$  is the electric field developed, and  $P$  is the poling direction [19]

One possibility of accessing the  $d_{15}$  mode displacements could be using torsional motion on a circular tube. Piezoelectric devices could be bonded to the outer surface of a cylindrical tube. The fabrication of such a device would be difficult, but nevertheless the concept is one that can extract a higher amount of energy directly as a consequence of the higher dielectric coefficient.

The design setup as shown in Figure 35 shows the possibility of using the  $d_{15}$  mode, where the piezoceramic would have to be poled in the tangential direction, when attached on the surface of the torsional tube. The torsional tube also presents the possibility of using the  $d_{36}$  mode, and in this case the poling direction would have to be in the radial direction, as depicted in Figure 37. No experimental or numerical work was presented in this study, and it remains a concept.

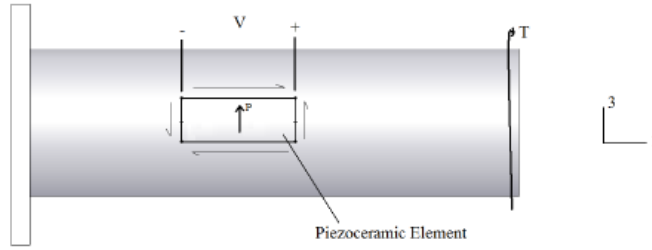


Figure 36: Poling and harvesting directions for the  $d_{15}$  shear mode harvester [19]

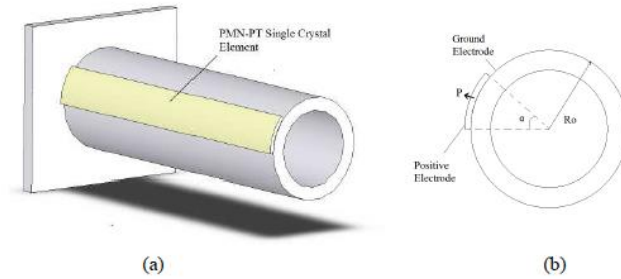


Figure 37: Poling and harvesting direction for the  $d_{36}$  mode energy harvester [19]

## 2.10: Studies on parameter identification and optimization

The previous section indicated studies on optimizing shape to enhance power output from cantilevered bimorph structures with changing geometry. Another approach to enhance power is by considering the enhancement of efficiency by identifying lumped parameters, and enhance coupling in the system. Shu and Lien presented two studies [45, 46] identifying an equivalent circuit based lumped parameter model based on the spring-mass-damper system in series with a AC-DC rectified energy harvesting system. In these studies, the importance of conversion efficiency, with regards to the generation of optimal power were identified by characterizing the coupling in the system, while introducing several non-dimensionless terms. In general, the harvested power per unit mass is described as:

$$\frac{P}{M} = \frac{A^2}{\omega_{SC}} \bar{P}(r, \Omega, k_e^2, \zeta_m) \quad (49)$$

Here, it can be seen that the power per unit mass is directly proportional to the square of the base acceleration  $A$ , and inversely proportional with the short-circuit resonance frequency of the cantilever beam. The short-circuit resonance frequency is equivalent to the resonance frequency of an uncoupled device, i.e. without any electrically induced damping due to the coupling effect in the piezoelectric system.

$k_e^2$  is the electromechanical coupling coefficient, and

$\zeta_m$  is the mechanical damping ratio, which is the inverse of the Quality factor  $Q_m$

The term  $\bar{P}$  represents non-dimensional power normalized by the input function, represented as:

$$\bar{P} = \frac{P}{\frac{F_0^2}{\omega_n M}} \quad (50)$$

The term  $r$  is the normalized resistance, based on the short circuit resonance frequency, and the inherent capacitance of the piezoelectric device, in conjunction with the external load resistor  $R$  as:

$$r = C_p \omega_{SC} R \quad (51)$$

The term  $\Omega$  represents the resonance frequency of the device normalized with the short circuit resonance frequency. Thus,

$$\Omega = \frac{\omega}{\omega_{SC}} \quad (52)$$

Therefore, the short circuit and open-circuit resonance frequencies are:

$$\Omega_{SC} = 1 \quad (53)$$

$$\Omega_{OC} = \sqrt{1 + k_e^2} \quad (54)$$

It can be quickly realized that with large electromechanical coupling coefficients, the shift from the short circuit resonance frequency to the open circuit resonance frequency would be large.

The magnitude of the electromechanical coupling coefficient and the mechanical damping ratio in fact has a much wider implication. It has been reported that small values of the figure of merit, i.e. where  $k^2 Q_m \ll 1$ , there exists one value for the optimal load resistance, where maximum power is generated. These are regarded as low coupling systems. In such cases, it is reported that the maximum power generated can never match the power available in the mechanical system. For higher coupling systems where  $k^2 Q_m \gg 1$ , there exist two values where power can be maximized.

This discussion was further refined in Goldschmidtboeing et. al (2011) [47], where a threshold value of 2 for the coupling figure of merit is presented, which is attributed due to the presence of resonance and anti-resonance. This publication highlights the use of a unimorph with a thick passive layer for a low coupling harvester, and the use of a bimorph with as the high coupling harvester, where a  $k^2 Q_m$  value of 8.2 was reached.

Lei et. al [48] provide an excellent explanation of the threshold value of 2 for the electromechanical coupling figure of merit. Based on their SDOF equivalent circuit model, and expressing impedance in terms of coupling and a transformation factor, it is found that the peak phase angle becomes zero when  $k^2 Q_m = 2$ . At this point, maximum power can be drawn from a single optimal load resistance, by performing a complex conjugate impedance match [49]. As the peak phase angle is greater than zero, two optimal load resistance values can be found, contributing to two optimal load resistance values. In the instance where the peak phase angle is less than zero, i.e. when it is negative, complex conjugate impedance matching is not possible.

Xiong and Oyadiji present an exhaustive numerical study [50] on parameterizing the electromechanical coupling coefficient, quality factor, and the mass ratio. The mass ratio is defined as the effective-mass-of-the-beam to the total mass of the beam. All three parameters

affect the electromechanical coupling figure of merit, and the study illustrates the transitioning of the low coupling harvesters with a single optimal load resistor, to an intermediate region that does not display optimal load resistance values as peaks, to high coupling systems where two distinct optimal load resistance values are found. They also present a numerical study on tapered piezoelectric beams, and report that the electromechanical coupling coefficient is enhanced with tapering beams.

This very short compendium of a set of exhaustive and important publications highlights a few key points. They describe the importance of electrical measurements for being able to characterize piezoelectric energy harvesters, by measuring capacitance, impedance, and determining the resonance and anti-resonance frequencies. The electromechanical coupling figure of merit is an important aspect that describes the behavior of piezoelectric energy harvesters, and the numerical studies so far indicate that they have a large impact on the power generated. Therefore, this forms a basis for characterization of these materials, an aspect that is taken into consideration for the entirety of this work.

## CHAPTER 3: METHODOLOGY

The methodology section is primarily divided into two sections; the first of which describes the setup of the piezoelectric bimorph coupled with circuit elements in ANSYS Mechanical APDL, and the second one describing the experimental approaches used for sample preparation, and testing and analysis.

### 3.1 Numerical Modeling

Several researchers [39, 41, 51] have employed the use of ANSYS for modeling piezoelectric energy harvesting devices for estimation of various parameters such as stress distribution, strain, and the analysis of output voltages. Zhu et. al [52, 53] have illustrated the use of the commercial code in the most detail that gives the basis for the formulation of the numerical model used in this study, while other studies such as carried out by Takacs [54] have also provided useful insights. Excerpts have been taken from these researchers to develop this model, as described in the following paragraphs. This particular study is carried out using ANSYS Mechanical APDL, Version 14.0. The ANSYS Mechanical Help files have been used numerous times in this study.

Figure 5 in the introduction section illustrated the makeup of a piezoelectric bimorph, which consists of two piezoelectric layers that sandwich a metallic brass layer. The two piezoelectric layers are connected in series, where they are poled opposite to each other, and are connected to an external load resistor. The metallic brass layer can be modeled using the 20-node SOLID186 element, which can be used as a brick-shaped or tetrahedral shaped element. The element option is chosen to be structural. The piezoelectric layer is modeled using the 20-node coupled-field SOLID226 element, which can also be shaped as a brick or a tetrahedron for meshing purposes, and the element behavior is chosen as electrostatic-piezoelectric (element option K3). The load resistor is modeled using the two-node CIRCU94 element. The two types of elements are illustrated in Figure 38 showing various possible element shapes for the SOLID186 and SOLID226 elements, and the CIRCU94 element is shown in Figure 38, which can form various types of electrical components.

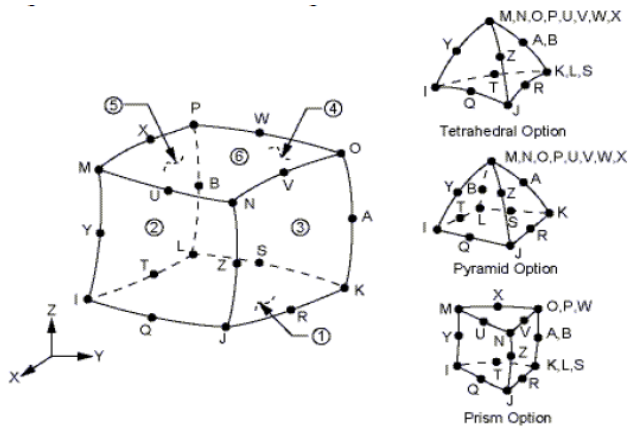


Figure 38: SOLID186 and SOLID226 element shapes

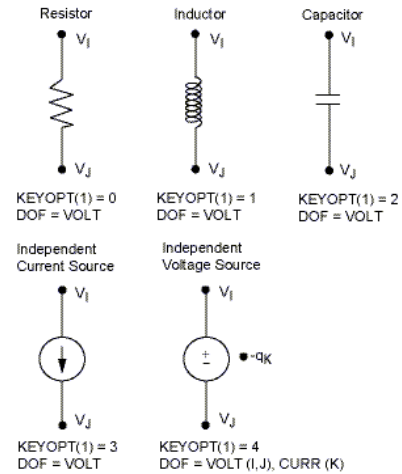


Figure 39: CIRCU98 Elements in ANSYS

Following the choice of elements, the requirement is the input of material properties for the various components of the bimorph. The brass is modeled as a linear isotropic material having an elastic modulus of 105 GPa, Poisson's ratio of 0.30 and mass density of  $9000 \text{ kg/m}^3$ .

The piezoelectric material that is modeled in this study is based on the PZT-5H material, which is the *PSI-5H4E* material from *Piezo Systems, Inc., Woburn, MA*. This material has a Poisson's ratio of 0.31 and a mass density of  $7500 \text{ kg/m}^3$ . The elastic properties of this material are anisotropic due to the fact that the stiffness (or compliance) are dependent on directions, and hence forms a  $6 \times 6$  matrix which is a 4<sup>th</sup> rank tensor. The piezoelectric coefficient is also anisotropic, which forms a 3<sup>rd</sup> rank tensor, while the permittivity values are formed as a 2<sup>nd</sup> rank tensor.

One critical thing to mention is that the compliance ( $s^E$ ) matrix, (or the stiffness matrix- $c^E$ ) when found in literature may be presented in the IEEE Standard 176 format [20]. In this format, the row order for the matrix is  $[x, y, z, yz, xz, xy]$ . ANSYS DOES NOT utilize this format. It is mentioned in the ANSYS Coupled Field Analysis Guide that ANSYS uses the standard structural matrix format, where the row order is in the form  $[x, y, z, xy, yz, xz]$ . Therefore, the  $xy$  from the IEEE format has to be inserted in as the 4<sup>th</sup> row in the matrix. Further, while entering the material properties for the compliance matrix, the matrix has to be adjusted for the direction of polarization as well. The problem set up in this project report has the piezo polarized in the  $y$ -direction, and hence the piezoelectric matrix is required to be rotated as well, since the IEEE standard usually provides the matrix polarized in the  $z$ -direction. These two

adjustments – the insertion of row xy, in the 4<sup>th</sup> row, and the rotation of the matrix to polarize the material in the z-direction are critical to performing a proper piezoelectric analysis.

The adjusted and rotated piezoelectric compliance matrix in ANSYS format for the PZT-5A material is given as [6, 7, 8]:

	X	Y	Z	XY	YZ	ZX	
	0.16400E-10	-0.72200E-11	-0.57400E-11	0.0000	0.0000	0.0000	
	-0.72200E-11	0.18800E-10	-0.72200E-11	0.0000	0.0000	0.0000	
	-0.57400E-11	-0.72200E-11	0.16400E-10	0.0000	0.0000	0.0000	(m/N <sup>2</sup> )
	0.0000	0.0000	0.0000	0.47500E-10	0.0000	0.0000	
	0.0000	0.0000	0.0000	0.0000	0.0000	0.0000	

The next property that is defined for the modeling of piezoelectric materials is the piezoelectric strain matrix [d]. Once again, the format prescribed in the IEEE 176 Standard is different than the one that ANSYS uses. The typical strain matrix is a 3x6 where the order of the 6 columns are [x, y, z, yz, xz, xy]. ANSYS requires the definition in terms of a 6x3 matrix. Therefore the matrix in the IEEE format is first transposed to the 6x3 form, and then the xy row is inserted in as the 4<sup>th</sup> row. The PZT-5A piezoelectric strain matrix (d), poled in the +Y direction is given as [6, 7, 8]:

	X	Y	Z	
X	0.0000	-0.17100E-09	0.0000	
Y	0.0000	0.37400E-09	0.0000	
Z	0.0000	-0.17100E-09	0.0000	
XY	0.58400E-09	0.0000	0.0000	(C/N)
YZ	0.0000	0.0000	0.0000	
XZ	0.0000	0.0000	0.0000	

Also, when the bimorph is used in series operation, one of the piezoelectric layers is poled in the -Y direction. This piezoelectric strain matrix has coefficients that are opposite in sign to the +Y coefficients [52]

The third required material property for modeling of piezoelectric devices is the dielectric permittivity matrix, which is an inherent material property. This is a 3x3 symmetric matrix for PZT-5A at constant stress, and the values for the material are [6, 7, 8]:

1700	0	0	
0	1730	0	(F/m)
0	0	1700	

The next step is to create the geometry of the piezoelectric bimorphs. Since Solid elements are being utilized in this work, the modeling is performed in 3-D. The piezoelectric bimorphs that are described here are described for a simple rectangular geometry. A rectangular layer with desired dimensions is modeled as an area, and then extruded to specific dimensions. The chosen bimorphs from Piezo Systems, Inc. are of the T220 series, where the thickness of

each piezoelectric layer is 0.19 mm and the thickness of the brass layer is 0.13 mm. the three extruded volumes are then glued together.

Following the generation of the structure, the volumes are meshed, but in order to do so, each layer must be assigned the proper element attributes; i.e. the top and bottom layers are modeled as SOLID226 layers, while the middle layer is assigned the SOLID186 element. The top and bottom layers are assigned material properties relevant to the piezoelectric materials, respective to poling directions, while the middle layer is assigned the material properties for the elastic isotropic brass material. Once element attributes are assigned, the mesh is setup such that the elements have an aspect ratio of 1:1 on the transverse plane (i.e. the xz plane as modeled). For example, for a rectangular bimorph that has a clamped length of 21.5 mm and width of 12.7 mm has its length divided into 50 parts, and width divided into 15 parts. A mapped mesh is then created resulting in brick shaped elements, giving an even distribution of nodes across the different layers.

The nodes on the top and bottom layers of the piezoelectric material are then coupled for voltages. This essentially creates a common node for each surface that can be used to create an electrode connection, and an external load resistor can be added in between these coupled nodes. The resistor is added by creating a single two-node CIRCU94 element between these coupled nodes, and the value of the resistance is defined as a real constant.

The next step is to enter the solution phase of the modeling, where appropriate loads and boundary conditions can be applied. The setup of the piezoelectric bimorphs is primarily as a cantilevered device, hence the areas (there are three areas due to three layers) on one of the ends of the beam are fixed in all three directions (i.e.  $U_x = U_y = U_z = 0$ ). In addition to this, one of the coupled nodes should be grounded by setting the voltage to nil, in order to provide a reference for the voltage generated by the bimorph.

At this point, a modal analysis for the structure may be performed in order to obtain its natural frequency. Therefore, the same is chosen from the “Analysis Type” menu, and the Block Lanczos algorithm is chosen. Since we are only interested in the fundamental frequency of the system, only one mode is expanded. The analysis is performed, and the fundamental frequency is recorded.

In order to simulate the piezoelectric bimorph under excitation, a harmonic analysis is performed, where the external excitation is applied by using the ACEL command. This

command is accessible as a gravity load from, under inertial loads in the Structural Loads menu. Since this load is applied at the Global Cartesian origin in the +Y direction, the beam should be modeled such that clamped end is centered on the y-axis, and the bottom layer is on the xz plane. This is shown in Figure 40. Also, harmonic analysis requires the definition of a start frequency and end frequency under the load step options menu. In order to reduce computational processing time, the frequency is swept for a range of 20 Hz around the resonance frequency. A constant damping ratio  $\zeta_p$  is defined here, which is chosen based on the quality factor  $Q$  of the piezoelectric material by using the relationship:

$$\zeta_p = \frac{1}{2Q} \quad (55)$$

Following this, the model is solved. Once the solution is completed, the voltage drop can be obtained by reading the solution at the resonance frequency substep, and either plotting the contour for electric potential, or simply listing the solution. The Time-history postprocessor can also be used to obtain the frequency response function for displacements, which provides both real and imaginary parts.

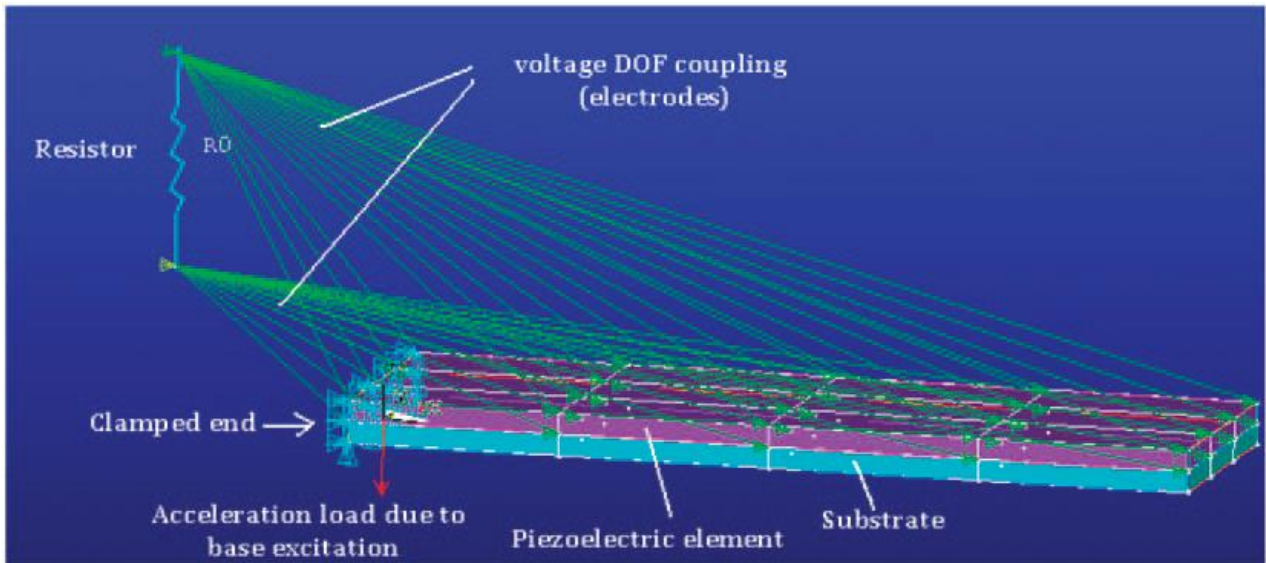


Figure 40: Example of a developed FEM model in ANSYS for a piezoelectric unimorph [51]

While a coupled-field finite element code such as the one described above has been developed for piezoelectric bimorphs, it has not been extensively used in this dissertation. A sample set of results using the ANSYS code is provided in APPENDIX A.

## 3.2 Experimental Procedure

### 3.2.1 Sample Preparation

Piezoelectric bimorphs are obtained from Piezo Systems, Inc. The material of choice is PSI-5H4E. The commercial bimorphs are available in a variety of sizes, with relevant sizes as pertaining to part numbers listed in Table 2.

Table 2: Piezoelectric Bimorphs dimensions as available from Piezo Systems, Inc

Part Number	Length (mm)	Width (mm)	Thickness of each piezo layer (mm)	Thickness of brass layer (mm)
T220-H4-103X	31.8	3.18	0.19	0.13
T220-H4-203X	31.8	6.35	0.19	0.13
T220-H4-303X	31.8	12.7	0.19	0.13
T220-H4-503X	63.5	12.7	0.19	0.13

It should be noted that the dimensions provided in Table 2 are of the piezoelectric benders as provided by the manufacturer. They do not represent the effective clamped lengths for the bimorphs. In order to maintain consistency between experiments, a standard rectangular bimorph has an effective length of 21.5 mm. This facilitates a small length for clamping, and a small area extending behind the clamp as a tail, where wires are soldered for electrical connections.

The samples that have a modified geometry, which until now has been of triangular shapes are cutouts from the above mentioned commercial bimorphs. They are usually cut from a T220-H4-303X or a T220-H4-503X bimorph, depending on the required dimensions based for parametric studies. So far two methods have been used for cutting the bimorphs, both of which have certain advantages and limitations. The first method to cut samples is done by using an Abrasive Slurry Saw – Model 850, South Bay Technology. The saw is equipped with a stainless steel wire blade, 0.15 mm in thickness. This wire-blade provides very fine cuts, but care must be taken to orient the samples properly, especially in the absence of a goniometer. Without a goniometer, the samples can be placed on a graphite holder inside a grooved pocked, angling the samples to obtain the desired shapes. An easier alternative is to print out the desired shape on a transparent film, and pasting it on the bimorph to obtain guidelines over which the blade can be placed for cuts.

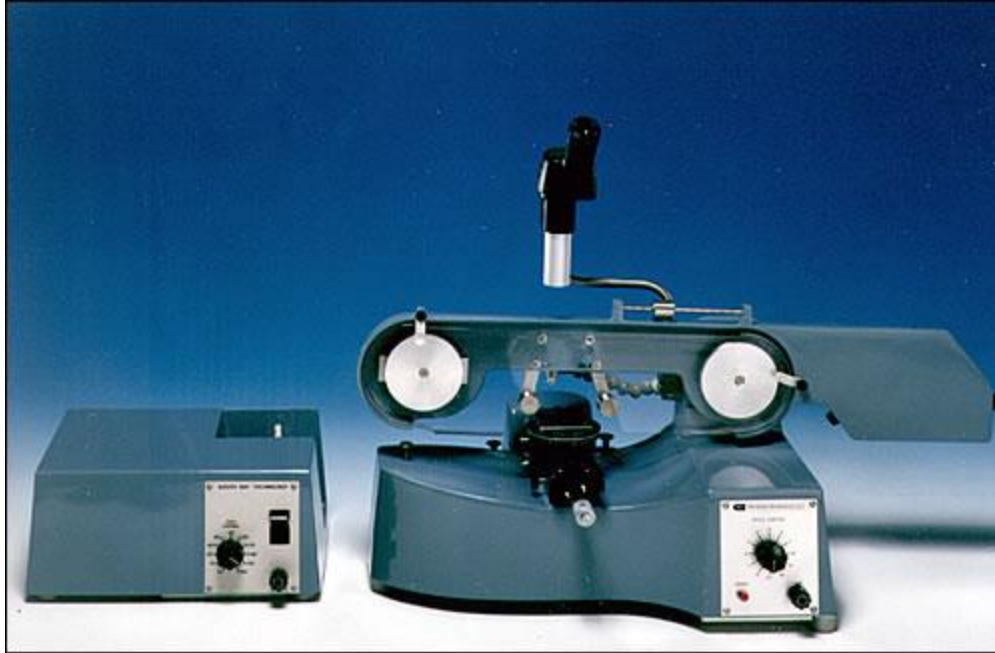


Figure 41: Abrasive Slurry Saw – Model 850, South Bay Technology

The other method used to cut samples is using a dicing saw that is furnished at the Auburn University Microfabrication lab. This is a DAD3220 Disco Automatic Dicing Saw, Disco Kiru. The blade used to cut the sample in this saw is a flanged diamond blade, 0.25 mm in thickness. This saw can provide highly precise cuts, but once again the limitation is in sample orientation prior to cutting. This saw uses a starting point and an end point to create a line through which a cut is to be made, and these points need to be marked out on the sample physically, which are displayed on a monitor using a microscope furnished with the saw. Precise marking of cutting points on the sample, and finding these in the dicing saw can be challenging.

### 3.2.2 Experimental Setup for Energy Harvesting

In order to test the piezoelectric device for energy harvesting characteristics, and power generation, the clamped piezoelectric bimorph is mounted on a shaker table (Labworks Inc. ET-132-203). This shaker table is driven by applying a sinusoidal excitation from a function generator (Agilent 33220A). The experiments are conducted at varying frequencies and constant excitation amplitude of  $2.4525 \text{ m/s}^2$  (0.25g). This acceleration is obtained by applying a 5 mV RMS alternating voltage from the function generator. This 5mV RMS signal from the function generator is amplified to 24.5 mV RMS using a linear power amplifier (Labworks Inc. PA-119).

This 24.5 mV RMS signal is obtained using an output signal from an accelerometer (PCB Piezotronics Inc. 480C02), that is connected to a channel on a digital oscilloscope (Tetronix TDS 3014B). The acceleration amplitude needs to be adjusted to 25 mV RMS each time the frequency is changed using the function generator. This adjustment is needed due to the fact that a constant voltage is supplied from the power amplifier. In order to keep acceleration constant with changing frequency, a constant current source could help, and would get the base acceleration relatively constant. A fool-proof method would be to employ the use a servo-feedback controller, adjusting the input power each time the frequency is changed to obtain the desired acceleration.

The two wires that are soldered on the outer surfaces of the series-poled piezoelectric device are connected to two probes that feed into a second channel on the digital oscilloscope. In addition, a load resistor is connected in parallel with the piezoelectric device and the digital oscilloscope. The value of this load resistor can be adjusted. In the absence of the load resistor, or very high resistance values ( $>1 \text{ M}\Omega$ ), the conditions are close to having an open circuit for with the piezoelectric bimorph. Under open circuit conditions, the dielectric displacement is zero, as there is no current flowing out of the device. Very low values of the load resistor provide short circuit conditions, and here the electric potential is zero as the top and bottom layers of the piezoelectric device are shunt. The digital oscilloscope reading from this channel provides the voltage generated from the piezoelectric device, which is recorded manually. Figure 42 provides a schematic for the experimental setup, which is also shown in a picture in Figure 43.

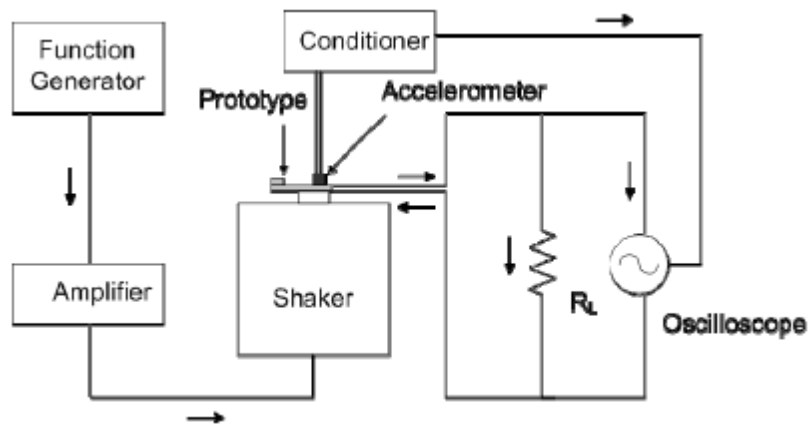


Figure 42: Schematic of energy harvesting experimental setup [22]

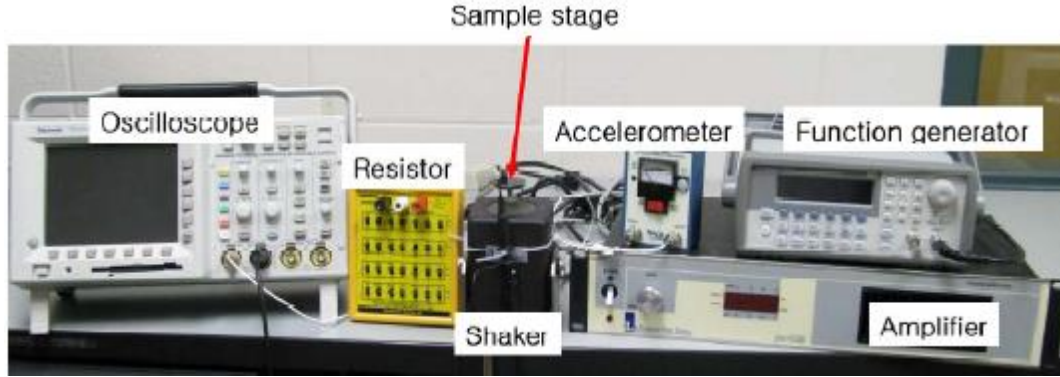


Figure 43: Energy Harvesting Experimental Setup in Laboratory [55]

### 3.2.3 Damping Ratio Measurements

The damping ration of a vibrating cantilever beam can be measured using a number of ways, as reported in any classical vibrations textbook. In piezoelectric energy harvesting, one of the most convenient ways to measure damping ratio is by utilizing the piezoelectric effect of the bimorph mounted as a cantilever, and measuring the voltage response from an impulse, and utilizing the logarithmic decrement method.

In order to perform this measurement, the “Burst” function from the Agilent 3220A function generator is chosen, and an impulse wave with a Time Period of 200 ms is chosen. The acceleration amplitude is chosen such that a sufficiently large signal-to-noise ratio is obtained. This typically relates to a reading of about 15-20 mV RMS from the accelerometer, which is kept constant in each experiment, when the load resistance is changing. Therefore, the voltage response obtained from the piezoelectric cantilever is in the form of repeating wave-packets, of which a single wave-packet is saved, as shown in Figure 44 [5]. A MATLAB script is used to export the peaks from each crest, through which an exponential trend-line is fitted to obtain the coefficient. The obtained coefficient can be set equal to the coefficient of the exponential term in the logarithmic decrement equation,

$$V(t) = V_0 \exp(-\omega_n \zeta t) \quad (56)$$

where,  $V_0$  is the voltage response at time = 0,  $\omega_n$  is the natural frequency, and  $\zeta$  is the desired damping ratio.

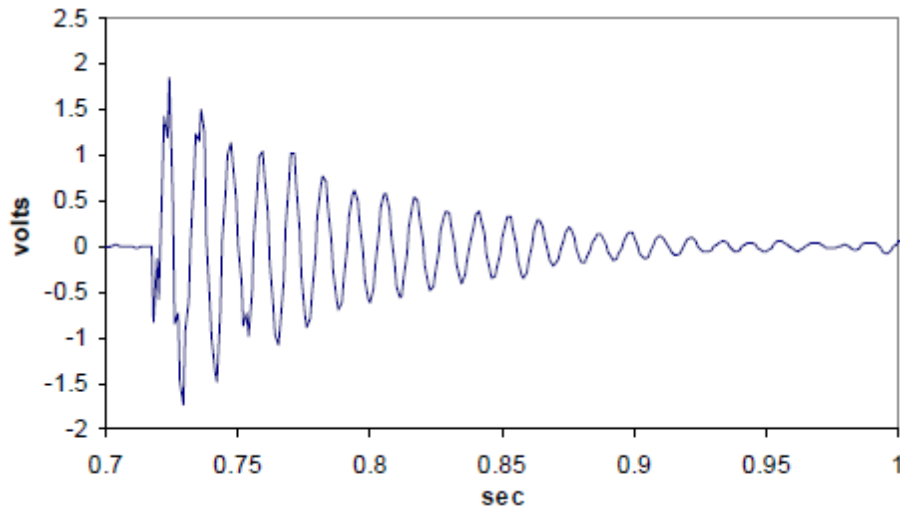


Figure 44: Piezoelectric voltage response to an impulse wave [5]

This analysis is performed for obtaining the quality factor at various load resistances. Chapter 6 in this research is dedicated for this study and characterization of damping ratio at varying load resistances for different cantilevers, with various proof mass loading conditions. In this chapter, it is shown that the damping ratio changes as a function of load resistance; but the damping ratio under open circuit and short circuit conditions are relatively the same. Therefore, due to a large signal to noise ratio under open circuit conditions, the mechanical quality factor is estimated using the open circuit damping ratio.

### 3.2.4 Impedance Analyzer Measurements

An impedance analyzer, Agilent 4294A is utilized to measure various dielectric properties as a function of frequency, and can be referred to as Dielectric Response Spectroscopy, or Impedance Spectroscopy. Prior to measurements, the instrument must be calibrated under both open circuit, and short circuit conditions, which is done by holding the probe such that the two ends are open, or touching each other respectively. Once the instrument is calibrated, the clamped piezoelectric bimorph is affixed on to a surface using a C-clamp to obtain a cantilevered condition. The wires on the piezoelectric bimorph surfaces are connected to the two ends of the probe. A frequency sweep of about 400 Hz around resonance is usually chosen for the dielectric response. The number of points for this frequency sweep is set to a maximum of 801 points possible (thus giving a resolution of ~0.5 Hz). Various responses as a function of frequency can be obtained such as  $Z-\theta$ , where Z is the impedance measured in ohms,

and  $\theta$  is the phase angle. Another response that is measured is  $C_p$ - $D$ , where  $C_p$  is the parallel capacitance of the piezoelectric device, and  $D$  is the dissipation factor, which is an inverse of the loss tangent. All these values provide peaks at specific frequencies, which primarily relate to the resonance and anti-resonance frequency of the device.

The peaks on the impedance curve provide some very important information. The impedance value is maximized at the resonance frequency of the structure, and minimum at the anti-resonance frequency of the structure. Moreover, the maximum impedance value at the resonance frequency is a very important factor to measure, since this value gives an indication of the internal resistance of the device. This value should be matched with an external load resistor for maximum power dissipation through it. The phase angle  $\theta$ , describes the phase difference between the current and voltage in an AC field. Therefore, impedance when expressed as a complex number has a real part, which is resistance, and the imaginary part is reactance.

The other quantity that is measured is equivalent parallel capacitance, which is an important quantity that needs to be measured since it is a function of area of the overhanging clamped piezoelectric beam. The effect of shape change on equivalent parallel capacitance would also be an important parameter to identify. The dissipation factor,  $D$  is an inverse of the quality factor of the piezoelectric device, and this can provide important information regarding the damping ratio of the material.

## CHAPTER 4: PRELIMINARY NUMERICAL ANALYSIS

This chapter primarily deals with numerical simulations and calculations that form the basis of the experimental work of this dissertation. The first set of numerical simulations are static calculations, that provide the impetus for the effect of geometry in terms of stress distribution. Following static simulations, the simulations are of a dynamic nature by means of modal analyses on the structures, to determine resonance frequencies, and design the devices to obtain target resonance frequencies.

### 4.1 Quasi-static numerical analysis for various shaped cantilevers

As mentioned in the literature review and depicted in the piezoelectric constitutive equations, one of the major factors that influences the generation of power in a device is the amount of strain produced in the device when it is loaded. Therefore, a cantilevered piezoelectric device under sinusoidal base excitation undergoing mode 1 vibration produces charge as a function of the strain produced in the material. This mode shape can be mimicked in a quasi-static state by applying a point load at the free end of a beam, and the bending characteristics of a cantilevered device can be studied. The magnitude and distribution of strain, which is directly related to stress by Hooke's law over the surface of a device can be influenced by changing the geometry of the device, and hence the effects of changing shapes is studied in this section in a quasi-static manner.

The cantilever beams that are generated in the software have dimensions adopted from commercially available piezoelectric bimorphs from Piezo Systems Inc. The adopted rectangular beam is 31.8 mm in length, 12.7 mm in width and overall thickness is 0.51 mm. These rectangular beams have been tapered into triangular shapes. The triangular beams that have been generated maintain the same length and thickness as the rectangular cantilevers, while the width at the base is altered to study the beams. The material properties applied utilize the  $d_{31}$  directional properties of PZT-5A from Piezo Inc. The Young's modulus is 62 GPa, Poisson's ratio of 0.31, and mass density of  $7750 \text{ kg m}^{-3}$ .

The geometry is constructed, using the 20 node SOLID186 element, and applying a brick shaped mesh, while attempting to maintain an elemental aspect ratio of 1:1. The back of the beam is fixed by setting displacements at the prescribed fixed end to zero. An arbitrary point load of 0.5N is applied at the free end; which is distributed at the free end in the case of the rectangular cantilevers, and a simple point load at the free end of the triangular cantilevers. Quasi-static analyses are performed, and nodal displacements, transversal stresses and strains along the mid-span (i.e. length at the center) on the surface are extracted from the numerical package and plotted and evaluated.

Three of the explored geometries, along with their meshes, load and boundary conditions are presented in Figure 45. Figure 45(a) shows the rectangular beam with the above mentioned dimensions. Figure 45 (b) (Triangle 1) is a triangular cutout from the rectangular geometry while maintaining the base width, and Figure 45 (c) (Triangle 2) is a triangular beam which has twice the base width of the Rectangular beam and Triangle 1.

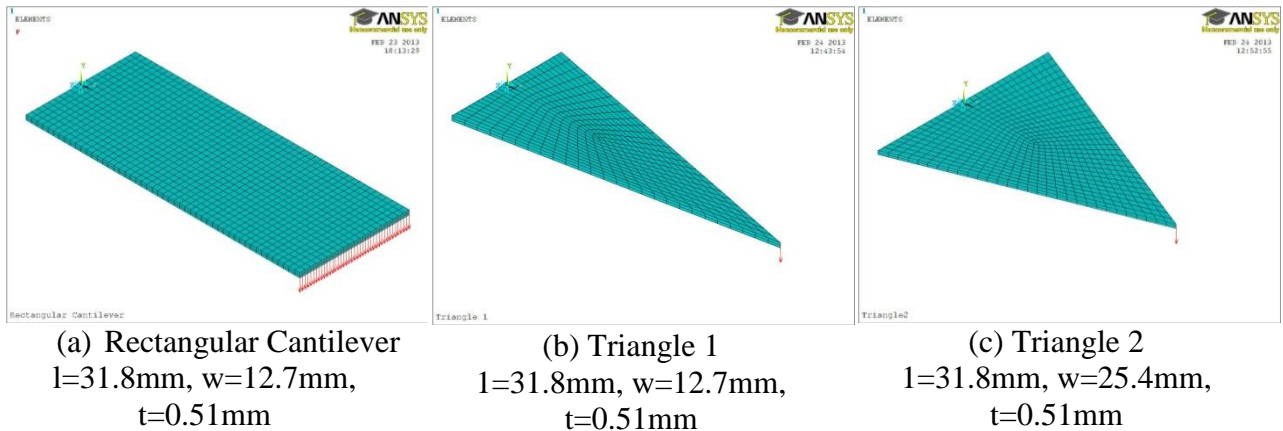


Figure 45: Geometric considerations for cantilevered devices

As the geometries mentioned above were constructed and meshed, the boundary conditions were applied to cantilever the structures, and the loads were applied. Static mode analyses were carried out in ANSYS, and the main parameters that were extracted include longitudinal deflection (y-direction), and axial stresses (x-direction). These parameters are shown in Figures 46-49, where Figure 46 gives an illustration of the deflection contour plots, and Figure 47 provides the numerical deflection data of the three structures. Similarly, Figure 48 and Figure 49 provide the axial stress contours and numerical data respectively.

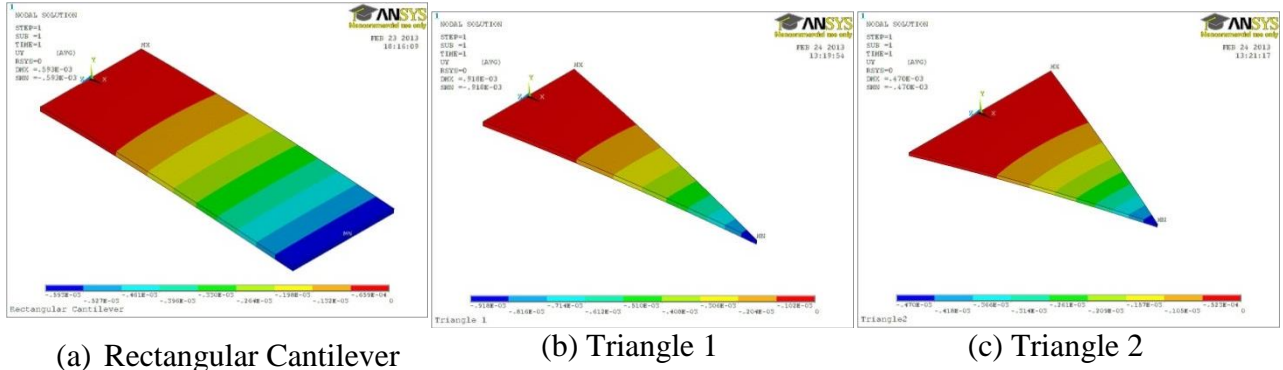


Figure 46: Deflection Contours of cantilevered devices

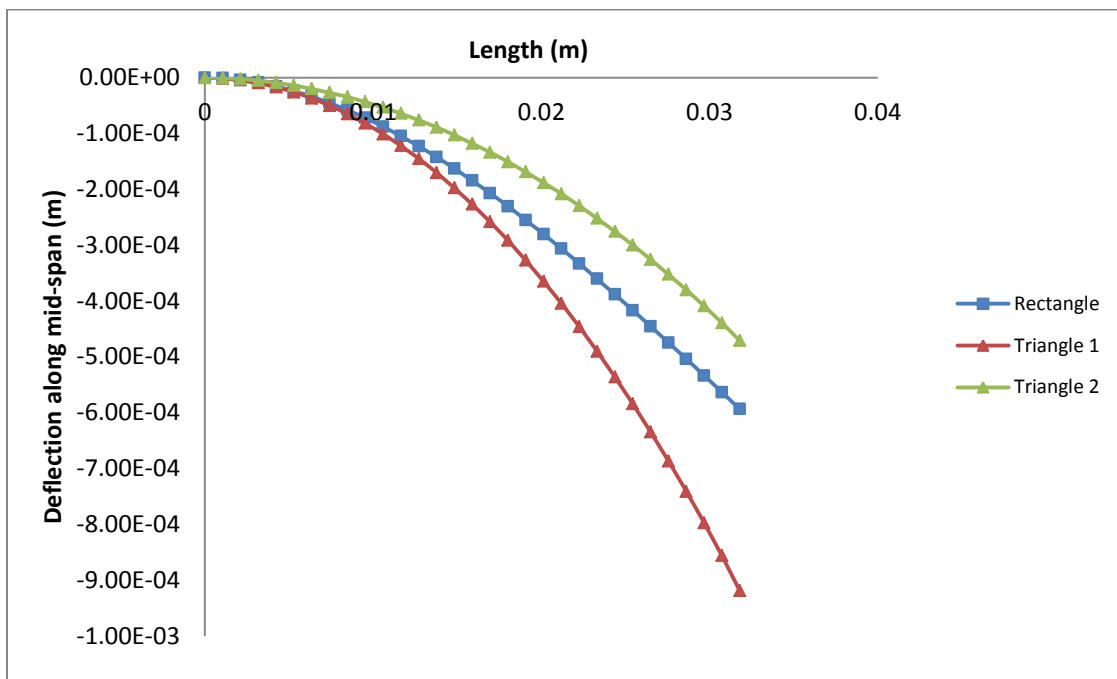


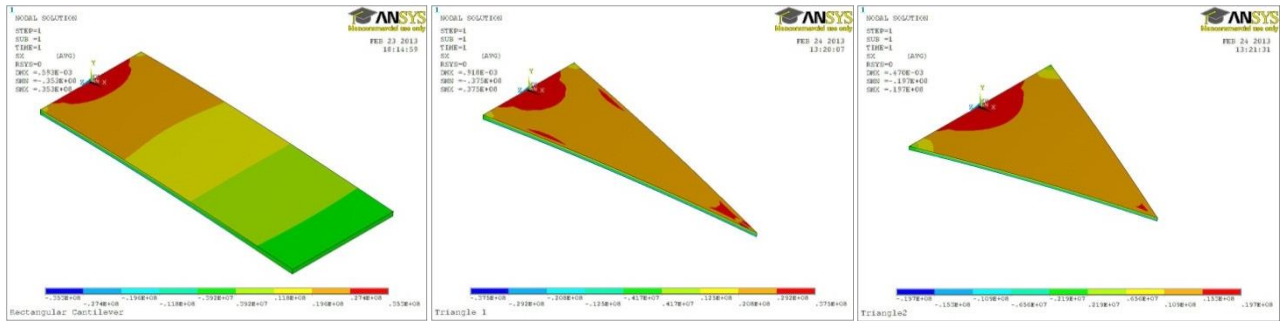
Figure 47: Deflection along mid-span of cantilevered devices

It is worthwhile noticing some of the subtle differences between the three cantilevered devices, indicative upon close inspection of Figure 47. As expected, the overall magnitude of deflection of Triangle 1 (0.92 mm) is about 54% of the Rectangular cantilever (0.59mm), since it has half the volume by comparison, and thus less amount of material to provide resistance to deformation. However, when comparing the rectangular cantilever, and Triangle 2, the tip deflection of Triangle 2 is 21% less (0.47mm) than the Rectangular cantilever, even though they have the same volume, and the same surface area. This is a direct effect of the changing geometry wherein the tapering in the triangular cantilevers provides a linear decrease in the area

moment of inertia from the fixed end to the free end. An effect of this can also be again noticed in Figure 47, where it can be seen that the slope of the curve is somewhat linear in the second half of deflection of the beam, whereas the deflection is more radial in the case of the triangular cantilevers; i.e. bending has a more constant radius of curvature. This behavior is further discussed upon inspection of the next two figures.

Figure 48, shows the axial stress contours for the three bimorphs, which is numerically plotted in Figure 49. In the case of the rectangular cantilever, it can be clearly seen that the stress along the length of the beam decreases linearly, while in the case of the triangular cantilevers, it remains constant for 90% of the length span. It is also important to notice the magnitudes of the stresses with the given geometries. The maximum stress on the rectangular cantilever is 34.6 MPa, and the minimum is 78.4 kPa, a two order of magnitude decrease over the length. However, when compared to Triangle 1, the maximum stress is 37.1 MPa, but in the linear region, the stress is 29.0 MPa in the linear region, which is only a 20% decrease and that too within a 10% length span. Hence, the average stress can be considered to be 29.0 MPa for Triangle 1. Therefore, Triangle 1, which has half the volume of the rectangular cantilever is stressed to the same level of stress over the entirety of the surface, as of the rectangular cantilever with the same applied load. In the case of triangular cantilever 2, the maximum stress and average stress are very similar, which is about 14.60 MPa. This stress is about half the average stress of Triangle 1 and maximum stress of the rectangular cantilever, with the same applied load. Therefore, in essence, changing the geometry of the rectangular cantilever to a triangular cantilever while maintaining the length and thickness, and varying the base (Triangle 2), in essence the loading capacity can be doubled, which would allow for a much greater strain on the device and at least double the power output with the same given area from a quasi-static - mechanical standpoint.

Overall, it can be seen that when a rectangular and triangular geometry with the same volume are compared, the maximum stress in the triangular cantilever is half as much as the rectangular counterpart, and also that it is linearly distributed. This analysis however is quasi-static, but forms the basis of the hypothesis, wherein a triangular device would perform more reliably.



(a) Rectangular Cantilever

(b) Triangle 1

(c) Triangle 2

Figure 48: Axial Stress Contours on cantilevered devices

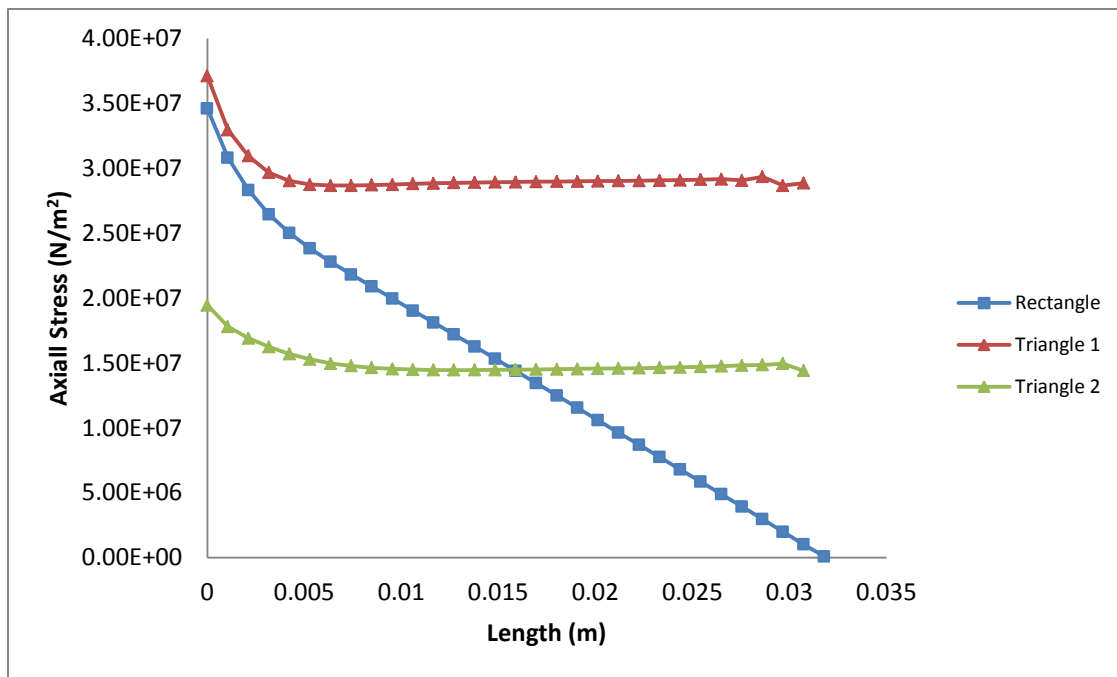


Figure 49: Axial Stresses along the length over the mid-span of the cantilevered devices

## **4.2 Effect of shape change on resonance frequency**

### **4.2.1 Resonance frequency with constant L**

The previous section provides an indication of the distribution of the stress states on triangles of various shapes as compared to rectangular counterparts. However, the analyses of piezoelectric bimorphs in this research are under harmonic loading conditions, and therefore the first step to evaluate the performance of the cantilevered devices is to determine each specimen's resonance frequency. For varying shapes, a convenient and accurate way of determining resonance frequency is by using the finite element method; hence ANSYS is employed here. Analytical solutions for rectangular bimorphs are available, but are valid for dimensions restricted to Euler-Bernoulli beam assumptions, and exact solutions are unavailable for triangular bimorph structures. Therefore, Finite Element solutions circumvent the inaccuracies that could be caused due to deviations from the Euler-Bernoulli beam assumptions.

The first set of geometries that are considered here are rectangular bimorphs, which are taken as “reference” geometries. These are based on the Piezo, Inc. samples, as described in Table 2, in Chapter 3.2. While the samples have overall lengths of 31.8 mm (1.25 in), clamping the sample in a holder, and soldering wire connections require a small overhang at the tail. Therefore, the clamped length for the rectangular geometries is chosen to be 21.5 mm in this study. Based on 1-D Euler-Bernoulli beam theory, changing widths does not affect the resonance frequency of the rectangular cantilevers; however, this is an approximation. Four 21.5 mm long, rectangular PZT-5H bimorphs, of the T-220 series, with a piezoelectric layer thickness of 0.19 mm, and overall thickness of with widths of 3.175 mm (1/8”), 6.35 mm (1/4”), 9.525 mm (3/8”), and 12.7 mm (0.5”) are chosen. Figure 50 shows that with increasing base width, hence increasing volume, the resonance frequency increases slightly. This can be easily deduced by considering the fact that with increasing width at the base, the stiffness increases, which is directly proportional to the resonance frequency of a triangular device. It must be noted that these resonance frequencies calculated from ANSYS do not include the piezoelectric effect; hence, these mechanical resonance frequencies are equivalent to the resonance frequency of the piezoelectric bimorphs under short circuit conditions; i.e. when the load resistance tends to zero, or very low values (typically  $<500 \Omega$  for these bulk scaled bimorphs) [29].

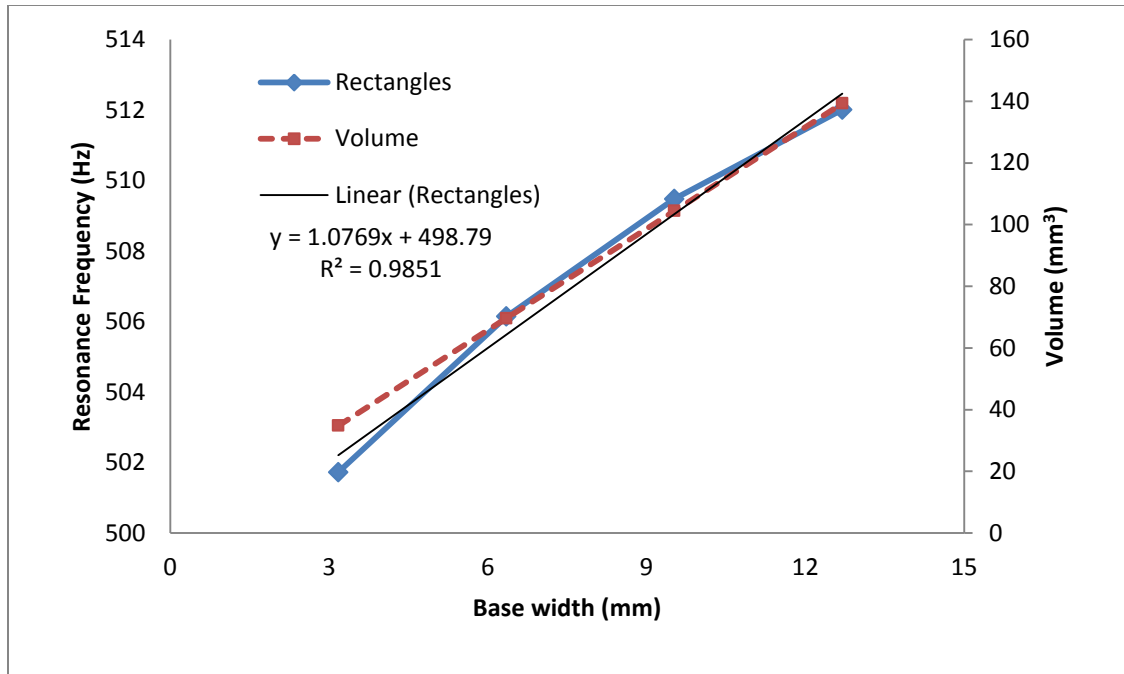


Figure 50: Resonance Frequency of Rectangular cantilevered bimorph structures with  $L=21.5\text{mm}$ ,  $t=0.51\text{mm}$  and varying widths

Sectioning out triangular cantilevers from rectangular counterparts (as presented in the previous section), i.e. samples that have the same length, thickness and base widths has a profound effect on the resonance frequency of the devices. The resonance frequency of the 21.5 mm long rectangular cantilevers, which varied from ~502 Hz to about ~512 Hz with changing widths, is roughly doubled. Comparing devices with the same base widths (hence, half the volume in a triangular cantilever), as shown in Figure 51 has resonance frequencies around 1000 Hz.

It is however interesting to note that in the case of triangular cantilevers, the resonance frequencies of the devices decrease with increasing base width. Therefore, unlike the rectangular bimorphs, increasing the volume as a function of base width actually decreases. With increasing base widths, while the stiffness at the base increases, the base angle (the angle between the base and the hypotenuse of the isosceles triangle) decreases. This decreasing base angle causes the device becoming increasingly triangular with a linearly decreasing moment of inertia (which is constant for rectangles).

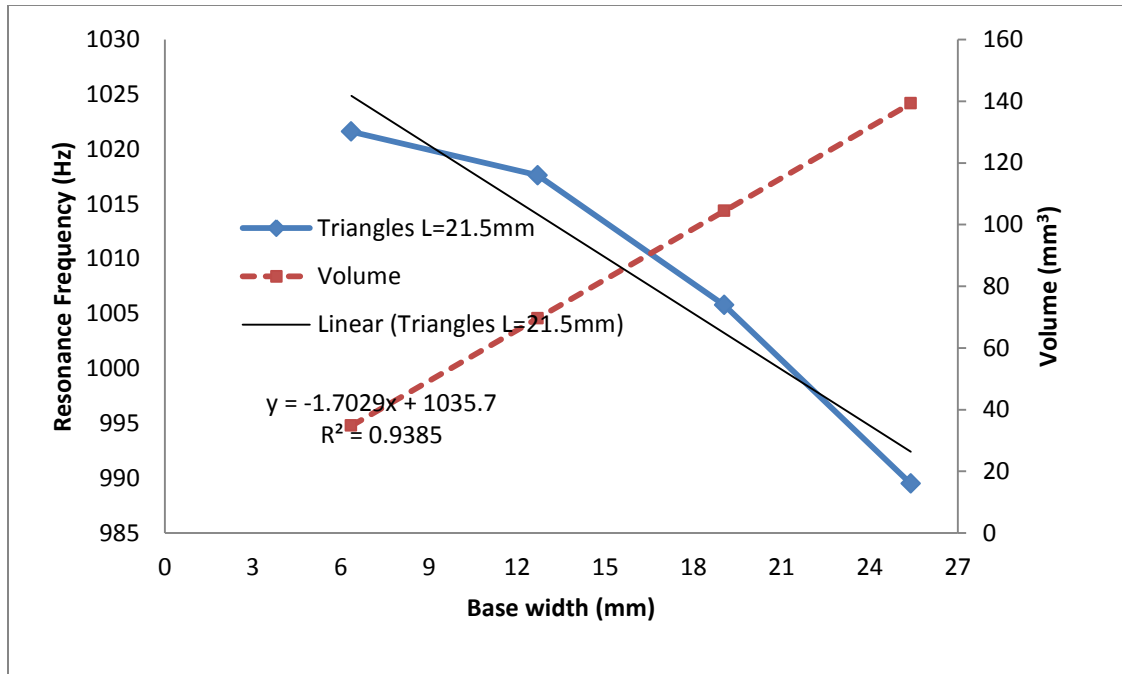


Figure 51: Resonance Frequency of Triangular Cantilevers with  $L=21.5\text{mm}$ ,  $t=0.51\text{mm}$  and varying widths

#### 4.2.2 Constant resonance frequency and volumes

The doubling of resonance frequency on devices greatly diminishes the power generated from the bimorph devices due to much lower levels of tip deflections and hence reduced strain in the devices in the dynamic mode. Therefore, in order to evaluate the effect of geometry, it is desired to find devices of comparable volume and resonance frequency. In order to do this, the  $70\text{ mm}^3$  ( $21.5\text{mm} \times 6.35\text{mm} \times 0.51\text{mm}$ ) rectangular geometry is chosen as reference. This device had a resonance frequency of 513 Hz. In order to obtain the same resonance frequency from a triangular counterpart of  $70\text{ mm}^3$  volume with 0.51 mm thickness, a parametric study with changing widths and lengths (altitudes) had to be performed, as shown in Figure 52. It was found that a triangular cantilever that has a base width of 8.95 mm, and length of 30.5 mm has a resonance frequency of roughly 515 Hz. Therefore, it can be seen that the length of the device, whether in the case of triangles, or rectangles plays a major role in determining its resonance frequency. Interestingly, it can be noticed in Figure 53 that when the resonance frequency is plotted in terms of the base angle, rather than the length of the device, the relationship is found to be linear. The triangular geometry with the matching resonance frequency as the  $90^\circ$  rectangle has a base angle of  $\sim 81.4^\circ$ , which describes it as a fairly long and slender device.

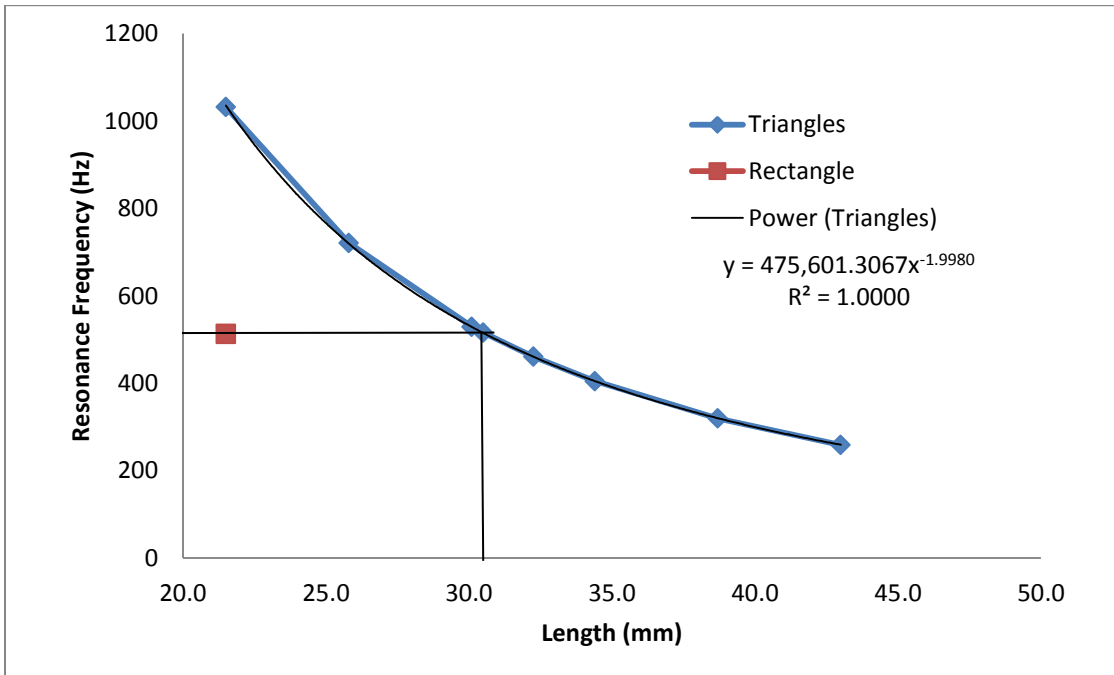


Figure 52: Effect of length on resonance frequency for triangles 70 mm<sup>3</sup> in volume

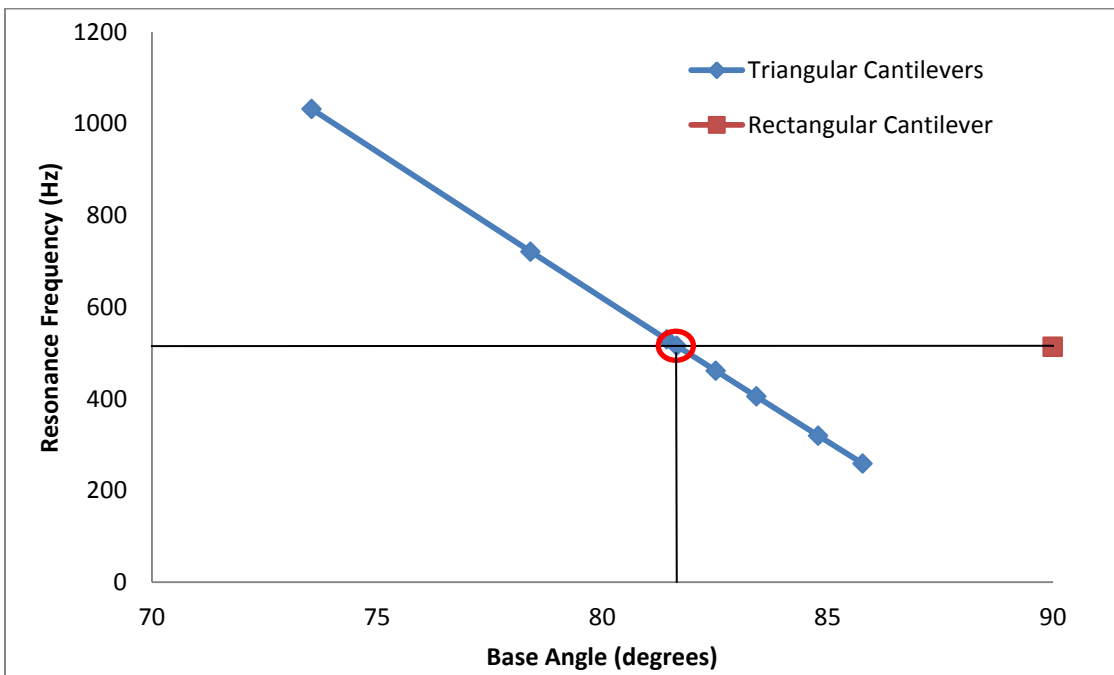


Figure 53: Effect of base angle on triangles 70 mm<sup>3</sup> in volume

### 4.2.3 Triangles with L=30.5mm and changing base widths

In order to get a device with matching resonance frequency and volume for the 70 mm<sup>3</sup> rectangular device, the triangular device found had a length of 30.5 mm. It was also shown in the case of the 21.5 mm altitude triangles with changing base width or angles, and constant length, the resonance frequency slightly decreased with increasing length. This scenario was also tested for triangles with a fixed length of 30.5 mm, and changing base widths. With increasing base width, increasing volume, and decreasing base angle, it is observed in Figure 54 that the resonance frequency of triangular bimorphs decrease. However, this decrease is not very large, and therefore, with constant thickness, the length of the isosceles triangular bimorph (i.e. the altitude) is the main contributing parameter behind determining the resonance frequency.

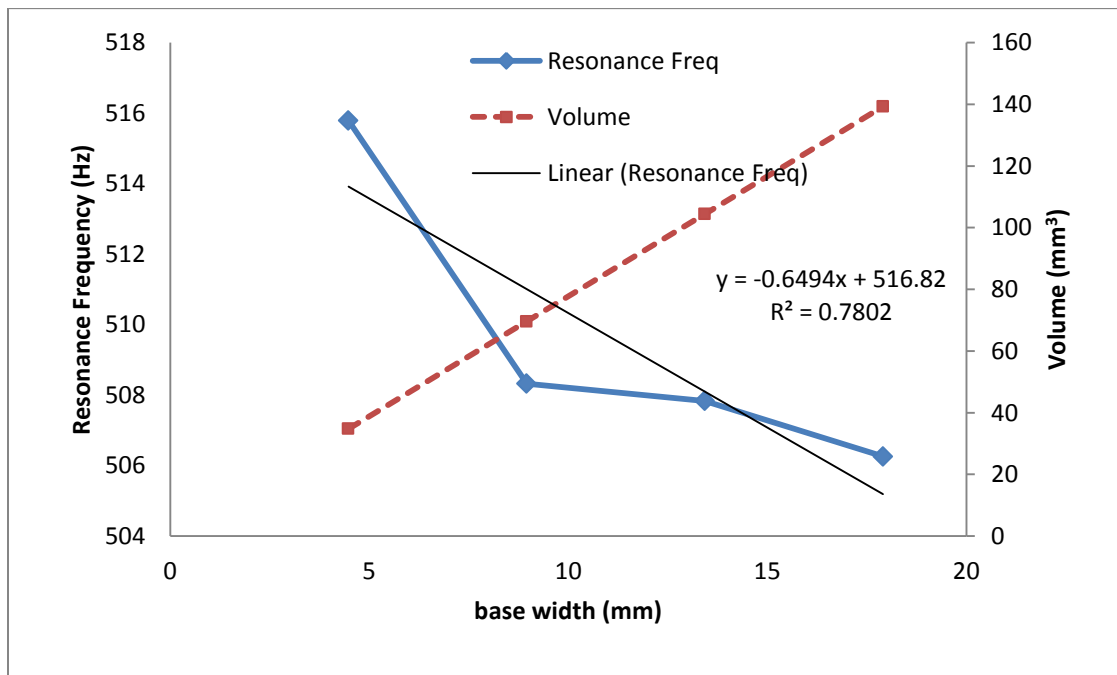


Figure 54: Resonance Frequency for triangular cantilevers with varying clamping widths

Therefore, since maintain length (or altitude) and thickness roughly maintains the resonance frequency within cantilevers of rectangular or triangular shapes, L=30.5 is chosen as a standard for triangles. This aids in reducing the number of geometric variables in the study, and also provides the opportunity for comparing devices in a more systematic fashion.

## CHAPTER 5: EXPERIMENTAL RESULTS

This chapter provides results and discussion from all the experiments carried out in this research. The chapter is broken down into several subsections. Section 5.1 provides results from a single experimental run to explain the flow of results and characterization samples in the following sections, where results from various geometries are compared with varying degrees of proof mass are compared.

### 5.1 Introduction to a single experimental run

The goal of this section is to provide an overview of the raw data that is obtained from a single experiment, and provide an interpretation of the data. The comparison between samples of various geometries and changing proof masses is deferred to future sections. The single experiment presented here is characterized by the voltage generated from the bimorph into varying load resistances, the electromechanical coupling coefficient, mechanical quality factor, and impedance spectroscopy.

The sample chosen for this illustration is the T220-H4-203X sample, with a clamped length of 21.5 mm, resulting in an overall volume of  $70 \text{ mm}^3$ , and mass of 0.622 milligrams. No proof mass is attached to this sample. The results presented here give an average of two tests performed on the same sample. The resonance frequency of this device was expected to be around 513 Hz from numerical calculations. As mentioned previously, this calculated mechanical resonance frequency is expected to be the short circuit resonance frequency of the device, due to the absence of electrically induced damping in the device. The average short circuit frequency of the device is experimentally found to be 512 Hz, as shown in Figure 55 at low values of load resistance. It can be observed that the resonance frequency at low values of load resistance remains constant up to about 2500 ohms, after which it starts increasing steadily with a constant slope. The resonance frequency approaches a threshold at about 100,000 ohms, and remains constant hereafter, and this is regarded as the open circuit resonance frequency. The increase in resonance frequency in the regime where it shifts is attributed to the electrically

induced damping, and impedance matching with the load resistor. More light on this phenomenon is shed from impedance analyzer measurements, presented in Figure 60 for this sample. For this sample, the open circuit resonance frequency is observed to be 528 Hz; therefore the change between open circuit and short-circuit resonance frequencies is 16 Hz. This fairly large shift can be very advantageous in real world applications, due to the fact that the power generated in this regime is less resonance frequency specific, i.e. the frequency response has wider peaks due to increased damping. The increased damping ratio at these levels of load resistance is illustrated in a future section. One of the most important parameters that can be derived from the data presented in Figure 55 is the electromechanical coupling coefficient. As presented in Chapter 3, this can be calculated from the two resonance frequencies, using the equation  $k^2 = \frac{\omega_{oc}^2 - \omega_{sc}^2}{\omega_{oc}^2}$ . With  $f_r = 528$  Hz, and  $f_a = 512$  Hz, this results in an average  $k_{31}$  value of 0.24, which is much lower than 0.39, as reported by the manufacturer.

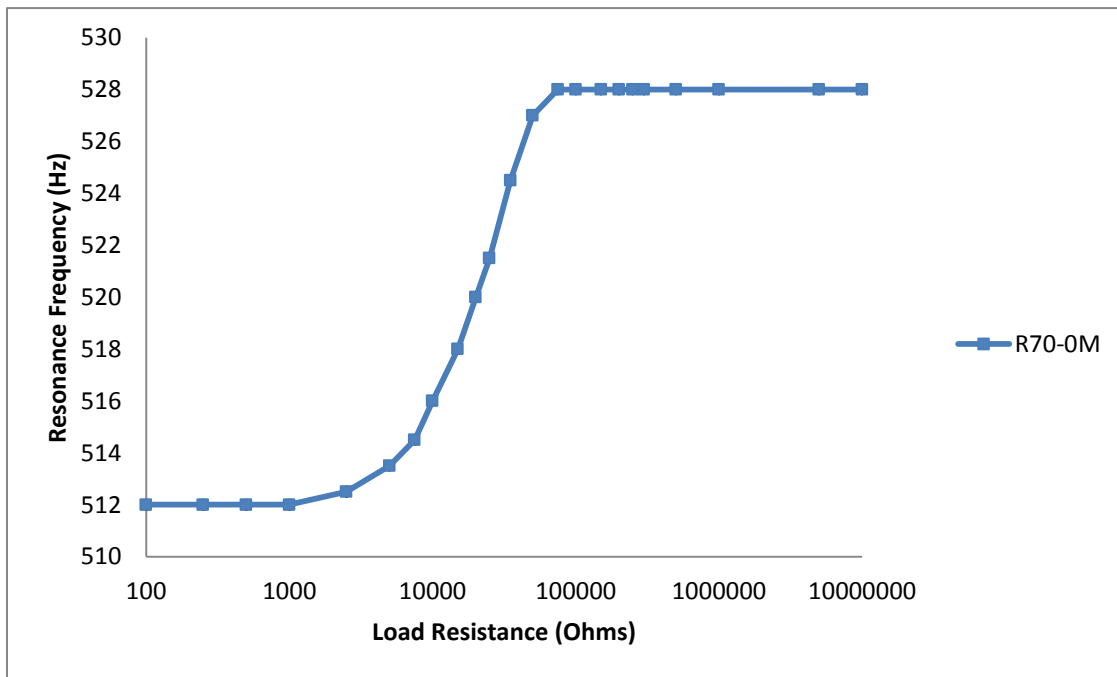


Figure 55: Resonance frequency as a function of load resistance for the 70 mm<sup>3</sup> rectangular bimorph

In order to illustrate the change in resonance frequency due to the change in stiffness in the system due to the external load resistor, one can normalize the resonance frequency to the short circuit resonance frequency in the system, where the open circuit resonance frequency is dependent on stiffness due to the electromechanical coupling. This can be represented as. Therefore, this would result in the short circuit resonance frequency normalized to unity, i.e.  $f_{SC} = 1$  and  $f_{OC} = \sqrt{1 + k^2}$  [45]. Therefore, Figure 55 can be normalized, and represented in Figure 56, illustrating the electromechanical coupling effect.

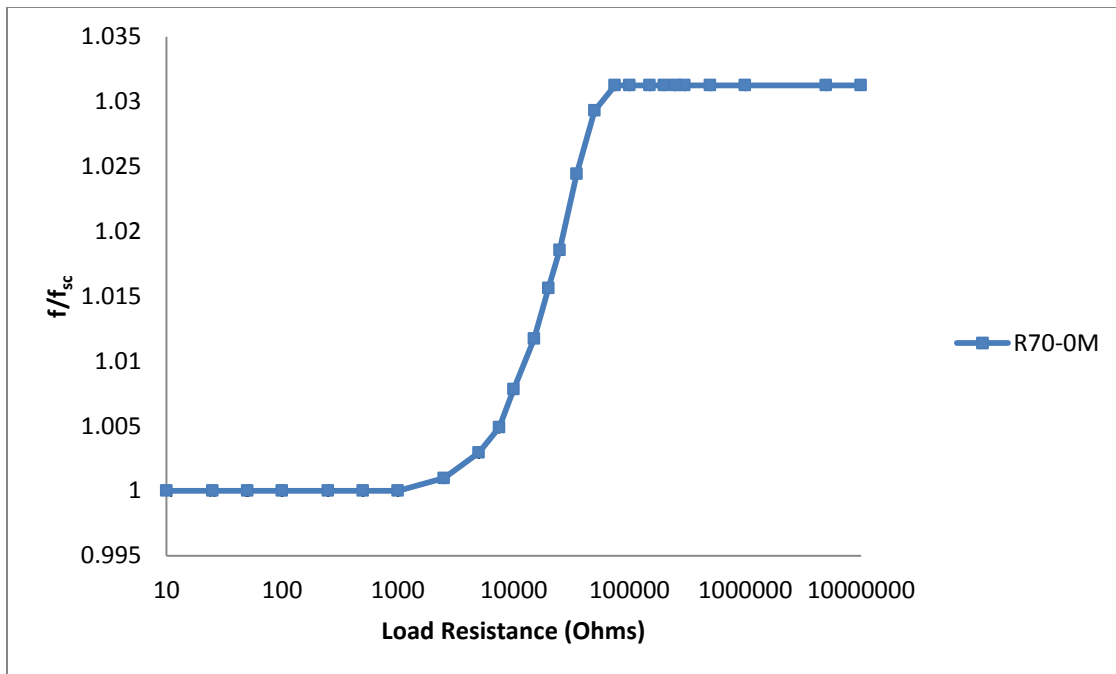


Figure 56: Normalized Resonance Frequency illustrating the electromechanical coupling in the system

The data collected in order to estimate the power generated from a piezoelectric bimorph is the RMS voltage into the load resistance at resonance. The voltage generated is also dependent on the load resistance, and is a little more intuitive, based on Ohm's law. At low values of load resistance, the voltage generated is very low with high currents, and vice versa. It is however interesting to notice in Figure 57 that the inflection points are noticeable in voltage generation as well, as they were in Figure 55 and Figure 56 for resonance frequencies. The voltages have the highest slope in the region where the maximum power is generated.

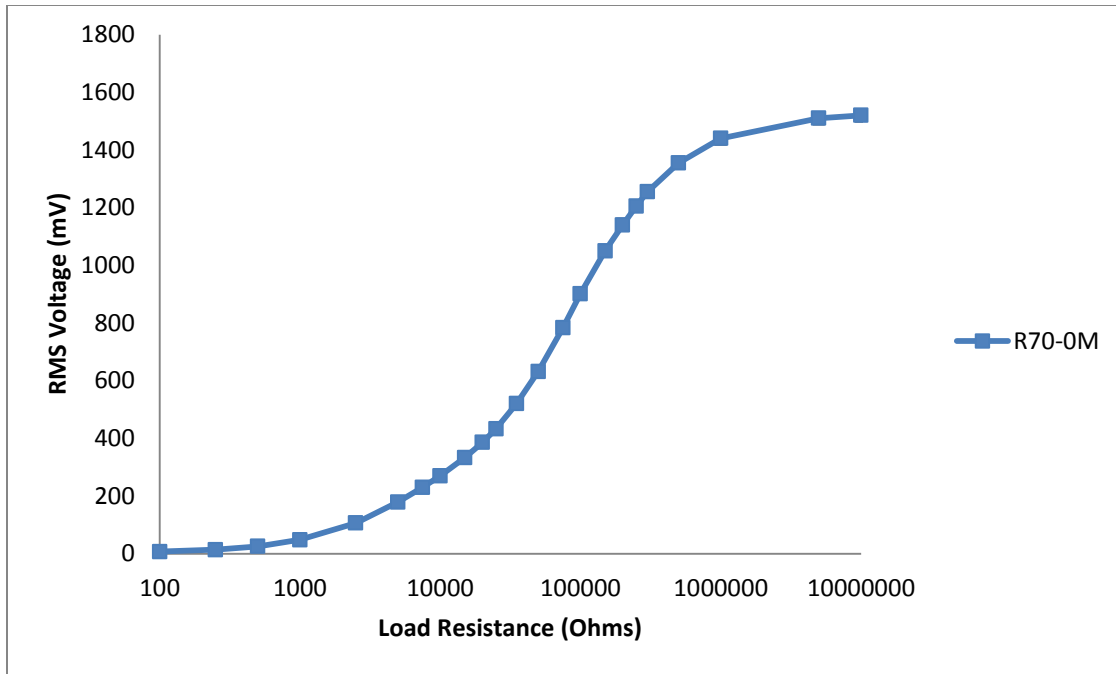


Figure 57: RMS voltage generated from the piezoelectric bimorph into various load resistors at resonance

Figure 58 shows the trend for the generation of power as a function of load resistance. The power is calculated by means of using the simple definition of power as  $P = VI$ , where the current  $I$  is replaced by  $V/R$  from Ohm’s law. Due to the presence of two piezoelectric layers, the resulting equation to calculate power becomes,

$$P = V_{rms}^2 / 2R \tag{57}$$

where,  $V_{rms}$  is the RMS voltage presented in Figure 58 at each given load resistance  $R_L$ .

The amount of power generated when the resonance frequency of the device is equal to the short circuit frequency is fairly low (the first four-to-five data points, corresponding to low values of load resistance. In the intermediate zone of load resistance values, where the resonance frequency in Figure 58 shifts, is the area where the most amount of power is generated. In fact, as reported in literature, the maximum power is generated at a specific load resistance, known as the optimal load resistance. In highly coupled systems, which are the nature of these bimorphs without a proof mass, there exist two values of optimal load resistance values. The optimal load resistance occurs when the impedance of the device matches the external load resistance. In the case of these highly coupled bimorphs, there exist two such impedance values, which are explained in the impedance analyzer measurements in Figure 60. From Figure 58, the two

optimal load resistance values are ~15,000 Ohms, and 75,000 ohms, generating 3.7  $\mu\text{W}$  and 4.1  $\mu\text{W}$  of power respectively.

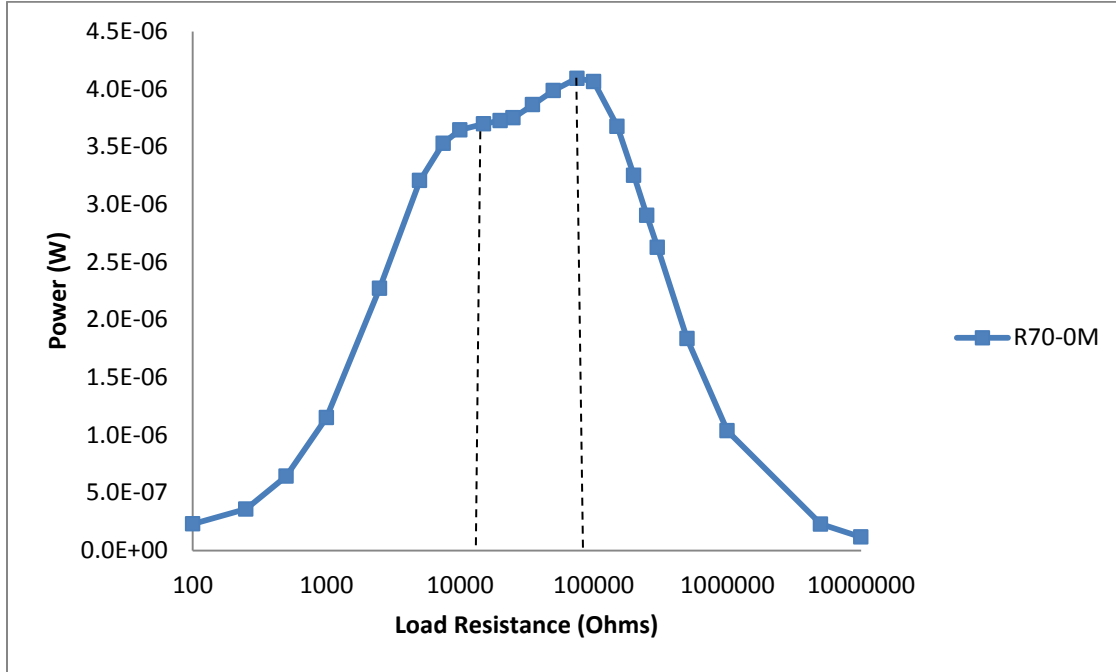


Figure 58: Power generated by the piezoelectric bimorph as a function of load resistance, each at their corresponding resonance frequency

The power generated can be normalized with the square of the base acceleration ( $2.4525 \text{ ms}^{-2}$ , which is kept constant in this study) and volume to represent an absolute value of power density [30]. This is especially useful when comparing various geometries and devices with or without proof masses. The normalized data from Figure 58 is shown in Figure 59, and it can be seen that the maximum power is about  $9.77 \text{ (mW/g}^2\text{)/cm}^3$ .

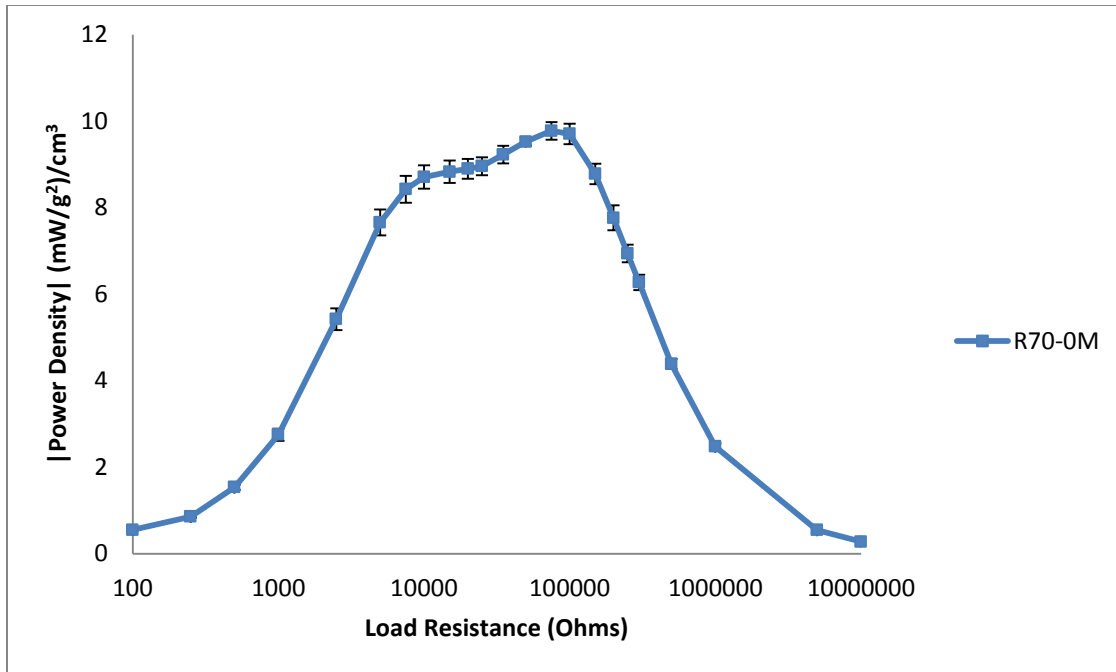


Figure 59: Power Density of 70 mm<sup>3</sup> device without a proof mass

The impedance analyzer measurements provide very useful insights, and also validation of experimental results from the shaker-table experiments. Impedance measurements are carried out by the impedance analyzer at a constant oscillating voltage of 100 mV (500 mV to 1V for measurements with samples resonating at lower frequencies ~100 Hz or below), as a function of frequency. Impedance being a complex quantity, represented by  $Z$ , which is the sum of resistance ( $R$ ) and imaginary ( $j$ ) reactance ( $X$ ), i.e.  $Z = R + jX$  is therefore presented in magnitude and phase form. As the phase angle goes to zero, the impedance becomes purely resistive. When the external load resistance matches the impedance value when the phase angle is zero, i.e. purely resistive loads, an optimal load resistance is found, since the dielectric loss ( $\tan\delta$ ) is minimum, or zero. In the case of highly coupled systems, the impedance measurements show two values for which the phase angle is zero, as indicated in Figure 60. The impedance value at which the phase angle is zero is 5,558 ohms. The second value where the impedance is purely resistive is 143,641 ohms. Both of these values are not outrageously far away from the values at which peak power was observed from the shaker table setup, especially considering the fact that measurements at load resistances, exactly at the purely resistive impedance's were not performed. Another worthwhile observation is that the zero phase angle abscissa crosses the

impedance curve at two locations. The impedance at this abscissa is about 75,000 ohms, almost exactly the load resistance at which the power was maximized.

In addition, another important characteristic of the impedance measurements where the phase angles are zero, are the frequencies at which impedance values are maximum and minimum. The frequency at which the impedance is at a minimum is known as the resonance frequency, and the value at which the impedance is maximum is the anti-resonance frequency. These values are observed to be 511 Hz and 530 Hz, corresponding almost exactly to the short-circuit and open-circuit resonance frequencies as measured from the shaker table setup respectively. Since the resonance frequencies are dominated by mechanical parameters, such as stiffness and mass, which are dependent on geometric and material properties respectively, the findings here provide very valuable experimental validation of the resonance frequency based on two transduction mechanisms – the generator effect for the shaker table measurements, and the actuator effect for the impedance analyzer measurements.

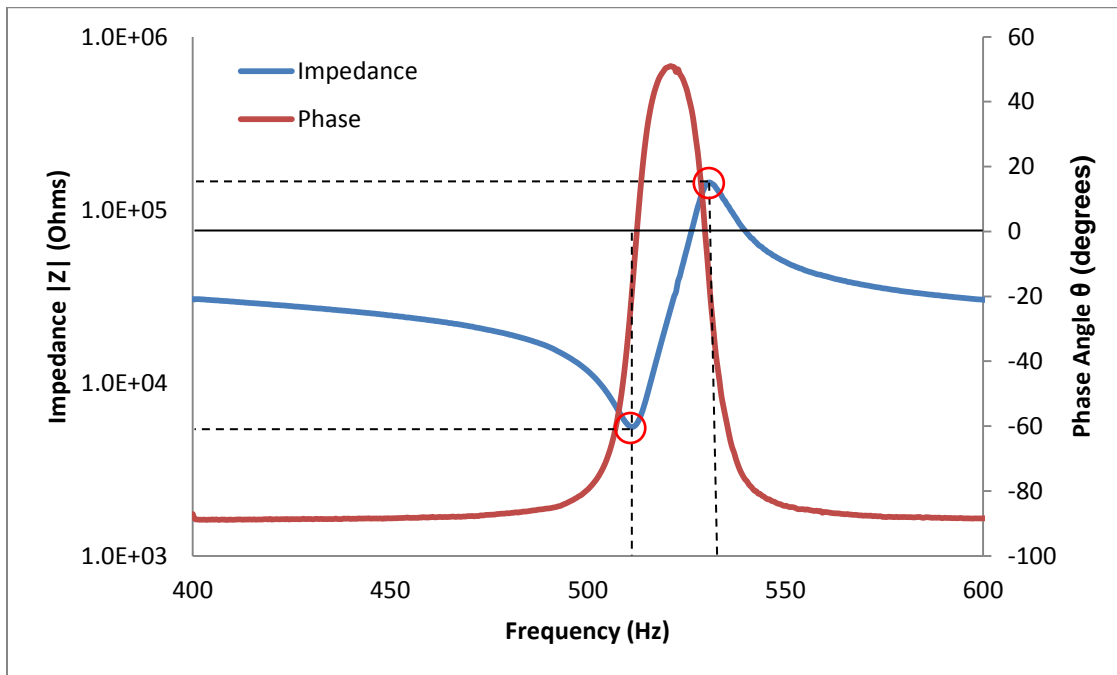


Figure 60: Impedance analyzer measurement for the 70 mm<sup>3</sup> rectangular bimorph with 100 mV oscillations as a function of frequency

Another parameter that can be measured from impedance spectroscopy is equivalent parallel capacitance. This is an important property, which is characteristic of the piezoelectric bimorph as a material property. As mentioned before, the piezoelectric bimorph is described as an inherent capacitor with a current source in parallel when it is generating power. While the capacitance is normally regarded as a constant value based on the permittivity, size and the thickness of the dielectric medium, it in fact has a frequency dependency. Due to the fact that this study is resonance specific, it becomes quite important to characterize the frequency dependent capacitance values at resonance. It can be seen in Figure 61 that the capacitance around resonance has two peaks. One of these peaks is a positive peak, which is useful as a capacitance enhancement mechanism in piezoelectric devices. The negative peak, i.e. where the capacitance is minimum also has important implications, such as in shunt damping applications for vibration attenuation [56].

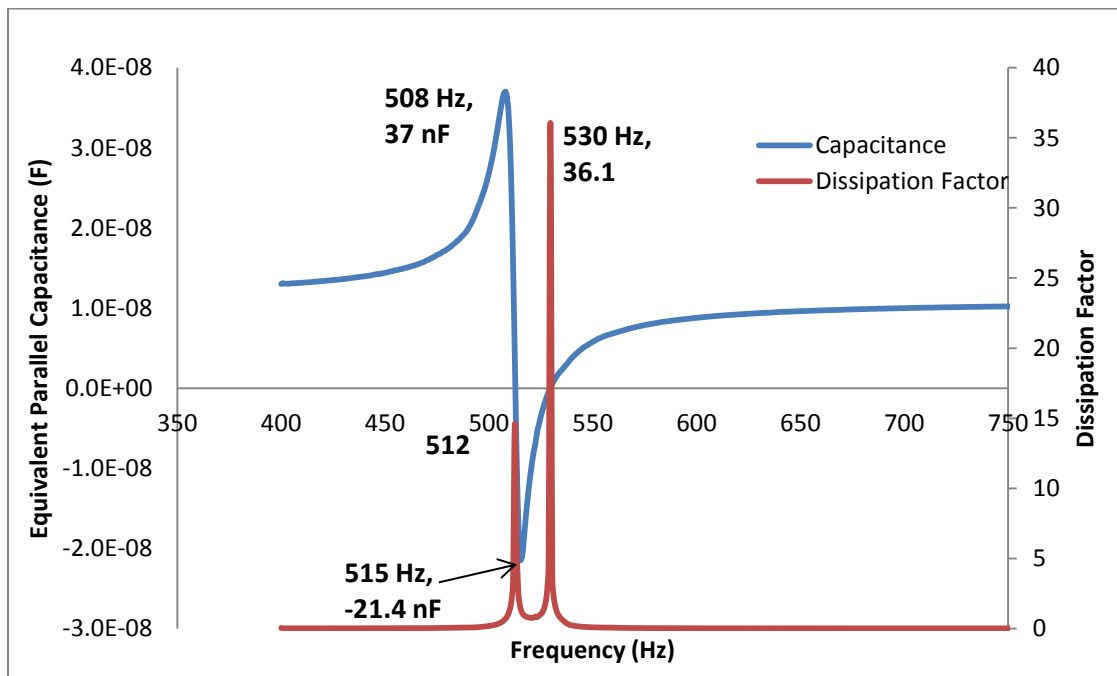


Figure 61: Capacitance and Dissipation factor for 70 mm<sup>3</sup> rectangular bimorph with 100 mV oscillations as a function of frequency

In order to fully characterize the electromechanical coupling behavior of the piezoelectric bimorphs, an important parameter required is the quality factor of the device. One of the ways to obtain the quality factor of the device is by measuring the damping ratio of the device. As

described in the methodology chapter, this is obtained by using the voltage response of the piezoelectric cantilever to an impulse wave. As an impulse is applied, the cantilevered bimorph resonates, but exponentially decays due to damping. This damped response is plotted as a function of time, as shown in Figure 62. The damped response is affected by the external load resistor, where the voltage response is greatest in open circuit conditions. In short circuit conditions, the voltage generated is nearly zero, and the only response that is observed is a noise signal. Therefore, a generalized quality factor is calculated based on the open circuit voltage response to an impulse wave. Section 5.6 shows a qualification for this measurement, where it is shown that the damping ratios (inverse of quality factor) under open-circuit and near short-circuit conditions are very similar, but do have a variation with load resistance.

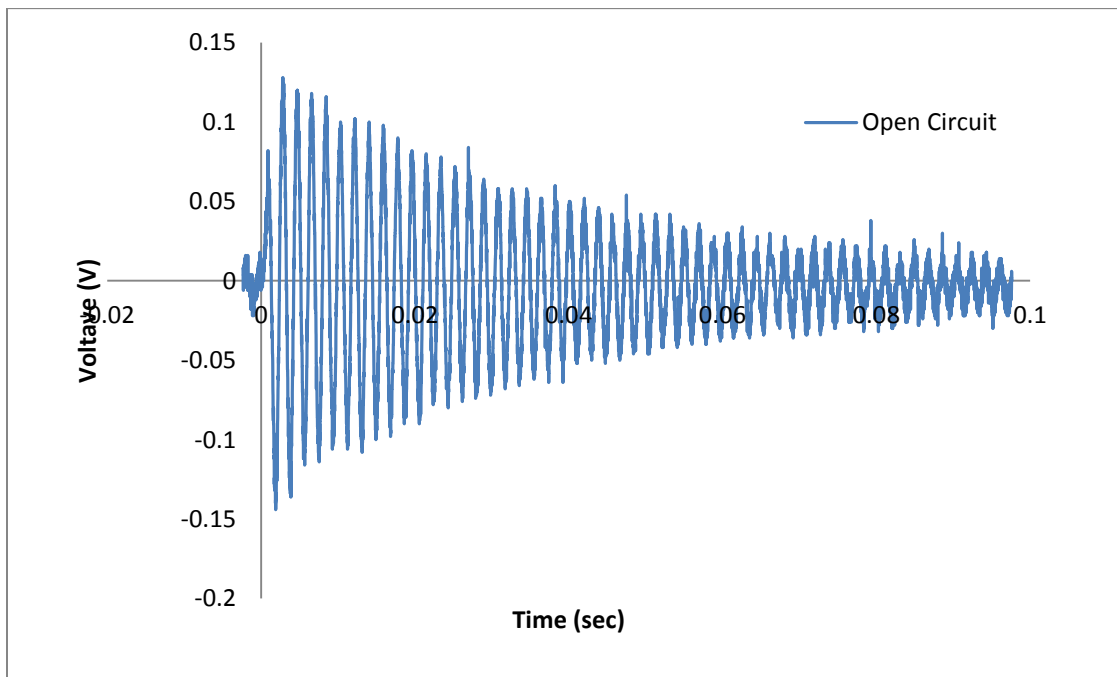


Figure 62: Damped voltage response to an impulse wave from the cantilevered bimorph

In order to obtain the damping ratio of the piezoelectric bimorph, the data points representing the crests of the wave-packet in Figure 62 are extracted using a MATLAB program, and an exponential curve is fitted to the peaks, as shown in Figure 63. The coefficient of the exponential is set equal to the exponential term in the equation  $V(t) = V_0 \exp(-\omega_n \zeta t)$ , where the resonance frequency is known (528 Hz, as reported), and can also be easily obtained or verified from the time period in Figure 62. Therefore, the damping ratio,  $\zeta$  is calculated to be

0.0085 for this particular case. Using the relation,  $Q = 1/2\zeta$ , the quality factor is found to be 75.4. This is a particularly high quality factor, indicating a relatively small damping ratio. The general quality factor reported for this device as used in a few studies is 32. However, it is clear that the quality factor can change due to various circumstances (clamping as a cantilever, dimensions, and electrical loads), and hence needs to be measured.

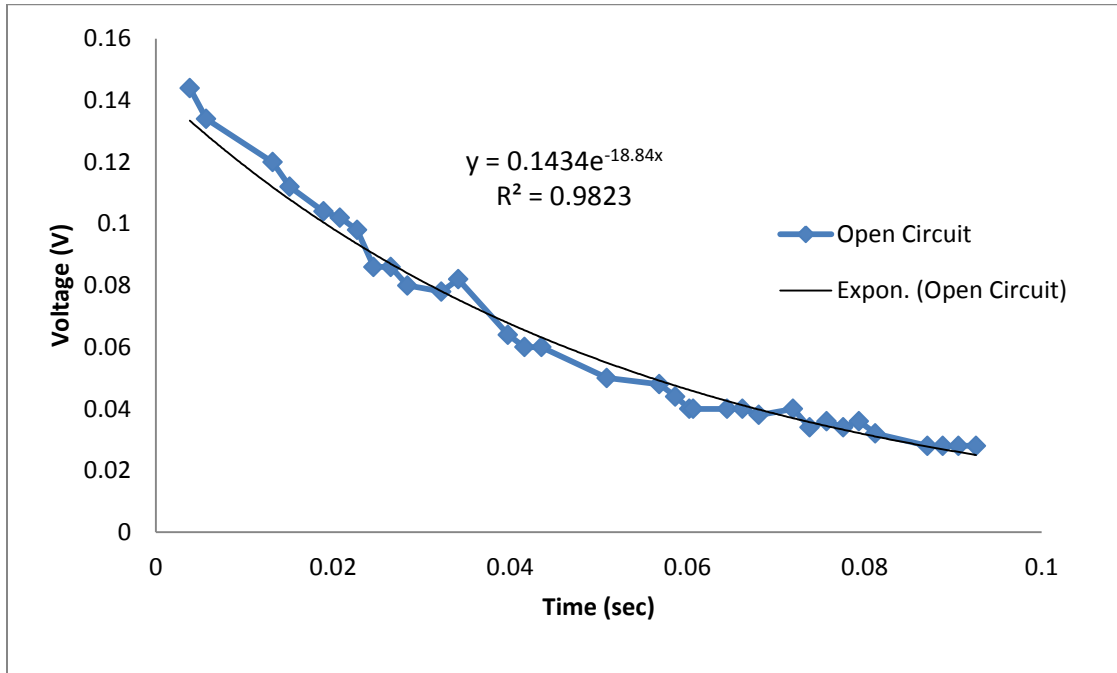


Figure 63: Calculation of damping ratio for 70 mm<sup>3</sup> Rectangle under Open Circuit Conditions

Based on the quality factor calculated, and the coupling coefficient obtained, a figure of merit based on the electromechanical coupling can be obtained. This figure of merit is calculated as the product of the square of the coupling coefficient and the quality factor, i.e.  $k^2Q$ . Therefore,  $0.24^2 \cdot 75.4$  provides an electromechanical coupling figure of merit of 3.61, which according to literature falls in the intermediate levels of coupled systems. Systems where this figure of merit is less than 2 are regarded as low coupled systems (as described in section 2.10).

The results and characterization presented in this section provide a premise for the work that is done to conduct this research. Piezoelectric cantilevers with varying geometry and proof masses are tested and characterized, and comparisons on normalized resonance frequency, power density and electromechanical coupling are presented. A further characterization of the damping ratio of the piezoelectric bimorphs with changing load resistances is also provided

## 5.2: Experimental Results with no proof mass

This section provides an overview of the results that were obtained, mainly from three sets of samples. The designations used are in the form of SV-XM, where S stands for shape (R for rectangles, T for Triangles), V for the volume of the device in  $\text{mm}^3$  ( $70 \text{ mm}^3$ ,  $104 \text{ mm}^3$  or  $140 \text{ mm}^3$ ), and X stands for the amount of proof mass (in this section, it is 0M for no proof mass). Initial results in this section represent three sets of samples – R70-0M, T70-0M; R104-0M, T104-0M; and R140-0M, T140-0M. The rectangles here have a fixed length of 21.5 mm, and the triangles have a fixed length of 30.5 mm. As the nomenclature describes, the goal is to compare samples with different shapes having the same volume, and resonance frequency. Chapter 4 described that the resonance frequency of these devices were relatively the same (around 500 Hz). In the case of the rectangles, with increasing width and constant length, the resonance frequency increases due to the increasing stiffness. In the case of the triangles, with increasing base width (i.e. increasing base angle), the resonance frequency decreases. The attempt is to compare these three described sets of geometries, and compare them at the same operating resonance frequency.

### 5.2.1: $70 \text{ mm}^3$ samples

The first set tested is samples that  $70 \text{ mm}^3$ , where the rectangles have dimensions of  $21.5 \times 6.35 \times 0.51 \text{ mm}^3$  and the triangles have dimensions of  $30.5 \times 8.95 \times 0.51 \text{ mm}^3$ . The two devices are illustrated in Figure 64.

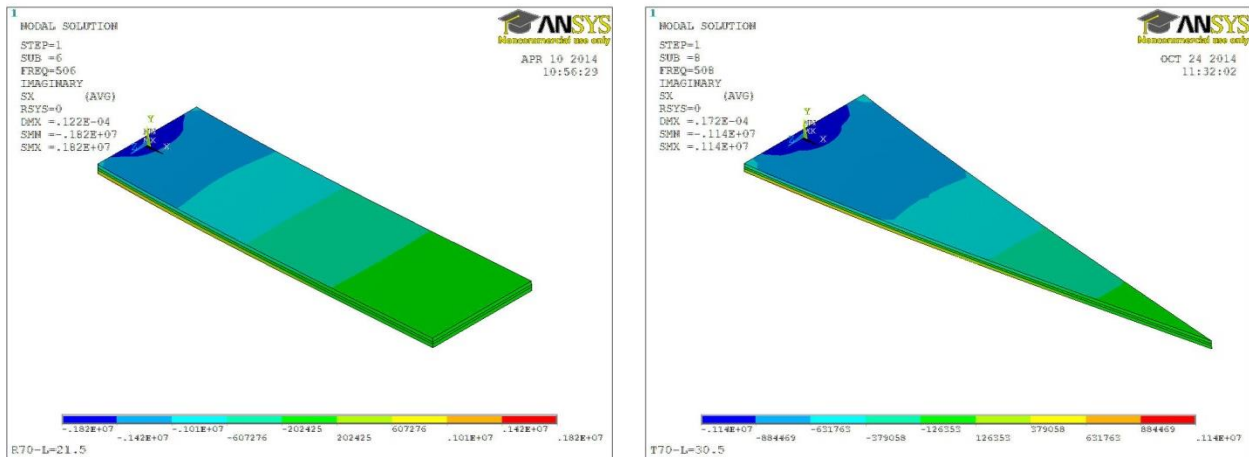


Figure 64: Schematics for  $70 \text{ mm}^3$  devices without a proof mass

From numerical simulations, the short circuit resonance frequency of these samples is expected to be around 515 Hz. This is in fact experimentally achieved for the rectangular samples with an average short circuit resonance frequency of 512 Hz. In the case of the triangular samples, the resonance frequency is found to be 500 Hz, which is a deviation of about 15 Hz, that amounts to a an error of 3%. This error can be attributed to fabrication or clamping length errors. The 3% error is not considered to be as huge, and comparisons between the two geometries are worthwhile.

Figure 65 and Figure 66 show the shift in resonance frequency for the rectangular and triangular piezoelectric bimorphs with changing load resistance. It can be seen that the shift in resonance frequency for the triangular samples is much larger at about 24 Hz, as compared to 17 Hz for the rectangular samples, which would result in a larger coupling coefficient for the triangles. This is the case indeed, as the coupling coefficients are calculated to be about 0.24 for the R70-0M samples, and 0.29 for the T70-0M samples. Therefore, the triangles give enhanced conversion efficiency, and also greater electromechanical damping.

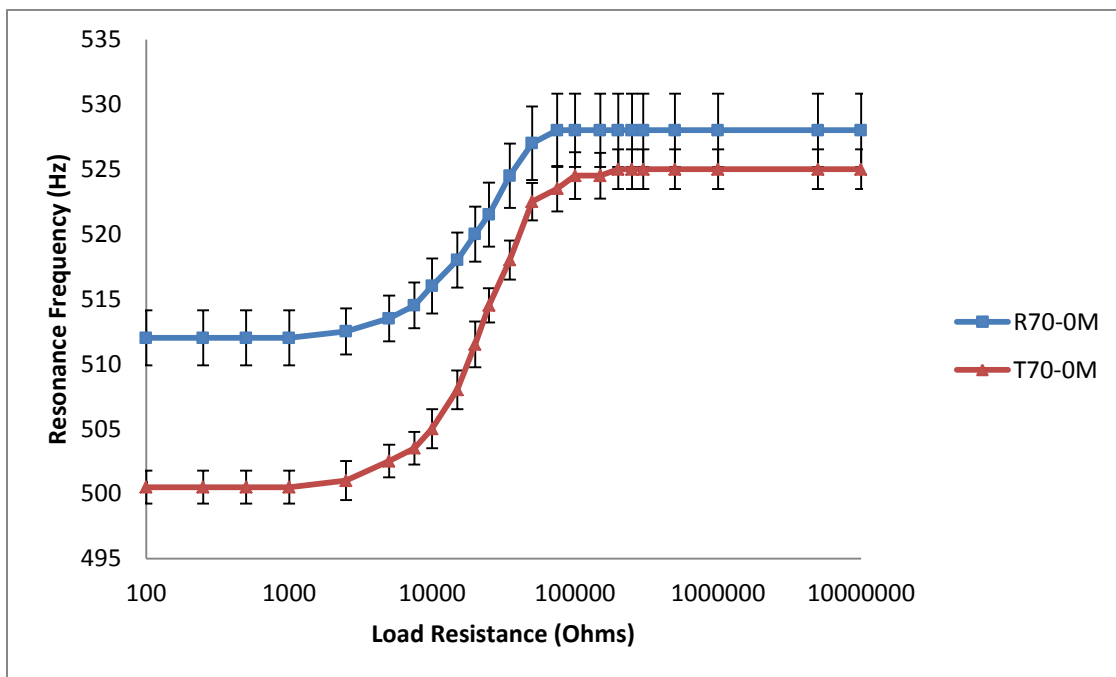


Figure 65: Resonance frequency as a function of load resistance for 70 mm<sup>3</sup> samples without a proof mass

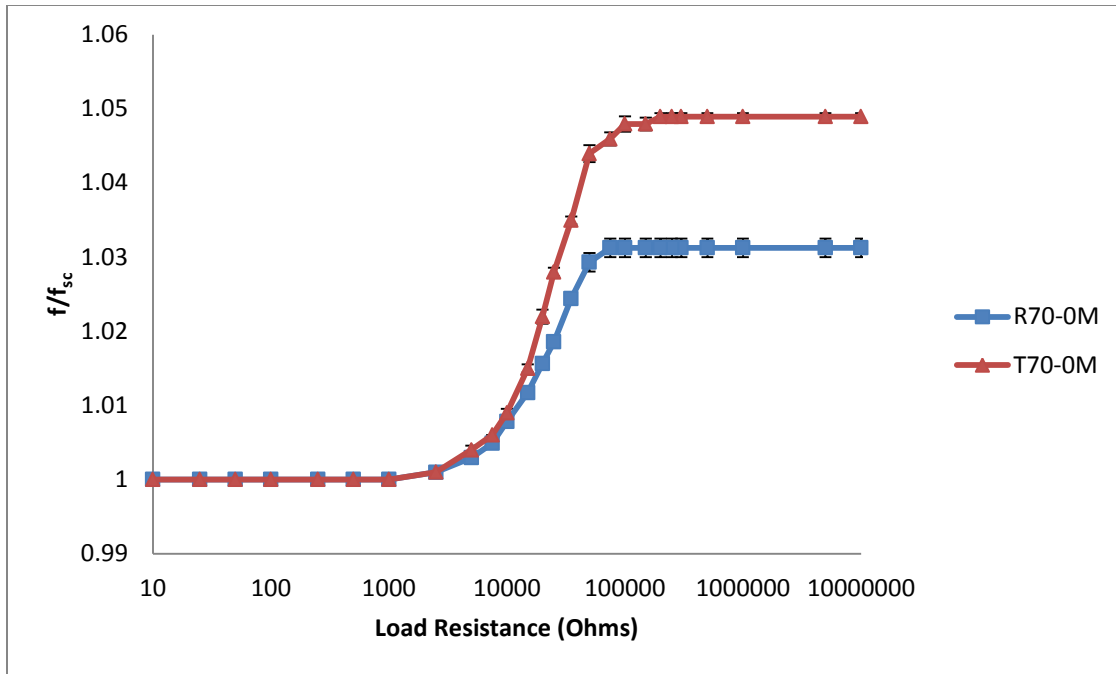


Figure 66: Normalized resonance frequency for 70 mm<sup>3</sup> samples without a proof mass

The power generated from the two samples is shown in Figure 67. It can be seen that the T70-0M barely outperforms R70-0M, only at certain load resistance values. The spread between the optimal load resistance's for the triangular samples is in fact larger, with two distinct peaks, as opposed to two shoulders for the rectangular samples; a clear indication of a higher coupling in the system. The power generated by R70-0M is about 3.64  $\mu$ W at 10,000  $\Omega$ , and 4.06  $\mu$ W at 100,000  $\Omega$ . The triangular samples show optimal load resistance's at 5000  $\Omega$  and 100,000  $\Omega$ , with maximum power of 3.52 and 4.31  $\mu$ W respectively. The dip in power for the triangular device at about 20,000 ohms is attributed to a maxima in damping at that frequency (illustrated in Section 5.6).

The damping ratio calculated for the two devices under open circuit conditions are found to be fairly similar to each other as 0.0085 for R70-0M, and slightly higher at 0.0097 for T70-0M. However, based on the larger electromechanical coupling coefficient, the  $k^2Q$  figure of merit for T70-0M is 4.71, larger than 3.61 for R70-0M. These two values describe the system in an intermediate coupling regime.

Table 3: Power output at optimal load resistance values for 70 mm<sup>3</sup> samples without proof mass

	R <sub>opt,1</sub> (Ω)	P (μW)	R <sub>opt,2</sub> (Ω)	P (μW)	ζ <sub>OC</sub>	k <sub>31</sub>	k <sup>2</sup> Q
R70-0M	10000	3.64	100000	4.06	0.0085	0.24	3.61
T70-0M	5000	3.52	100000	4.31	0.0097	0.29	4.71

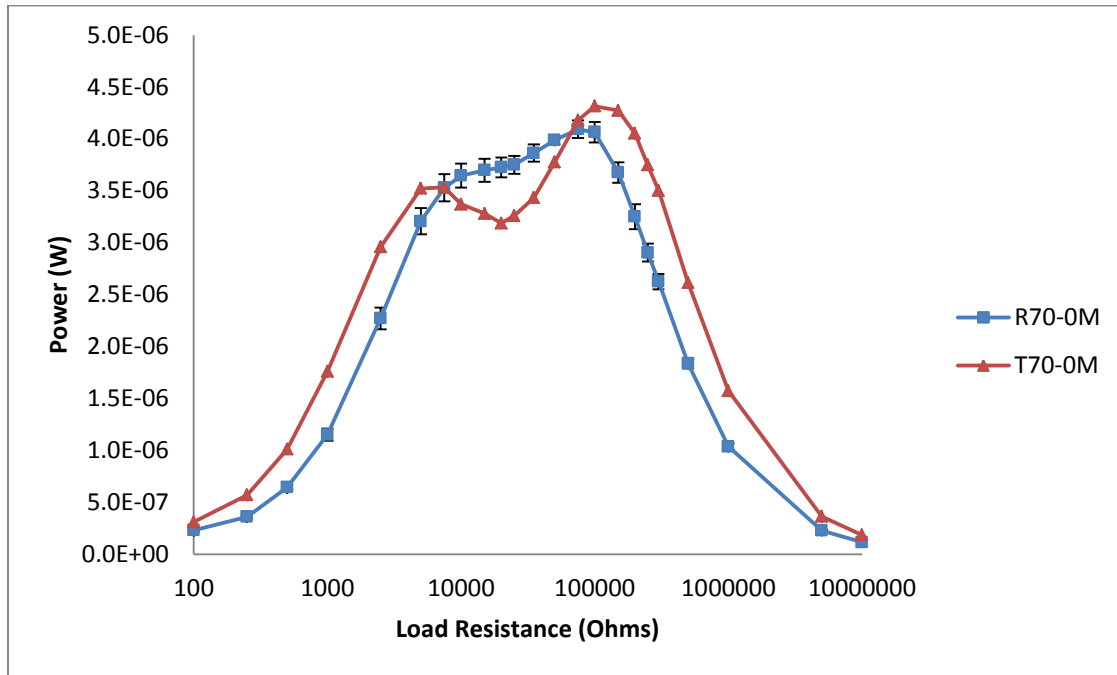


Figure 67: Power Generated from 70 mm<sup>3</sup> geometries without a proof mass

In order to understand the lack in performance for the triangular cantilever as compared to the rectangular counterpart, it is worthwhile understanding the state of deflection and stress in these cantilevers. This exercise has been performed numerically, with a harmonic analysis in ANSYS with a base acceleration of 2.4525 ms<sup>-2</sup> and a frequency sweep of 20 Hz around resonance. This harmonic analysis here is done for a non-coupled system, hence the results shown for deflection and stress relate to short circuit conditions in a piezoelectric bimorph. The results at resonance for deflection, plotted in Figure 68 and Figure 69 show that the deflection at the tip for the triangular bimorph is about 0.017 mm (17 μm), as compared to the rectangular bimorph, with 0.012 mm (12 μm). This result can be qualitatively anticipated due to the longer length of the triangular cantilever.

However, the results in Figure 70 and Figure 71, indicate the state of axial stresses are more important for correlating the amount of power generated from the piezoelectric bimorphs. It can be seen that the maximum stress, which is highly concentrated towards the fixed end of the beam in the rectangular cantilever is higher in magnitude as compared to the triangular cantilever. The maximum stress in the rectangular cantilever is 1.8 MPa, while in the case of the triangular bimorph, even with greater deflection at the tip is lower at 1.1 MPa. This indicates that the triangular structure, with the same volume, and roughly the same resonance frequency (not much error between the two structures in ANSYS), is capable of handling a greater load at the base due to its ability to distribute the stress in the structure more evenly.

This phenomenon is more apparent in Figure 72 and Figure 73, where the deflection and stresses along the length of the beam, on the top surface are plotted. Even though the resonance frequencies of the two devices are very similar, the deflection is greater in the case of the rectangular bimorph everywhere it exists, while the triangular bimorph has a greater deflection only where it is longer than the rectangular cantilever. The most likely explanation for this difference in deflection between the two devices is due to the fact that with the tapering of the beam, there is very little effective mass at the top of the beam in the case of the triangular device. Therefore, unlike the rectangular device R70-0M, the triangular device T70-0M suffers from a lack of inertial loading.

This lack of inertial loading at the tip shows a very apparent effect at the maximum stress, at the base of the cantilevered triangular bimorph. It can be observed in Figure 73 that the maximum stress in the case of the rectangular bimorph is 1.8 MPa, and in the case of the triangular bimorph is 1.14 MPa. Moreover, with the absence of the tip loading, the desired constant axial stress through the length of the device is not achieved. Overall, this indicates that the triangular device, with the same given inertial loading due to base excitation is operating at much lower levels of stress due to a stiffer base due to increased clamping width, and also slightly more even distribution of stress (not up to the desired level though) with a smaller declining slope over the axial stress profile.

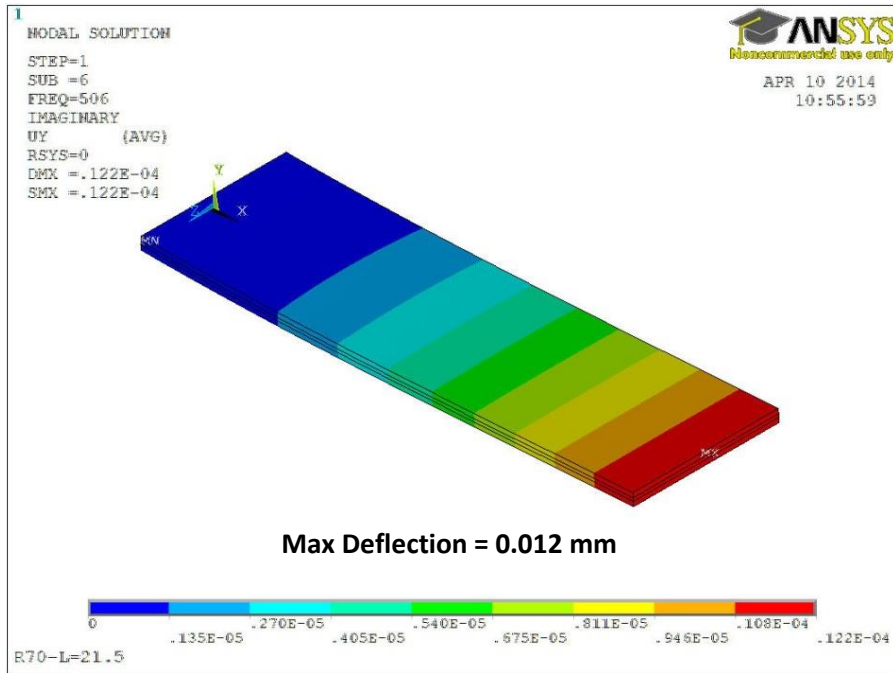


Figure 68: Deflection for 70 mm<sup>3</sup> Rectangular Cantilevered bimorph structure (non-piezoelectric) at resonance

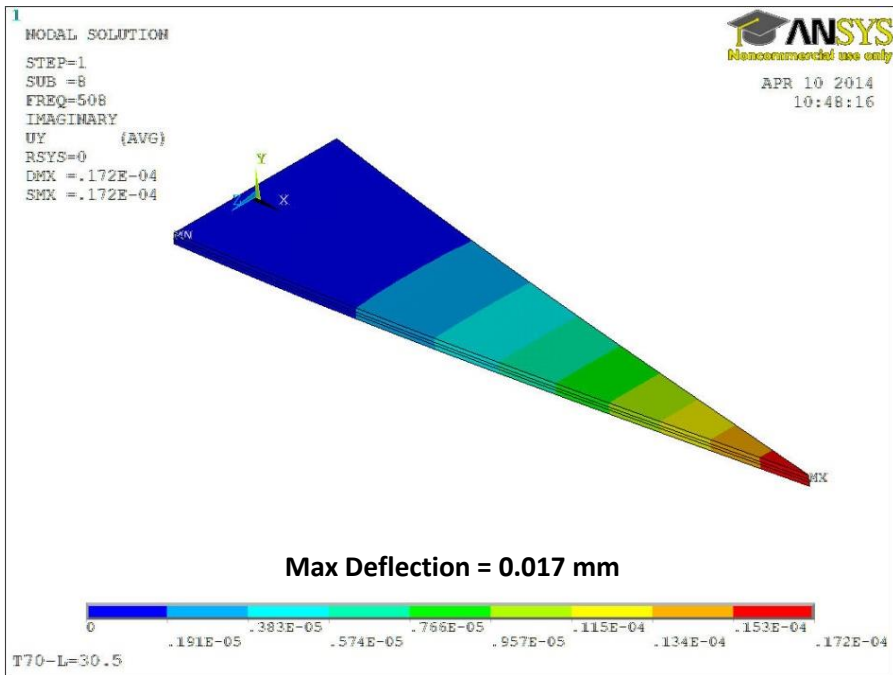


Figure 69: Deflection for 70 mm<sup>3</sup> Triangular Cantilevered bimorph structure (non-piezoelectric) at resonance

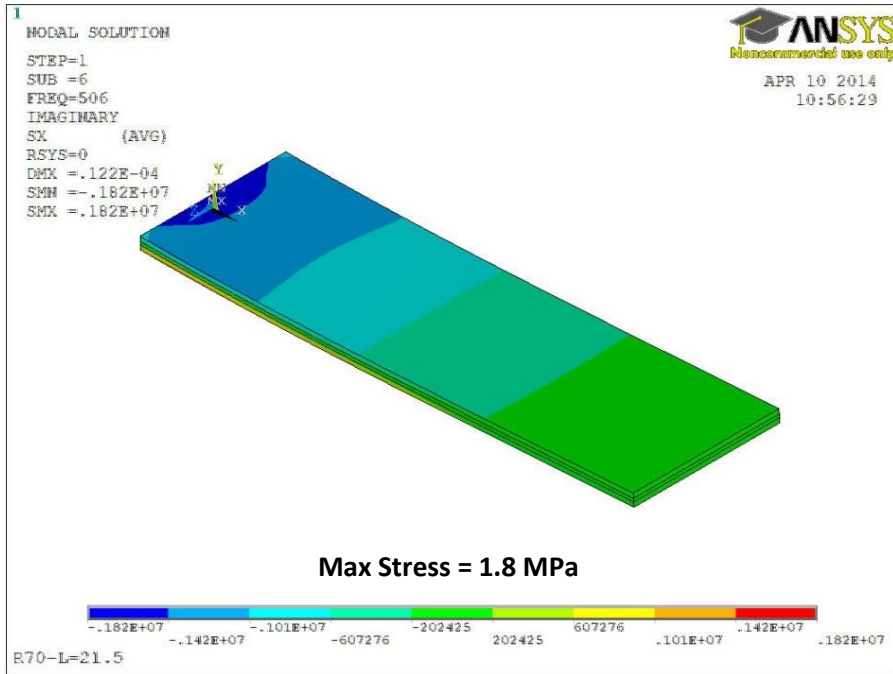


Figure 70: Axial Stress for  $70 \text{ mm}^3$  Rectangular Cantilevered bimorph structure (non-piezoelectric) at resonance

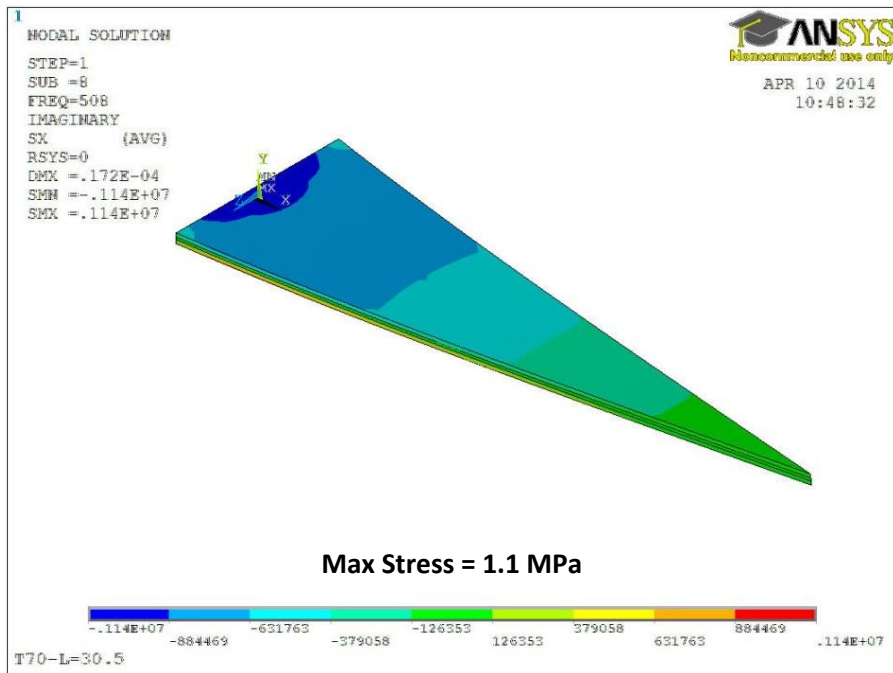


Figure 71: Axial Stress for  $70 \text{ mm}^3$  Rectangular Cantilevered bimorph structure (non-piezoelectric) at resonance

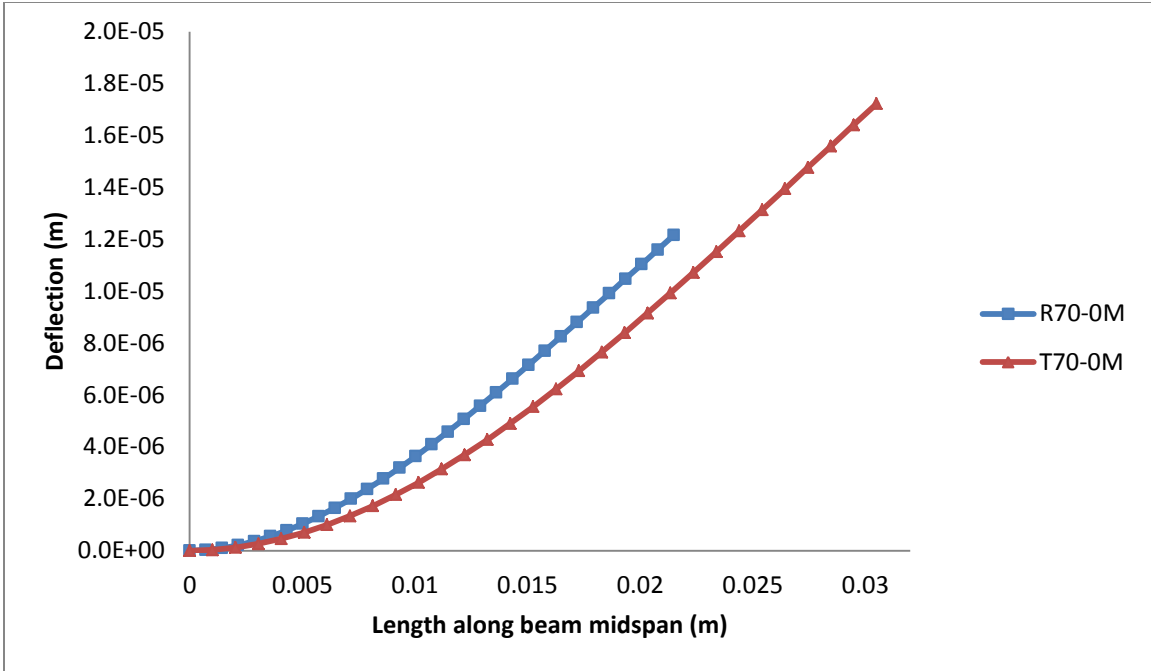


Figure 72: Deflection of the 70 mm<sup>3</sup> cantilevers along the beam mid-span

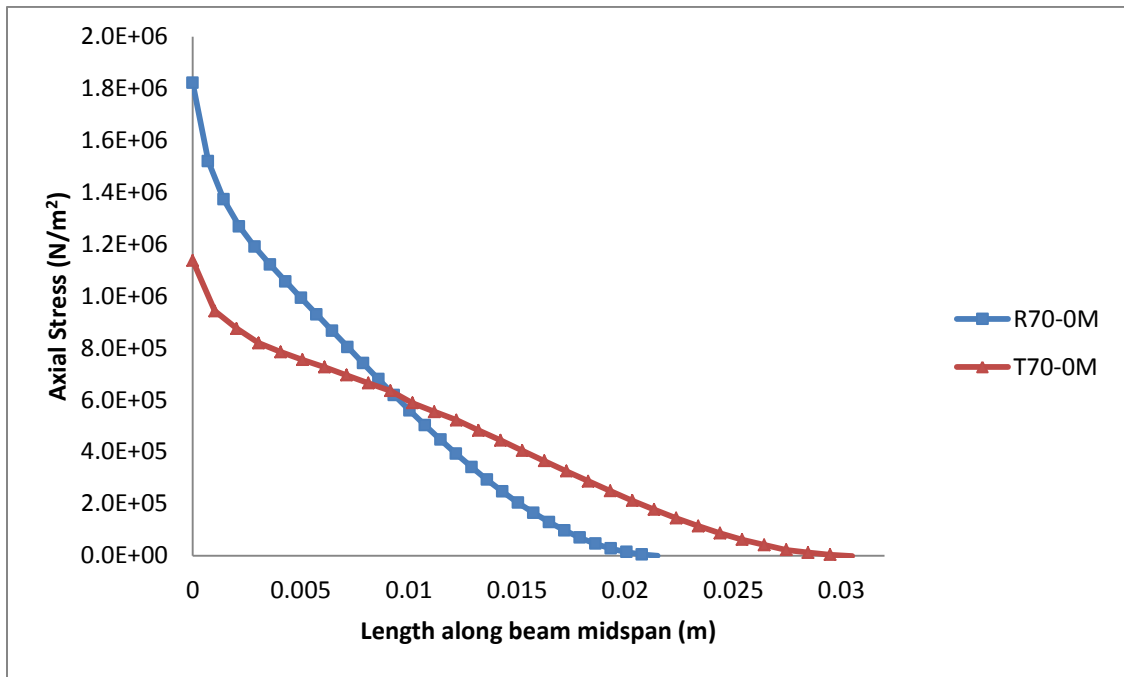


Figure 73: Axial stress per unit width along the beam midspan for 70 mm<sup>3</sup> cantilevers

An impedance spectroscopy analysis of the two sets of samples can also illustrate the effect of geometry on coupling. The  $|Z|-\theta$  plots are given for the two samples in Figure 74 and Figure 75, where it can be seen that the impedance at which the phase angle is zero is far more spread out in terms of the frequency (20 Hz for rectangles, and 29 Hz triangles). In addition, the difference between the maximum and minimum impedance (i.e. impedance at anti-resonance and resonance frequency) is larger for the triangular cantilevers. The impedance at the resonance frequency for the rectangular sample is higher, at 5558  $\Omega$  as compared to 3010  $\Omega$  for the triangle. The impedance at anti-resonance however is lower at 143,641  $\Omega$  for the rectangle and higher at 223,137  $\Omega$  for the triangular cantilever. Both of these observations are consistent with enhanced coupling in the system. Another indication of this is the wider peak seen for the triangular cantilevered bimorph. Interestingly, the magnitude of the peak of the phase angle is also higher in the case of the triangle at 66 degrees, as compared to 51 degrees for the rectangle. This larger phase angle at the peak implies a larger dielectric loss due to damping, which was seen in the case of the triangular cantilever, as the dip in Figure 69. The larger dielectric loss causes a dip in power generation, but increases the frequency bandwidth in that region, where power can be extracted from. These results are summarized in Table 4.

Table 4: Impedance characteristics for 70 mm<sup>3</sup> devices with no proof mass

Sample	$f_r$ (Hz)	Z (Ohms)	$f_a$ (Hz)	$ Z $ (Ohms)	Peak Phase <sup>o</sup>
R70-0M	511.2	5558	530.5	143,641	51
T70-0M	501	3023	530	223,137	66

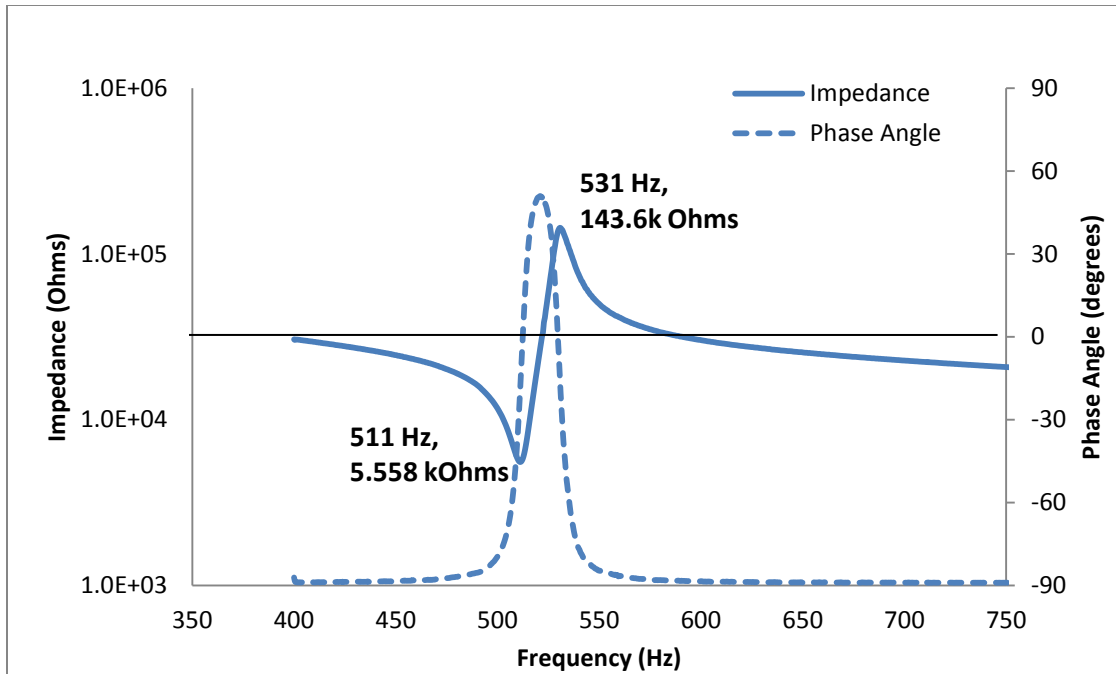


Figure 74: Impedance and Phase angle for R70-0M

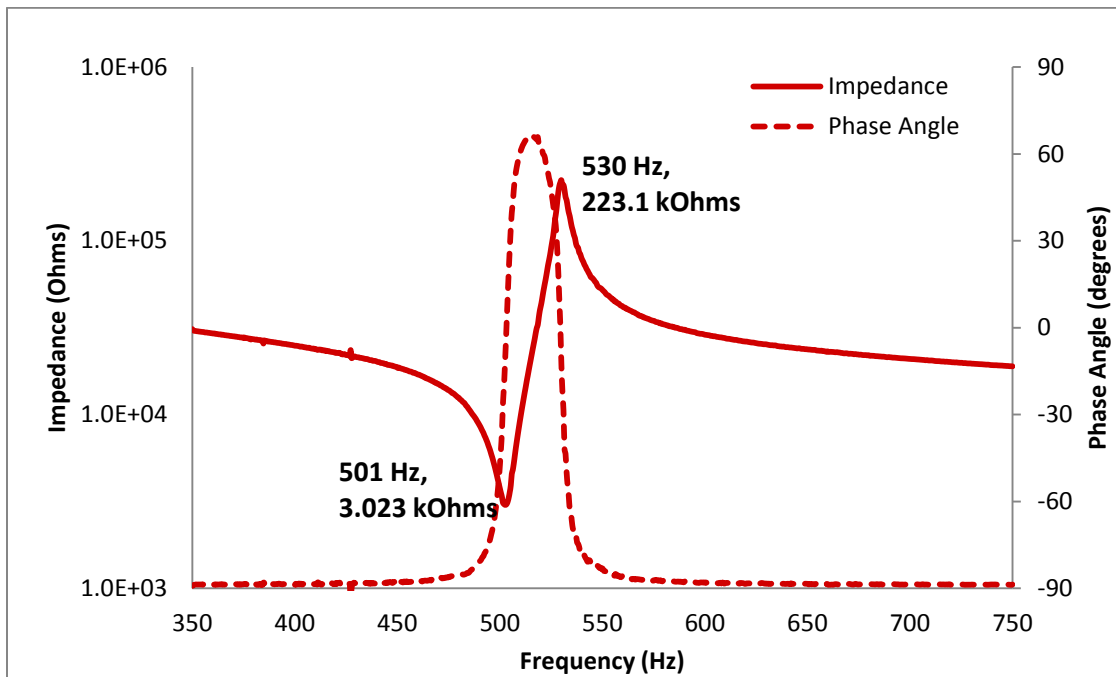


Figure 75: Impedance and Phase angle for T70-0M

From the impedance analyzer, the data for equivalent parallel capacitance and dissipation factor is also compared, which is presented in Figure 76 and Figure 77, and summarized in Table 5. While the bulk capacitance for the devices with equal volumes remains the same based on the constant dielectric permittivity; the capacitance changes around resonance.

The maximum capacitance for the rectangular sample is 37 nF, and for the triangular sample, with the same volume is 63.7 nF, a 42% increase. The negative capacitance in the triangular sample is also greater by 53%, which shows a capacitance of -46.1 nF, and the rectangle shows a negative capacitance of -21.4 nF. This larger absolute value is also indicative of larger electromechanical coupling in the system, and also has implications in circuitry applications. A larger capacitance is more compliant with the circuitry attached in series with the bimorph, and a large negative capacitance, which indicates that the dielectric material becomes conductive at this frequency, is applicable in shunt damping applications for vibration attenuation [56].

Table 5: Capacitance characteristics for 70 mm<sup>3</sup> devices with no proof mass

Sample	Positive capacitance peak (nF)	Negative capacitance peak (nF)
R70-0M	37	-21.4
T70-0M	63.7	-46.7

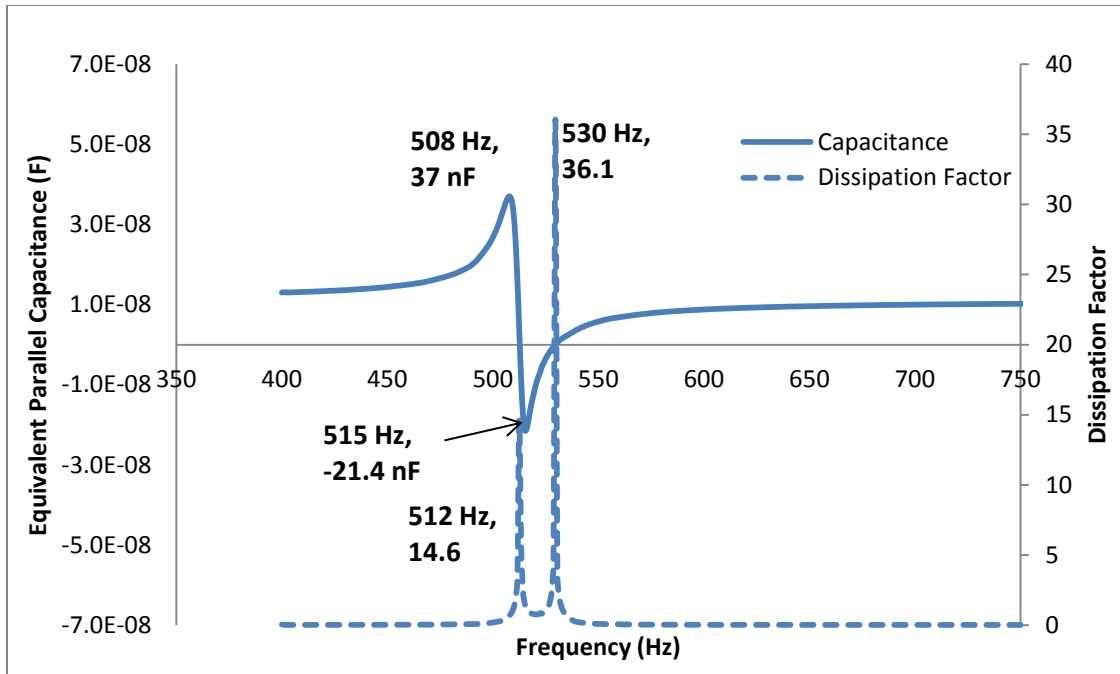


Figure 76: Capacitance and Dissipation factor for R70-0M

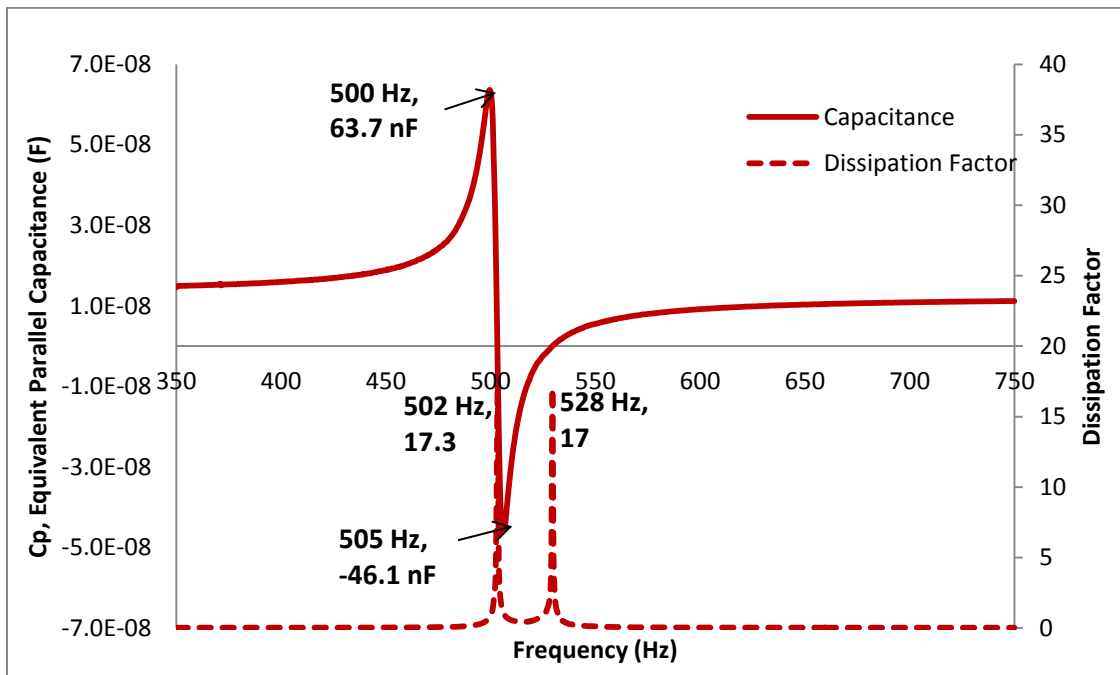


Figure 77: Capacitance and Dissipation factor for T70-0M

## 5.2.2 104 mm<sup>3</sup> samples

Another set of samples that was created was rectangular and triangular geometries that were 104 mm<sup>3</sup> in volume. The clamped lengths of the rectangles were fixed at 21.5 mm, and 30.5 mm for the triangular bimorphs. The rectangular bimorphs were 9.525 mm in width, and triangles had a base width of 13.43 mm, resulting in a base angle of 77.6°. Schematics for these devices are shown in Figure 78.

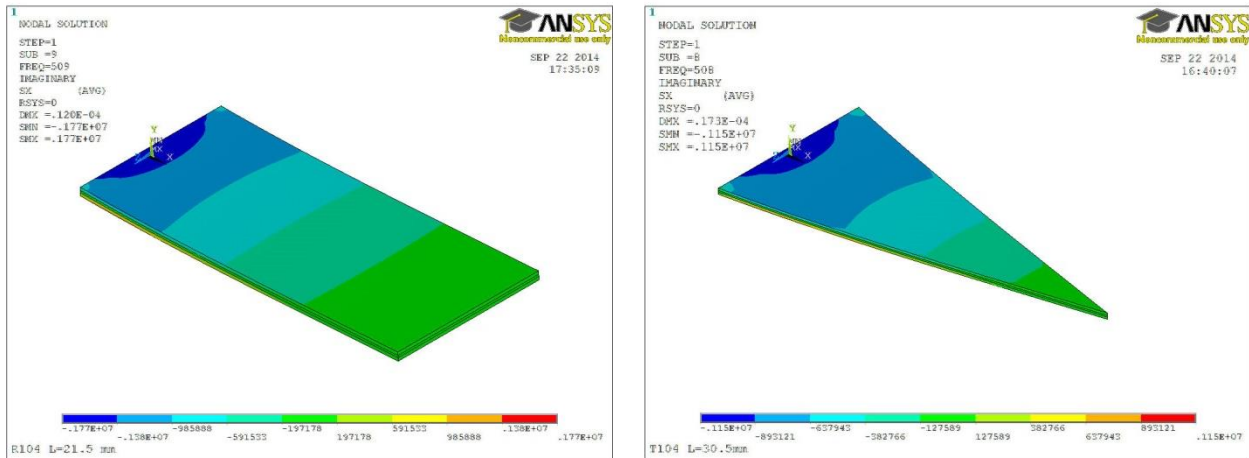


Figure 78: Schematic for 104 mm<sup>3</sup> devices with no proof mass

The resonance frequency of these devices was around 528 Hz for both samples. With the increase in base width, there was a substantial increase in the coupling coefficient for the rectangular sample, which has a coupling coefficient that was calculated to be 0.286, an increase of 17% from the 70 mm<sup>3</sup> sample. The coupling coefficient for the triangular sample also increased, but only by 2% from the 70 mm<sup>3</sup> sample, which is 0.308 for the 104 mm<sup>3</sup> triangle. Nevertheless, the triangular bimorph still shows an advantage here with respect to its rectangular counterpart in terms of the coupling coefficient, which can be noticed in Figure 79 and especially in Figure 80, where the normalized resonance frequency under open-circuit conditions for the triangular bimorphs is larger. It is important to notice that, with increasing base (clamping) width, the electromechanical coupling coefficient is increasing.

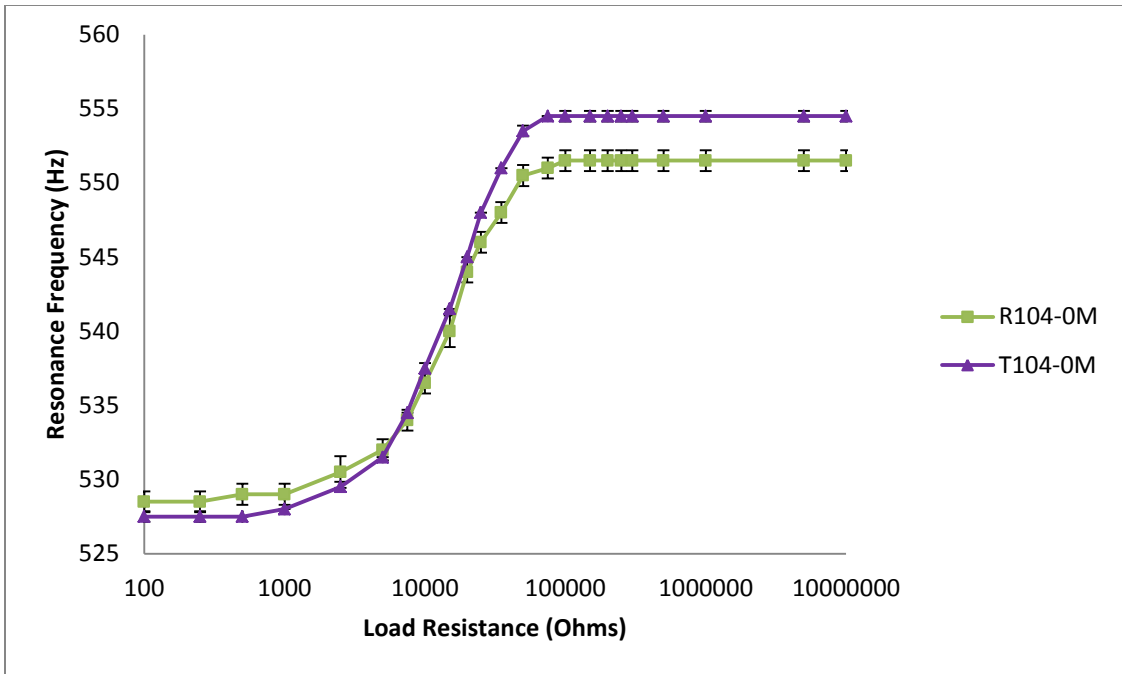


Figure 79: Resonance Frequency for 104 mm<sup>3</sup> devices

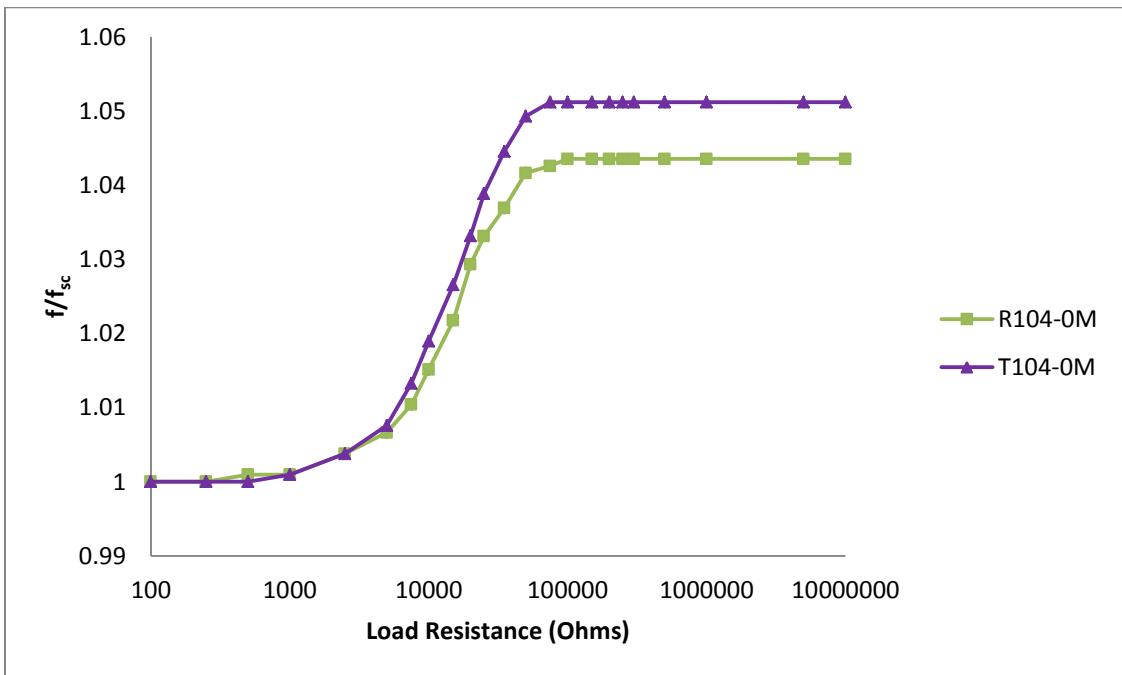


Figure 80: Normalized resonance frequency for the 104 mm<sup>3</sup> samples

Figure 81 compares the power generated from the  $104 \text{ mm}^3$  samples, where it can be seen that the power output from the triangular bimorphs is a substantially lower compared to the rectangular bimorphs, as presented in Table 6. The rectangular bimorphs produce  $5.35 \text{ }\mu\text{W}$  and  $5.85 \text{ }\mu\text{W}$ , as compared to  $3.68 \text{ }\mu\text{W}$  and  $4.38 \text{ }\mu\text{W}$ , at their optimal load resistance values. Both of these optimal load resistance values are represented by two distinct peaks in Figure 81, indicative of the increased electromechanical coupling figure of merits.

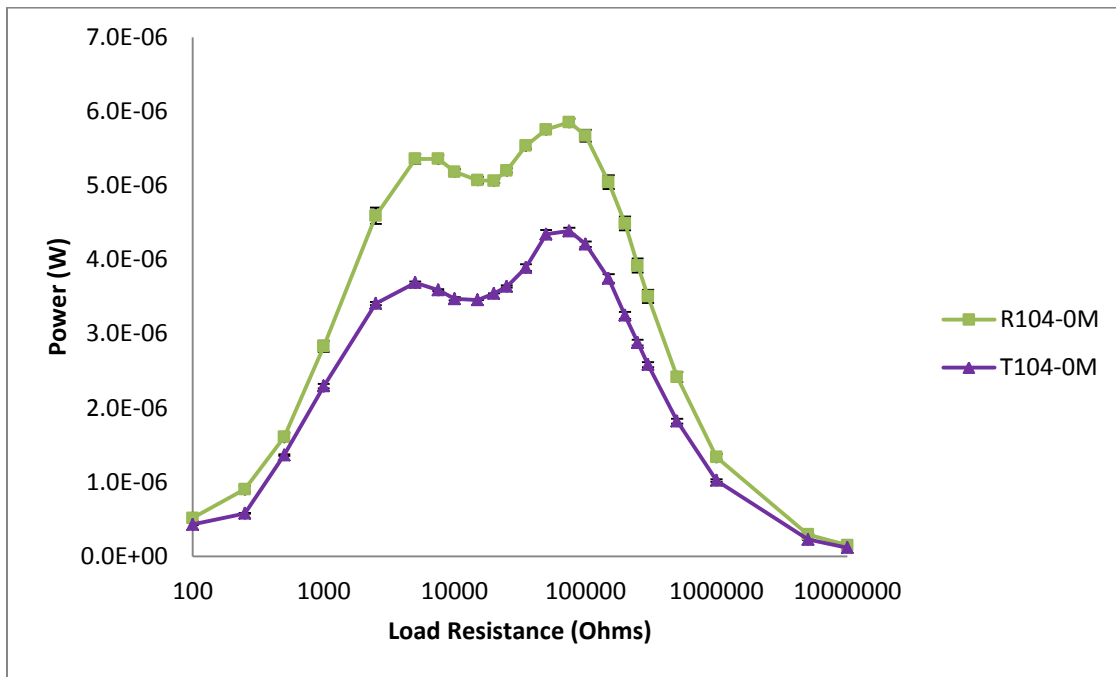


Figure 81: Power generated from  $104 \text{ mm}^3$  samples without a proof mass

Table 6: Power output at optimal load resistance values for  $104 \text{ mm}^3$  samples without proof mass

	$R_{\text{opt},1}(\Omega)$	$P (\mu\text{W})$	$R_{\text{opt},2}(\Omega)$	$P (\mu\text{W})$	$\zeta_{\text{OC}}$	$k_{31}$	$k^2Q$
R104-0M	5000	5.35	100000	5.85	0.0086	0.29	4.76
T104-0M	5000	3.68	75000	4.38	0.0095	0.31	5.64

The deflections and stresses for the  $104 \text{ mm}^3$  samples, shown in Figure 82 and Figure 83 are nearly identical to the results found for the  $70 \text{ mm}^3$  devices. This is seen mainly due to the fact that the devices have very similar resonance frequencies and the same base excitation, and therefore, in the absence of any proof mass loading, the differences between the two sets in terms

of maximum stress at the base are negligible. It is once again seen that the triangular device operates at much lower levels of maximum stress compared to its rectangular counterpart.

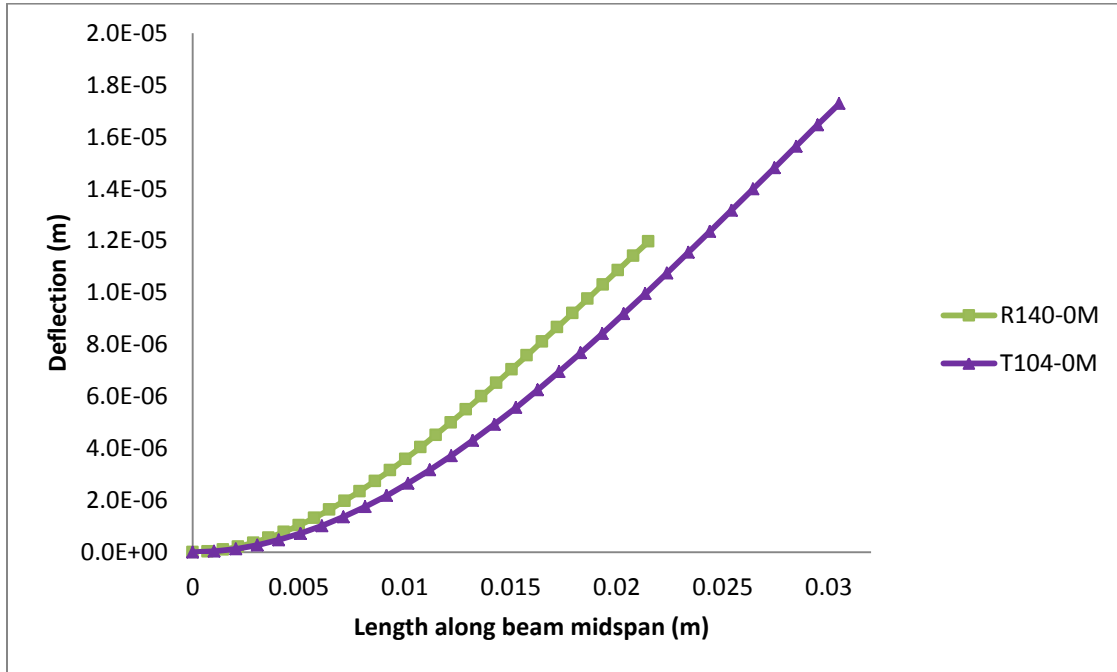


Figure 82: Deflection of 104 mm<sup>3</sup> cantilevers without a proof mass

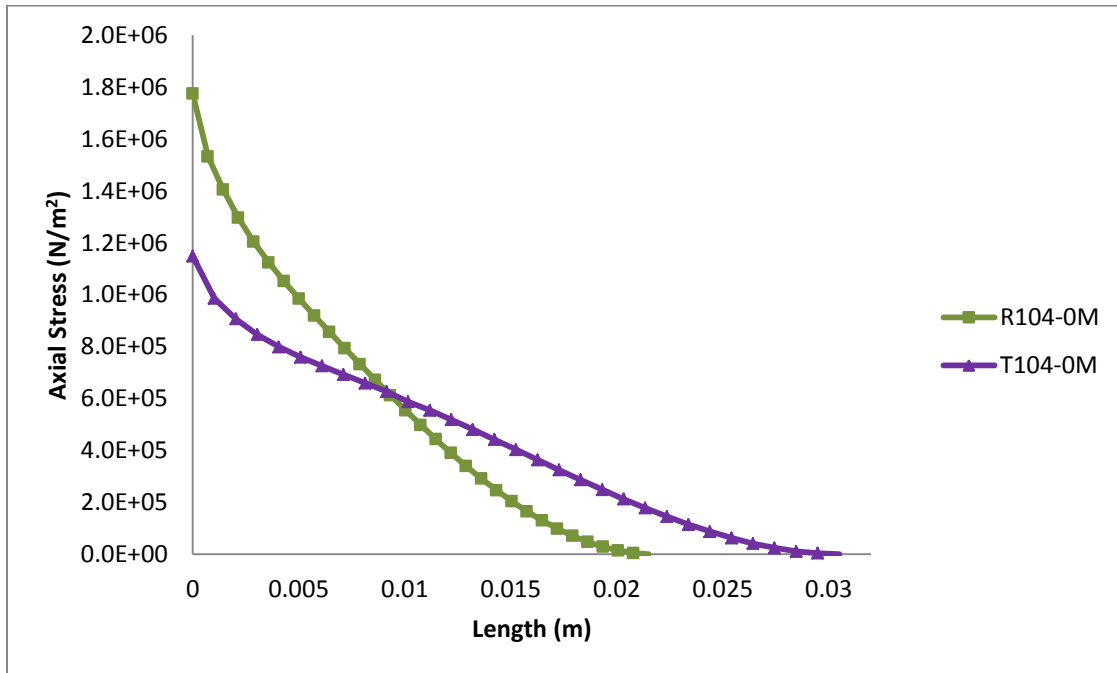


Figure 83: Axial Stress for 104 mm<sup>3</sup> samples

The results from the impedance spectroscopy here reinforce the results based on electromechanical coupling from resonance frequency measurements and the occurrence of double peaks at optimal load resistance values for the power generated between the two devices. It can be clearly seen in Figure 84 and Figure 85 that the difference between the minimum and maximum impedance for the triangular sample, as summarized in Table 7. It can be seen that the triangular device has a lower impedance value (1979  $\Omega$ ) at resonance and higher impedance at anti-resonance (156,866  $\Omega$ ) compared to the rectangular bimorph (3279  $\Omega$  and 107,373  $\Omega$  respectively). Therefore, with the triangular device, peak power can be generated at lower load resistance values with high voltages, which can be beneficial for external circuitry to extract power with lower currents. Moreover, the wider spread between the optimal load resistance values with the triangular devices would allow a greater number of load resistance values at which appreciable power can be generated.

Table 7: Impedance measurements for 104 mm<sup>3</sup> devices with no proof mass

Sample	$f_r$ (Hz)	Z (Ohms)	$f_a$ (Hz)	$ Z $ (Ohms)	Peak Phase <sup>o</sup>
R104-0M	523	3,297	547.5	107,373	55.15
T104-0M	521.5	1979	550.6	156,866	67.09

The capacitance measurements for the two devices with the same device volume are presented in Figure 86 and Figure 87. The capacitance peaks for the two devices are appreciably increased for the triangular device, with a 35% increase in the case of the positive peak, and a 50% increase in the case of the negative capacitance peak. This is again in relation with the enhanced electromechanical coupling in the triangular device, at very similar resonance frequencies, providing enhanced capacitance properties, for energy harvesting, or vibration attenuation.

Table 8: Capacitance measurements for 104 mm<sup>3</sup> devices with no proof mass

Sample	Positive capacitance peak (nF)	Negative capacitance peak (nF)
R104-0M	60.96	-34.70
T104-0M	93.45	-70.59

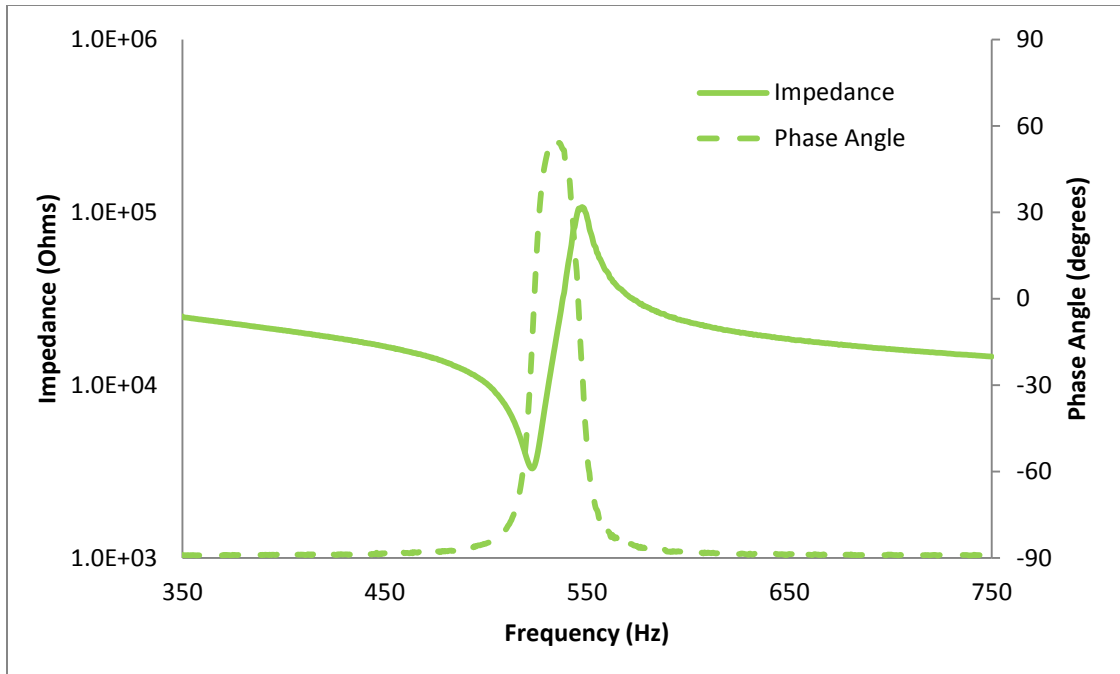


Figure 84: Impedance-Phase Angle for R104-0M

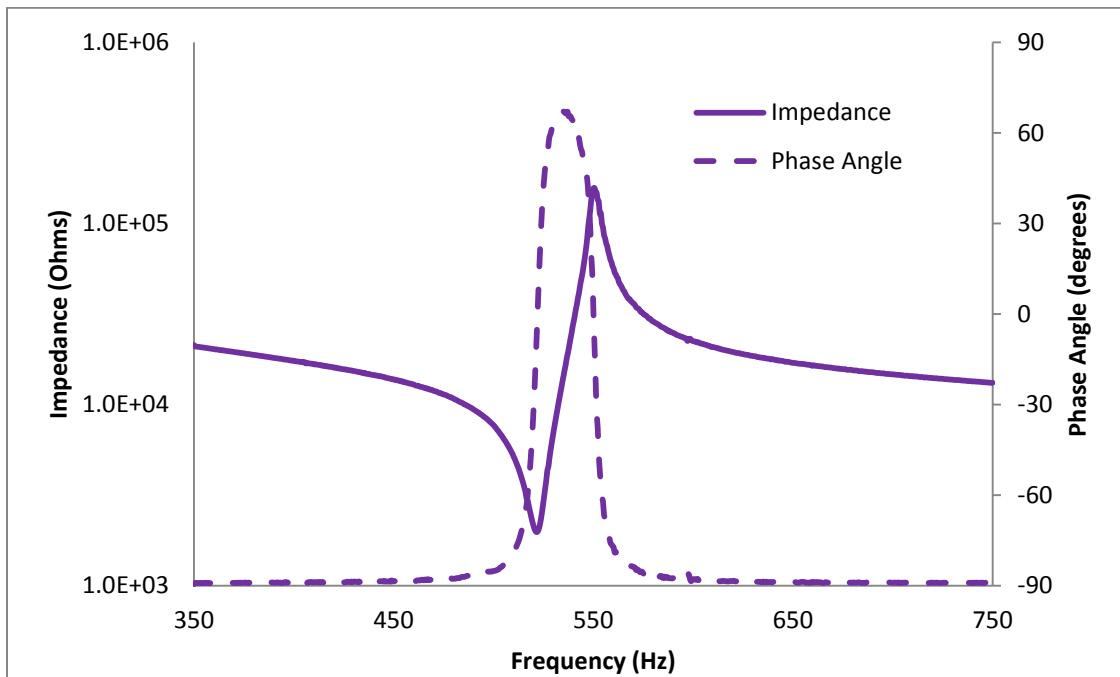


Figure 85: Impedance-Phase Angle for T104-0M

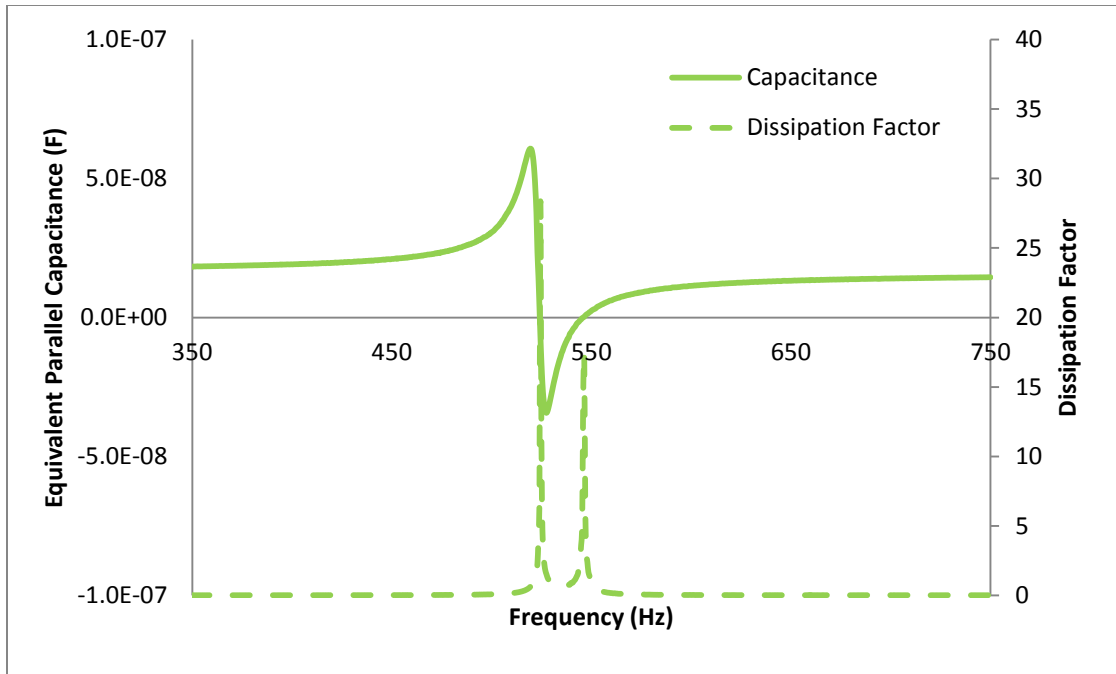


Figure 86: Capacitance-Dissipation factor for R104-0M

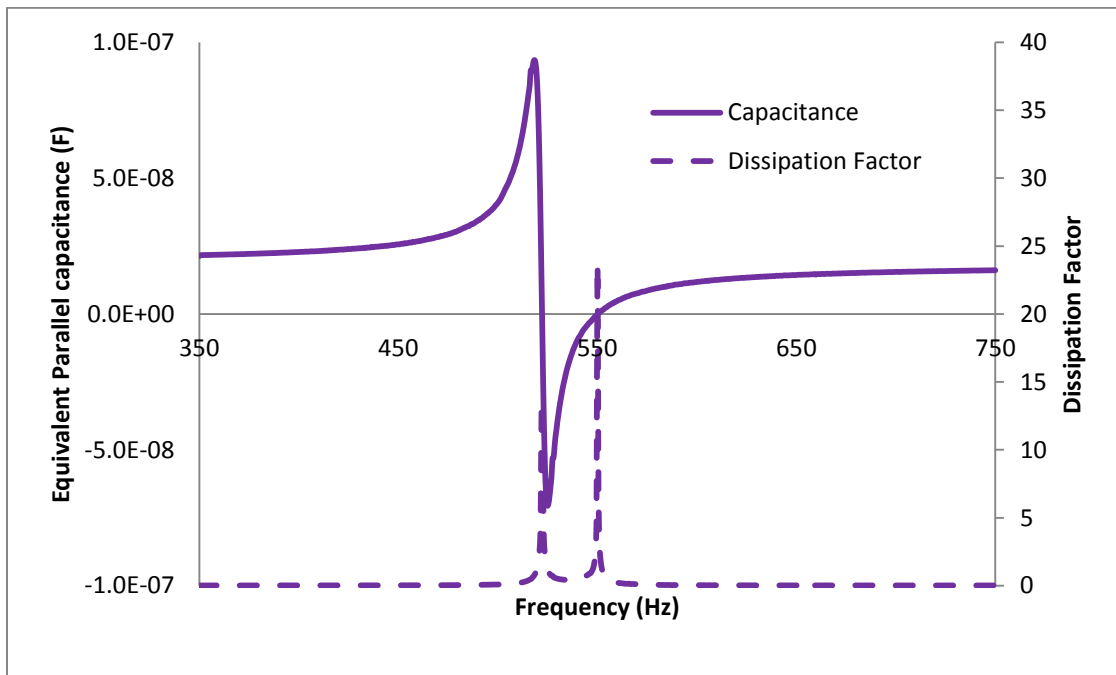


Figure 87: Capacitance-Dissipation Factor for T104-0M

### 5.2.3 140 mm<sup>3</sup> samples

This set of samples includes geometries that are 140 mm<sup>3</sup> in volume. In similar fashion to the previous two cases, the thickness for both sets is 0.51 mm, and the length of the rectangular bimorphs is set at 21.5 mm, while the triangles are set at 30.5 mm length. The width of the rectangular bimorph was 12.7 mm, while the triangle was calculated to be 19.05 mm, as illustrated in Figure 88. This results in a base angle of 73.64 degrees.

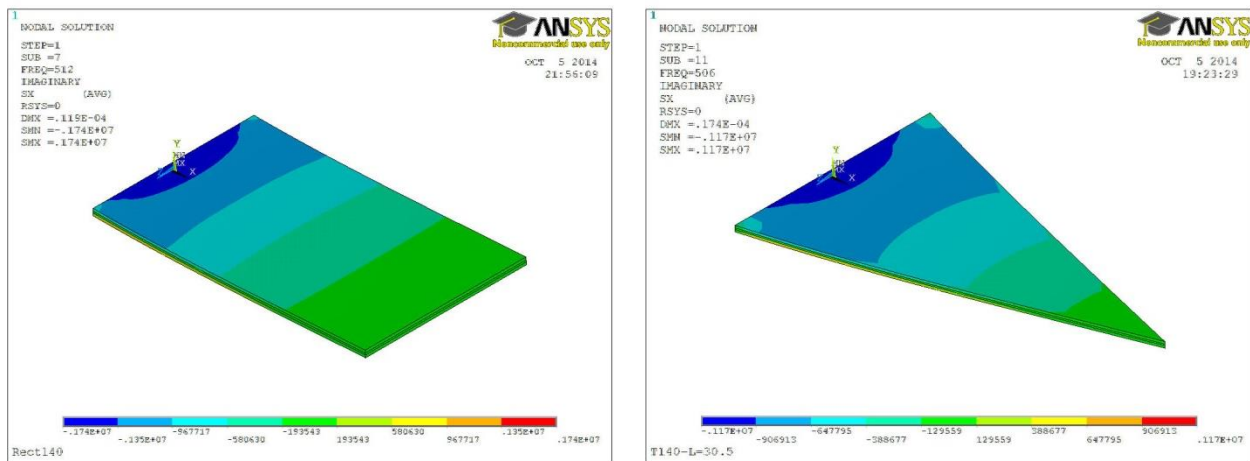


Figure 88: Schematics for 140 mm<sup>3</sup> devices without a proof mass

The resonance frequency of the rectangular sample(s) was expected to rise from the previous case of 104 mm<sup>3</sup> samples, however it is found to be around 516 Hz, as shown in Figure 89. This can be attributed to a combination of experimental errors, and also due to increased damping due to stiffness and viscous damping due to a larger surface area, due to which the damped natural frequency could be lower. The modal analysis predictions report un-damped natural frequencies, which is the limiting nature of these simulations, when the experimental damping ratio is unknown prior to simulations. However, the experiments do depict a trend that follows previous results, and the error in resonance frequencies is not outrageous.

Figure 90 shows the normalized resonance frequencies of the 140 mm<sup>3</sup> samples, again indicating a larger coupling coefficient in the case of the triangular bimorph as compared to the rectangle. The trend for increasing coupling coefficients with increasing base width also follows as it did in the 104 mm<sup>3</sup> samples from the 70 mm<sup>3</sup> samples. The average coupling coefficient for the 140 mm<sup>3</sup> rectangles is found to be 0.29, while for the 140 mm<sup>3</sup> triangles is found to be 0.32.

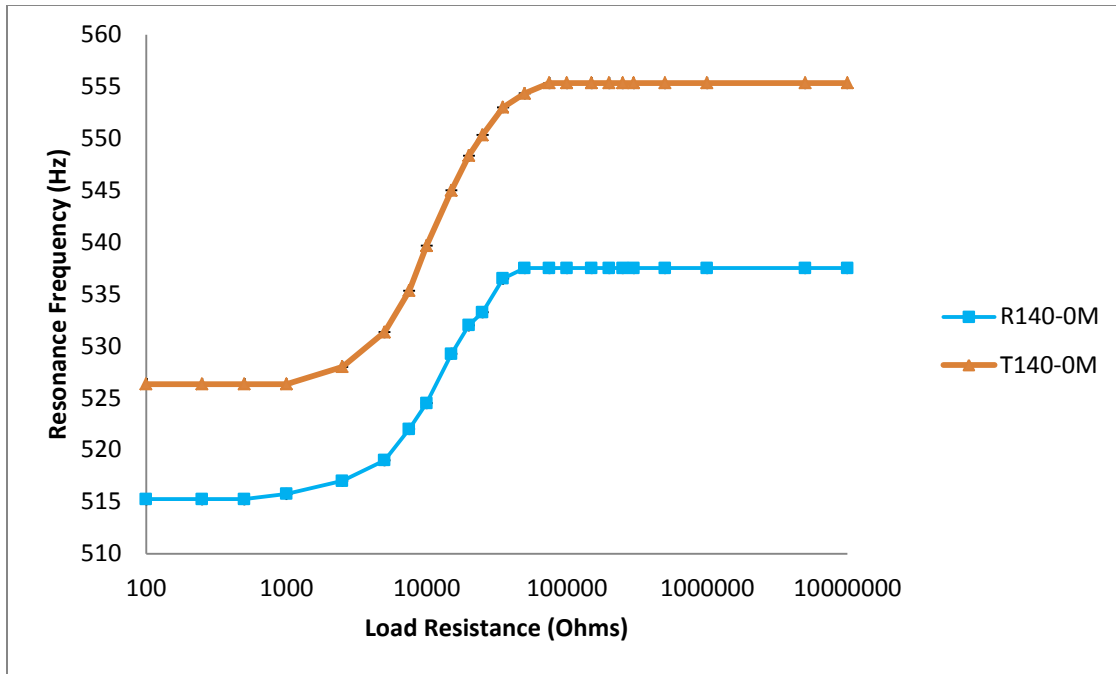


Figure 89: Resonance frequency for 140 mm<sup>3</sup> cantilevered bimorphs without proof mass

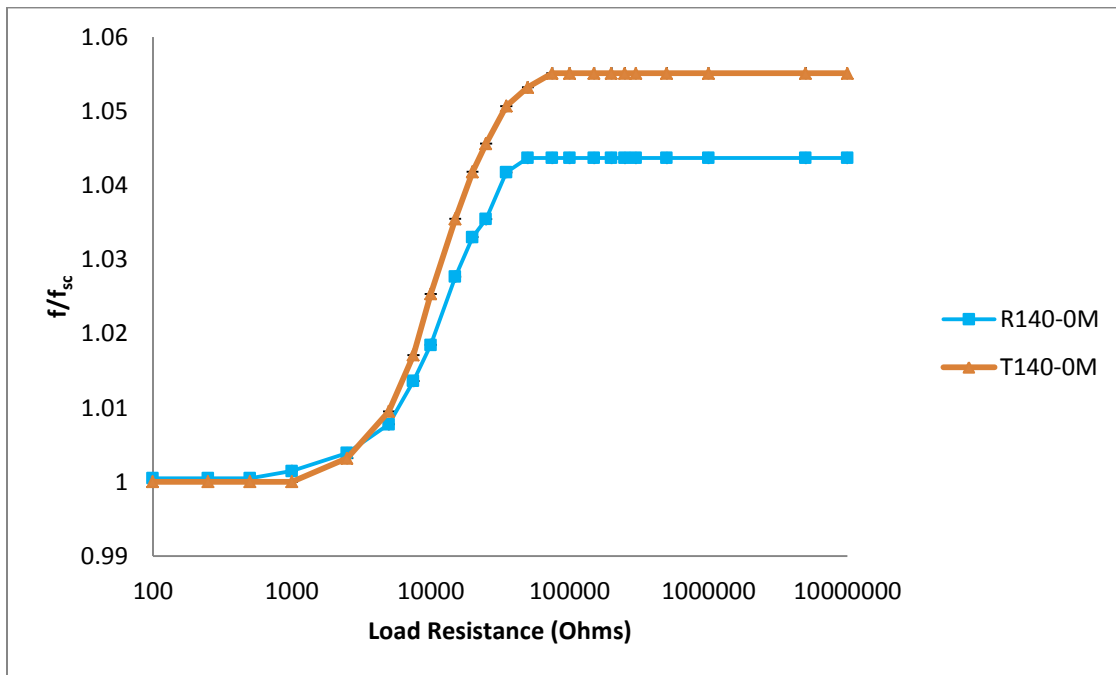


Figure 90: Normalized Resonance frequency for 140 mm<sup>3</sup> cantilevers without proof mass

The power generated from the rectangular bimorphs again increases slightly in magnitude, at roughly 5000 and 50000 ohms peak load resistance. For the triangular bimorphs,

the optimal load resistances are now found to be at 2500 ohms 75000 ohms. Therefore, in both these samples, the optimal resistance values are shifting to lower values compared to previously tested samples (104 mm<sup>3</sup> devices and 70 mm<sup>3</sup> devices), with enhanced coupling. This would be a desired effect, since devices with lower impedances would relate to lower dielectric losses. This phenomenon is discussed in results from the impedance analyzer measurements. The powers with optimal load resistance values for 140 mm<sup>3</sup> samples are summarized in Table 9.

Table 9: Power output at optimal load resistance's for 140 mm<sup>3</sup> devices without proof mass

	$R_{opt,1}(\Omega)$	P ( $\mu$ W)	$R_{opt,2}(\Omega)$	P ( $\mu$ W)	$\zeta$	$k_{31}$	$k^2Q$
R140-0M	5000	6.53	50000	7.41	0.0088	0.29	4.73
T140-0M	2500	3.14	75000	3.48	0.0087	0.31	5.86

Similar to the trends as followed in previous sections, it can be seen that the absolute power generated for R140-0M increases from R104-0M, whereas it decreases for T140-0M from T104-0M. The reasoning behind this is again enhanced stiffness for the triangular cantilevers, with increasing base width, allowing a larger inertial loading capacity.

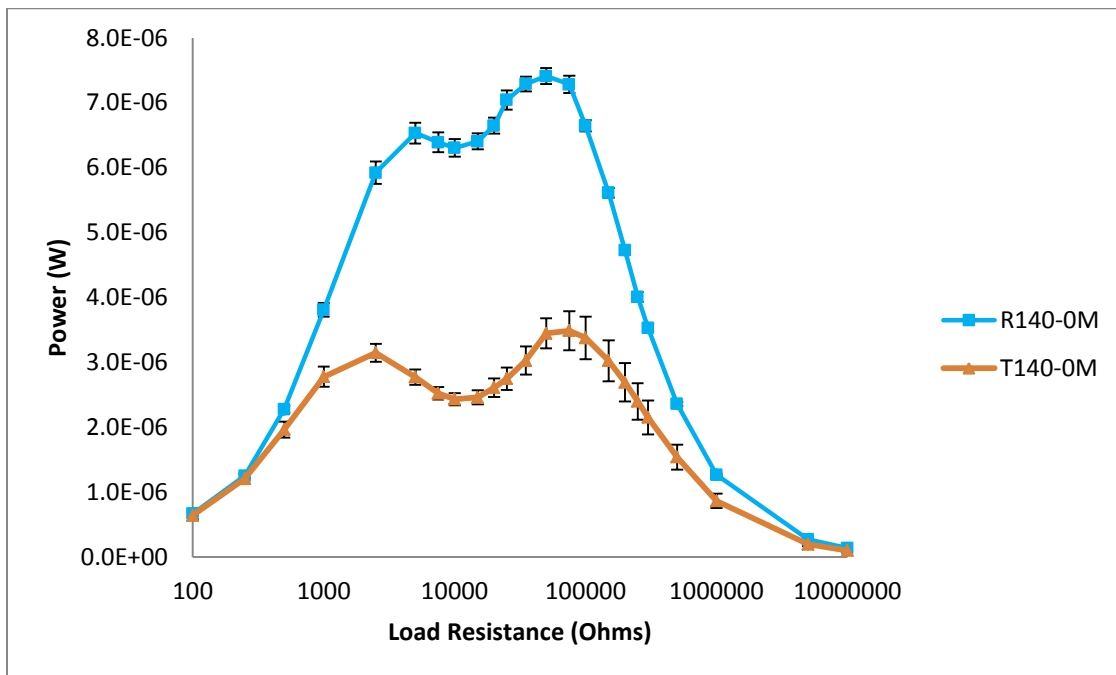


Figure 91: Power generated from 140 mm<sup>3</sup> cantilevered bimorphs without proof mass

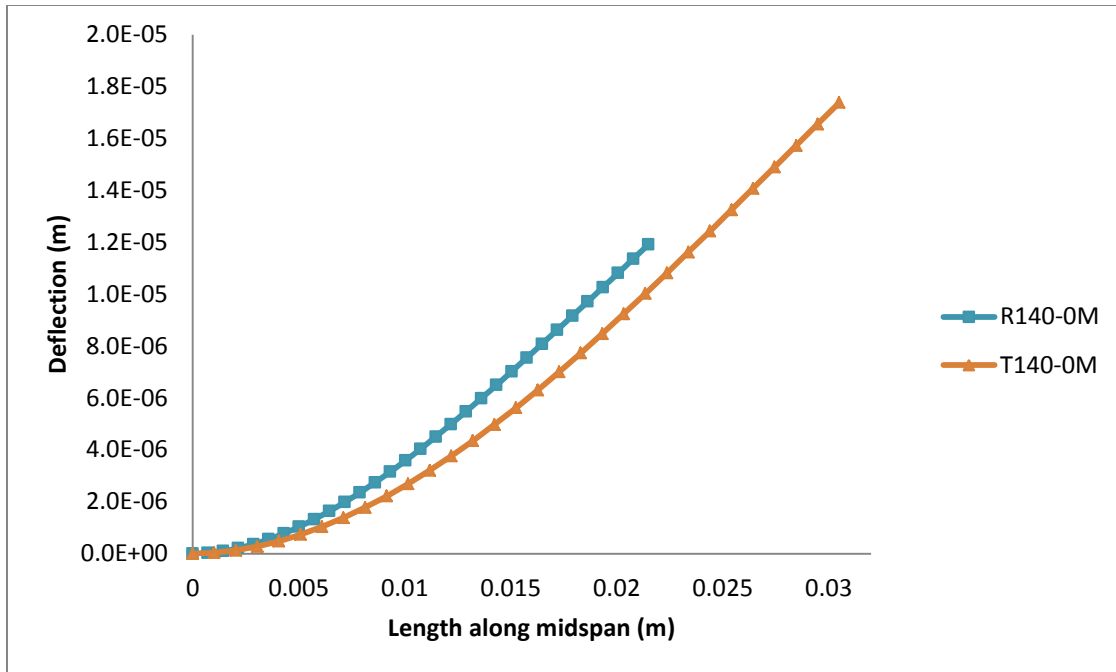


Figure 92: Deflection along the mid-span for the 140 mm<sup>3</sup> cantilevered bimorphs without proof mass

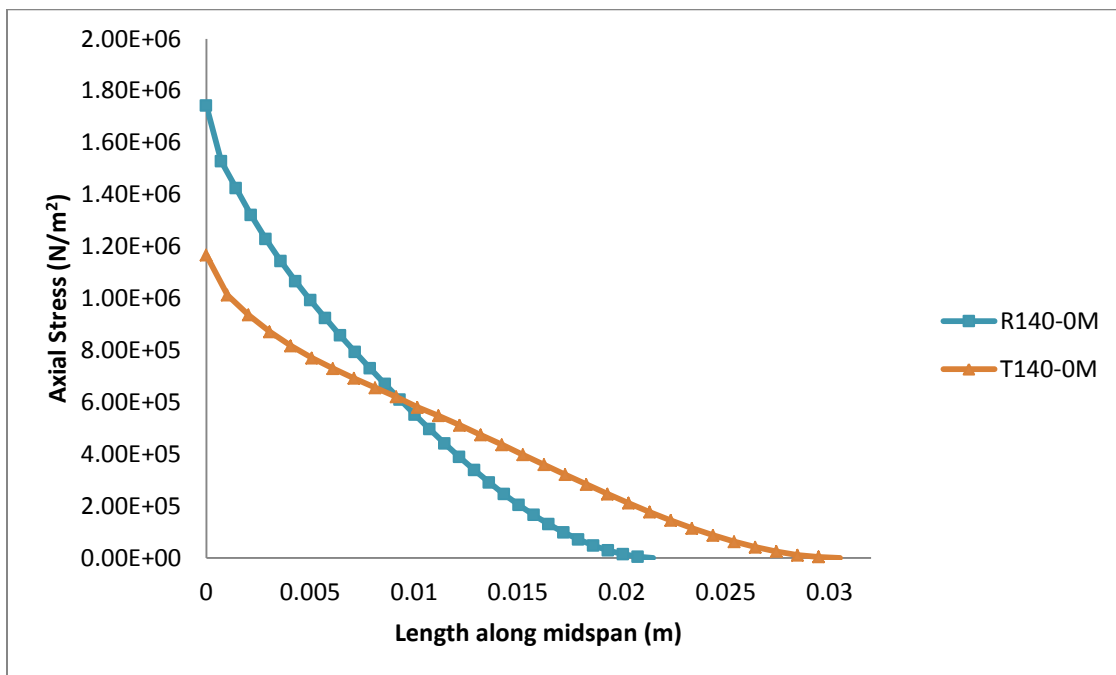


Figure 93: Axial Stress for 140 mm<sup>3</sup> cantilevered bimorphs without proof mass

The impedance analyzer measurements, presented in Figure 94 and Figure 95 show a consistent trend from previous cases. In the case of the triangular cantilevers, the spread between the resonance and anti-resonance frequencies is larger, and also the spread between the differences in magnitude of impedance values is also larger, compared to rectangular counterparts. Both of these phenomena, as reported in Table 10 are related to enhanced stiffness in the device with the change in shape.

Table 10: Impedance measurements for 140 mm<sup>3</sup> samples with no proof mass

Sample	f <sub>r</sub> (Hz)	Z (Ohms)	f <sub>a</sub> (Hz)	Z  (Ohms)	Peak Phase°
R140-0M	511.3	2471.7	537.1	90,831.3	56.4
T140-0M	524	1291.1	556	152,511.6	71.26

The capacitance measurements also follow a similar trend from the 104 mm<sup>3</sup> and 70 mm<sup>3</sup> devices. As the shape of the device is changed from the rectangular to triangular bimorph, the peak capacitance values are increased. The positive capacitance peak measured for the 140 mm<sup>3</sup> triangular bimorph is 40% greater than the rectangular device, and the negative capacitance peak is 60% greater, as presented in Table 11.

Table 11: Capacitance measurements for 140 mm<sup>3</sup> samples with no proof mass

Sample	Positive capacitance peak (nF)	Negative capacitance peak (nF)
R140-0M	84.16	-48.24
T140-0M	139.81	-117.69

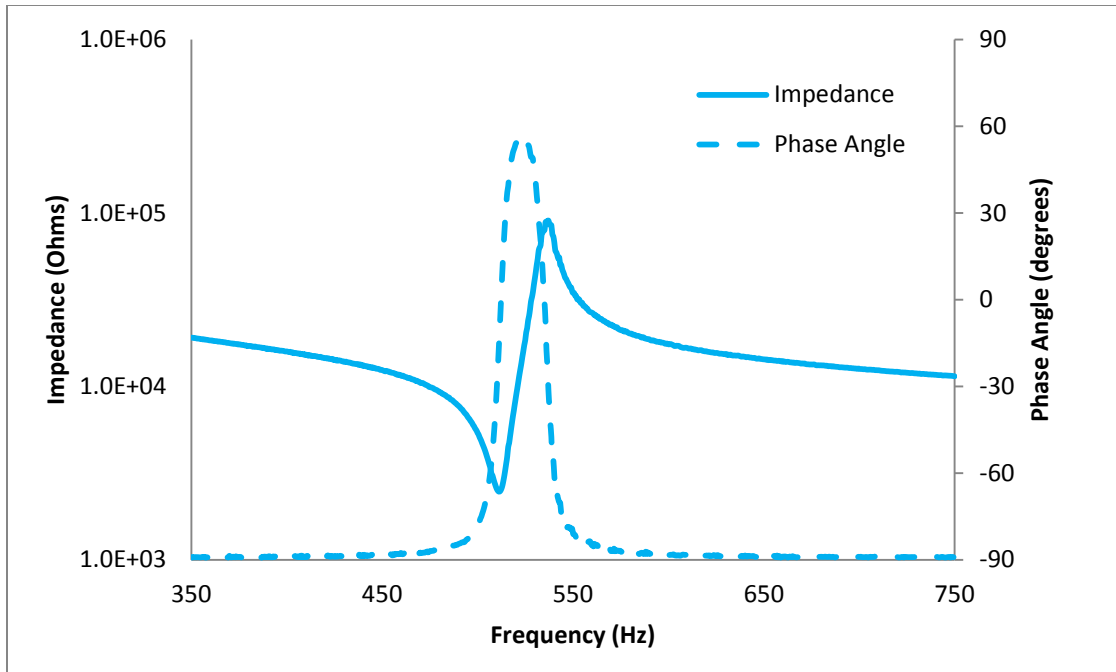


Figure 94: Impedance-Phase Angle for R140-0M

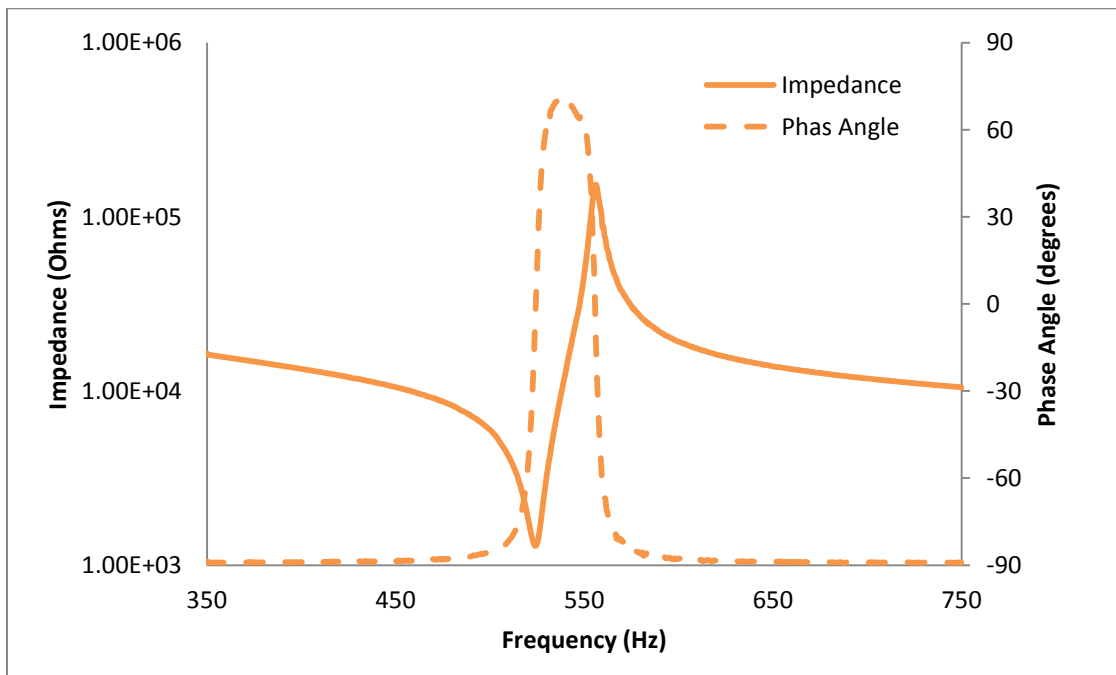


Figure 95: Impedance-Phase Angle for T140-0M

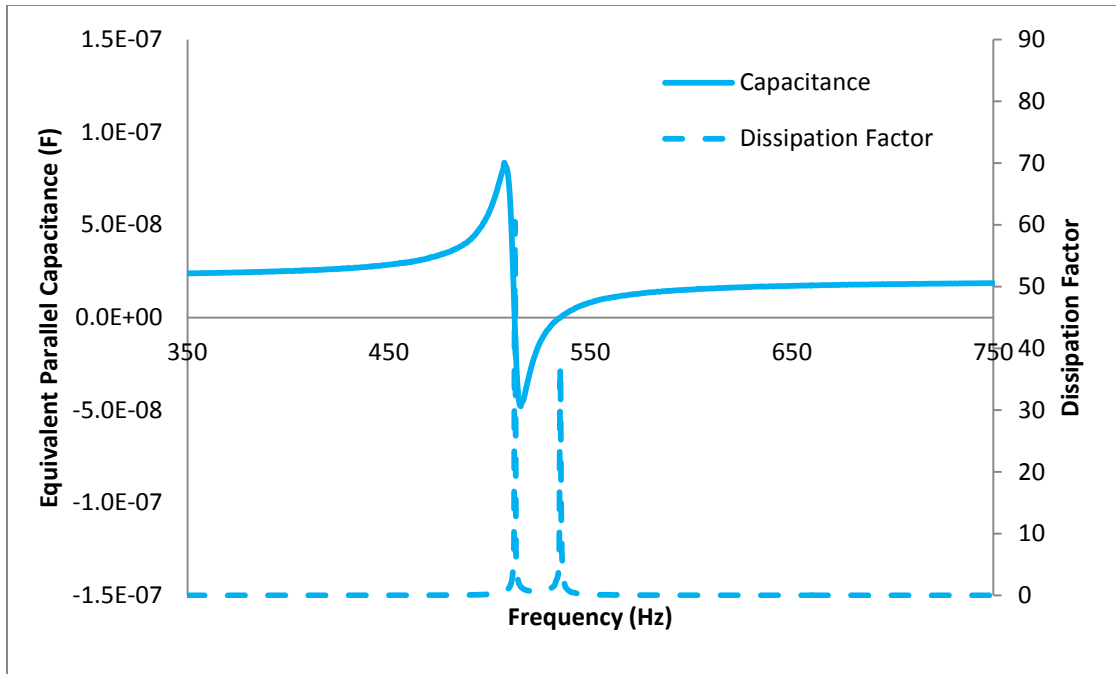


Figure 96: Equivalent Parallel Capacitance-Dissipation Factor for R140-0M

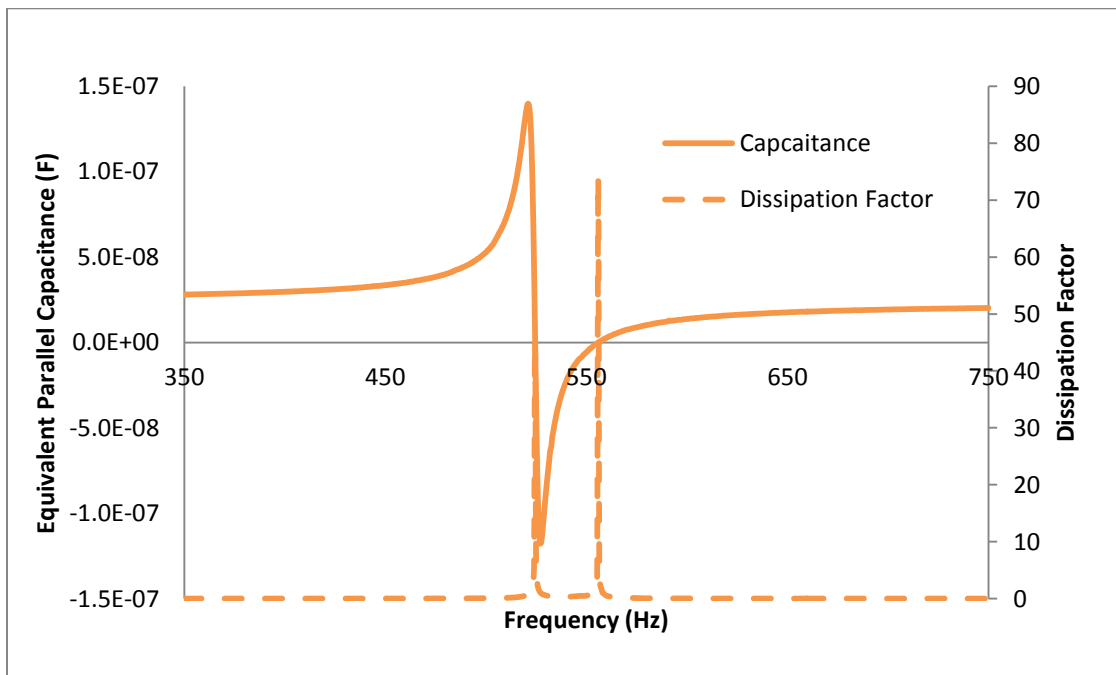


Figure 97: Equivalent Parallel Capacitance-Dissipation Factor for T140-0M

#### 5.2.4 Summary for no proof-mass samples

The results in the previous sections have given an overview for three sets of samples with matching volumes, and similar resonance frequencies. Here, the goal is to normalize the power generated from these samples and per unit volume and compare them, in order to see trends for the effect of changing geometry.

Figure 98 shows the Power Density for the three rectangular bimorphs. In the previous sections, it was reported that the power was increasing with increasing base widths (and hence volumes), though these increases were not substantial. Comparing the devices on a per unit volume basis (i.e.  $70 \text{ mm}^3$ ,  $104 \text{ mm}^3$  and  $140 \text{ mm}^3$ ), it can be seen that the power density actually decreases. The reasoning behind this is again two-fold: decreased stress per unit width with increasing volume due to increasing stiffness, and increased damping ratios with increasing volumes. These effects are far more pronounced in the case of the triangular bimorphs, shown in Figure 99. Here, with increasing stiffness with increasing size, the bimorphs have an enhanced inertial loading capacity, hence are under lower states of stress with increased size.

Also, as previously reported, and more clearly illustrated in Figure 98 and Figure 99 is the changing optimal load resistance. As the samples are getting stiffer, and have a lower effective inertial load per unit volume, with enhanced electromechanical coupling, the optimal load resistances shift to lower values. The arrows pointing downwards in both Figures Figure 98 and Figure 99 indicate this phenomenon. Therefore, beams with wider clamping widths provide lower internal impedance, leading to lower dielectric losses, and enhanced coupling.

The enhancement in the electromechanical coupling coefficient is summarized in Figure 100 for the samples without the proof masses. Clearly, the electromechanical coupling coefficient in the case of triangular cantilevered bimorphs is much greater in each case compared to their rectangular counterparts, indicating enhanced efficiency due to a more even stress distribution over the surface of the device. Therefore, the triangular devices are capable of handling a much larger mechanical load, which can potentially serve the application for a target resonance frequency with a larger inertial loading capacity with enhanced coupling. The damping ratios for the devices without proof masses remain fairly similar in all cases, as shown in Figure 101. Therefore, the system coupling, represented by the figure of merit, as shown in Figure 102 in this case is mainly controlled by the electromechanical coupling coefficient, which

increases with increasing volume, hence increasing stiffness at the base, and hence always remains greatest for the triangular cantilevered piezoelectric bimorphs.

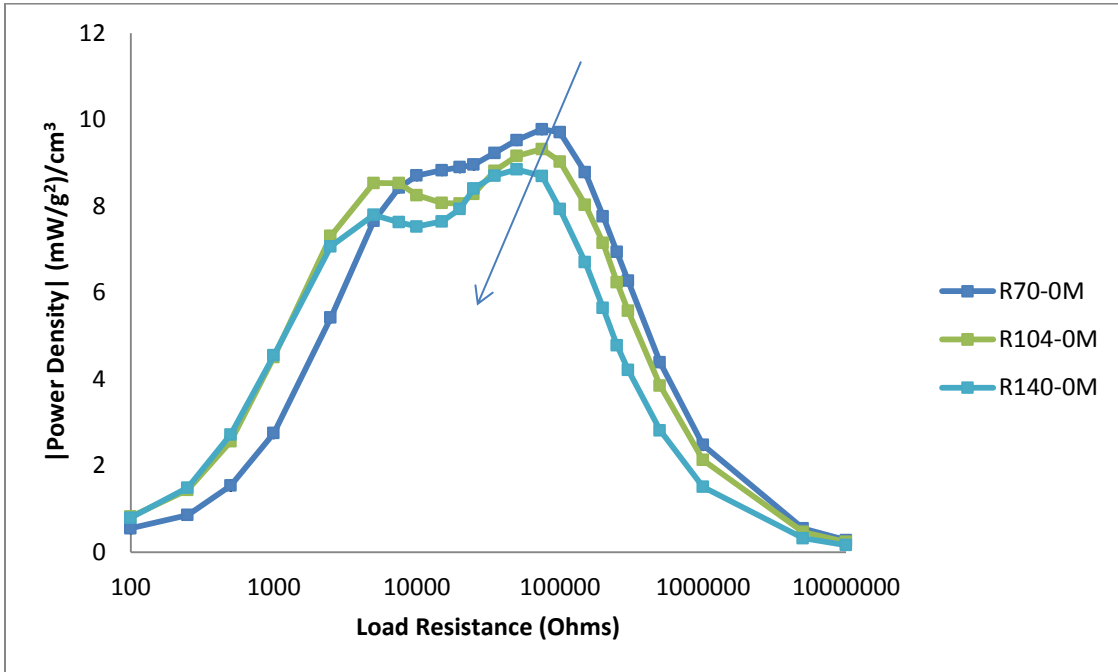


Figure 98: Power density for rectangular cantilevered bimorphs without proof mass

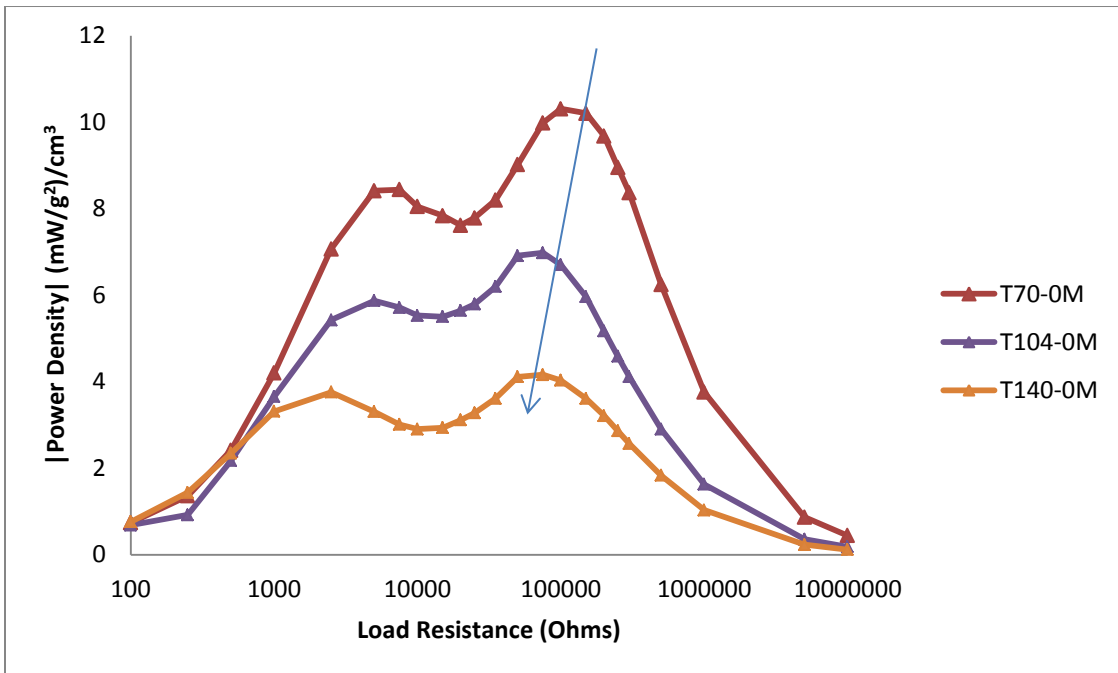


Figure 99: Power density for triangular cantilevered bimorphs without proof mass

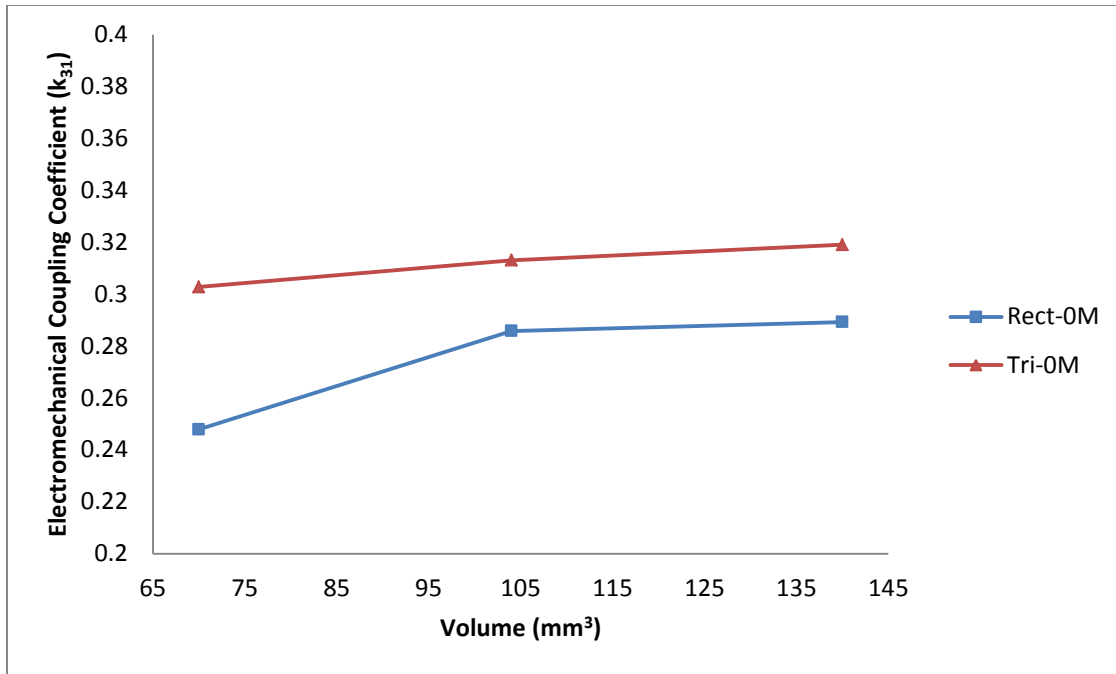


Figure 100: Effect of changing geometry on the electromechanical coupling coefficient for cantilevered piezoelectric bimorphs without a proof mass.

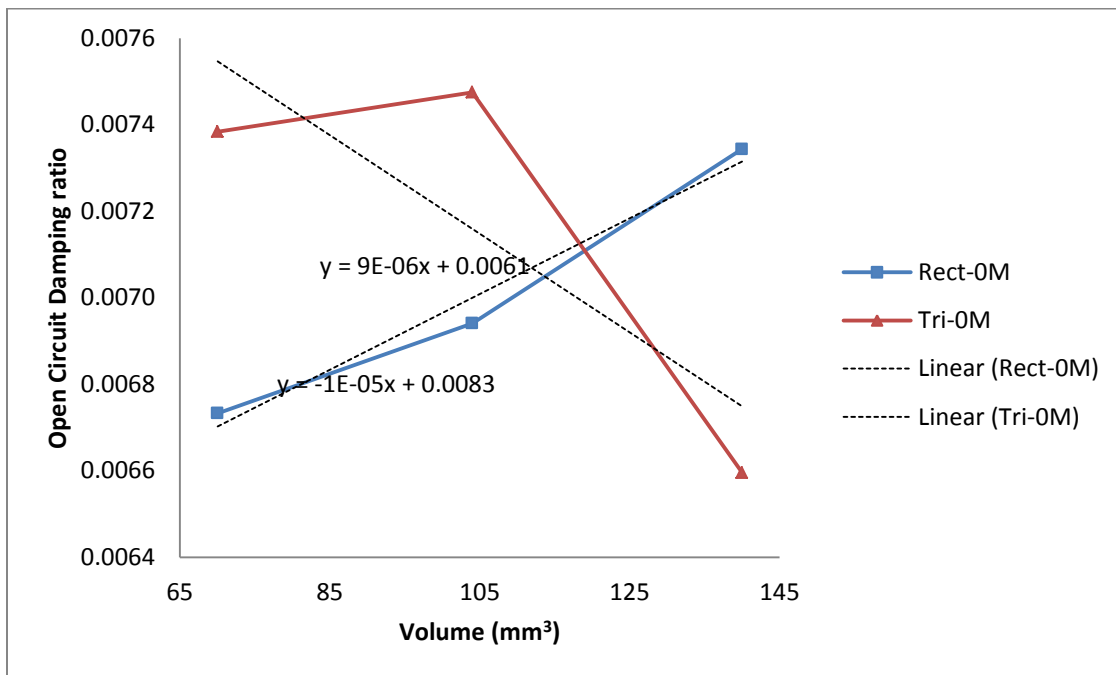


Figure 101: Damping Ratio in open circuit conditions for cantilevered piezoelectric bimorphs without a proof mass

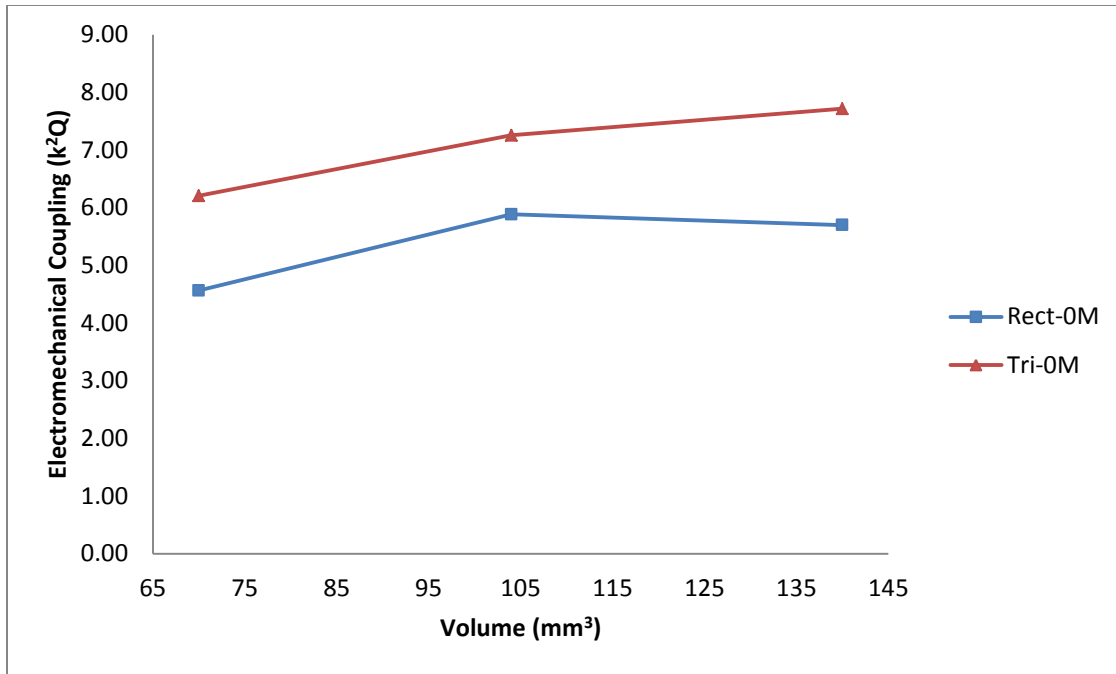


Figure 102: Electromechanical Coupling figure of merit for cantilevered bimorphs without proof mass

The impedance measurements at resonance and anti-resonance frequencies as a function of device volume are summarized in Figure 103. It can be seen that for each sets of devices, the impedance at resonance for the triangular bimorphs is lower than the rectangular counterpart; and at anti-resonance, the impedance for the triangular counterparts is greater than the rectangular counterparts. With increasing volume as a function of increasing clamping width, which increases stiffness in the device, the impedance values decrease. Decreased impedance values provide the opportunity for producing peak power at lower external resistance values, which would aid in producing less heat in real device applications.

Capacitance is a property dependent on size; therefore with increasing volume, the capacitance theoretically increases. In these measurements, peak positive and negative capacitance values are found around the resonance frequency. For rectangular cantilevers, the positive and the absolute value of the negative capacitance increase linearly, while in the case of the triangular cantilevers, they seem to fan out, as shown in Figure 104. These capacitance values do seem to be increasing proportionally with volume for the rectangular bimorphs (as volume is doubled, peak capacitance values are doubled), but normalizing these values on a per volume basis could be an approximation unsuitable for the dynamic mode around resonance, hence this is avoided.

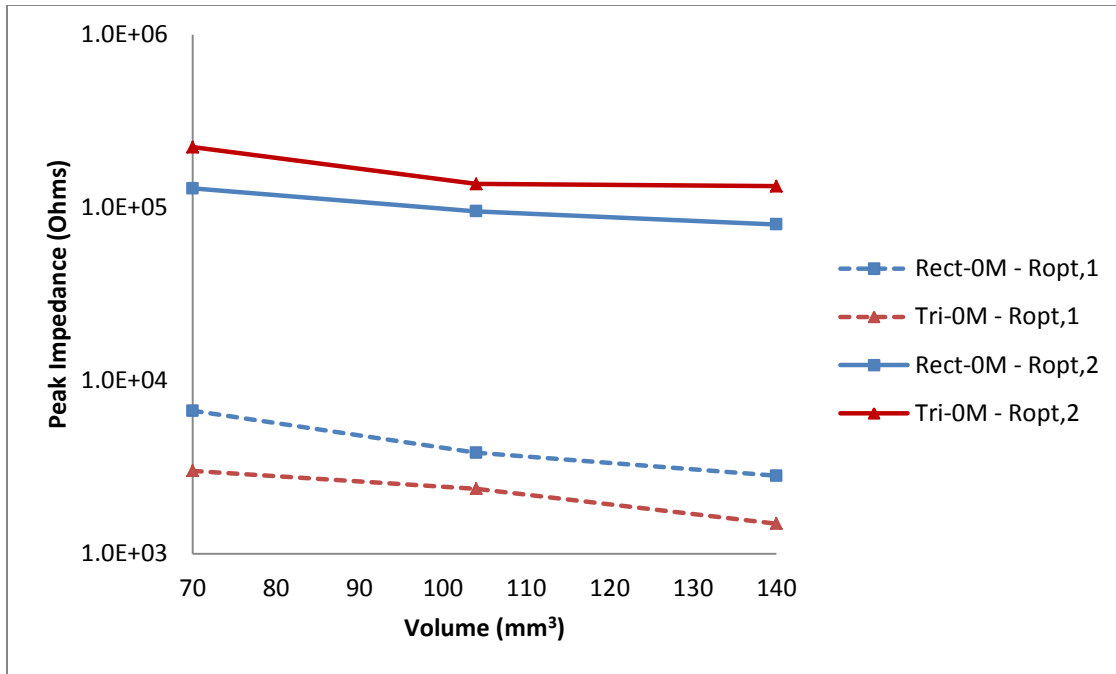


Figure 103: Maximum and Minimum Impedance values for cantilevered piezoelectric bimorphs with no proof mass

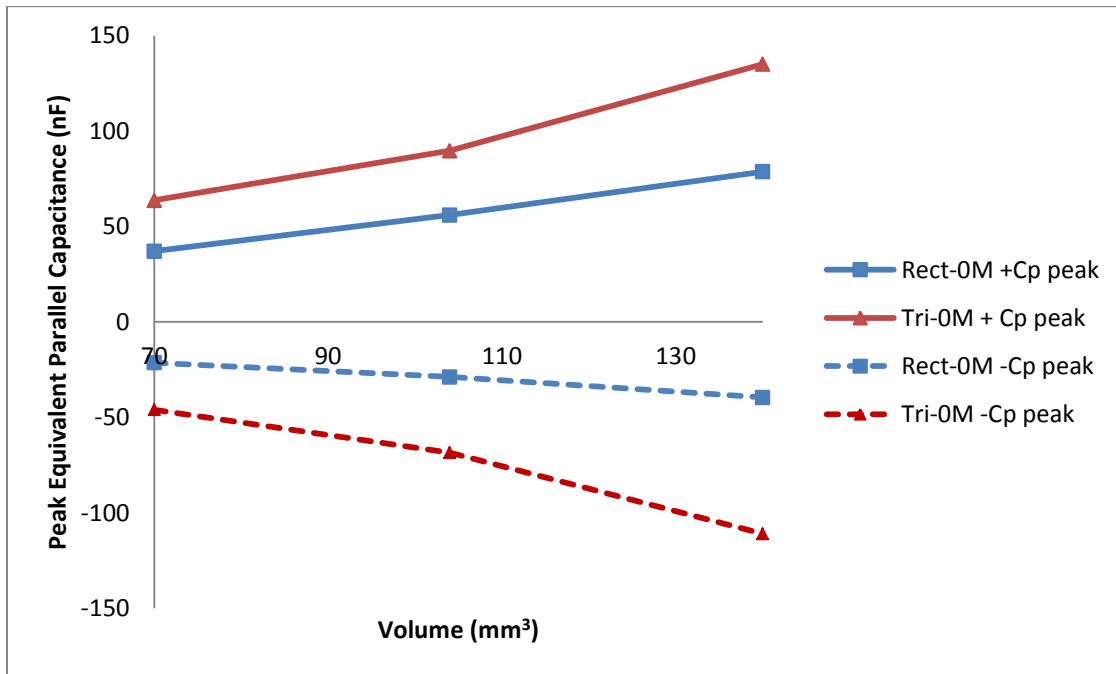


Figure 104: Maximum and Minimum Equivalent Parallel Capacitance for piezoelectric bimorphs with no proof mass

### 5.3 Studies with 2 gram Proof Mass Samples

The previous section provided results on three sets of samples without a proof mass, and the overall results indicated that while the triangular cantilevers show enhanced coupling due to increased stiffness, they fail to outperform the rectangular counterparts. This is primarily due to a lack of inertial loading, which is more pronounced in the case of triangular cantilevers, which effectively have no mass at the free end, due to the nature of the shape. Therefore, samples from the previous case are loaded with a nominal tip mass. The tip mass is a  $6.35 \times 6.35 \times 6.35 \text{ mm}^3$  block of stainless steel, which amounts to 2 grams. The effect of the tip mass is illustrated on the three sets of samples as R70-1M, T70-1M; R104-1M, T104-1M, and R140-1M and T140-1M.

Subsequently, another sample is presented, designated as T70-1M-P, where P stands for position (i.e. proof mass has been positioned to match resonance frequency). Another two samples are presented, designated as T35-1M-L and T70-1M-L, where L stands for length (here length matches rectangular samples). The premise for these subsequent samples is given as the results are presented.

#### 5.3.1 RT70-1M

The first set of samples is the RT70-1M samples. As mentioned, the 1M stands for 1 block of mass, amounting to 2 grams, which is placed at the tip of the bimorphs, as shown in Figure 105. It can be noticed that the proof mass, when placed on the tip of the triangular bimorph has a small amount of area where the bimorph is absent (due to the tapered geometry). In order to account for this, the proof mass on the rectangular bimorph is placed such that half of the proof mass overhangs from the bimorph. The resonance frequencies of the uncoupled beams, i.e. under short circuit conditions are found to be 116 Hz for the Rectangular bimorph, and 92 Hz for the Triangular bimorph with the proof masses (verified from ANSYS modal analyses – 120 Hz for Rectangle, and 85 Hz for Triangle), there is a 20% difference between them. Therefore, in order to compare the devices at matching resonance frequencies, an attempt was made to do so by changing the position of the proof mass on the triangular cantilever. The cubic proof mass, which has dimensions of  $6.35 \text{ mm}^3$ , was pulled back by about half of its dimension, i.e. 3.175 mm, which gave a short-circuit resonance frequency of 115 Hz. Therefore, R70-1M, and T70-1M-P are more comparable. Nevertheless, results from all three devices are presented, in order to evaluate any penalty that there may be from changing the position of the proof mass, and to see the effect of the lower resonance frequency on T70-1M.



The difference between the short circuit and open circuit resonance frequencies for R70-1M is 6 Hz, T70-1M is 7 Hz, and 7.25 Hz for T70-1M-P. These differences seem much smaller than they were in the case of the no-proof mass samples, where R70-0M had a difference of 17 Hz, and T70-1M had a difference of 24 Hz, but the percentage differences here is in fact larger: 5%, 7%, and 6.3% respectively for R70-1M and T70-1M, T70-1M-P, as opposed to 3.2% 4.6%, for R70-0M and T70-0M. This results in a  $k_{31}$  coupling coefficients of 0.31 for R70-1M and 0.34 for T70-1M and 0.34 for T70-1M-P again. Therefore, a larger coupling is still observed for the triangular bimorph compared to its rectangular counterpart, and this can be seen in the plot for short-circuit resonance frequency normalized resonance frequency plot in Figure 107. However, positioning the proof mass has no apparent effect on the electromechanical coupling coefficient in this case.

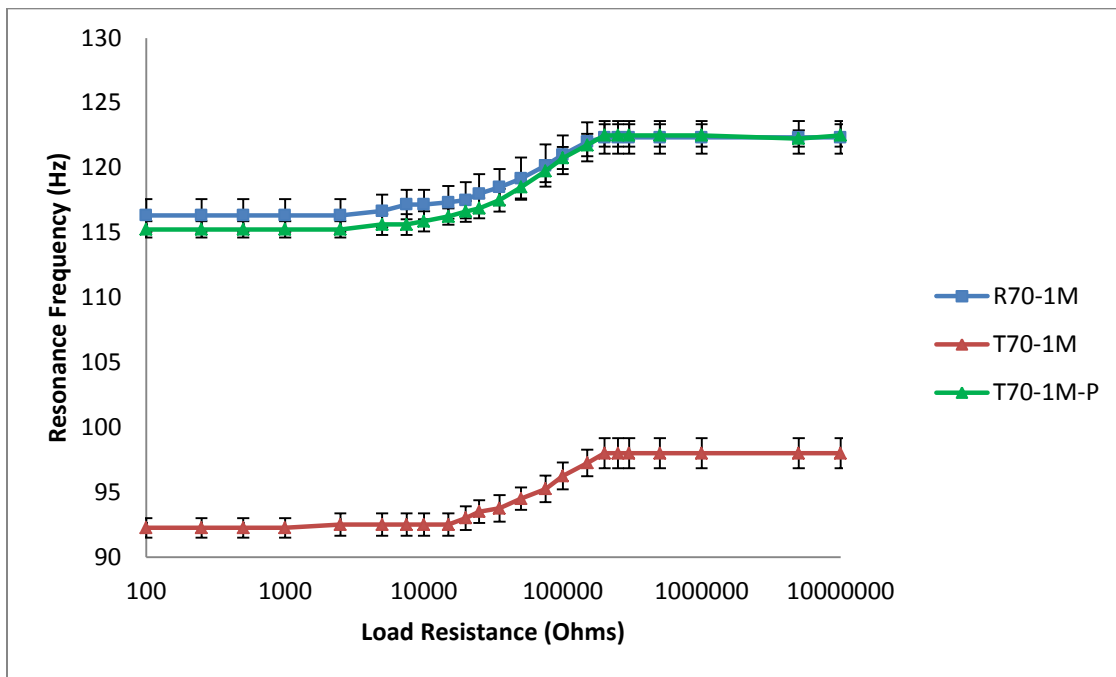


Figure 106: Resonance frequency as a function of load resistance for R70-1M and T70-1M

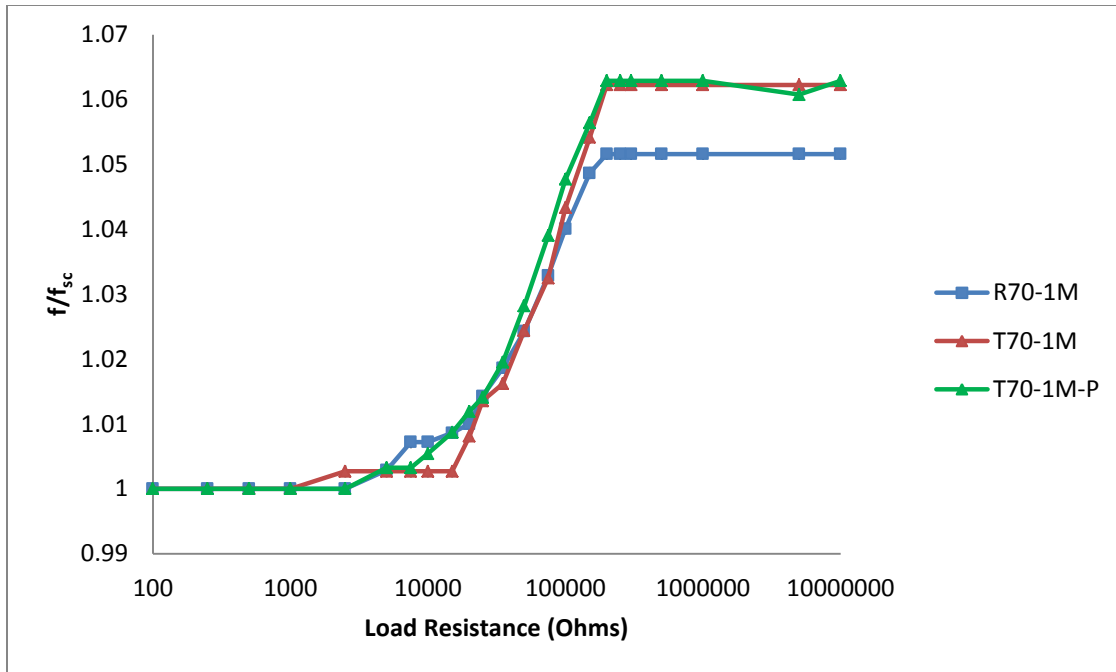


Figure 107: Normalized resonance frequencies as a function of load resistance for R70-1M and T70-1M

One of the major aspects of results from no proof mass samples was that the power generated by the triangular counterparts almost never outperformed their rectangular counterparts. One of the reasons was increased stiffness in triangular devices due to its ability to linearize strain, but an important aspect was the absence of any effective mass at the tip, due to which there was a loss of torque at the base. With the added proof masses, the first observable fact in Figure 108 is that the triangular counterparts substantially outperform the rectangular bimorph. A stress analysis to characterize the bending is presented following the discussion on the power generated.

It is worth highlighting the magnitude of power generated. The power generated from the two devices at their optimal load resistances, with the nominal 2 gram proof mass is about 55  $\mu\text{W}$  for R70-1M, and 76  $\mu\text{W}$  for T70-1M, which is an order of magnitude greater than it was without the proof mass. This is a significant gain in power, and therefore shows the importance of added proof masses for the moment it creates at the base. In the case of T70-1M-P, the positioning of the proof mass increases the resonance frequency of the device from 92 Hz to 115 Hz, and the effect on power generated is quite noticeable. With the increased resonance frequency, which is now closer to that of the rectangular bimorph resonating at 116 Hz, the

power generated by T70-1M-P into a 50,000 ohm resistor is 67.65  $\mu\text{W}$ , and 66.14  $\mu\text{W}$  into a 300,000 ohm resistor. In order to reason this loss in power, it is important to consider the damping ratio that is calculated. The damping ratio for R70-1M, and T70-1M, with the proof masses located at the tip are quite close to each other, at 0.0091 and 0.0092, but larger for the device with the positioned proof mass, at 0.013. Therefore, as illustrated in Table 7, with the similar damping ratios, and increased coupling in T70-1M, as compared to R70-1M, the system electro-mechanical coupling increases, but it is relatively strongly affected with the increased damping in the case of the triangular bimorph where the proof mass is positioned to match the rectangular bimorph's resonance frequency.

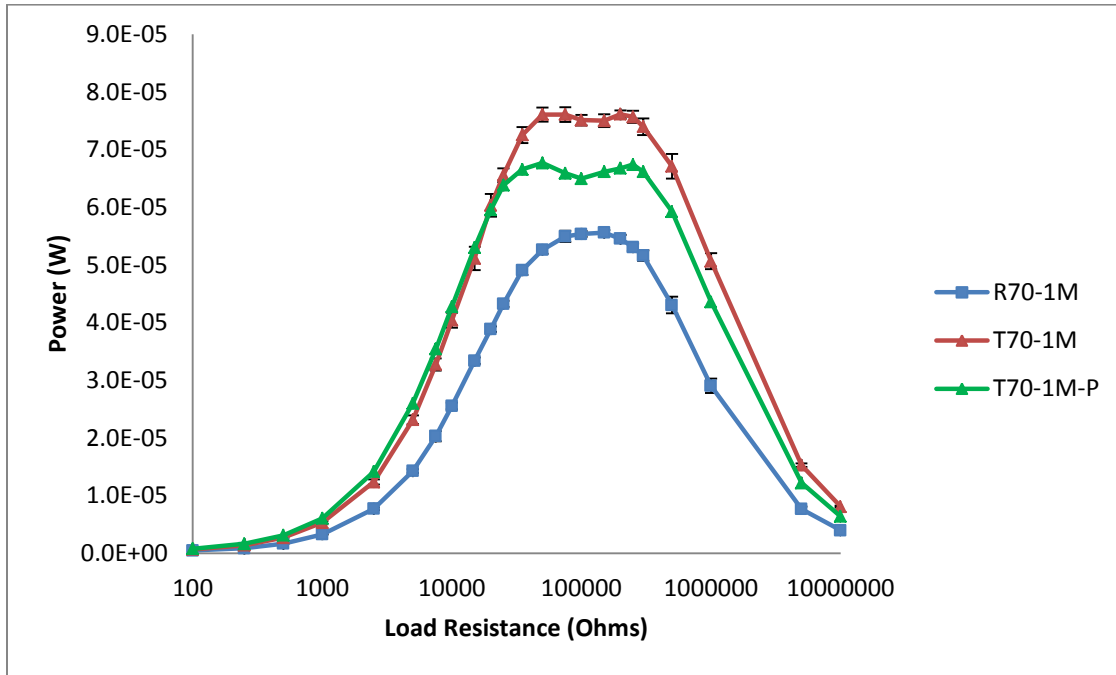


Figure 108: Power generated by R70-1M and T70-1M into various load resistors

Table 12: Summary of Power generated from 70mm<sup>3</sup> bimorphs with a 2 gram proof mass

	$R_{\text{opt},1}(\Omega)$	P ( $\mu\text{W}$ )	$R_{\text{opt},2}(\Omega)$	P ( $\mu\text{W}$ )	$\zeta$	$k_{31}$	$k^2Q$
R70-1M	75,000	54.92	200,000	54.53	0.00914	0.31	5.232
T70-1M	50,000	76.05	200,000	76.11	0.00939	0.34	6.63
T70-1M-P	50,000	67.65	300,000	66.14	0.01294	0.34	4.402

In order to visualize the effect of the differences in resonance frequency, and its effect on the state of stress, Figure 109 and Figure 110 show representative plots for the three devices being discussed, generated from numerical simulations. It can be seen that, while the resonance frequency for T70-1M is lower, the deflection in comparison to the rectangular counterpart is smaller at every point where it exists. This is an (intuitively) unexpected result, but the difference could possibly be explained due to the fact that the moment generating device, i.e. the proof mass is located farther away, and the fact that the radius of curvature for deflection is relatively more constant. This explanation is amplified by looking at T70-1M-P, where the resonance frequencies between the rectangular and triangular bimorphs are very similar. It can be seen that the magnitude of deflection at the matching resonance frequency at the tip of the rectangle is the same for both devices, but the triangular device has a more pronounced radius of curvature. In the case of T70-1M-P, the deflection is linear from the location of the base of the proof mass to the tip of the device, where the stresses are negligible.

The stress curves in Figure 110 also provide useful insights, and also validation for the original hypothesis of this thesis. It can be seen that the stress in the case of R70-1M is highly concentrated at the fixed end, and linearly decreases, unlike T70-1M, where the stress is linearly distributed through the length of the device. The only region where the stress drops down to negligible values is the area where the proof mass exists, since that particular area is not strained. The average stress for T70-1M is about 8 MPa, and the maximum value is about 12 MPa, as compared to 18 MPa for the rectangular cantilevered bimorph, which has the same volume and mass.

The mass positioned sample, T70-1M-P shows somewhat hybrid characteristics for stress. This is because of the fact that the proof mass positioning effectively makes the device into a trapezoid. It can be seen that due to tapering, the maximum stress, which is about 13 MPa, is lower than the R70-1M, but this device with the same resonance frequency has a small linearly decreasing slope for axial stress along the length of the beam. Triangular devices therefore are the only ones that provide a linear stress profile.

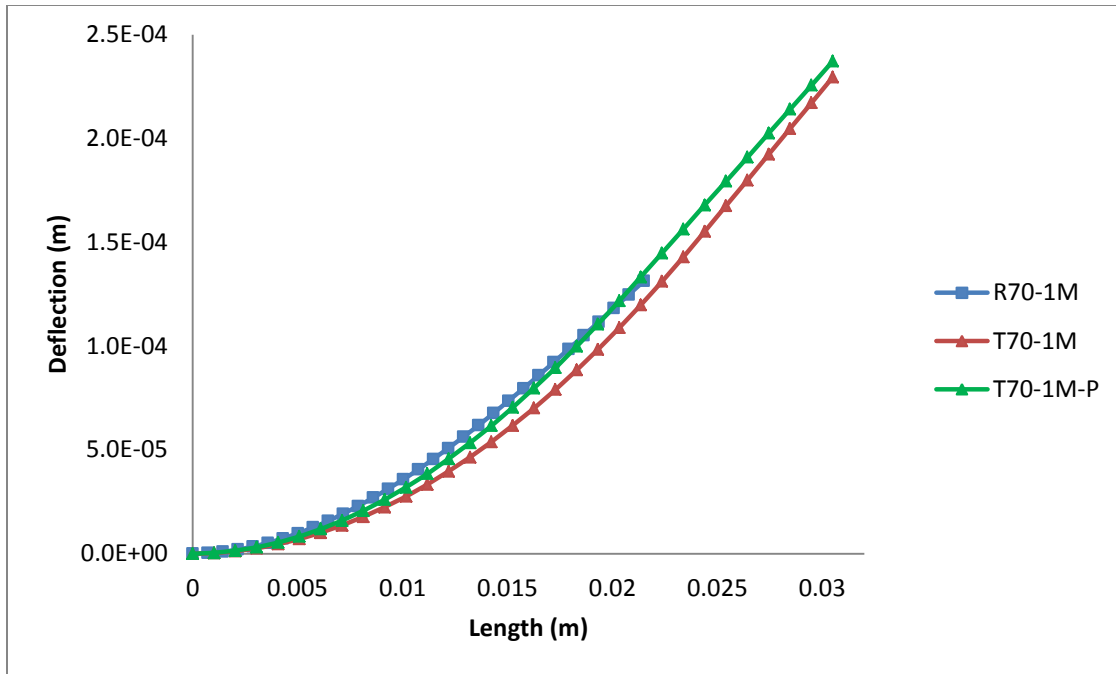


Figure 109: Deflection for 70 mm<sup>3</sup> bimorphs with a 2 gram proof mass

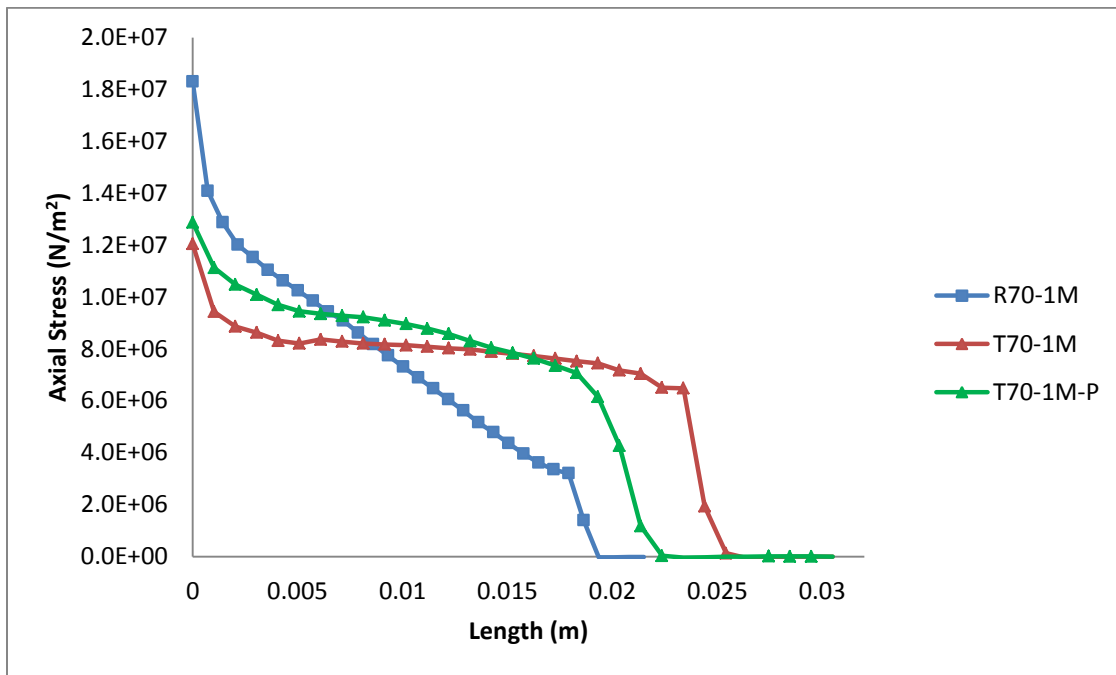


Figure 110: Axial Stress along the length over the surface for 70mm<sup>3</sup> bimorphs with a 2 gram proof mass

The impedance characteristics for the three aforementioned devices are described in Figure 111, Figure 112 and Figure 113, and summarized in Table 13. In the previous section, one of the conclusions from the impedance analysis was that the difference between the impedance values at resonance and anti-resonance frequencies increases with increasing electromechanical coupling coefficients. Simply comparing R70-1M and T70-1M, this behavior is observed here as well, and depicted in Table 12, where the electromechanical coupling increases as the shape of the cantilever beam is changed from rectangular to triangular beams. With the larger electromechanical coupling coefficient of 0.34 for T70-1M, as compared to 0.31 for R70-1M, the impedance value at resonance frequency is lower at 17,165 ohms as compared to 37,171 ohms for R70-1M; while the impedance at the anti-resonance is greater at 1,192,406 ohms for T70-1M, as compared to 246,245 ohms. While the electromechanical coupling coefficient for T70-1M-P is nearly the same as that of T70-1M, the impedance characteristics do indicate that the electromechanical coupling is somewhat smaller when the mass is positioned, and the device is turned into an effective trapezoid. The impedance at resonance here is smaller than the rectangular bimorph, and larger at anti-resonance, still indicating larger coupling for the triangular device.

Another correlation that can be made here is of coupling and impedance with the maximum stress of the device, which is in fact related to stiffness. With the largest maximum stress, as is the case for R70-1M, the impedance at resonance is the largest, and the smallest maximum stress results in a lower impedance at resonance. The converse trend at anti-resonance is also true, as the anti-resonance impedance increases with increasing maximum stress.

Table 13: Summary of impedance analysis for 70 mm<sup>3</sup> devices with a 2 gram proof mass

Sample	$f_r$ (Hz)	Z (Ohms)	$f_a$ (Hz)	Z  (Ohms)	Peak Phase°
R70-1M	120	37,172	130.2	246,245	18.3
T70-1M	95.3	17,165	102	1,192,406	67.5
T70-1M-P	117	22,852	125	983,238	56.21

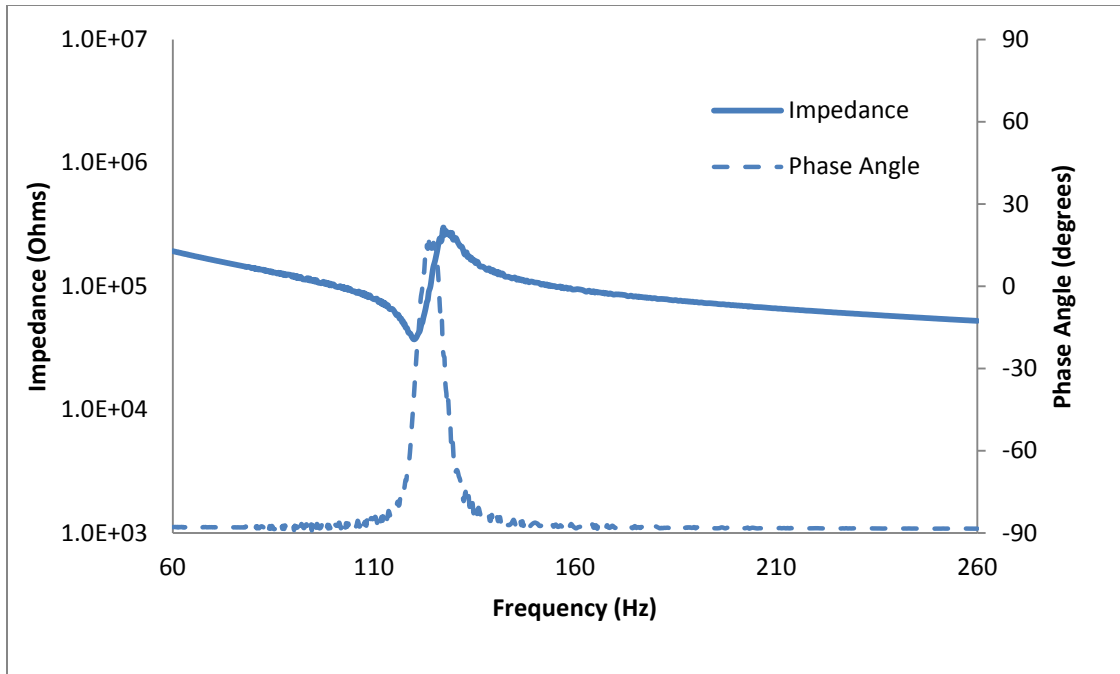


Figure 111: Impedance-Phase Angle for R70-1M

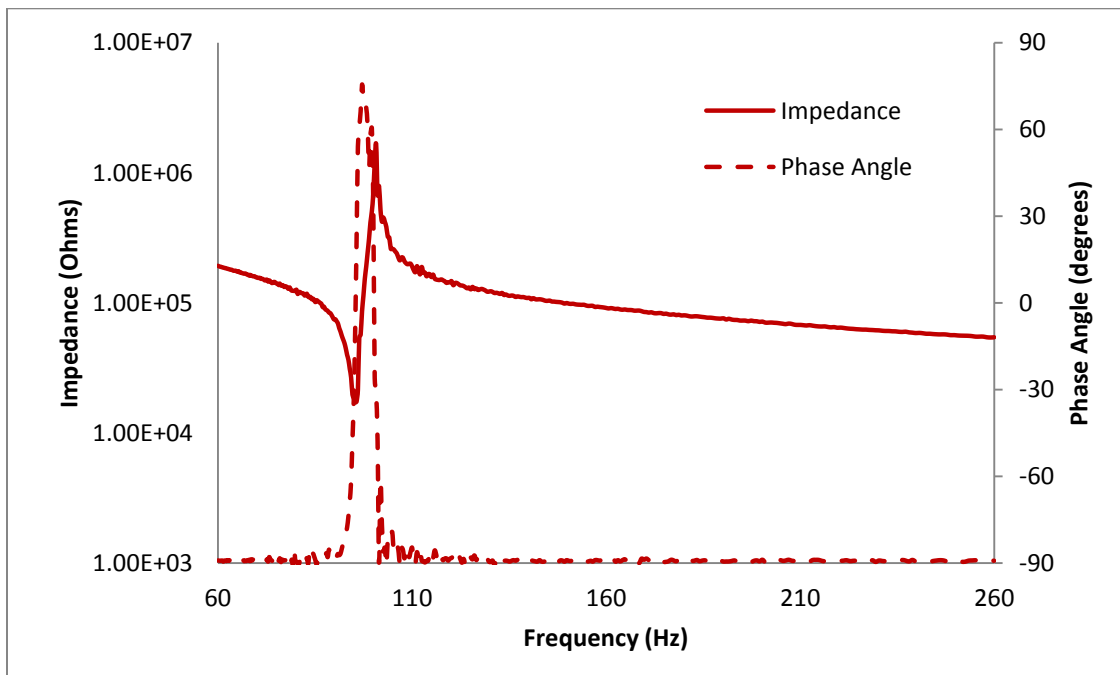


Figure 112: Impedance-Phase Angle for T70-1M

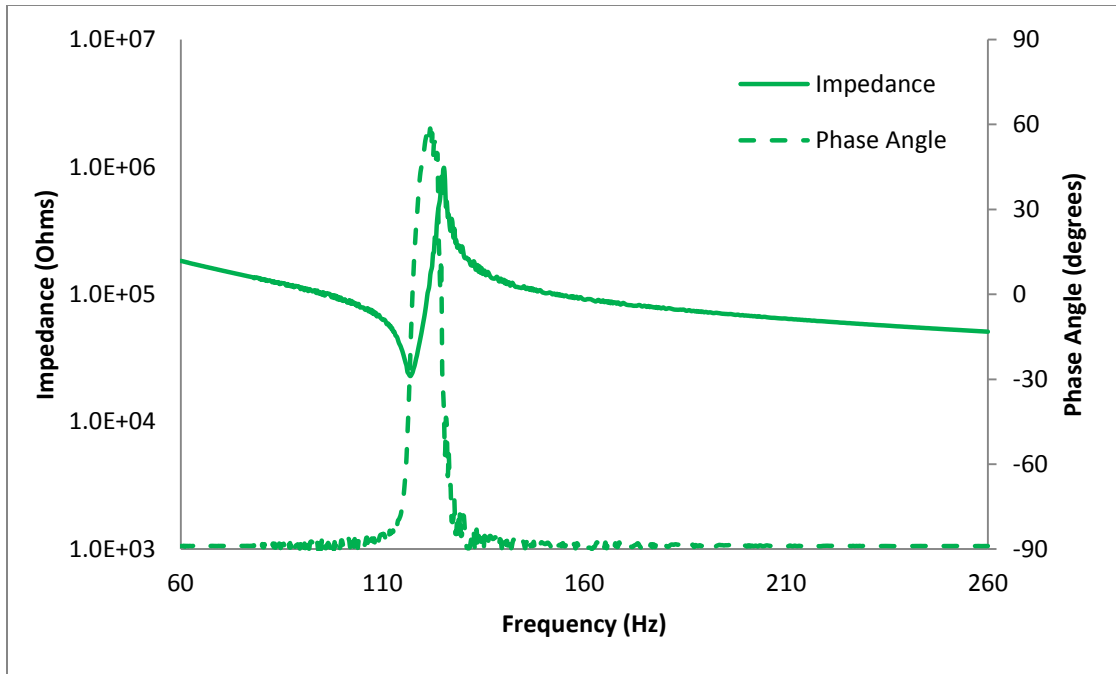


Figure 113: Impedance-Phase Angle for T70-1M-P

The implications of the shape change with the proof mass are quite profound in the case of capacitance measurements, as presented in Figure 114, Figure 115, and Figure 116, and summarized in Table 14. As R70-1M, T70-1M-P and T70-1M are compared, with decreasing values of maximum stress, and increased coupling, the positive capacitance at resonance increases, and so does the absolute value of the negative capacitance. As the piezoelectric device is described as a capacitor in parallel with a current source, increasing values of capacitance with the same volume, and similar frequencies can have major advantages in circuit applications. It is observed that with changing the geometry, T70-1M has larger peak capacitance values compared to its rectangular counterpart. However, as for the mass-positioned sample, it can be seen that the capacitance peaks suffer with the apparent trapezoidal shape.

Table 14: Capacitance measurements for 70 mm<sup>3</sup> devices with 2 gram proof mass

Sample	Positive capacitance peak (nF)	Negative capacitance peak (nF)
R70-1M	39.1	-21.31
T70-1M	62.74	-61.40
T70-1M-P	42.82	-21.27

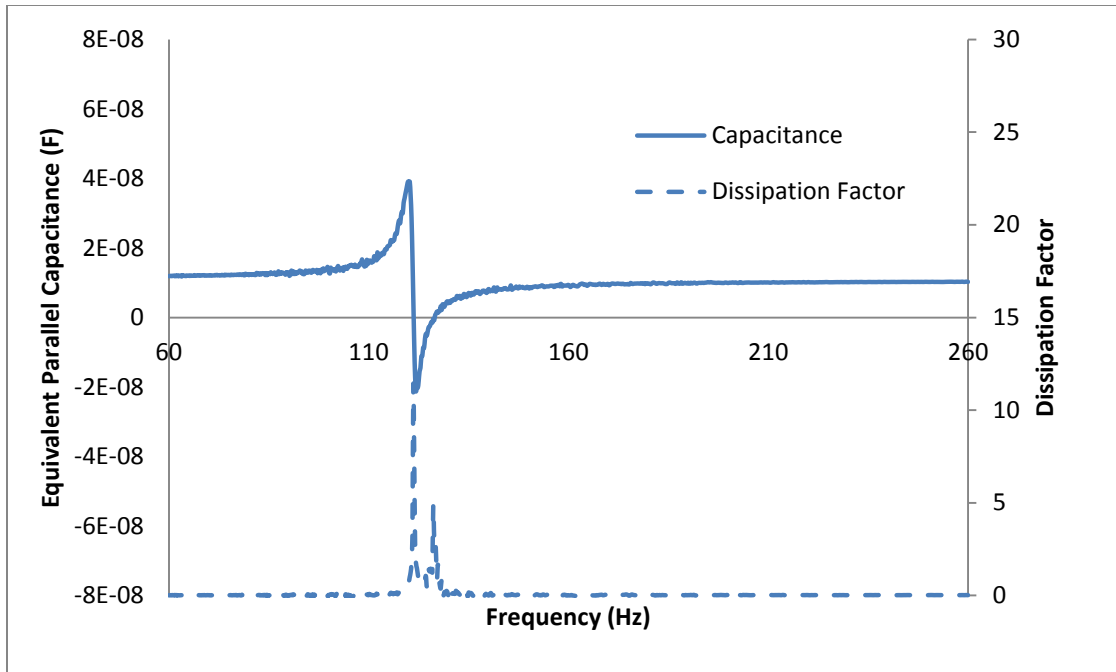


Figure 114: Capacitance-Dissipation Factor for R70-1M

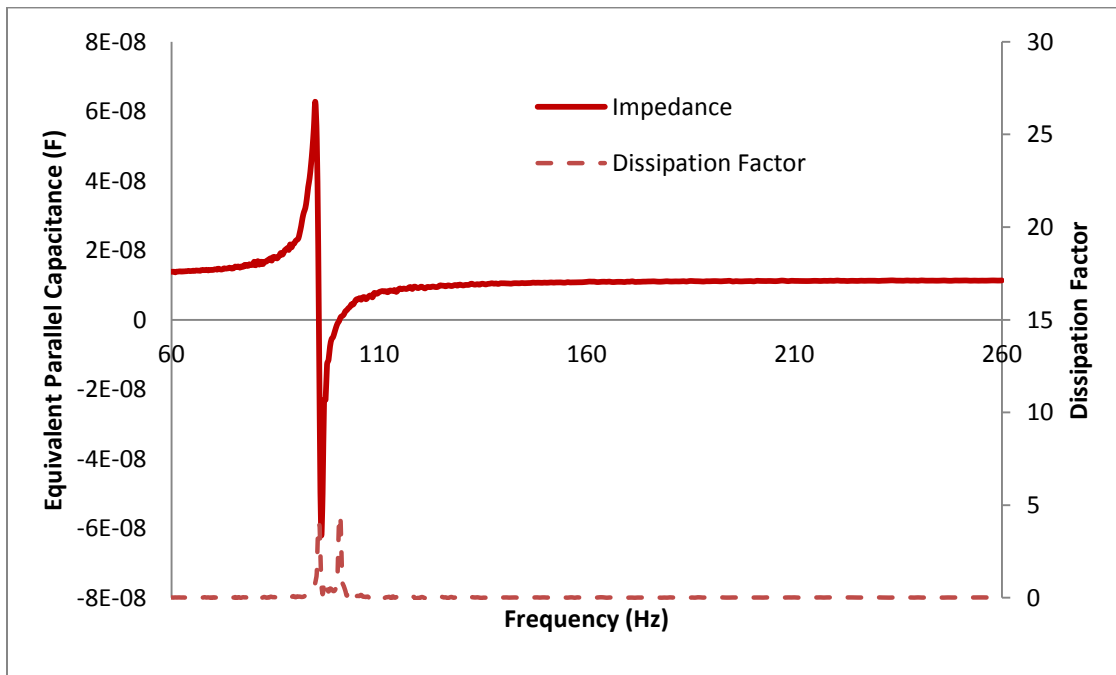


Figure 115: Capacitance-Dissipation factor for T70-0M

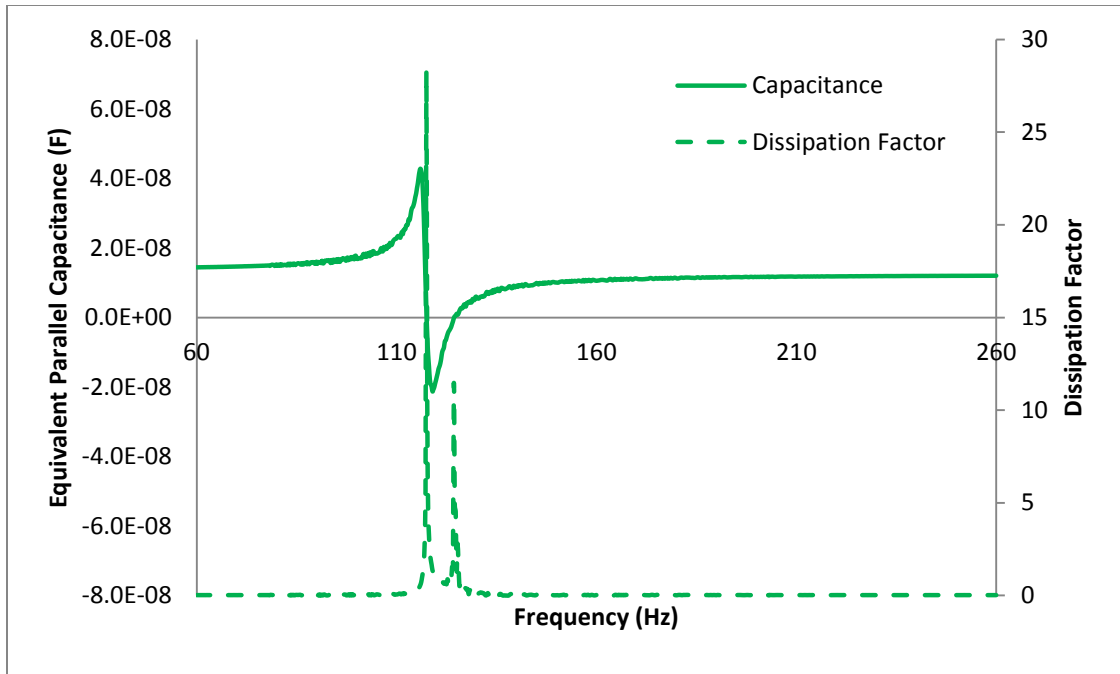


Figure 116: Capacitance-Dissipation Factor for T70-1M-P

### 5.3.2 RT104-1M

The next set of samples that are considered are the 104 mm<sup>3</sup> devices, as it was done in Section 5.2.2 in the absence of proof mass. The same samples are now tested with the 2 gram proof mass, as illustrated in Figure 117.

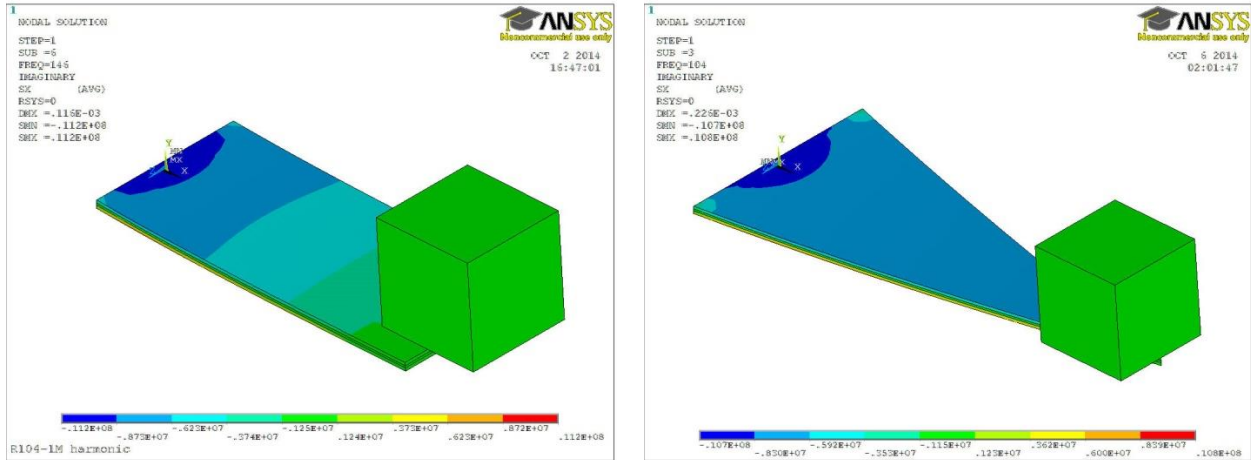


Figure 117: 104 mm<sup>3</sup> devices with a 2 gram proof mass

The parameter of primary interest is the short circuit resonance frequency, which for comparison purposes is being targeted at 115 Hz. In the case of the triangular bimorph, as mentioned, this was achieved by adjusting the position of the proof mass slightly for the 70 mm<sup>3</sup> devices. In the case of the 104 mm<sup>3</sup> devices, the 115 Hz resonance frequency is achieved by placing the proof mass, flush to the tip, as it was done for the un-positioned 70 mm<sup>3</sup> device. Therefore, the positioning adjustment in the previous case was quite minor.

However, in the case of the rectangular device, Figure 118 shows that the short circuit resonance frequency with identical proof mass positioning diverges, and goes to 145 Hz (verified with ANSYS modal analyses), which is thought to be a significant difference. Physically lowering the resonance frequency of the rectangular device down to 115 Hz in this case is not possible with the given length and thickness constraints. However, in order to assess the penalty of this divergence, in terms of losing comparability, the tests are carried out, and presented. This is an aspect that is often missed in literature.

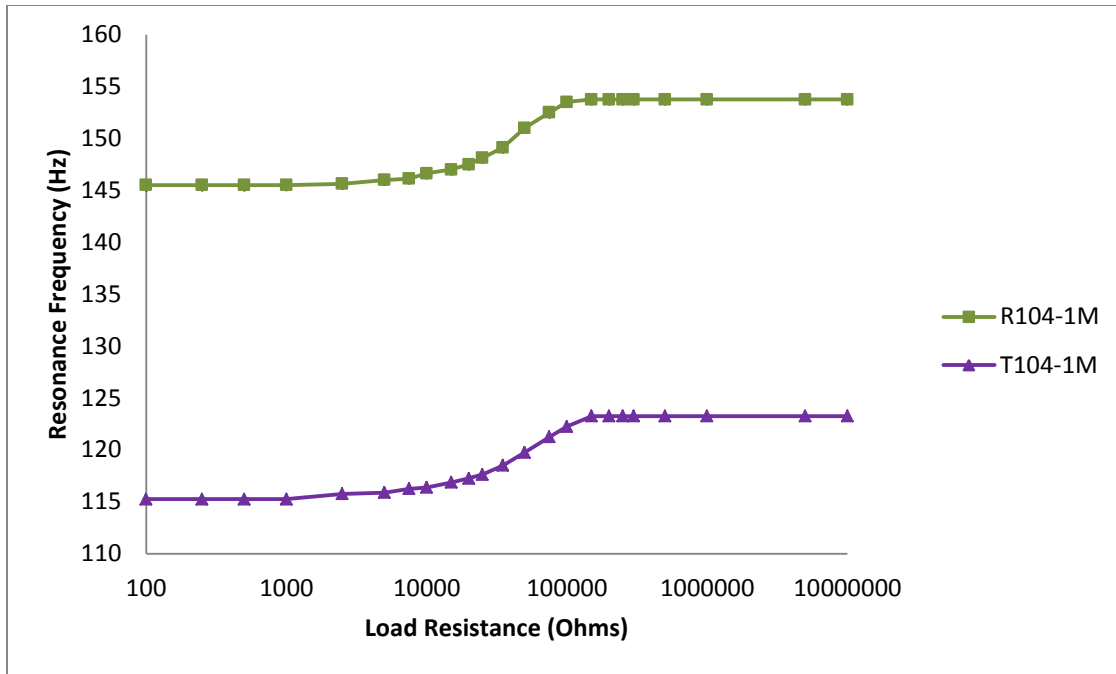


Figure 118: Resonance frequency of the 104 mm<sup>3</sup> devices with a 2 gram proof mass as a function of load resistance

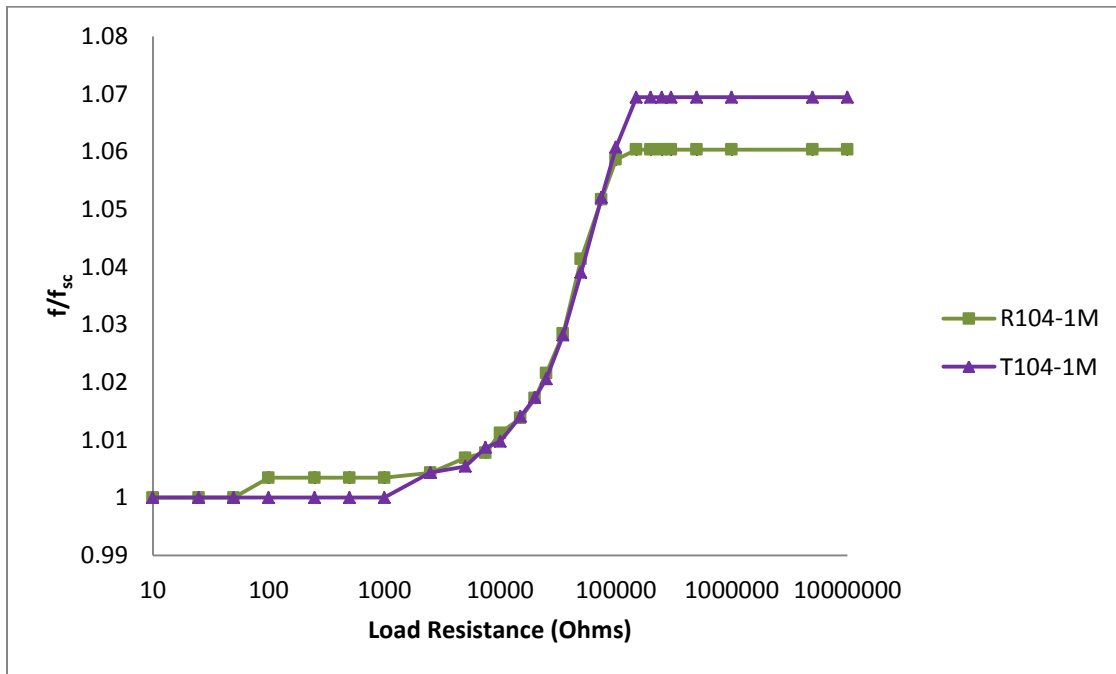


Figure 119: Short circuit normalized resonance frequency for 104 mm<sup>3</sup> devices as a function of load resistance

The short circuit normalized frequencies of the two devices presented in Figure 119 do indicate that T104-1M provides a larger coupling coefficient than R104-1M, which has been a consistent trend so far. With the larger coupling coefficients, the spread between the optimal load resistance values is expected to be larger, which happens to be the case, as shown in Table 15; the optimal load resistance values for T104-1M are 25,000 ohms and 250,000 ohms, as compared to a narrower regime in R104-1M, where the optimal load resistance values are 35,000 ohms and 150,000 ohms. It is interesting to notice that the damping ratios for the two devices are quite similar to each other, with T104-1M being very slightly larger at 0.0088 as compared to 0.0080. However, it is important to recall here that the resonance frequency for the T104-1M is lower, which provides larger deflections, hence could provide the larger damping ratio. Nevertheless, the system coupling, or the  $k^2Q$  figure of merit is indeed larger for T104-1M, as compared to R104-1M.

Table 15: Power generated at optimal load resistance values for the 104 mm<sup>3</sup> devices with a 2 gram proof mass

	$R_{opt,1}(\Omega)$	P ( $\mu$ W)	$R_{opt,2}(\Omega)$	P ( $\mu$ W)	$\zeta$	$k_{31}$	$k^2Q$
R104-1M	35000	63.7	150000	67.2	0.0080	0.32	6.53
T104-1M	25000	62.3	250000	65.7	0.0088	0.35	7.12

It can be noticed in Figure 120 that the amount of power generated between the two devices is very similar, around 65  $\mu$ W at the optimal load resistance values. It is expected that the power generated from the rectangular device would suffer here due to the higher resonance frequency, which would cause a smaller displacement amplitude. This in fact happens to be the case, as shown in Figure 121. Unlike previous comparisons where the displacement of the triangular cantilever compared to a rectangular counterpart is always smaller at every location where it exists, in this case, this trend does not hold with the large difference in resonance frequency. The maximum deflection at the tip (i.e. L=21.5 mm) of R104-1M is 89  $\mu$ m, at which point T104-1M has a deflection of 111  $\mu$ m, and has a maximum deflection of 213  $\mu$ m. This is a clear indication that the comparison between the two devices in Figure 120 on a merit basis is unfair.

While the trends indicate that comparisons between R104-1M and T104-1M are unfair, and that there is a loss of performance in the case of the rectangular cantilever, the magnitude of power generated from T104-1M should also be considered, and especially comparing it with T70-1M, and T70-1M-P. It can be noticed that the amount of power generated from T70-1M-P, and T104-1M, both resonating at 115 Hz is nearly the same, at about 65  $\mu\text{W}$ . This loss of power is again attributed to increased stiffness at the base, and hence a larger inertial loading capacity in the case of the triangular cantilevers. The axial stress plot in Figure 122 (and Figure 110 for T70-1M-P) shows that the maximum stress on the triangular cantilever is decreased to 9 MPa with the larger triangle, as compared to 11 MPa previously for the 70 mm<sup>3</sup> triangle. Moreover, in the case of T104-1M, the axial stress profile over the surface of the beam is not constant, as a small negative slope is observed, which was not the case for the T70-1M devices.

While comparing R104-1M and R70-1M, it can be seen that while the narrower beam was generating around 55  $\mu\text{W}$  at resonance around 115 Hz, R104M-1M does manage to produce a greater amount of power of about 65  $\mu\text{W}$ . Even though this amount of power generated is smaller on a per volume basis, the comparison is difficult to make due to the mismatch between the resonance frequency, hence lower deflections, and hence smaller stresses.

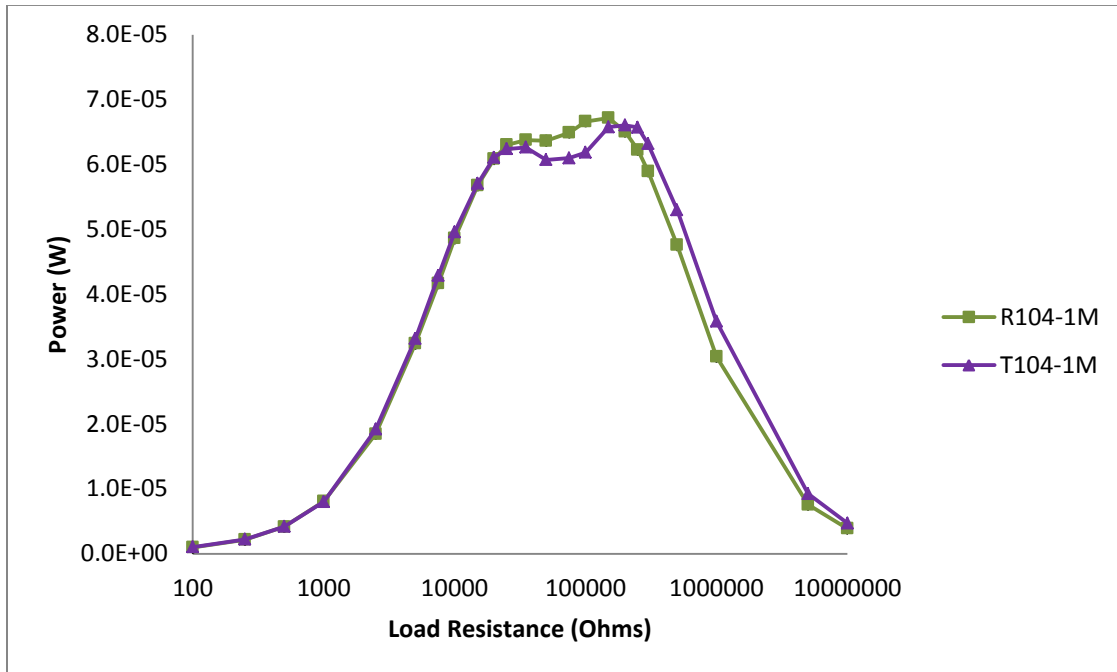


Figure 120: Power generated by the 104 mm<sup>3</sup> devices with a 2 gram proof mass into various load resistors

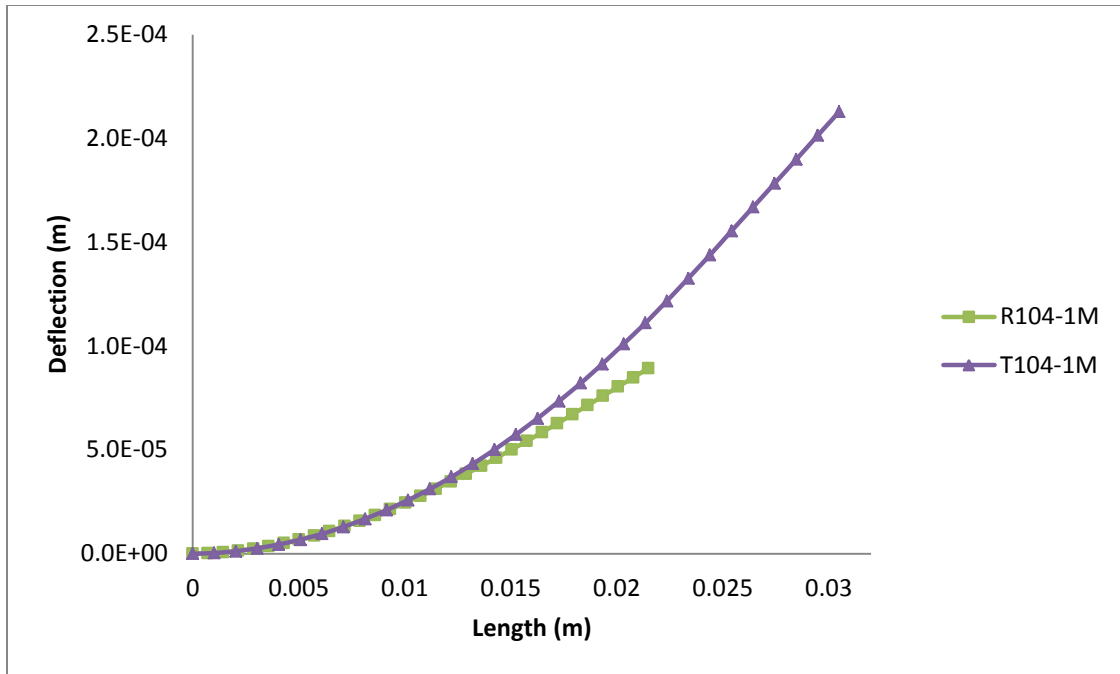


Figure 121: Deflection for 104 mm<sup>3</sup> devices with a 2 gram proof mass

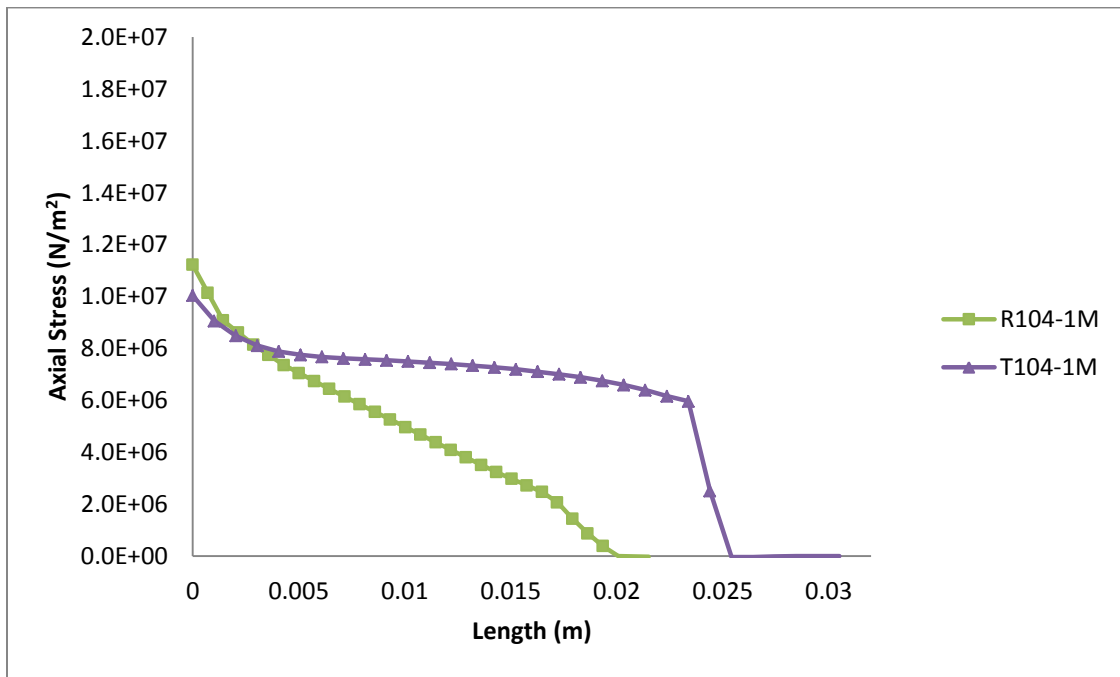


Figure 122: Axial stress along the mid-span length over the surface for the 104 mm<sup>3</sup> devices with a 2 gram proof mass

The impedance spectroscopy from the two devices also indicates the mismatch between R104-1M and T104-1M. However, the larger coupling for the triangular device at the lower resonance frequency is apparent, with the impedance values at the resonance and anti-resonance frequencies are presented in Table 16. While the two samples do not present a viable comparison, T104-1M is comparable with T70-1M, hence Table 16 is generated.

Table 16: Impedance characteristics for 104 mm<sup>3</sup> devices with a 2 gram proof mass

Sample	$f_r$ (Hz)	Z (Ohms)	$f_a$ (Hz)	Z  (Ohms)	Peak Phase°
R104-1M	150	12,914	160	423,002	56
T104-1M	117	16,115	125	641,920	59

Similarly, the equivalent parallel capacitance characteristics are presented for the two devices, and the triangular device. The capacitance values obtained for the two devices are very similar to each other, as the power generated was. However, these are at different resonance frequencies, hence only T104-1M can be compared to T70-1M-P, but it was seen that due to the positioning of the proof mass, the effect on the capacitance measurements was quite noticeable. It is however quite interesting to notice the direct correlation between the power produced, and the capacitance peaks. These comparisons will be consolidated in the summary in section 5.3.4

Table 17: Equivalent Parallel Capacitance for 104 mm<sup>3</sup> devices with a 2 gram proof mass

Sample	Positive capacitance peak (nF)	Negative capacitance peak (nF)
R104-1M	57.67	-29.78
T104-1M	59.89	-29.74

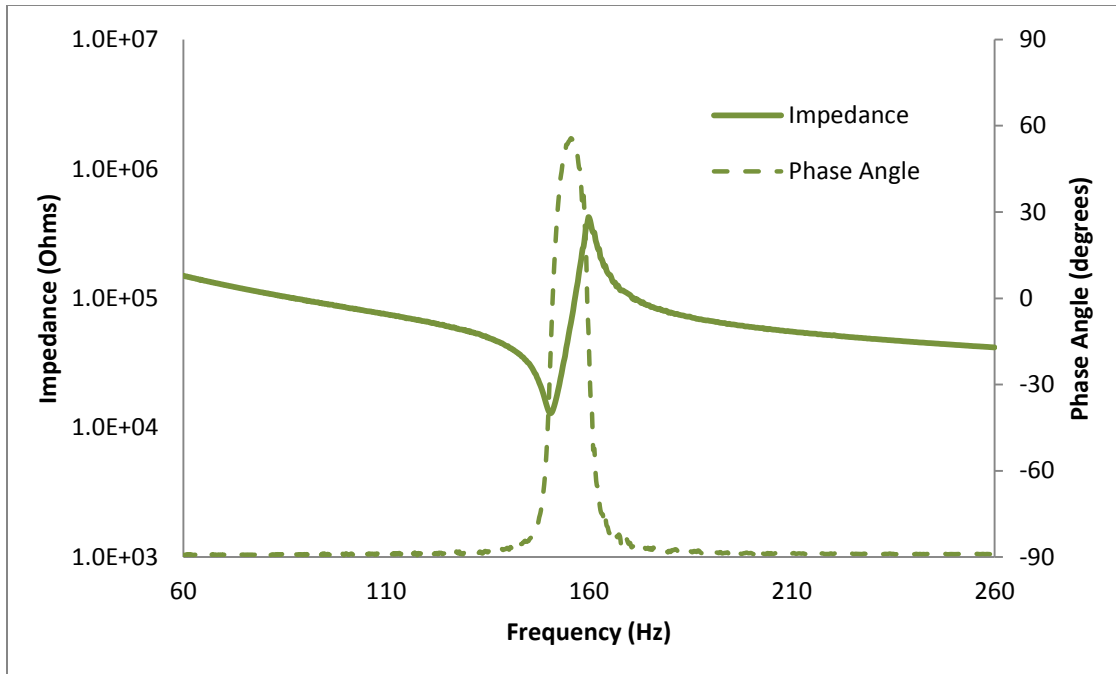


Figure 123: Impedance - Phase Angle for R104-1M

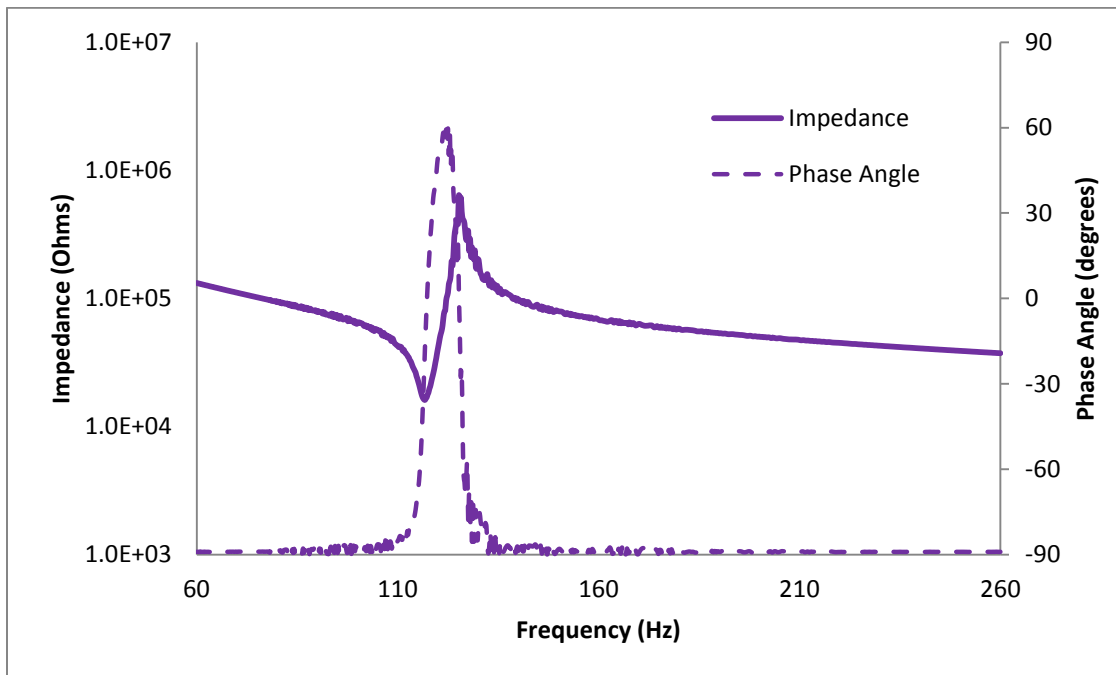


Figure 124: Impedance - Phase Angle for T104-1M

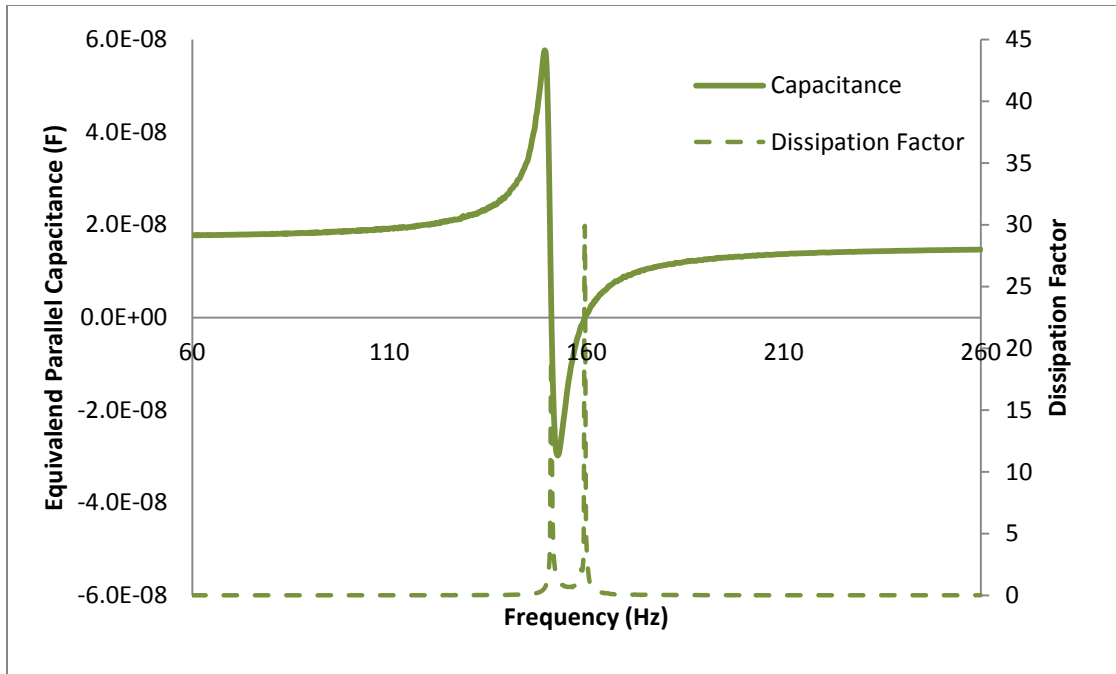


Figure 125: Capacitance – Dissipation Factor for R104-1M

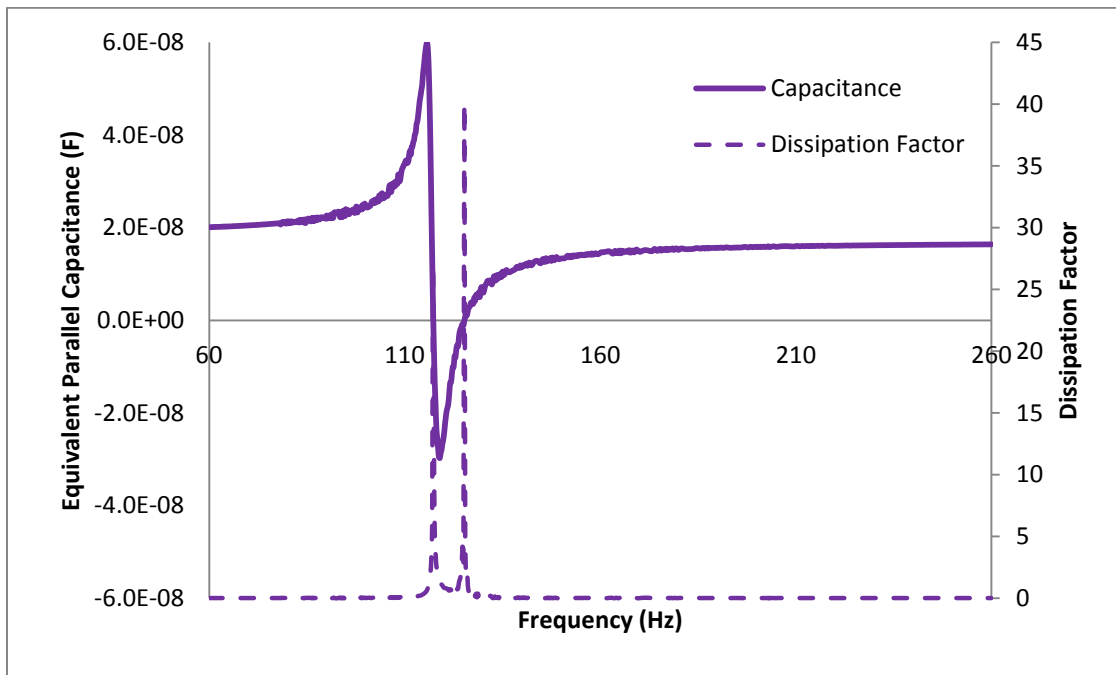


Figure 126: Capacitance – Dissipation Factor for T104-1M

### 5.3.3 RT140-1M

Following the 104 mm<sup>3</sup> samples, the third set of samples that was prepared were the 140 mm<sup>3</sup> bimorphs with the rectangle having a length of 21.5 mm and triangular bimorph being 30.5 mm. These samples are now tested with the given 2 gram proof mass as shown in Figure 127.

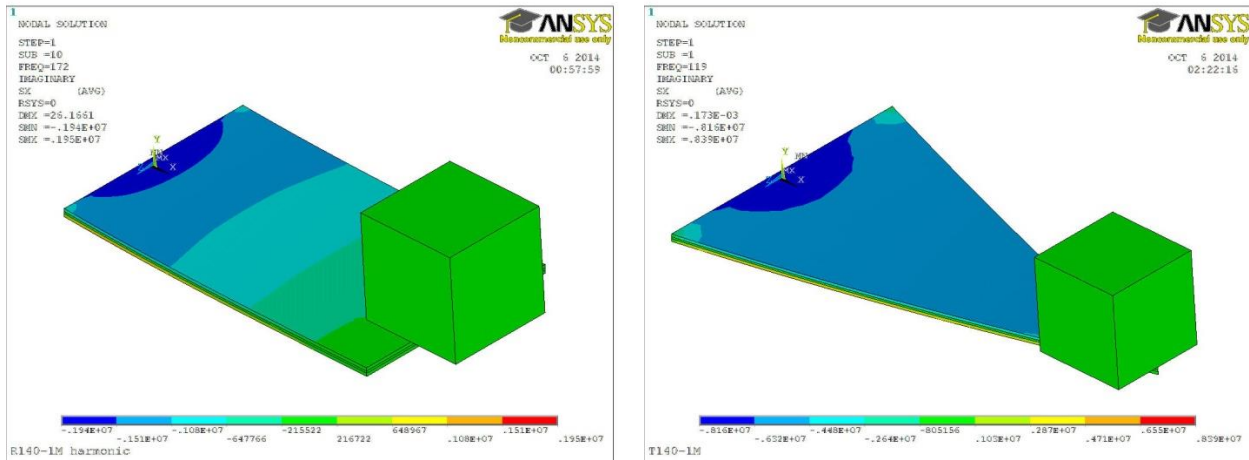


Figure 127: 140 mm<sup>3</sup> devices with a 2 gram proof mass

Following the 70 mm<sup>3</sup> devices, where both the samples had a resonance frequency of about 115 Hz, as the 2 gram proof mass was placed on the 104 mm<sup>3</sup> rectangular device, the short circuit resonance frequency increased to 145 Hz. As the same proof mass is now placed on the 140 mm<sup>3</sup> devices, the resonance frequency for the rectangular device further increases to 162 Hz (shown in Figure 130), presenting a diverging trend. However, it is very interesting to notice that the resonance frequency for T140-1M remains at 115 Hz. This geometric/design factor can have major implications from a design point of view for a target resonance frequency, where the size of the device is not greatly affecting the resonance frequency, as opposed to the rectangular device, which increases with increasing size and width, which would call for larger proof masses to maintain the resonance frequency.

Even though the devices have matching volumes and proof masses, it was shown in the case of the 104 mm<sup>3</sup> devices that it is difficult to compare these, as the performance of the rectangular device is affected due to lower deflections. This conclusion is amplified from results in this section that are presented. However, the set T140-1M set of results would be quite useful with other triangular bimorphs with the same proof mass and matching resonance frequency.

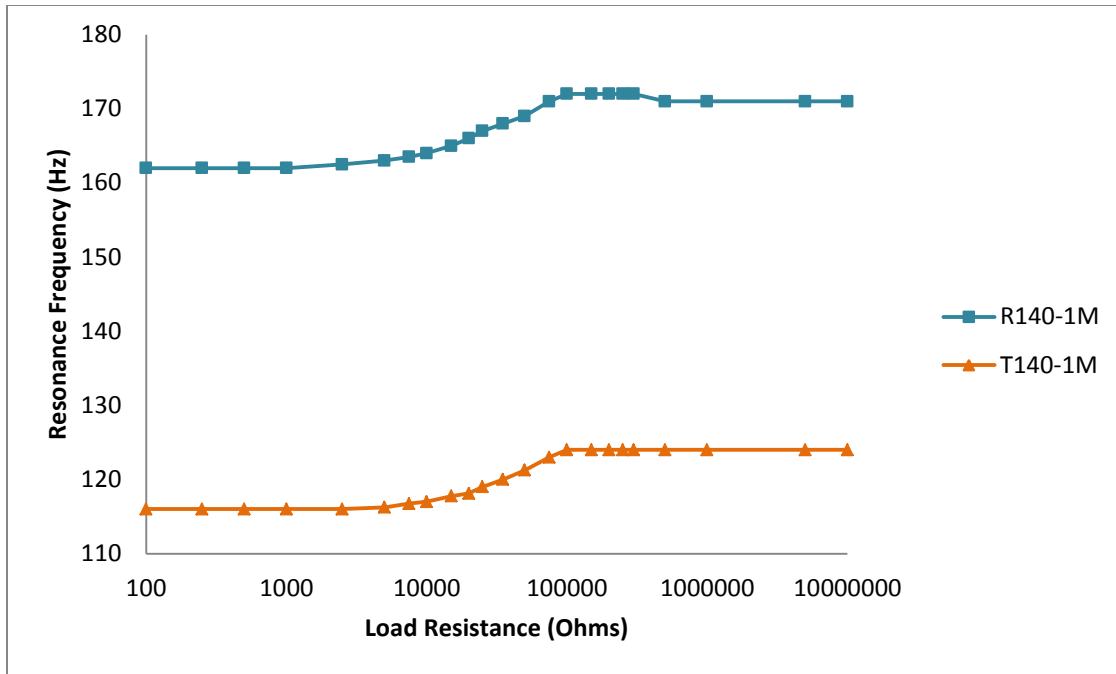


Figure 128: Resonance frequency for 140 mm<sup>3</sup> devices with a 2 gram proof mass with varying load resistance

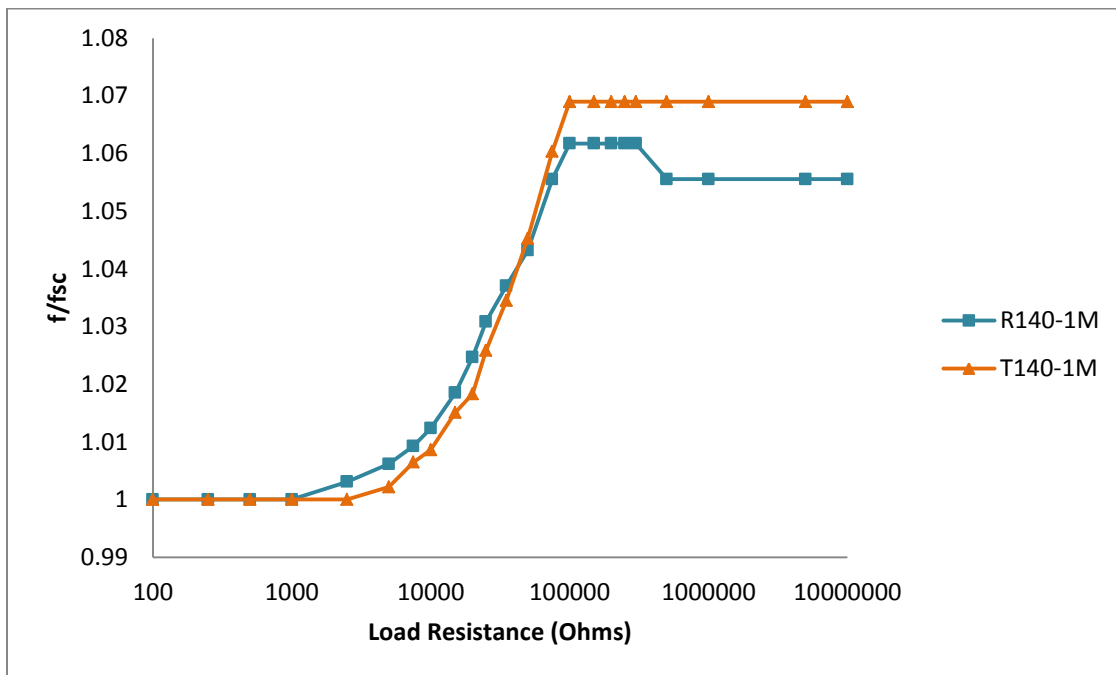


Figure 129: Short circuit normalized resonance frequency for 140 mm<sup>3</sup> devices with a 2 gram proof mass

Once again, with the triangular cantilevers, enhanced coupling is observed, as depicted in Figure 129. The coupling coefficient calculated for the two devices, R140-1M and T140-1M is found to be 0.32 and 0.35 respectively. Damping ratios are also calculated and presented in Table 18, and it is observed that the damping in the T140-1M sample is lower than the R140-1M samples. Therefore, with the enhanced quality factor, the resulting figure of merit of T140-1M is found to be 8.16, which is in the very high coupling regime. This is similar to the case for the 140 mm<sup>3</sup> triangle without the proof mass, where the large coupling figure of merit showed distinct optimal load resistance values. However, it must be mentioned that the figure of merit for R140-1M at 5.33 is also quite large, and in fact quite comparable to T140-0M, but the presence of unique load resistance values is absent. More comparisons and observations on this will be presented in the conclusions chapter of this section.

One of the major implications of the increased resonance frequency for R140-1M is the diminishing performance for producing power. In fact, in this case, as shown in Figure 130, where a 2 gram proof mass is placed on the two devices, the triangular device outperforms the rectangular device. Therefore, the apparent effect of the lower resonance frequency for the triangular device is quite strong; i.e. the rectangular device R140-1M greatly suffers due to the increase in resonance frequency.

Table 18: Power generated at optimal load resistance values for the 140 mm<sup>3</sup> devices with a 2 gram proof mass

	$R_{opt,1}(\Omega)$	P ( $\mu$ W)	$R_{opt,2}(\Omega)$	P ( $\mu$ W)	$\zeta$	$k_{31}$	$k^2Q$
R140-1M	25,000	66.97	100,000	69.19	0.00962	0.32	5.33
T140-1M	15,000	88.34	200,000	88.75	0.00767	0.35	8.16

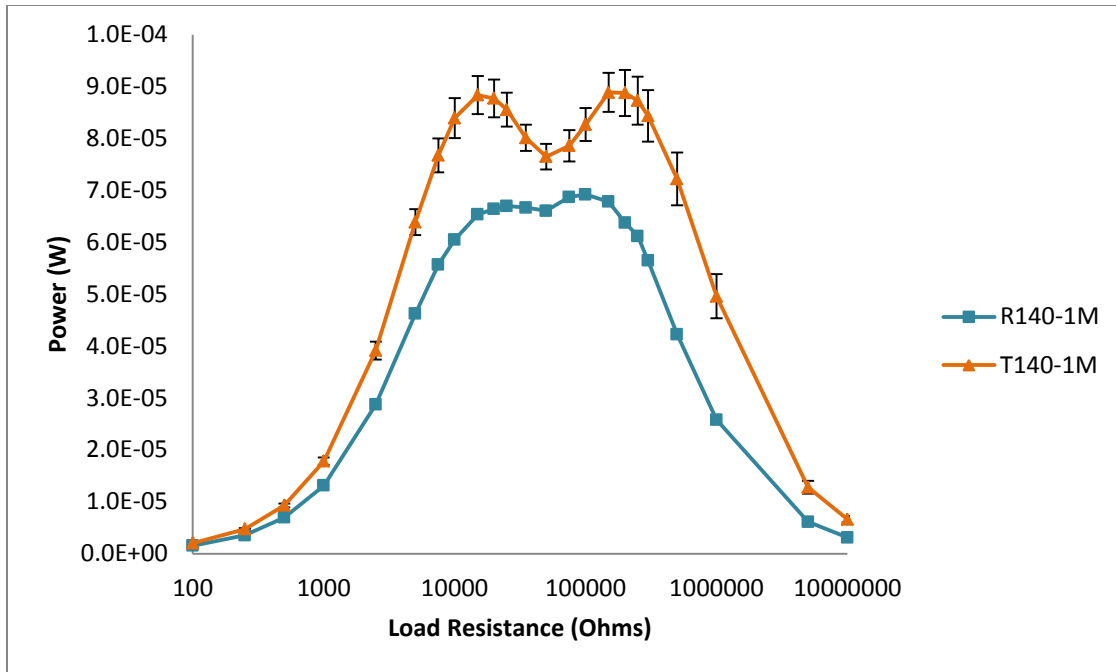


Figure 130: Power generated by 140 mm<sup>3</sup> devices with a 2 gram proof mass into various load resistors

Therefore, these two devices do not provide a viable comparison, as it can be seen in Figure 131, where the maximum deflection in the case of R140-1M is even further reduced to 70 μm, down from 88 μm when R104-1M was resonating at 145 Hz at the short circuit resonance frequency. It is however interesting to report the maximum deflection for T140-1M, and compare it with T104-1M especially, both resonating at 115 Hz. Even though the frequency is the same, the maximum deflection is now reduced to 163 μm, as compared to 213 μm for T104-1M, and 237 μm for T70-1M-P. This is a direct result of the enhanced inertial loading capacity, and decreasing maximum stresses. In fact, Figure 132 shows the state of axial stresses, and it can be seen that for R140-1M, with the reduced deflection due to higher resonance frequency, the maximum stress is decreased. The deflection and maximum stress for T140-1M is also decreased, even though the resonance frequency for other comparable triangular counterparts is the same. More light will be shed on this aspect when compared on a power per volume basis, presented in the summary section.

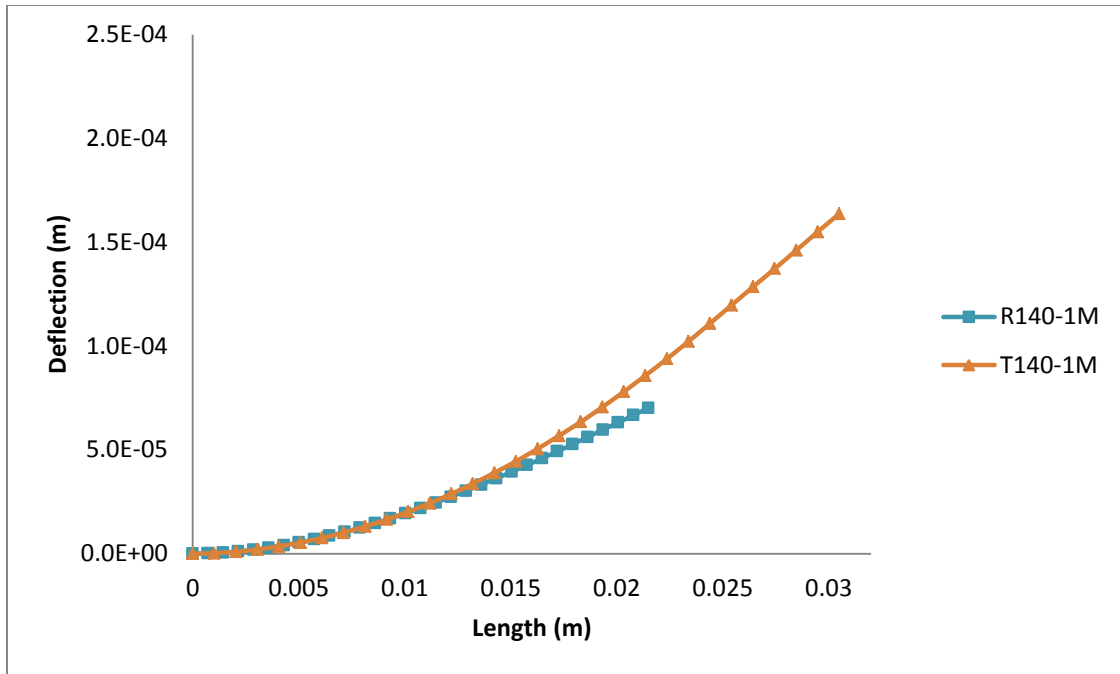


Figure 131: Deflection for the 140 mm<sup>3</sup> devices with a 2 gram proof mass at resonance

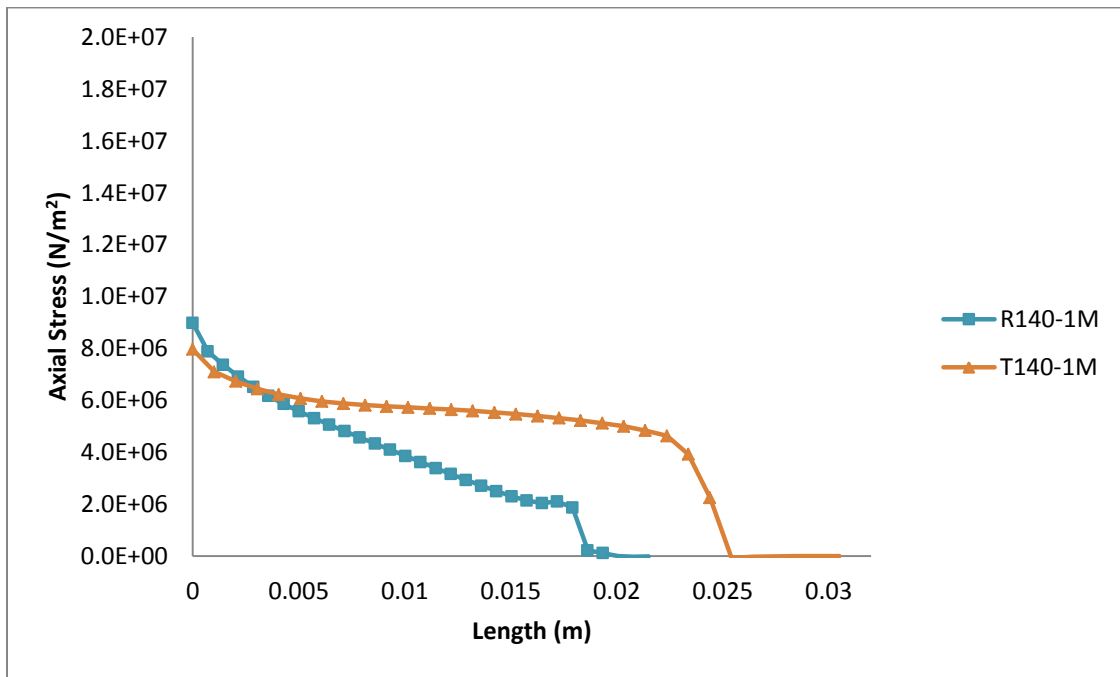


Figure 132: Axial stress along the mid-span length over the surface for the 104 mm<sup>3</sup> devices with a 2 gram proof mass

The impedance analyzer measurements for the two devices, presented in Figure 133 and Figure 134, and show that the two devices with the same proof mass and volume, even though at different frequencies have fairly low impedance values at the resonance frequency. R140-1M in fact shows lower impedance compared to T140-1M at the resonance frequency, the first instance for such a scenario. This lower impedance is attributed to the low stress in the device due to the higher resonance frequency and lower deflections. The impedance at the anti-resonance frequency for T140-1M is double as that of R140-1M, although it must again be emphasized that these resonance and anti-resonance frequencies do not match. The 2 gram proof mass triangles are compared in the conclusions section.

Table 19: Impedance – Phase Angle for 140 mm<sup>3</sup> devices with a 2 gram proof mass

Sample	f <sub>r</sub> (Hz)	Z (Ohms)	f <sub>a</sub> (Hz)	Z  (Ohms)	Peak Phase°
R140-1M	168.1	9833	178.7	227,071	45
T140-1M	116.4	10,105	125.5	508,239	63

The capacitance measurements presented in Figure 135 and Figure 136 show that once again, the capacitance at their respective peaks for the two devices are greater in the case of T140-1M as compared to R140-1M. This has mostly been a consistent trend so far, while comparing devices with or without matching resonance frequencies.

Table 20: Capacitance – Dissipation Factor for 140 mm<sup>3</sup> devices with a 2 gram proof mass

Sample	Positive capacitance peak (nF)	Negative capacitance peak (nF)
R140-1M	68.13	-29.65
T140-1M	94.46	-55.28

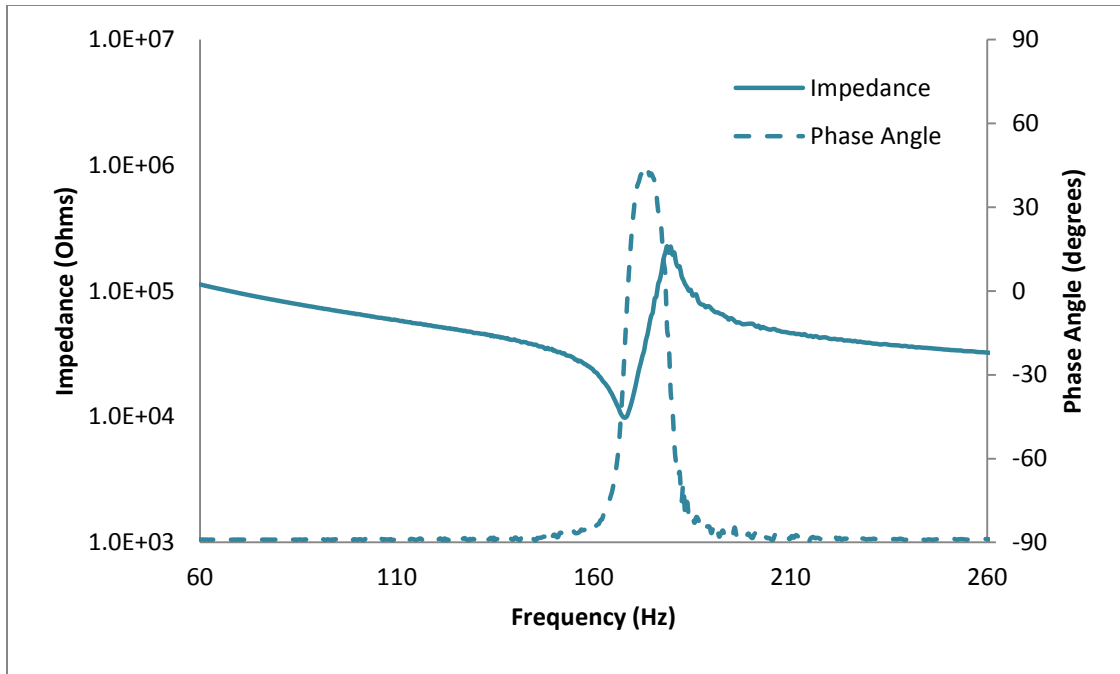


Figure 133: Impedance – Phase Angle for R140-1M

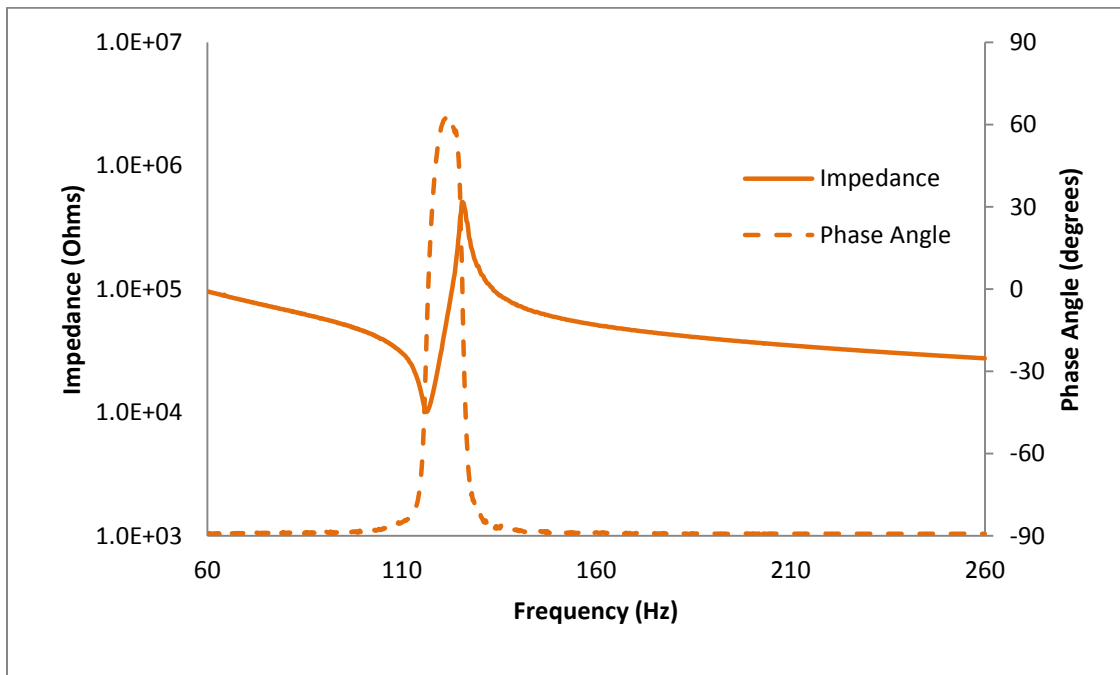


Figure 134: Impedance – Phase Angle for T140-1M

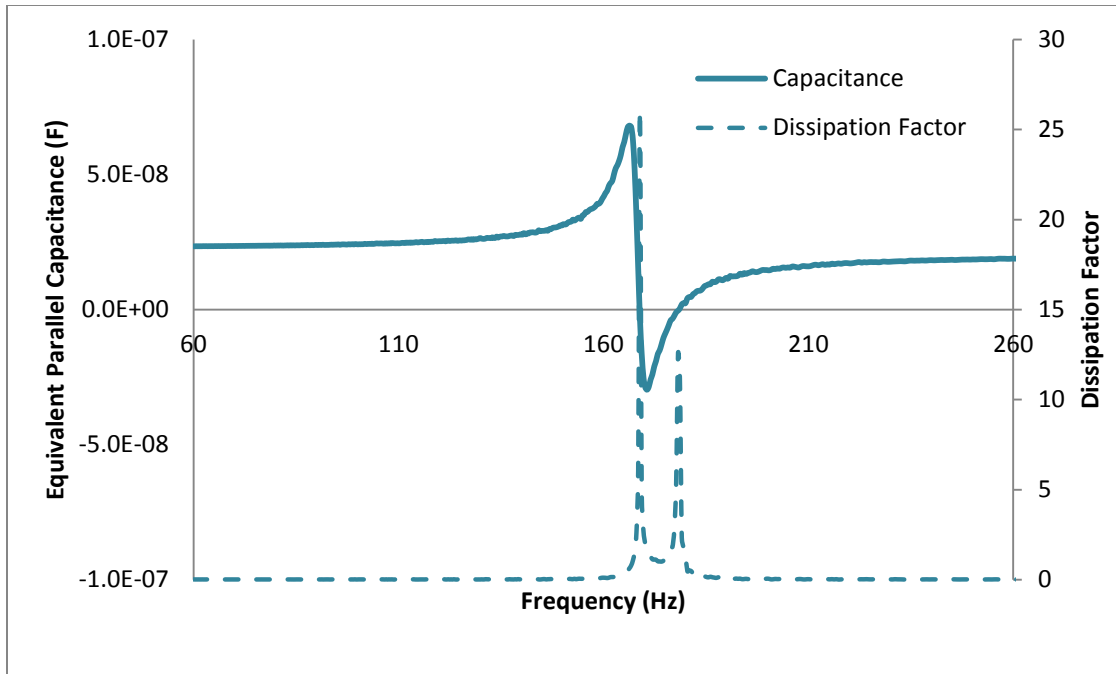


Figure 135: Capacitance – Dissipation Factor for R140-1M

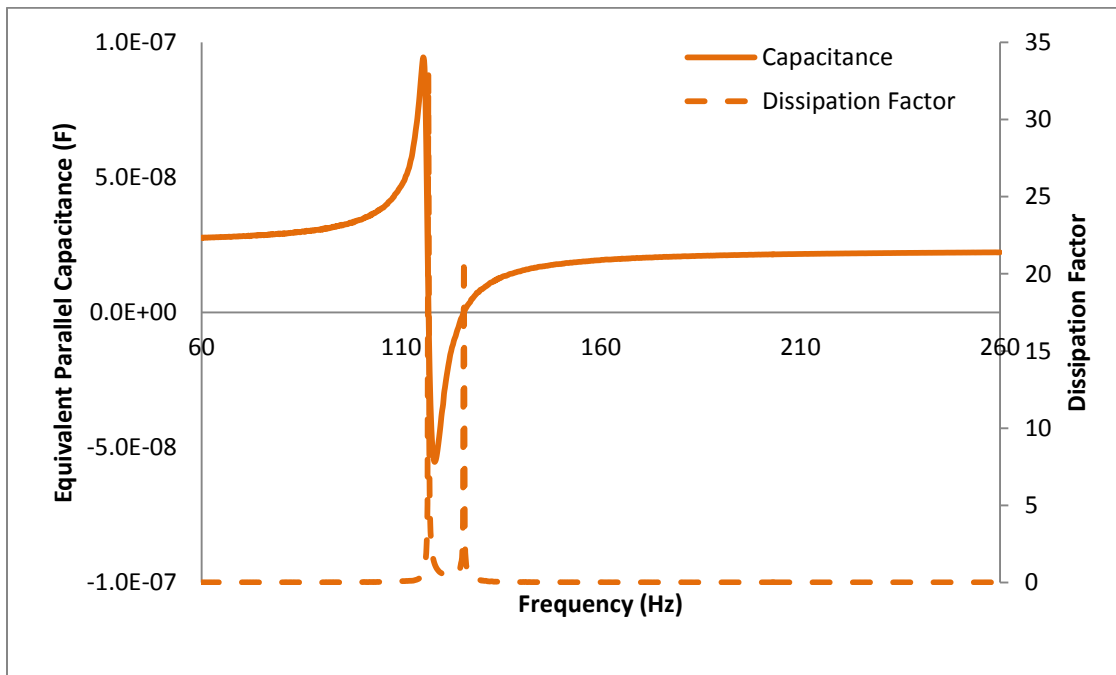


Figure 136: Capacitance – Dissipation Factor for T140-1M

### 5.3.4 Summary for devices with 2 grams proof mass

The three sets of devices considered in this section had volumes of  $70 \text{ mm}^3$ ,  $104 \text{ mm}^3$  and  $140 \text{ mm}^3$ . In section 5.2, it was seen that these devices had relatively the same resonance frequencies, and hence could be easily compared with each other. In this section however, it is seen that as the devices are loaded with a 2 gram proof mass, the resonance frequencies are much more difficult to manage. In the case of the rectangular bimorph, when the 2 gram proof mass is placed on the three devices, the resonance frequencies increase from 115 Hz, to 145 Hz, to 160 Hz. In the case of the triangular cantilevers, with minor adjustments in the positioning of the proof mass, the resonance frequencies can be maintained. The proof mass in the triangular devices could possibly be positioned to meet the 145 Hz and 160 Hz frequencies on T104 and T140 devices. However, this method is not followed up with due to the fact that a considerable amount of area on the tip of the triangular bimorphs would be present in front of the proof mass, which could create external effects such as segmented nodes that are beyond the scope of this study.

However, some important insights can be gained from Figure 137 and Figure 138, which present the power density of the rectangular and triangular devices. These power densities that are calculated include the volume of the proof mass as part of the device volume. Therefore, as the volume of the proof mass dominates the entire volume, it can be observed that the power density of these devices under the base excitation load of  $2.45 \text{ ms}^{-2}$  and 2 gram proof mass is quite close to each other. There are some subtle differences that must be pointed out however.

In Figure 137, it can be seen that the overall power density of the three devices is relatively the same, even though the resonance frequencies are changing appreciably. Therefore, the proof mass is clearly dominating the amount of power density of these devices. However, with the change in size, hence changing tip mass per volume of the beam, the optimal load resistance values are shifting. As the devices become larger ( $R140-1M > R104-1M > R70-1M$ ), the tip mass to beam mass ratio decreases proportionally, and the optimal load resistance values shift to lower values. In fact, in the case of R70, only a single optimal load resistance is observed, while the other two devices present either a plateau, or two peaks.

A similar trend is observed in Figure 138 for the triangular devices with the 2 gram proof mass, where more viable comparisons can be made, with the resonance frequency maintained at about 115 Hz. It can be observed that the power density from the triangular devices with the 2

gram proof mass is somewhat higher than the rectangular counterparts, even though the maximum stresses reported each time are lower. This is a great advantage provided by the triangular devices, as they would be operating much more reliably compared to the rectangular counterparts. Moreover, the effect of enhanced strain distribution and lower stresses with the same tip mass to beam ratios as rectangular counterparts also show an advantage. While the R70-1M device shows only one optimal load resistance, the triangular device T70-1M-P (at 115 Hz) shows the presence of two peaks.

In both cases, the position of the optimal load resistance shifts to lower values, and with increasing size and lowering of stresses, the presence of two peaks becomes more apparent. This is especially distinctive in the case of the T140-1M device, with the lowest value for the first optimal load resistance, and presence of two distinct peaks.

The resulting electromechanical coupling coefficient, damping ratios, and figure of merits are presented in Figures Figure 140, Figure 141 and Figure 142. In these figures, the data points for the rectangular devices are not connected due to the mismatch in resonance frequency. It can be clearly seen that the  $k_{31}$  coupling coefficients for triangular devices with the 2 gram proof mass are always higher compared to the rectangular counterparts. The figure of merit also keeps increasing in the triangular devices with the decreasing tip mass to beam mass ratios; however, this is affected in the case of the rectangular devices due to the increasing resonance frequency.

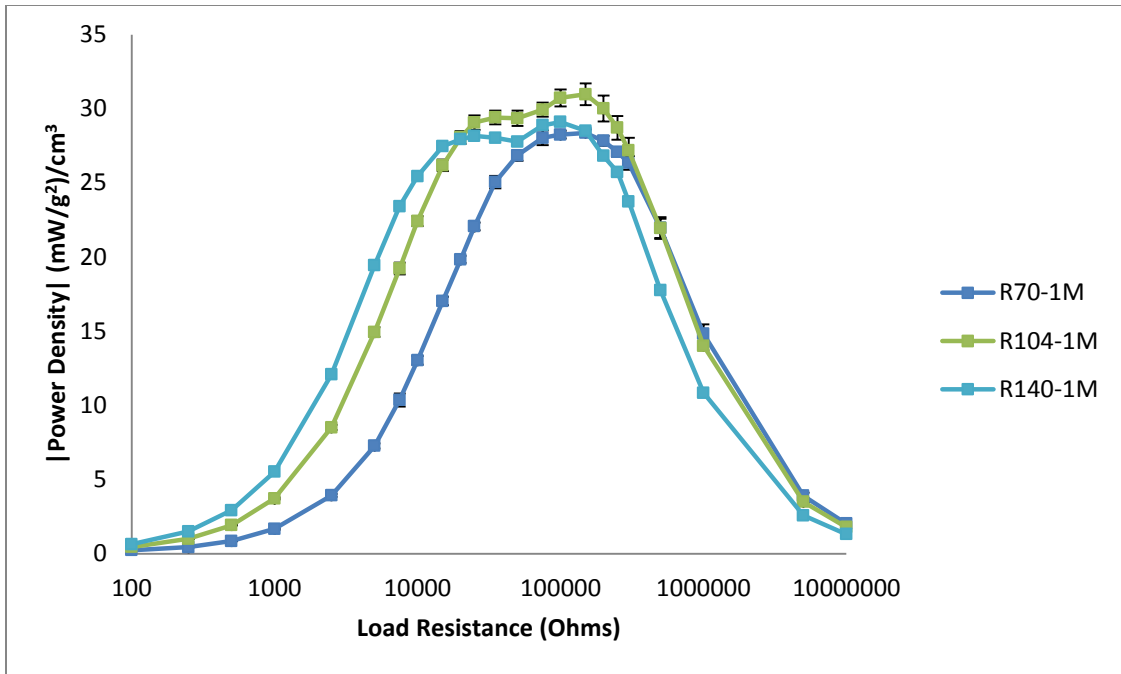


Figure 137: Power Density for 2 gram proof mass rectangular bimorphs as a function of load resistance

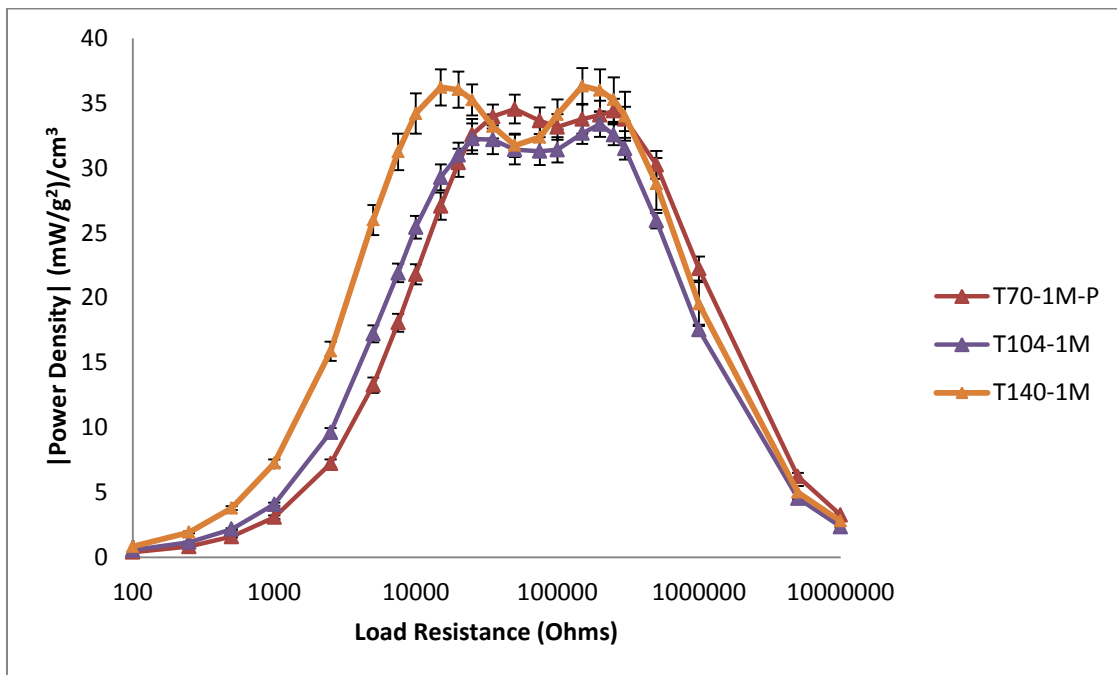


Figure 138: Power Density for 2 gram proof mass triangular bimorphs as a function of load resistance

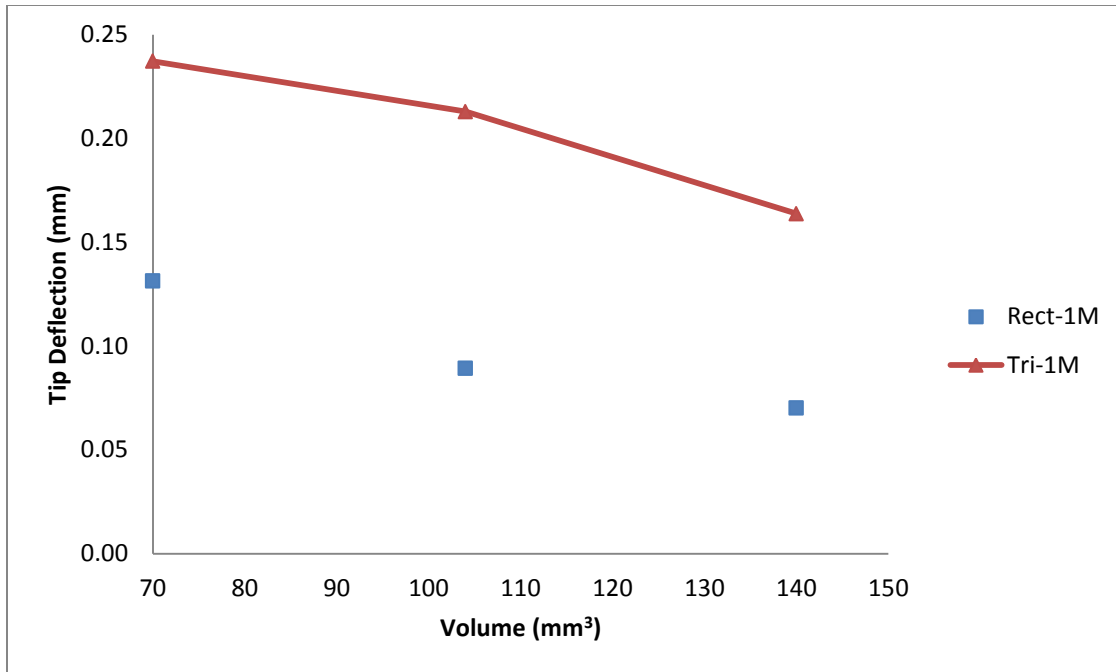


Figure 139: Maximum tip deflection for 2 gram proof mass bimorphs

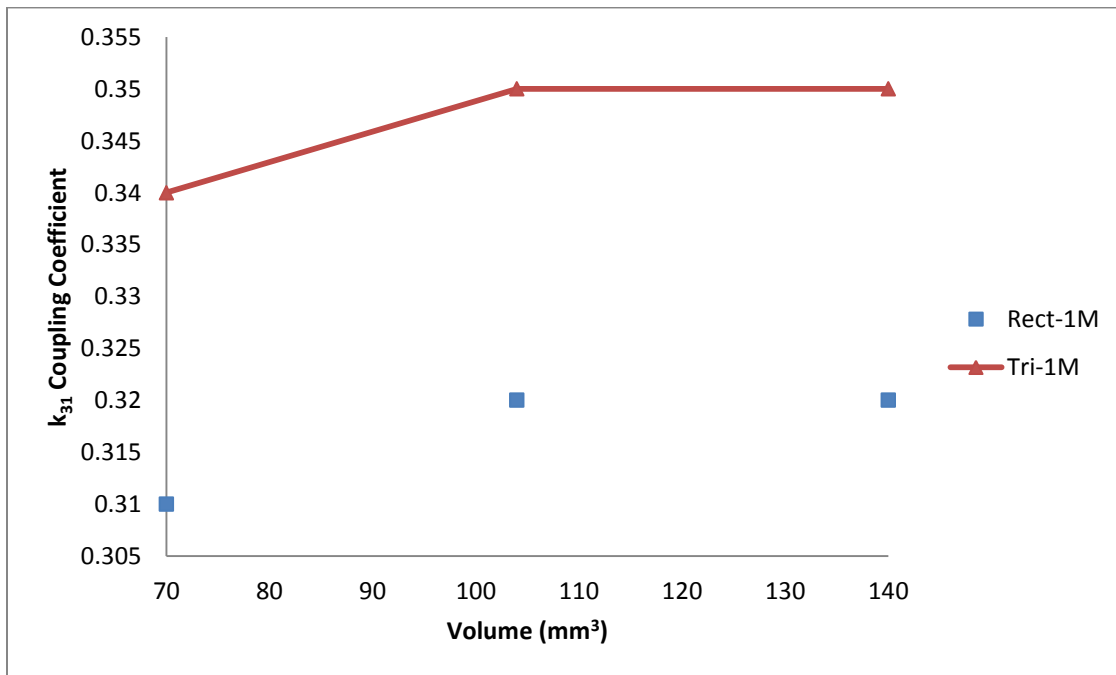


Figure 140: Electromechanical Coupling Coefficient for devices with 2 gram proof mass

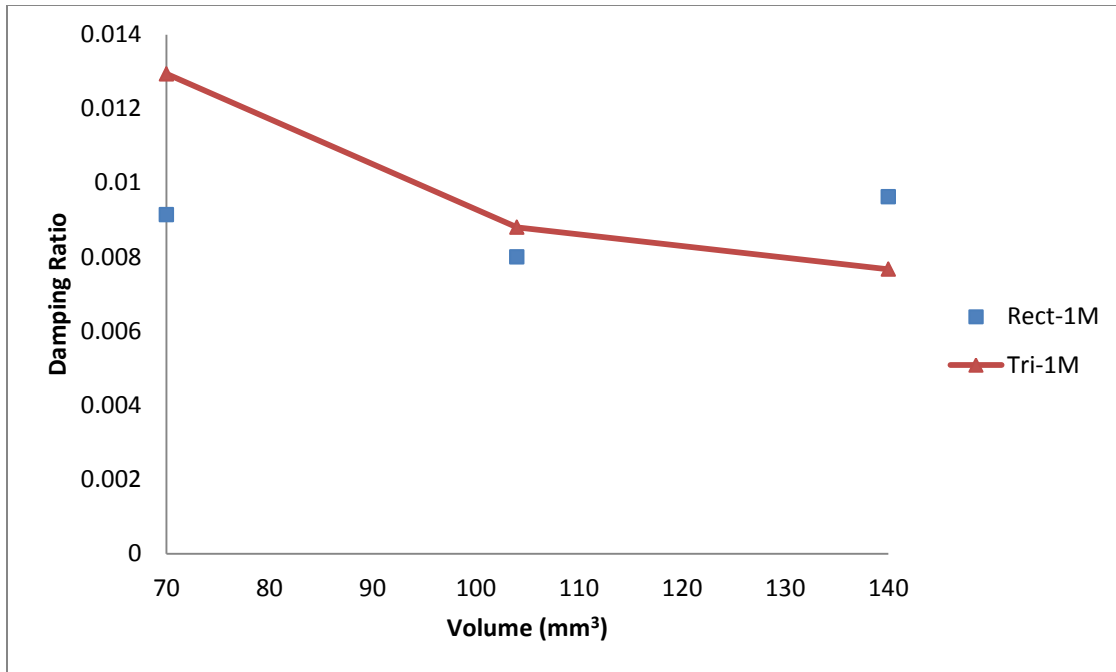


Figure 141: Damping Ratio for 2 gram proof mass devices

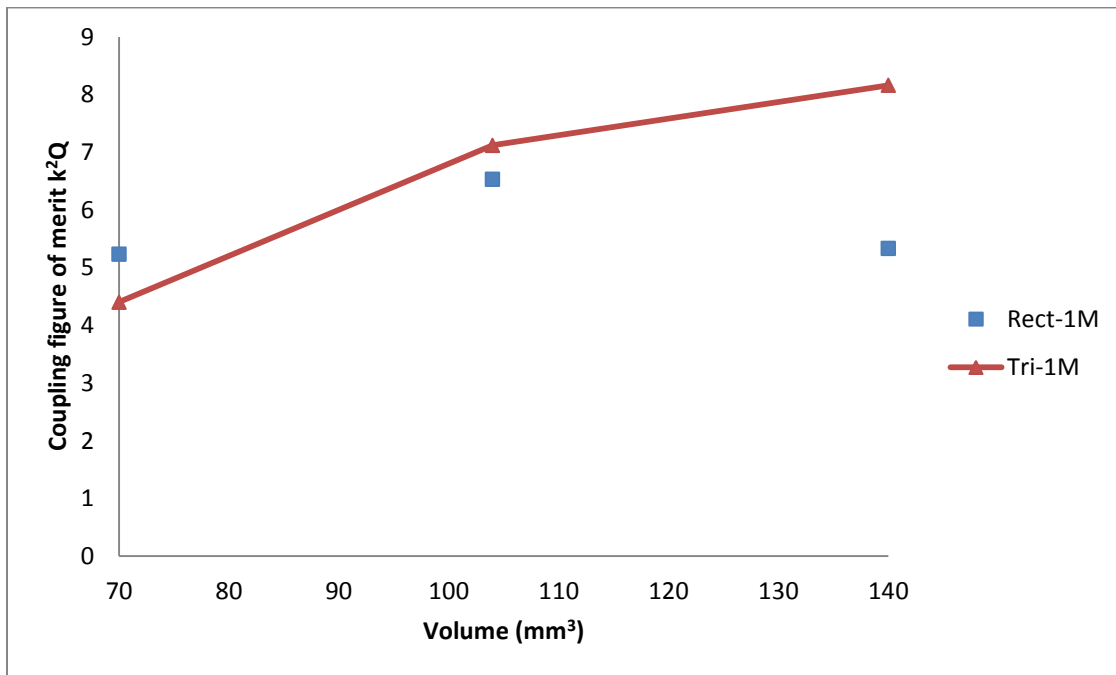


Figure 142: Coupling Figure of Merit for 2 gram proof mass devices

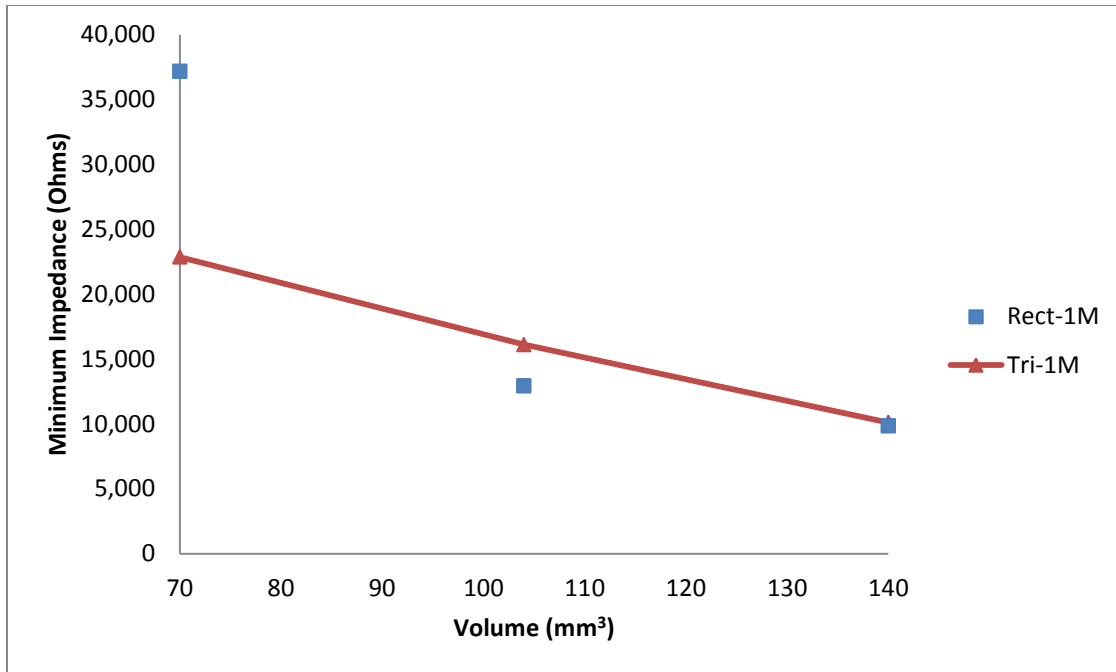


Figure 143: Minimum Impedance for 2 gram proof mass devices

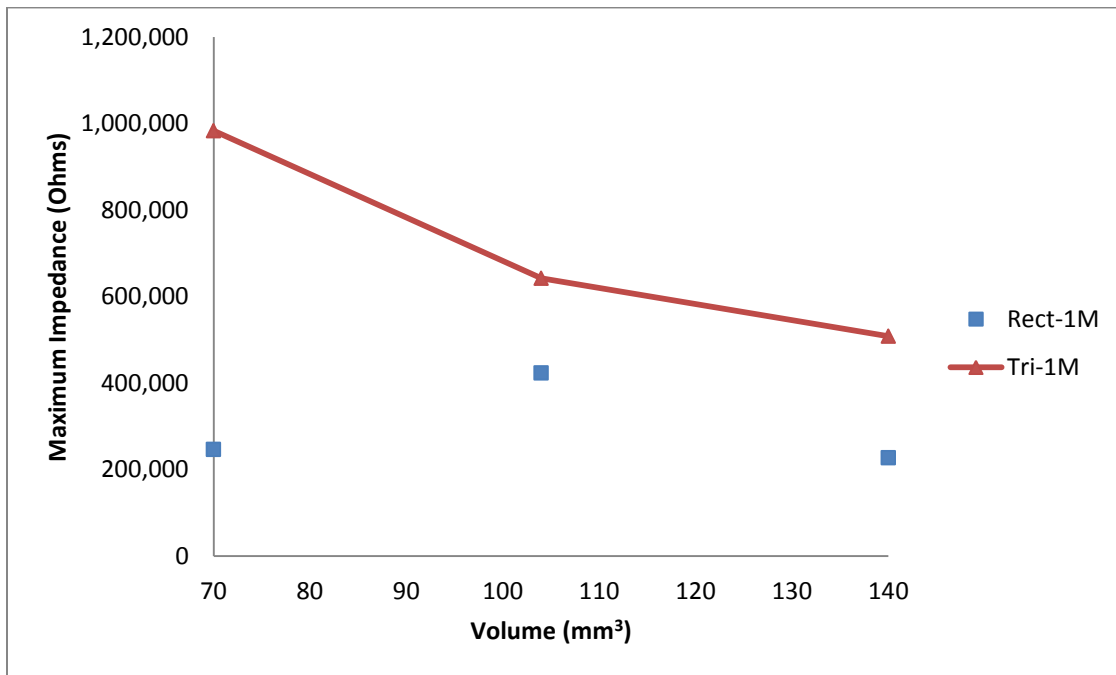


Figure 144: Maximum Impedance for devices with 2 gram proof mass

The peak impedance measurements at resonance and anti-resonance for the two devices are also shown in Figures Figure 143 and Figure 144. As expected, and consistent with the power generation plots especially in the case of the triangular devices, the impedance peaks shift to lower values with increasing size. Figure 144 shows expected behavior, where the impedance at anti-resonance for triangular devices is always higher than rectangular devices. However, in the case of the impedance at resonance, the impedance measurement is not always lower for triangular devices. The sole case where the resonance frequency matches between the two devices, at  $70 \text{ mm}^3$ , the triangular device shows the advantage of lower impedance at resonance.

The capacitance measurements for the three sets of devices, as consolidated in Figure 145 do maintain the trend of increased capacitance in the case of the triangular peaks as opposed to the rectangular peaks. From the electrical domain point of view for the piezoelectric cantilevers, where capacitance is a key characteristic to describe the piezoelectric bimorph, changing geometry into triangular shapes to enhance strain distribution and lower the maximum stress levels in the device provide enhanced capacitance, a marked advantage.

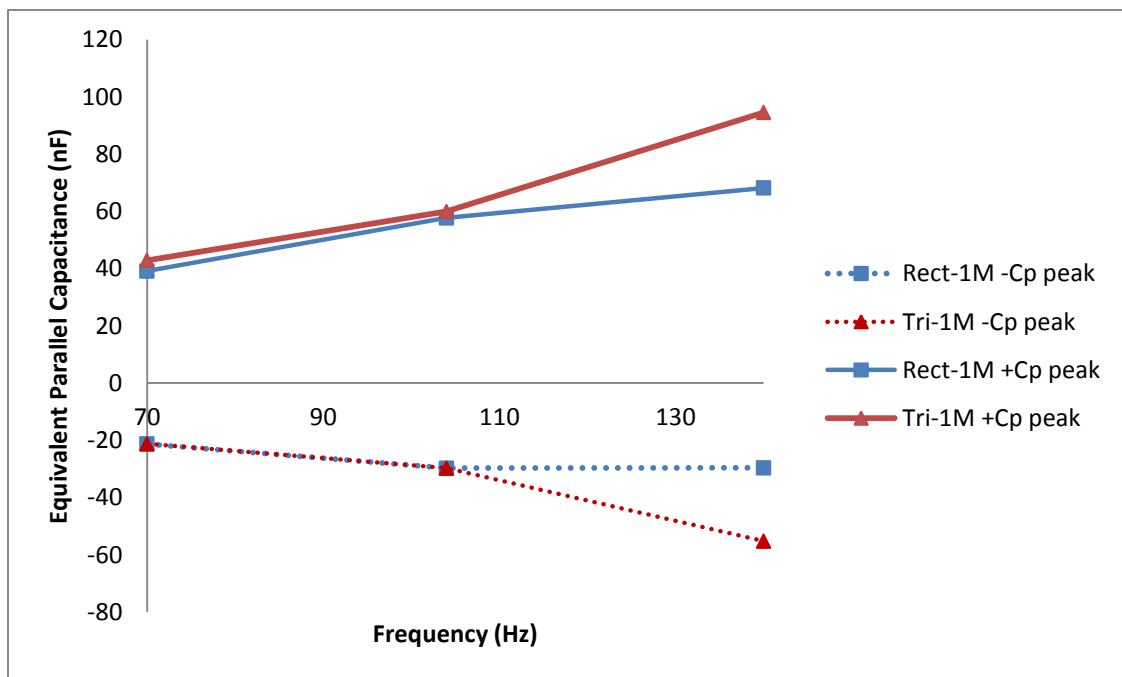


Figure 145: Capacitance peaks for 2 gram proof mass devices

## 5.4 Increased Proof Masses

### 5.4.1: 70 mm<sup>3</sup> devices with 4 grams proof mass

In section 5.3, it was seen that as the proof mass is added on to the 70 mm<sup>3</sup> rectangular and triangular devices, the resonance frequency drops from 512 Hz to about 115 Hz. The 115 Hz resonance frequency was achieved on triangular samples with small adjustments in the positioning of the proof mass. However, in the case of the rectangular bimorphs, as the clamping width is increased (i.e. increasing volume), and the proof mass is kept constant, the resonance frequency increases with decreasing effective loading at the tip.

Due to the fact that the resonance frequency is dominated by the proof masses, it was desired to study the effect of increasing proof masses, and see if the resonance frequencies converge. Therefore, an additional 2 gram proof mass was attached on the bottom surface of the beam, resulting in a total of 4 grams. These samples, designated as R70-2M and T70-2M are shown in Figure 146.

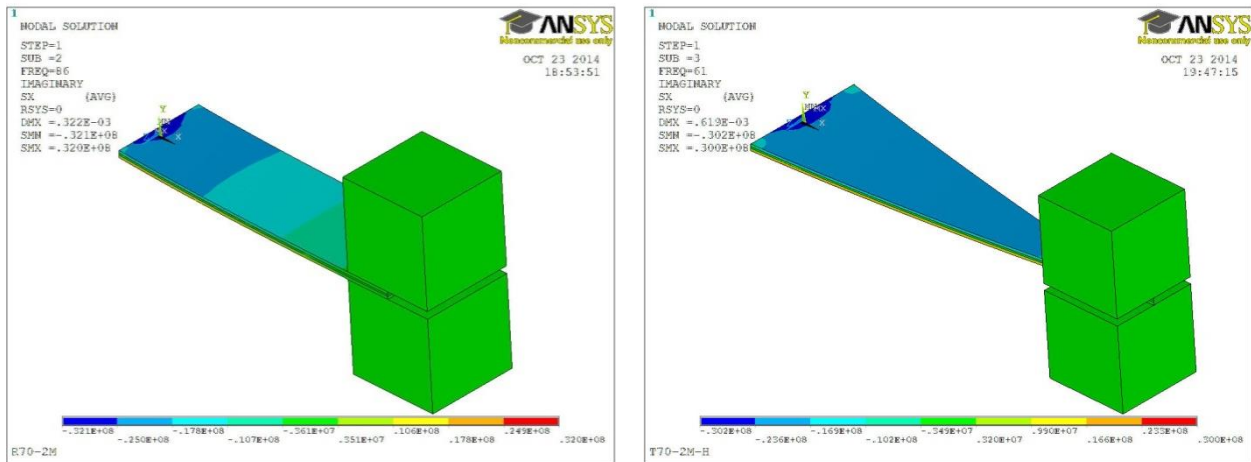


Figure 146: Schematic for R70-2M and T70-2M

The short circuit resonance frequencies of the two devices, the 21.5 mm long rectangular bimorph, and the 30.5 mm long triangular bimorph, with 4 grams of proof mass are found to be 81 Hz and 64 Hz respectively, shown in Figure 147. These resonance frequencies do not match with each other; hence viable comparisons between the samples are not possible.

However, with the addition of a nominal proof mass, from the no proof mass case, there was an order of magnitude improvement in power generated by the devices. Therefore, the effect of doubled proof mass is worth exploring, which is presented in the following section.

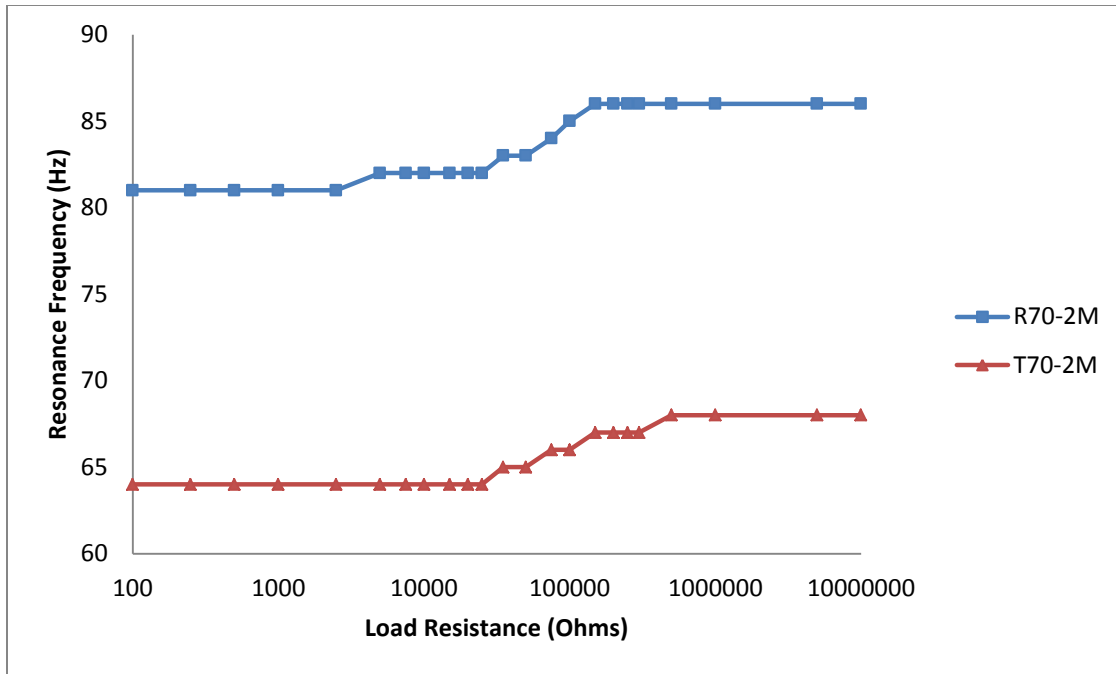


Figure 147: Resonance frequencies as a function of load resistance for 70 mm<sup>3</sup> devices with 4 grams proof mass

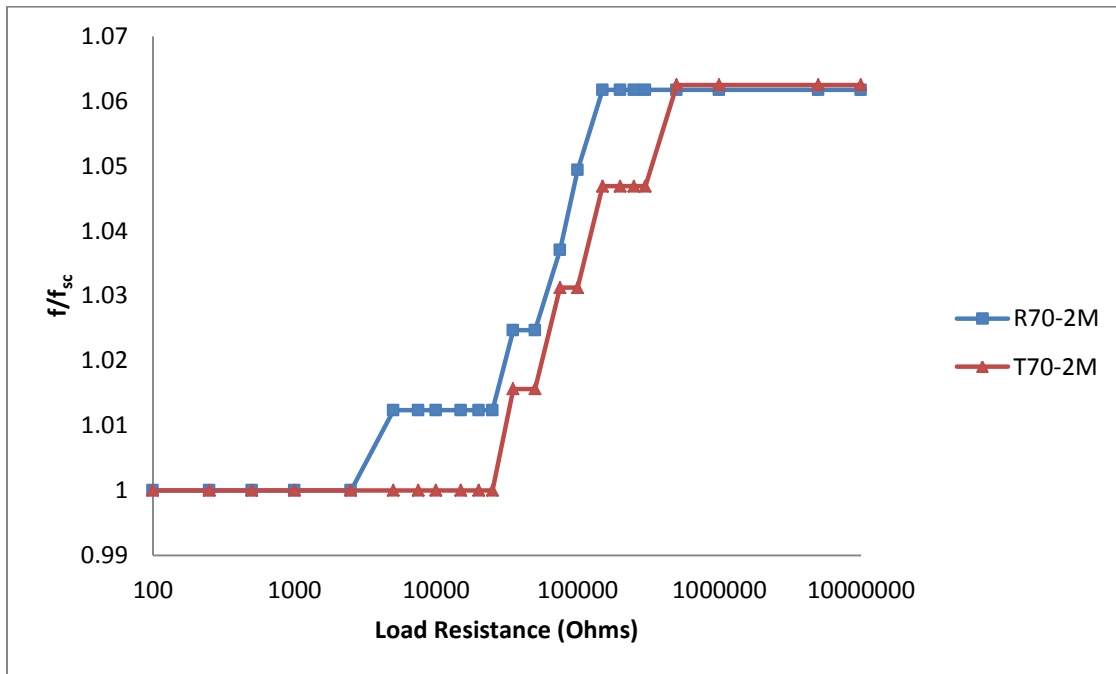


Figure 148: Short circuit resonance frequency normalized resonance frequencies as a function of load resistance for 70 mm<sup>3</sup> devices with 4 grams proof mass

The power generated by the two devices is shown in Figure 149, where two major things are of interest – the magnitude of power generated, and the peaks for optimal load resistance values. In terms of power generated, the maximum power for R70-2M is 125  $\mu\text{W}$  with a resonance frequency of about 84 Hz at the optimal load resistance. The power generated by R70-1M was about 55  $\mu\text{W}$  at a resonance frequency of 119 Hz. Therefore, with the addition of mass, and lowering of resonance frequency, the power generated is directly proportional to the addition of mass and inversely proportional to the resonance frequency. This relates to the simple analytical expression by Williams and Yates’ lumped parameter model,  $P = \frac{mA^2}{4\omega_n\zeta_T}$  presented in section 2. A similar conclusion can be drawn for the triangular cantilevered bimorph, where the power generated by T70-1M at the optimal load resistance at the resonance frequency of 95 Hz is about 76  $\mu\text{W}$ , which goes up to 163  $\mu\text{W}$  at 66 Hz.

One of the aspects that is quite noticeable is the similarity in the electromechanical coupling coefficient between the two devices. It can be seen that with the same proof mass, the coefficients are very close to each other, roughly equal to 0.34, as shown in Table 21. In fact, with the increasing proof mass, the optimal load resistance value is converging to a single point, rather than the double peaks or plateau behavior, which is especially seen for the triangular device. In the case of R70-2M, a damping ratio of 0.0161 is found, resulting in a  $k^2Q$  figure of merit of 3.51, while in the case of T70-2M, a larger damping ratio (largest one measured in this thesis), resulting in a  $k^2Q$  of 2.79. Therefore, with increasing proof mass, and in the case of the longer triangular sample, with the larger moment arm, the device goes towards the low coupling regime, and becomes more resonance frequency, and optimal load resistance specific.

Table 21: Power generated at optimal load resistance values for 70 mm<sup>3</sup> devices with 4 grams proof mass

	$R_{\text{opt},1}(\Omega)$	P ( $\mu\text{W}$ )	$R_{\text{opt},2}(\Omega)$	P ( $\mu\text{W}$ )	$\zeta$	$k_{31}$	$k^2Q$
R70-2M	75,000	125	200,000	128	0.0161	0.3360	3.51
T70-2M	75,000	159	100,000	163	0.0205	0.3379	2.79

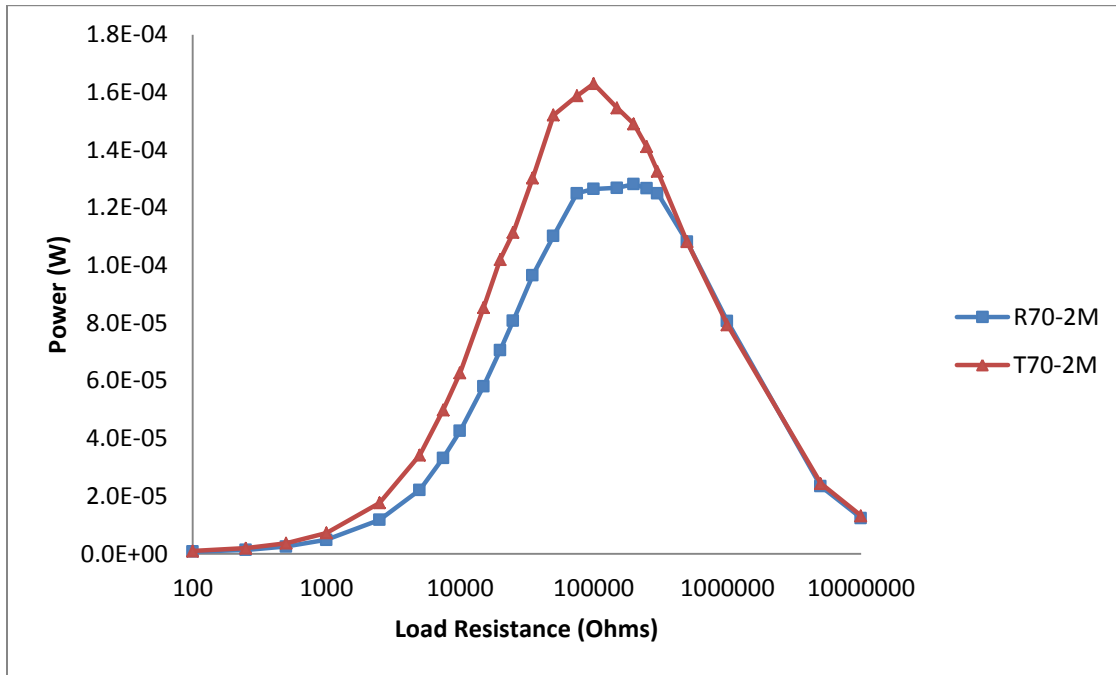


Figure 149: Power generated by 70 mm<sup>3</sup> samples with 4 grams proof mass as a function of load resistance

The numerical analysis calculating longitudinal deflections and axial stresses are shown in Figure 150 and Figure 151. It can be seen that with the resonance frequencies not matching, and the triangular device having lower frequencies, the deflections are larger. The constant radius of curvature in the triangular sample with the 4 grams proof mass is quite apparent.

The maximum value of stress is quite interesting to notice though. With the same proof mass in the triangular device (however unmatched resonance frequency), the maximum stress in the device is very close to the maximum stress in the rectangular device, and gives the advantage of the linear stress profile.

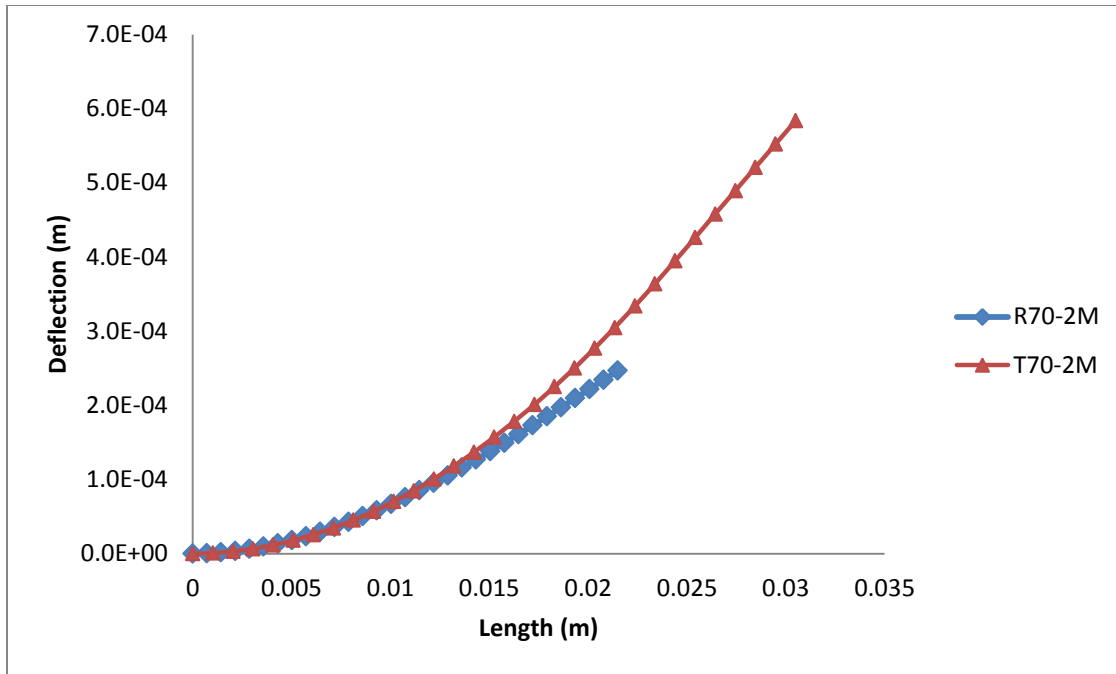


Figure 150: Deflection at resonance for R70-2M and T70-2M

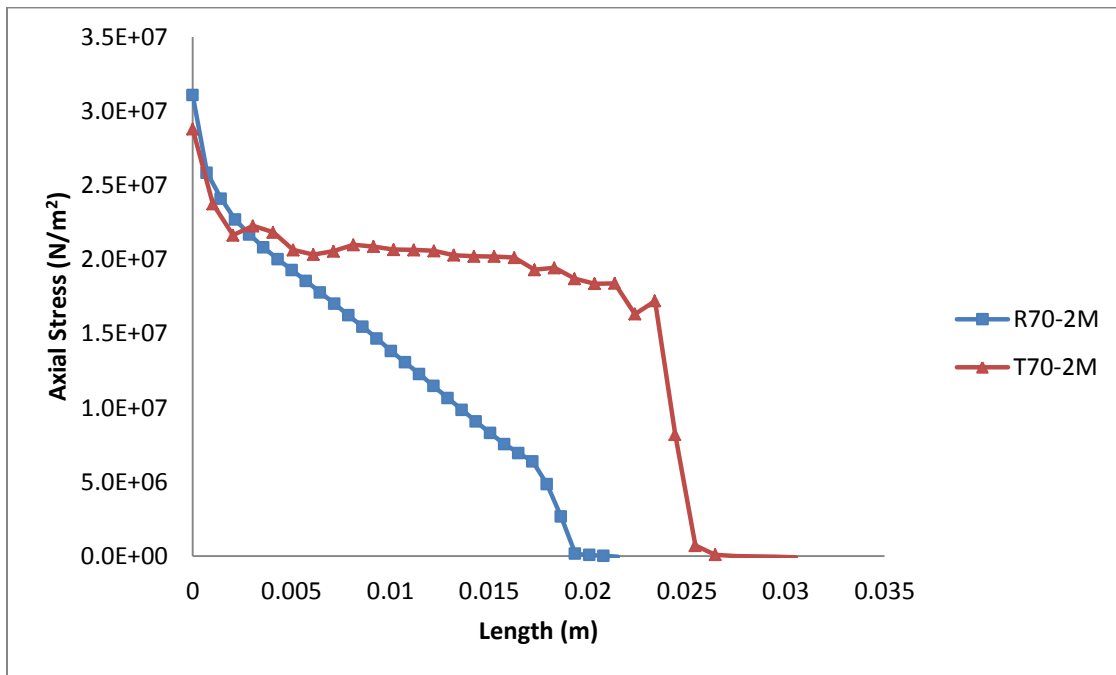


Figure 151: Axial stress along the mid-span length for R70-2M and T70-2M

The impedance analyzer measurements for the two devices are presented in Figure 152 and Figure 153. The results from these measurements indicate that the coupling in the case of the triangular sample, T70-2M is indeed larger, with a wider spread between the minimum and maximum impedance values. The impedance value at resonance for the two devices, although at different frequencies are close to each other. However, the impedance at anti-resonance for T70-2M occurs at greater than 3 Mega-Ohm, which is a very high number.

Table 22: Impedance – Phase Angle for 70 mm<sup>3</sup> devices with 4 grams proof mass

Sample	f <sub>r</sub> (Hz)	Z (Ohms)	f <sub>a</sub> (Hz)	Z  (Ohms)	Peak Phase°
R70-2M	86.8	24,392	90.9	1,650,976	65.8
T70-2M	67.8	27,326	72.4	3,373,502	69.02

The peak capacitance values, presented in Figure 154 and Figure 155 maintain the trend presented so far, that with the changing geometry, and same volume, the triangular device provide larger peak capacitance values. With the 4 gram proof mass, it can be seen in Table 23 that both peak values, i.e. the positive capacitance and negative capacitance are roughly doubled. This is quite an interesting find due to the fact that with unmatched resonance frequency, it was seen that the triangular device T70-2M had a larger maximum stress, which was in fact matching the stress of the rectangular cantilevered bimorph, R70-2M.

Table 23: Capacitance – Dissipation Factor for 70 mm<sup>3</sup> devices with 4 grams proof mass

Sample	Positive capacitance peak (nF)	Negative capacitance peak (nF)
R70-2M	45.76	-32.23
T70-2M	85.88	-73.26

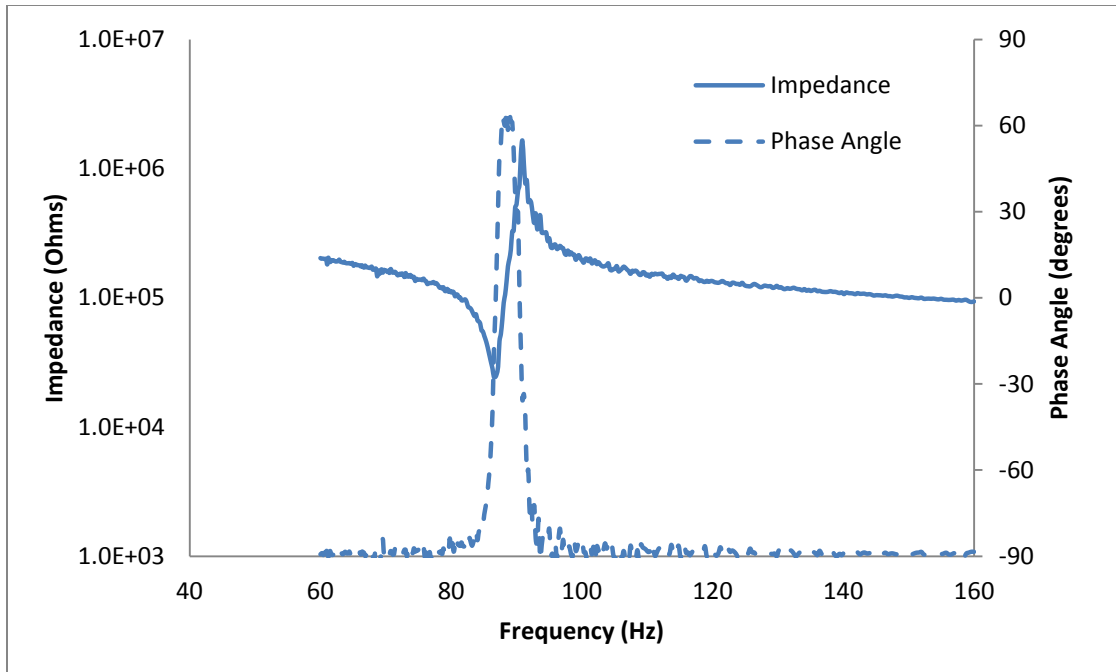


Figure 152: Impedance – Phase Angle for R70-2M

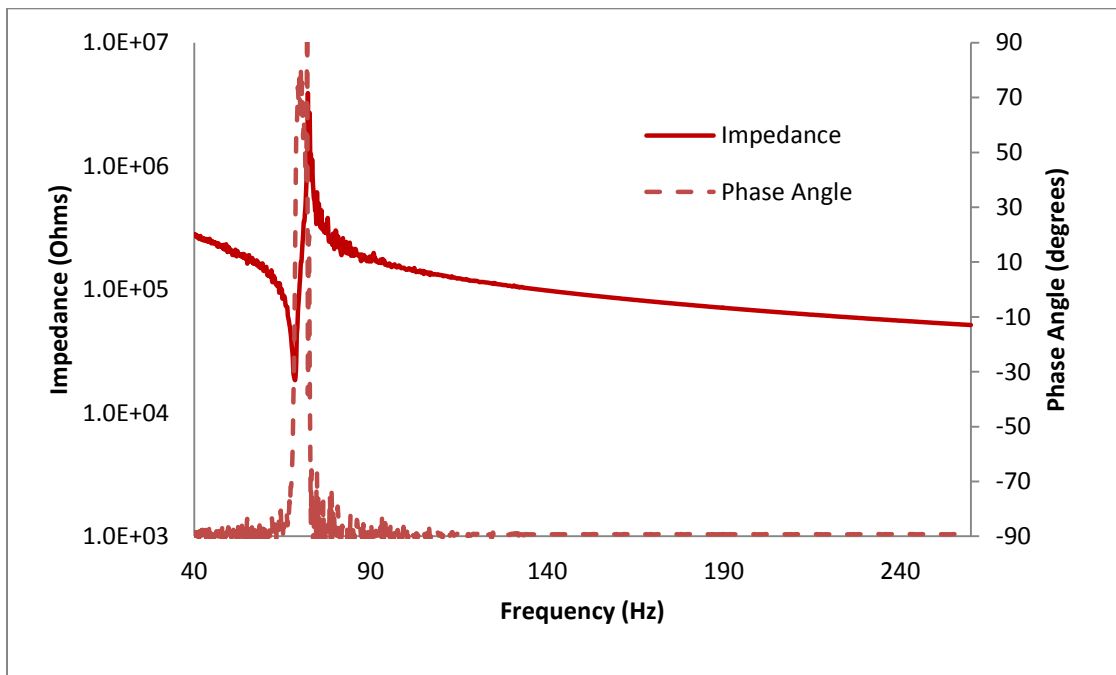


Figure 153: Impedance – Phase Angle for T70-2M

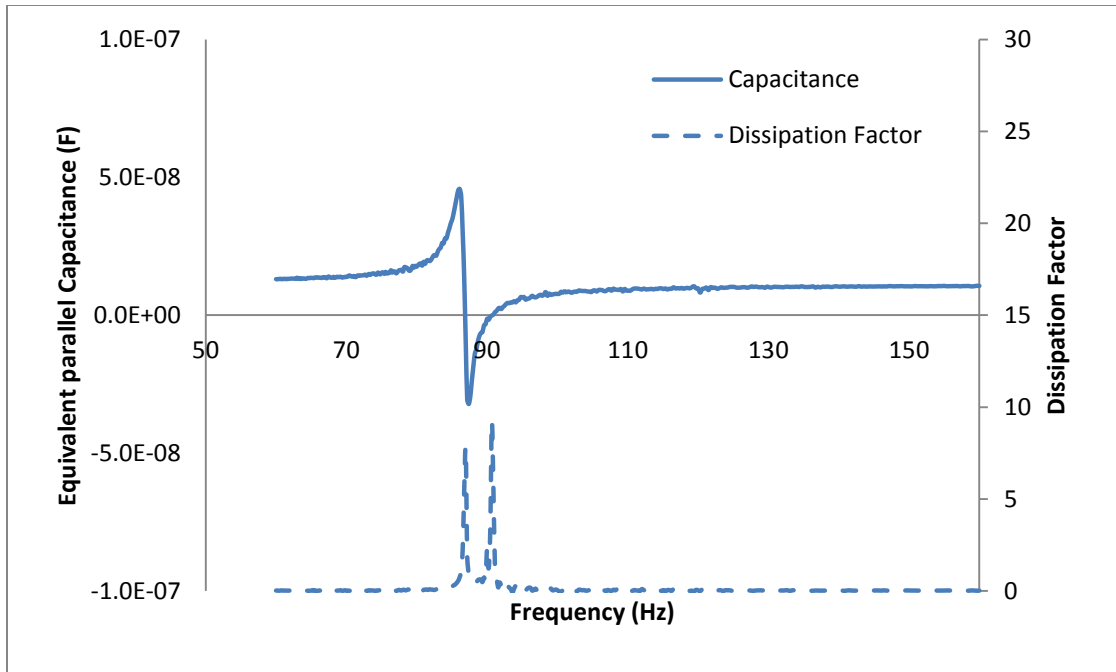


Figure 154: Capacitance – Dissipation Factor for T70-2M

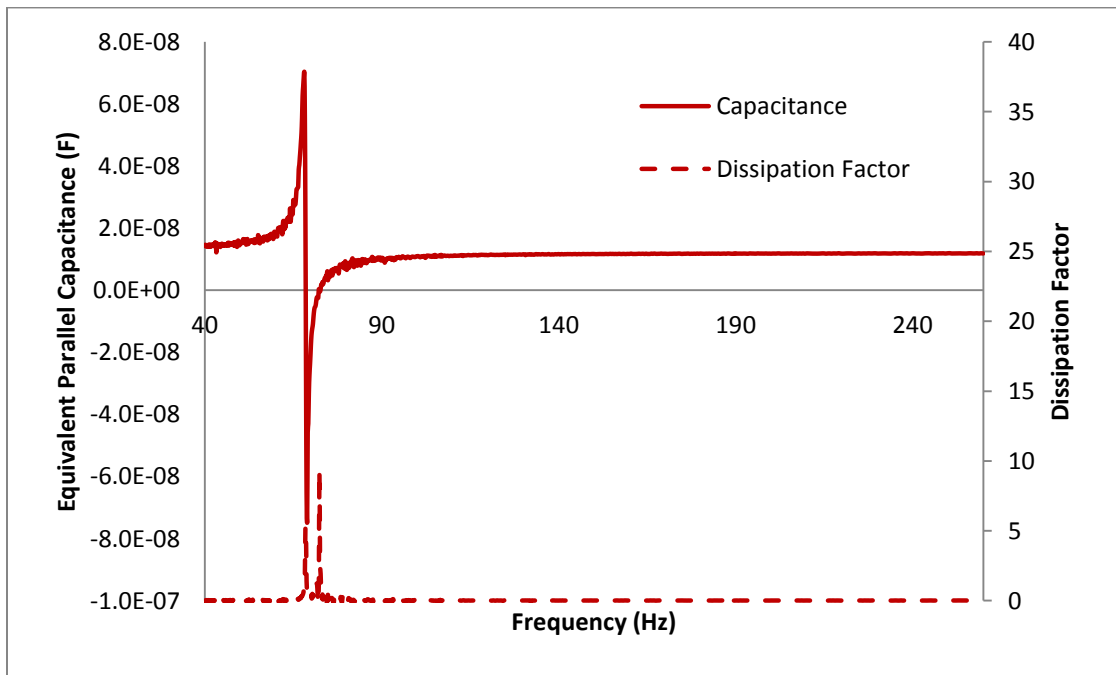


Figure 155: Capacitance – Dissipation factor for T70-2M

#### 5.4.2: Summary on 70 mm<sup>3</sup> devices as a function of proof mass

The first set of samples that were created, were the 70 mm<sup>3</sup> devices which were designed in a manner that the resonance frequency of the two devices matched. This resonance frequency matching was performed for the devices without any proof mass loading. Keeping the thickness and overall volume as constraints, the R70-0M device has an overhang length of 21.5 mm, width of 6.35 mm, and thickness of 0.51 mm. The T70-0M counterpart with the same resonance frequency and above mentioned constraints was found to be 30.5 mm in altitude, 8.95 mm in base width, and 0.51 mm thickness. As a nominal 2 gram proof mass was added, the resonance frequency for R70-1M was found to be 115 Hz. This resonance frequency on the triangular device was achieved by positioning the proof mass on the device, as T70-1M-P, which was effectively a pseudo trapezoidal shape. Addition of a further 2 grams of proof mass caused further divergence in the resonance frequency, as the device R70-2M resulted in a short circuit resonance frequency of 81 Hz, and the device T70-2M resulted in a short circuit resonance frequency of 64 Hz. Therefore, comparing the three sets of data as a function of proof mass loading falls does not allow proper comparison of the devices due to the dynamic nature of the problem, and drastic changes in tip deflections and power generated.

However, one of the most noticeable facts was the change in the behavior of the Power vs. load resistance curves for each of the three sets, which is related to the electromechanical coupling coefficient, damping, and more importantly the electromechanical coupling figure of merit,  $k^2Q$ . It was observed that with the addition of proof mass, the double peaks for optimal load resistance turned into a plateau when a 2 gram proof mass was added. As a subsequent proof mass was added for a total of 4 grams, the T70-2M sample showed a unique optimal load resistance as opposed to two optimal load resistance values. While the electromechanical coupling coefficient increased with increasing proof mass, as shown in Figure 156, the increase in the damping ratio, giving a small quality factor for the 4 gram samples causes the  $k^2Q$  figure of merit to decrease drastically (shown in Figure 158), which relates to the low electromechanical coupling regime, where only one optimal load resistance is found.

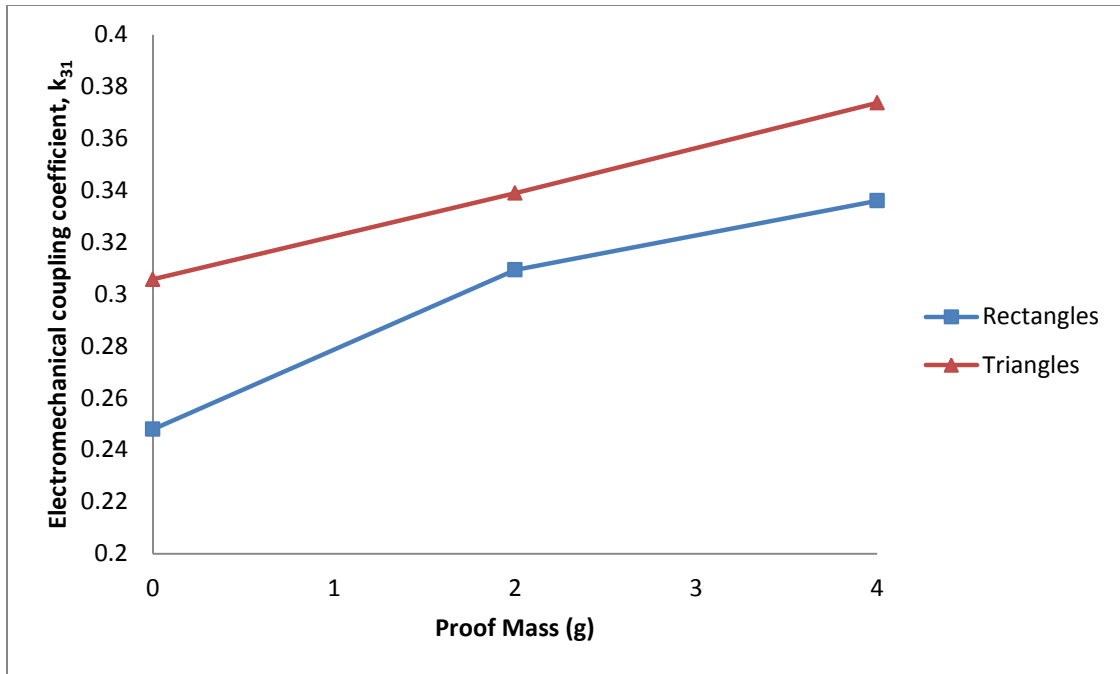


Figure 156: Electromechanical coupling coefficient for  $70 \text{ mm}^3$  devices as a function of proof mass

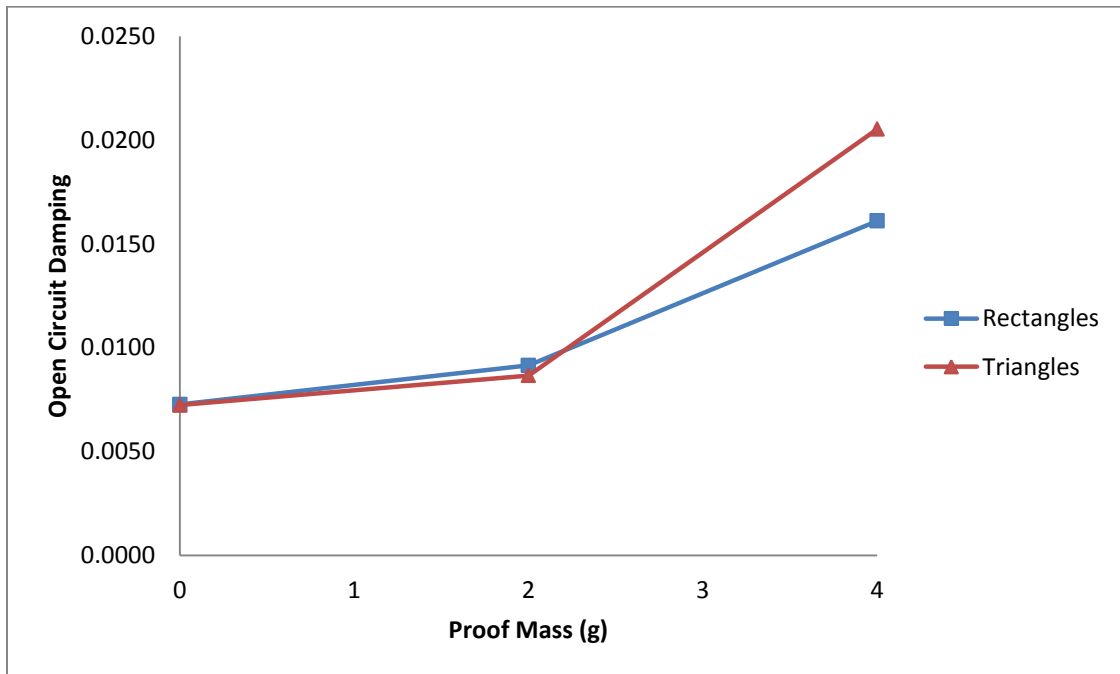


Figure 157: Open Circuit Damping Ratio for  $70 \text{ mm}^3$  devices as a function of proof mass

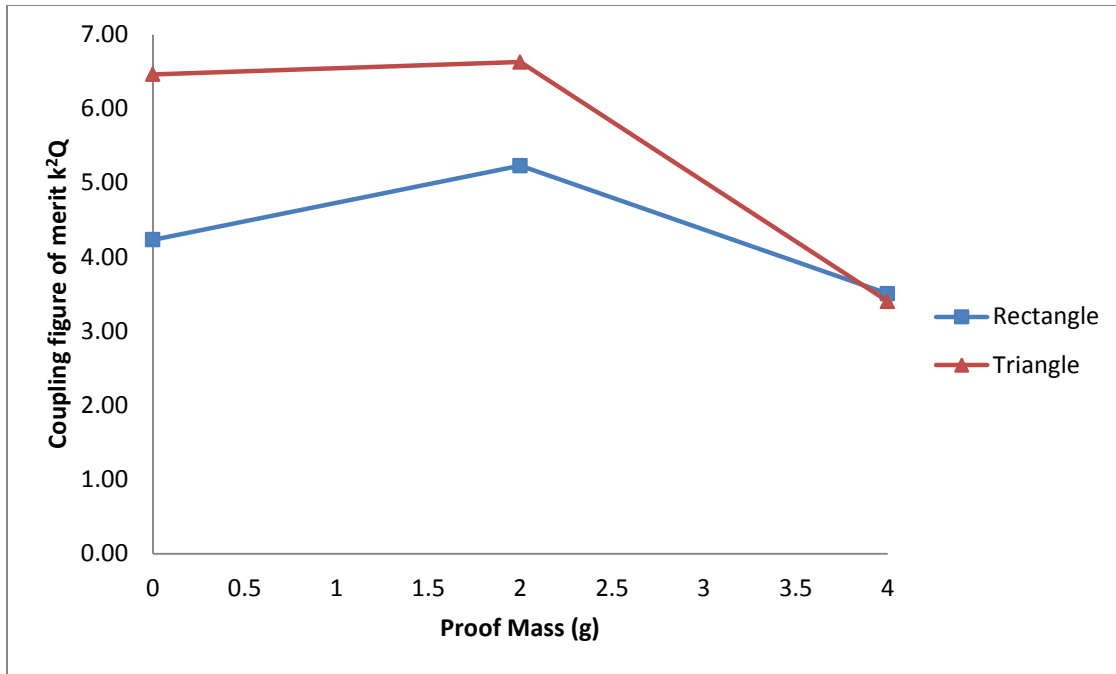


Figure 158: Electromechanical coupling figure of merit for 70 mm<sup>3</sup> devices as a function of proof mass

As it has been reported, the electromechanical coupling can also be determined using impedance spectroscopy, and its characteristics are indicative of the coupling in the system. The impedance measurements as a function of proof mass for the 70 mm<sup>3</sup> devices are consolidated in Figure 159 and Figure 160, which present the minimum and maximum impedance peaks respectively. With the addition of proof mass, the impedance values tend to increase, although there seems to be an anomaly in the case of the 4 gram rectangular device, where the impedance value seems to be decreasing, which could be due to noise in the measurements. It must again be emphasized here that the resonance frequencies between these devices do NOT match; hence it is difficult to quantitatively compare these. However, due to the fact that the impedance values were decreasing with increasing base width in the case of the no proof mass devices, which indicates that as the stiffness is increasing, and impedance is decreasing, the qualitative analogy can be extrapolated to expect that with increasing proof mass, the impedance values would increase. That seems to be the case in Figure 159, a little more convincingly, especially for the T70 sample. Also, the trend here is consistent that the minimum impedance peak for T70 is always lower than R70, and the maximum impedance peak for T70 is always higher than R70.

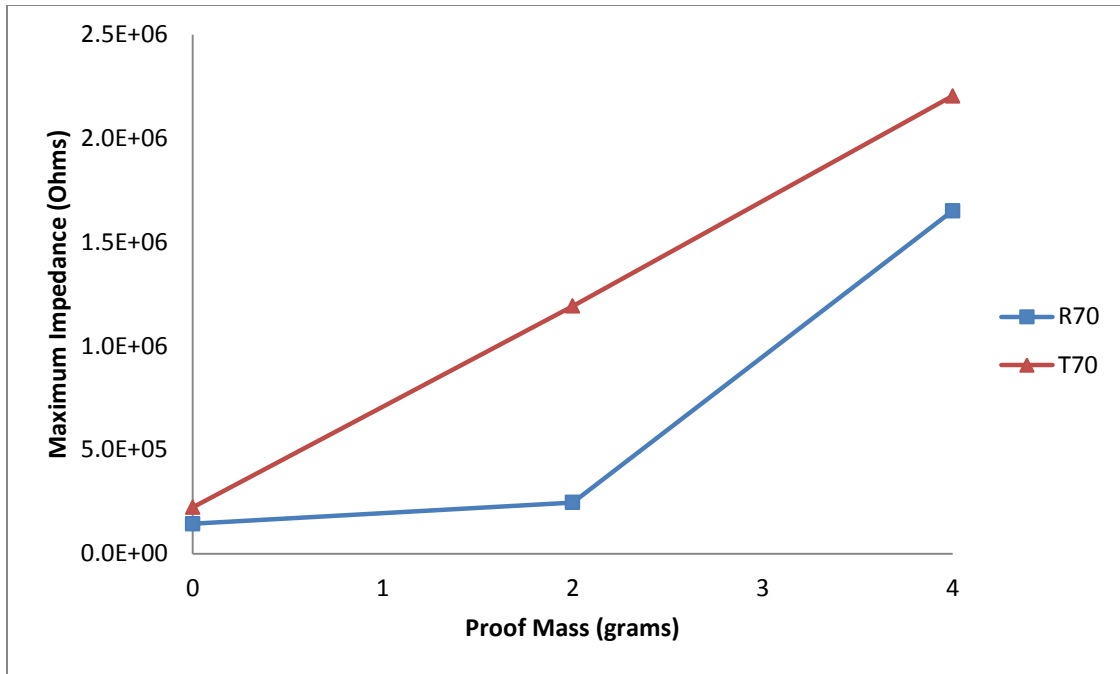


Figure 159: Minimum Impedance peaks for 70 mm<sup>3</sup> devices as a function of proof mass

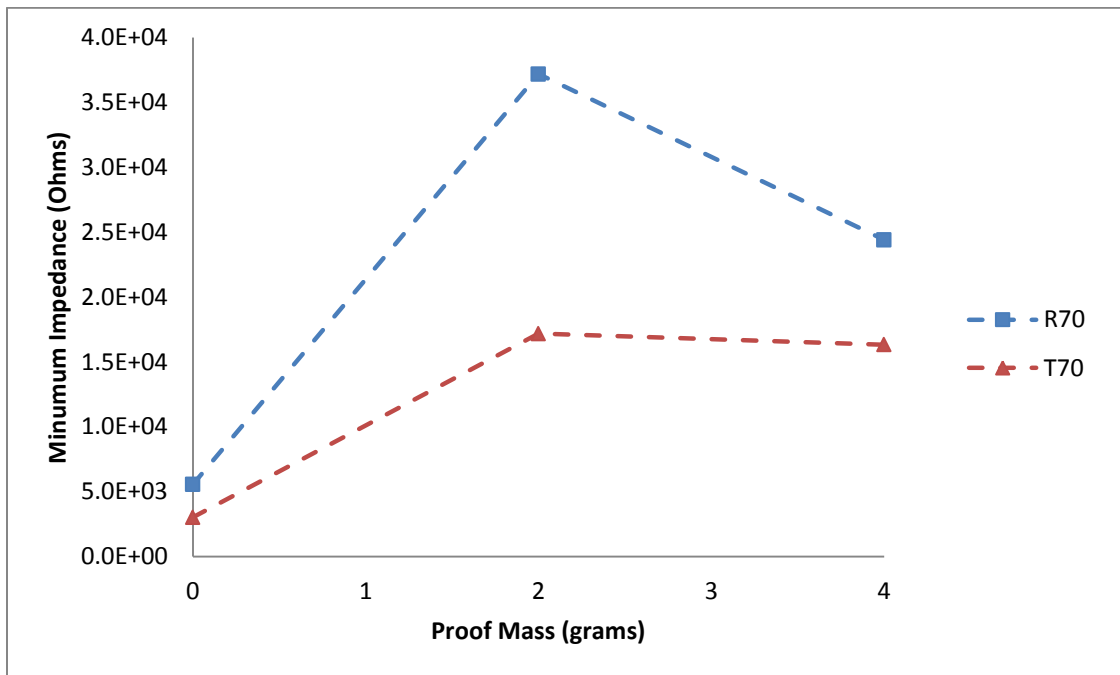


Figure 160: Maximum Impedance peaks for 70 mm<sup>3</sup> devices as a function of proof mass

In the case of the capacitance measurements for the 70 mm<sup>3</sup> devices, as shown in Figure 161, the positive peak measurements do not show much change as proof masses are added on. However, the negative capacitance peaks do seem to be decreasing more steadily (barring the unexpected R70-1M measurements). The negative capacitance peaks decrease more steadily than the increase in the positive peaks. Also, once again, the absolute value of the capacitance measurements are greater for the T70 than R70 in each case; clearly an indication of the advantage provided by the triangular device which enhances the distribution of strain. It is however again worth mentioning that the resonance frequency change with increasing proof mass is quite drastic. However, the triangular devices consistently outperform the rectangular counterparts for capacitance characteristics.

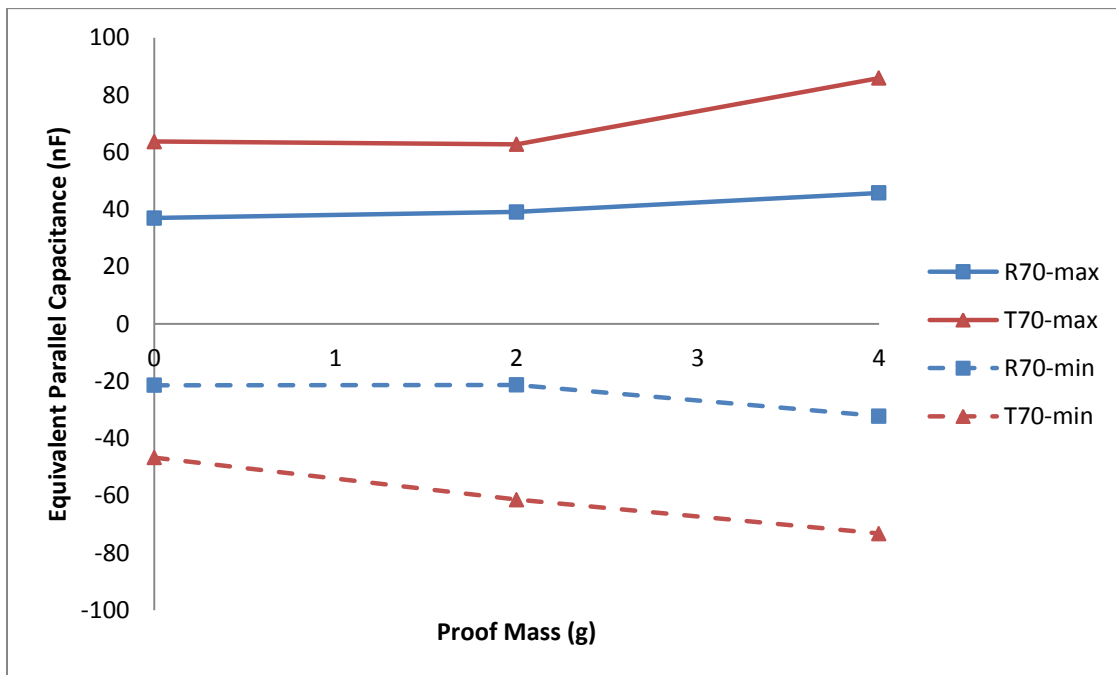


Figure 161: Capacitance measurements for 70 mm<sup>3</sup> devices as a function of proof mass

## **5.5: Comparison with Triangles with L=21.5 mm**

Section 5.2 showed that for each rectangular cantilevered bimorph there exists one triangular counterpart with matching resonance frequency, when the volume and thickness are constrained, and the topology is allowed to be altered. For rectangular cantilevers of length 21.5 mm, and varying widths, it was found that the resonance frequency of the devices roughly matched when the altitude for the isosceles triangles were maintained at 30.5 mm, and the clamping widths were allowed to vary to match the size. However, when a nominal proof mass is placed on the tip of the cantilevers, the frequencies of the two devices are difficult to match. In the case of the 70 mm<sup>3</sup> devices, resonance frequency matching was achieved by positioning of the proof mass, while in the other two cases, this scenario did not work.

In this section, another scenario for matching resonance frequency is presented. This comes from the hint provided by the mass positioned device, which gave an indication that the resonance frequencies of the two devices could match when the relative position of the mass on the device, independent of the shape is the same, especially when the mass of the tip is greater than the mass of the beam. Therefore, the devices presented here have the same length (or altitude for triangles), set at 21.5 mm, and the corresponding counterparts also have the same clamping widths. Hence, the two devices are compared with unequal volumes, i.e. the volume of the triangle is essentially truncated in half, as a cutout from the rectangular device.

It was shown in Chapter 4 that when two such devices are compared, the resonance frequency of the triangular device doubled from the rectangular sample, i.e. the resonance frequency of triangular devices with an altitude of 21.5 mm was over 1030 Hz, as compared to the rectangular counterpart with a resonance frequency of about 515 Hz. This behavior remarkably changes with the addition of a proof mass, as presented in the following two subsections.

### **5.5.1: R70-1M vs. T35-1M**

The first set of comparison presented is between R70-1M, and the resulting triangular cutout, which is T35-1M. The data presented for R70-1M here is repeated from section 5.4.1. A schematic of the two devices side-by-side is shown in Figure 162.

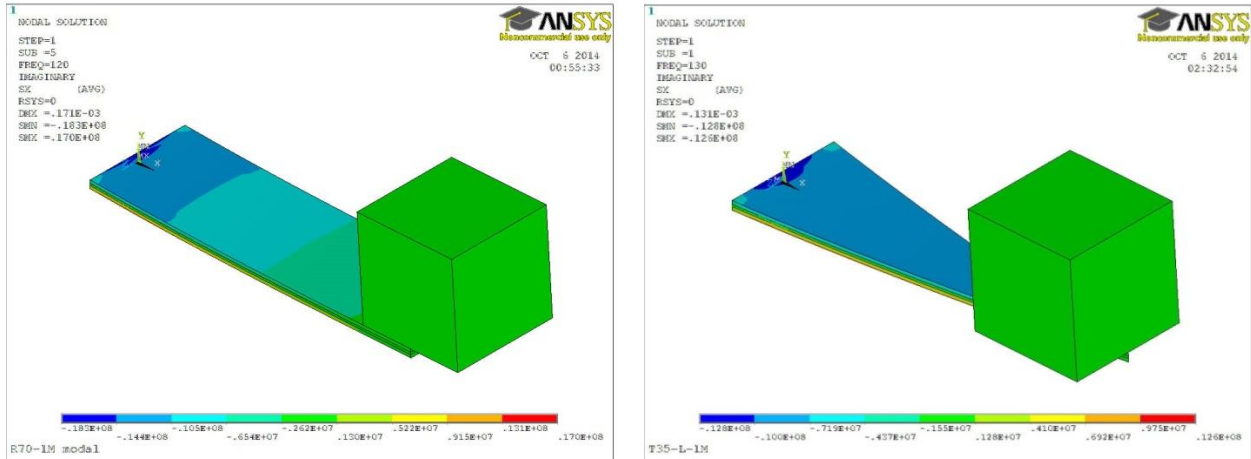


Figure 162: R70-1M and T35-1M

The two devices, T70-1M and T35-1M as shown in Figure 162 were prepared, and have resonance frequencies that are very close to each other indeed. R70-1M has a short circuit resonance frequency of 116 Hz, while the triangular counterpart with half the volume, i.e. T35-1M has a resonance frequency of 123 Hz. Therefore, there is a small difference from the target resonance frequency, of 115 Hz. However, this difference can be described due to the fact that there is no overhang length from the triangular cantilevered bimorph to the point where the force from the proof mass could be exactly resolved at the tip, as in the case of the rectangular bimorph. Physically placing the proof mass at the tip of the triangular device with a narrow angle was difficult, and made the mass unstable. Hence, the proof mass was placed such that the outer edge was flush with the tip of the bimorph. Therefore, the resonance frequency with the shorter effective length can be expected to be slightly higher, which happens to be the case.

The coupling behavior for the two devices, based on the resonance frequency as a function of load resistance can be seen in Figure 163 and Figure 164. So far, in every case the coupling has been greater in the case of the triangular device. However, the coupling coefficient for the two devices here is nearly identical: 0.3093 for R70-1M and 0.3122 for T70-1M. The difference between the short circuit and open circuit resonance frequency between the two devices is nearly identical, at 6 Hz for R70-1M, and 6.5 Hz for T35-1M.

It is quite remarkable that the resonance frequency of T35, without a proof mass is 1032 Hz (numerically), and drops down to 123 Hz with the 2 gram proof mass, while for R70, the drop to 116 Hz with a proof mass is from 515 Hz without one.

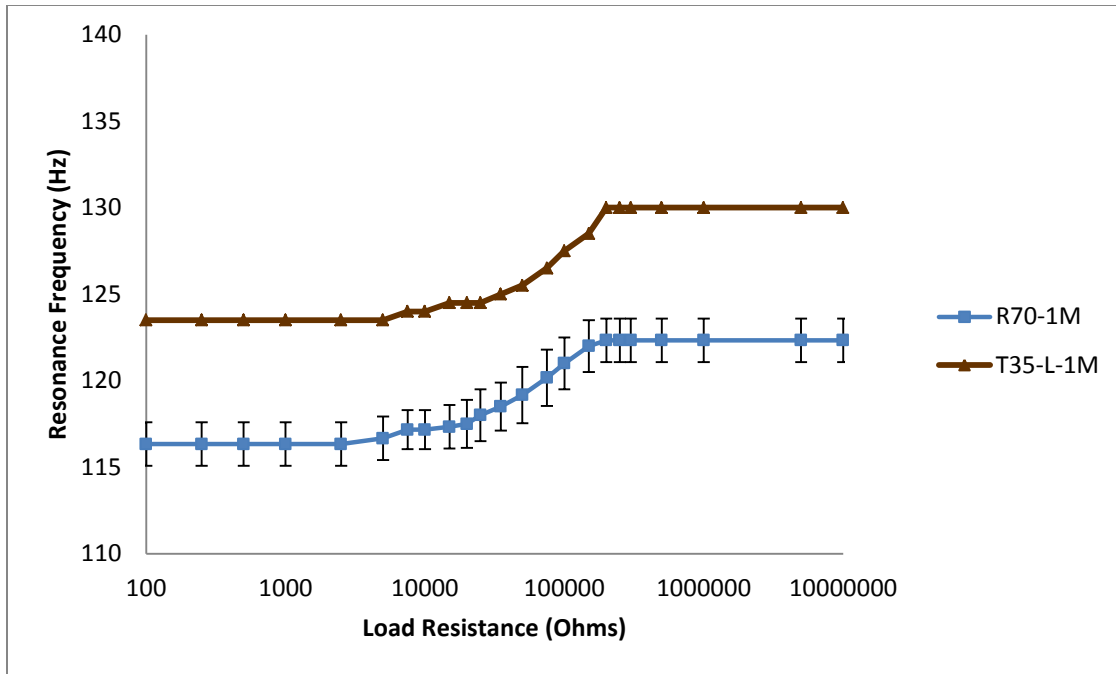


Figure 163: Resonance frequency for R70-1M and T35-1M as a function of load resistance

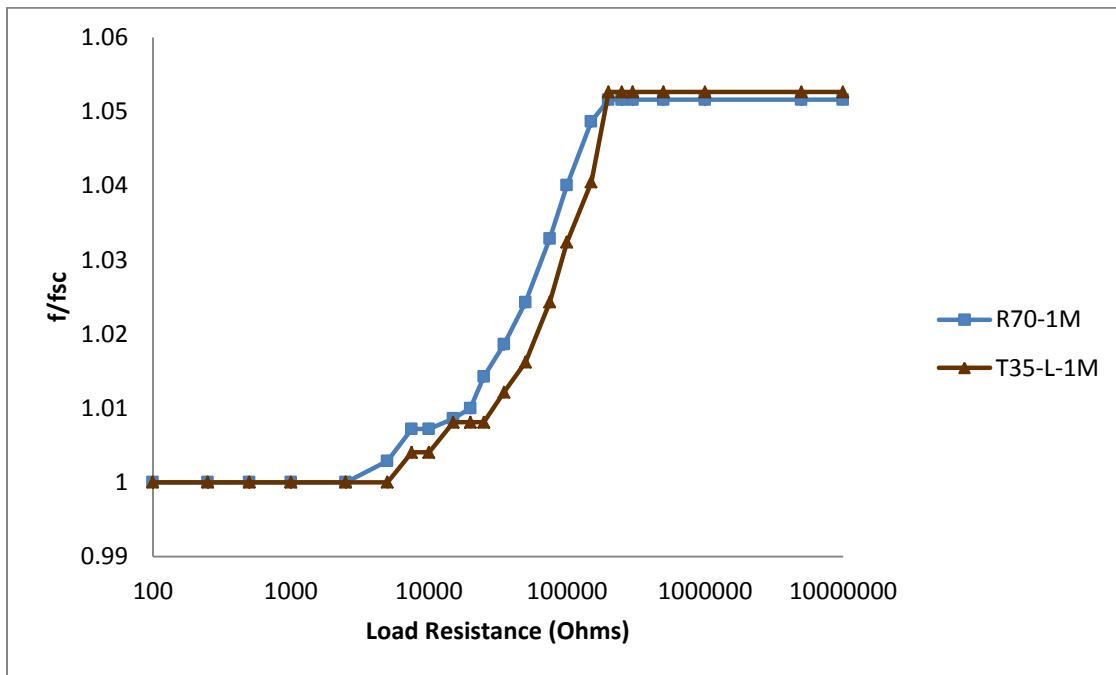


Figure 164: Short Circuit normalized Resonance frequency for R70-1M and T35-1M as a function of load resistance

The power generated by the two samples as a function of load resistance values is presented in Figure 165. It can be seen that the power generated by both samples do not two well-defined peaks, rather a plateau of about three or four measurements. Two maximum values for power are considered as the optimal load resistance values (hence impedance analysis is quite useful to determine the proper optimal load resistance). The power generated from R70-1M at 75,000 ohms and 200,000 ohms is about 55  $\mu\text{W}$ . In the case of R35-1M, the device with half the volume produces about 45  $\mu\text{W}$  into 200,000 and 250,000 ohm load resistors. Therefore, two major observations are apparent here. The first one is that the power generated by the device that has half the volume is only about 18-20% less than the device with twice the volume, implying that it could be in a greater amount of stress. The second observation is that the optimal load resistance, which relates to peak impedance values shifts to higher values.

Due to the fact that the power generated from these two devices is from unequal volumes, it is imperative to compare them from a power density point of view. However, the total device volumes are in fact quite close to each other, since the identical proof masses dominate these. The resulting volumes for R70-1M and T35-1M-L are 0.326  $\text{cm}^3$ , and 0.256  $\text{cm}^3$  respectively. The maximum power density from the rectangular device R70-1M is about 28 ( $\text{mW}/\text{g}^2$ )/ $\text{cm}^3$ , while for the triangular device is about 25( $\text{mW}/\text{g}^2$ )/ $\text{cm}^3$ ; which are quite close to each other. This is a remarkable feat, since the triangular device has half the active piezoelectric volume as compared to the rectangular device. Even though there are no apparent peaks for optimal load resistance in Figures Figure 165 and Figure 166, the T35-1M-L peak power is certainly shifting towards higher load resistance values. This indicates that the triangular device could have a similar maximum stress, which is presented following the discussion on coupling coefficients.

Table 24 summarizes the data in terms of the power generated at the optimal load resistance values, and the coupling coefficients. It can be seen that when the two devices with the same base width and proof mass are compared, the electromechanical coupling coefficients are found to be virtually identical. The triangular device shows substantially higher levels of damping, hence the electromechanical coupling figure of merit decreases substantially, which is 5.23, as compared to 3.14 for T35-1M-L. At this point, one of the comparisons that can be made between the two samples is the tip mass to beam mass ratio, which is 7.28 for T35-1M-L, which is twice as much as 3.64 for R70-1M. Hence, with half the piezoelectric material, and the same proof mass, the electromechanical coupling figure of merit is decreasing.

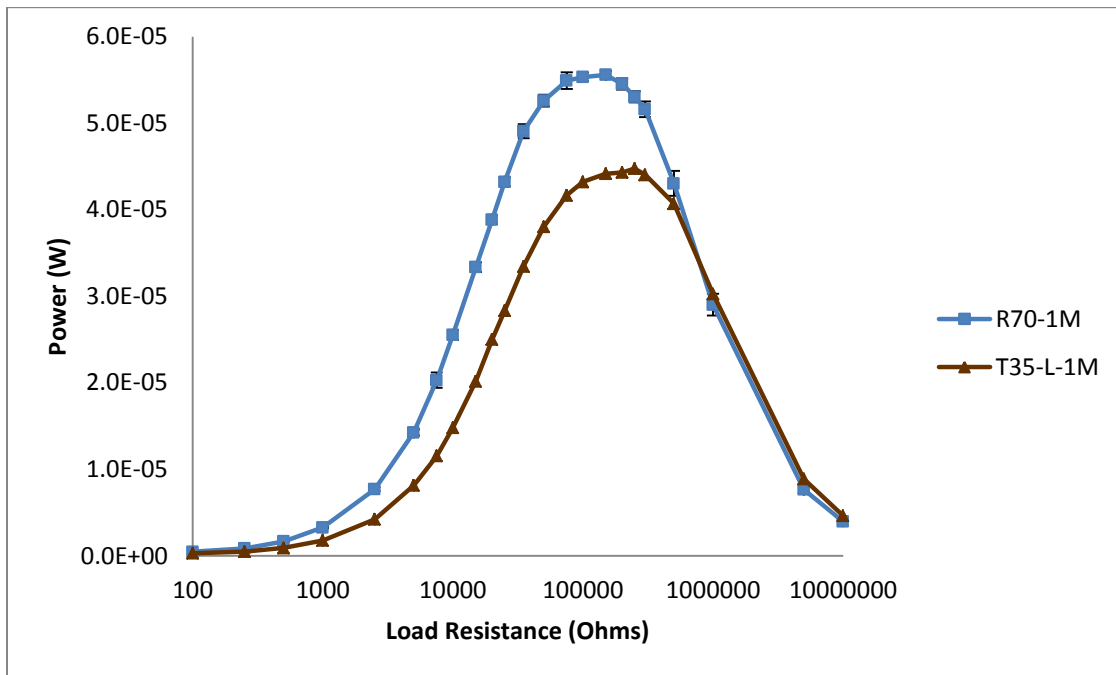


Figure 165: Power generated by R70-1M and T35-1M-L into various load resistors

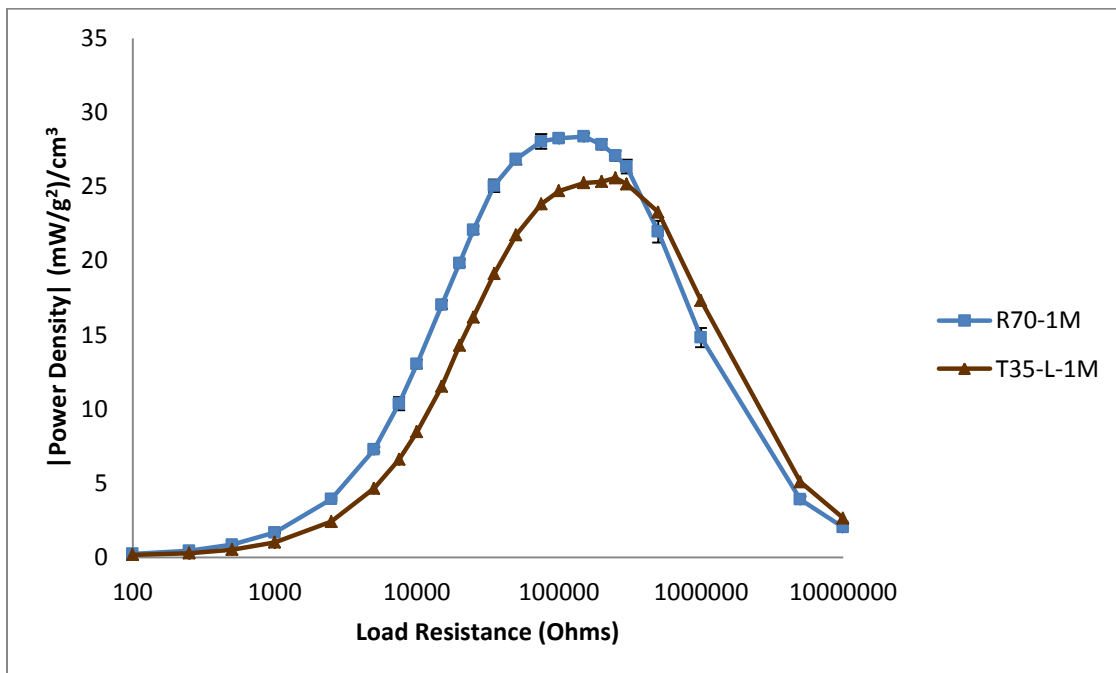


Figure 166: Power density for R70-1M and T35-1M into various load resistors

Table 24: Power generated by R70-1M and T35-1M at optimal load resistances

	$R_{opt,1}(\Omega)$	P ( $\mu$ W)	$R_{opt,2}(\Omega)$	P ( $\mu$ W)	$\zeta$	$k_{31}$	$k^2Q$
R70-1M	75,000	54.92	200,000	54.53	0.00914	0.3123	5.232
T35-1M-L	200,000	44.31	250,000	44.74	0.01553	0.3122	3.139

One of the most important comparisons between the two devices R70-1M and T35-1M is for the longitudinal tip deflection, and axial stresses at resonance, which are shown in Figure 167. The two devices, with the same overall length, and almost the same tip mass position show relatively similar deflections, although slightly lower for T35-1M, which has a much more constant radius of curvature. The deflection of the T70-1M sample is provided for reference purposes, and it can be seen that the deflections overlap by a high degree. The maximum deflection at the tip for rectangular device, R70-1M is 131  $\mu$ m, while for the 21.5 mm long triangular device is 118  $\mu$ m. These two maximum deflections are not too far apart, hence this proves that it is very important to compare devices with matching resonance frequencies.

The stresses generated by the two devices are shown in Figure 168. From the results obtained as shown in Figure 166, intuitively it was expected that the maximum stress in the triangular device, T35-1M would be very close to T70-1M, due to the similar amounts of power generated from a device with half the volume. However, the stress analysis in Figure 168 shows that the maximum stress at the base is still much lower than R70-1M, and in fact very slightly higher than T70-1M. While this result is somewhat unexpected, it gives a marked advantage for using triangular samples with the same length (altitude) and proof masses due to the fact that these devices are operating at lower levels of maximum stress, thus providing reliable operation. While the optimal load resistance values have increased in the case of T35-1M, the maximum stress does not.

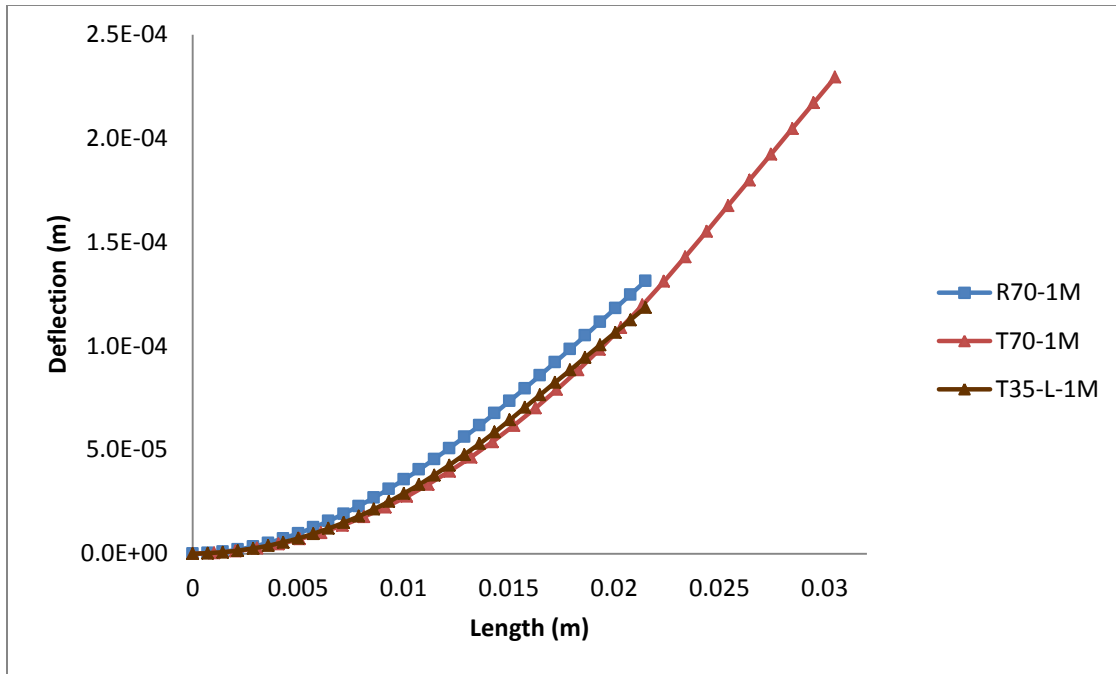


Figure 167: Longitudinal deflection along the mid-span for R70-1M and T35-1M-L

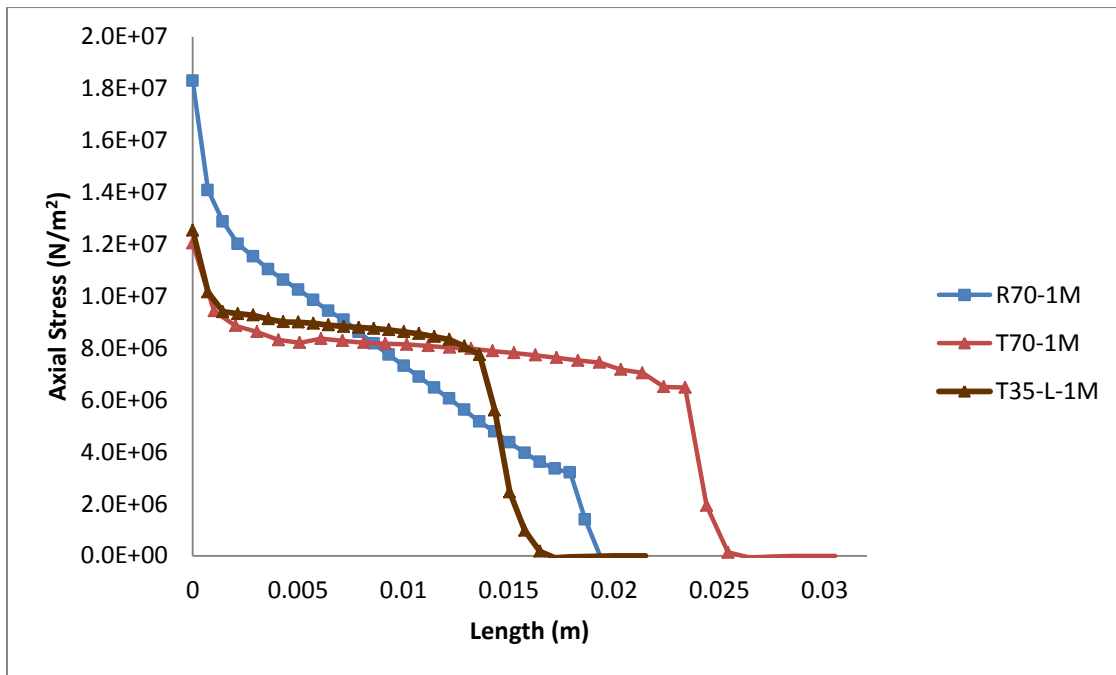


Figure 168: Axial Stress over the midspan for R70-1M and T35-1M

The discussion on Figure 165 and Figure 166 mentioned the absence of distinct optimal load resistance values for power generation. However, the impedance analyzer measurements

can shed more light on these, as they have in previous sections. The impedance analyzer measurements, as presented in Table 25 and Figure 169 for R70-1M as previously mentioned show minimum impedance of 37,172 ohms and maximum impedance of 246,245 ohms. While the minimum impedance does not match very well with the first reported optimal load resistance of 75,000 ohms, the maximum impedance is relatively close to the reported 200,000 ohms, as the power generated at the next measured load resistance of 250,000 ohms is quite similar at 53  $\mu$ W, compared to 54.5  $\mu$ W in Figure 165. In case of the triangular bimorph, T35-1M-L, the optimal load resistance values reported are 200,000 and 250,000 ohms. These values are far off from the impedance analyzer measurements in Figure 170. While the external load resistor may not have captured the optimal load resistance values based on peak power, since measurements at these values of load resistance were not made, the impedance measurements do provide useful data in terms of providing peak values for impedance matching. However, it is important to note that with increased proof mass to beam mass ratios, the impedance peaks are substantially increased.

Table 25: Impedance measurements for T70-1M and T35-1M

Sample	$f_r$ (Hz)	Z (Ohms)	$f_a$ (Hz)	Z  (Ohms)	Peak Phase $^\circ$
R70-1M	120	37,172	130.2	246,245	18.3
T35-1M-L	129	41,439	139	850,758	45

The capacitance measurements for the two devices under discussion are presented in Table 26, and Figure 171 and Figure 172. Here, the capacitance measurements for the T35-1M-L sample are roughly half as that of the rectangular R70-1M sample, clearly showing the dominance of the size dependency of capacitance measurements. It also becomes difficult to compare these with different tip mass to beam mass ratios, where there was an apparent dependency in the 4 gram proof mass study on 70 mm<sup>3</sup> devices.

Table 26: Capacitance peaks for R70-1M and T35-1M-L

Sample	Positive capacitance peak (nF)	Negative capacitance peak (nF)
R70-1M	39.1	-21.31
T35-1M-L	21.99	-8.6

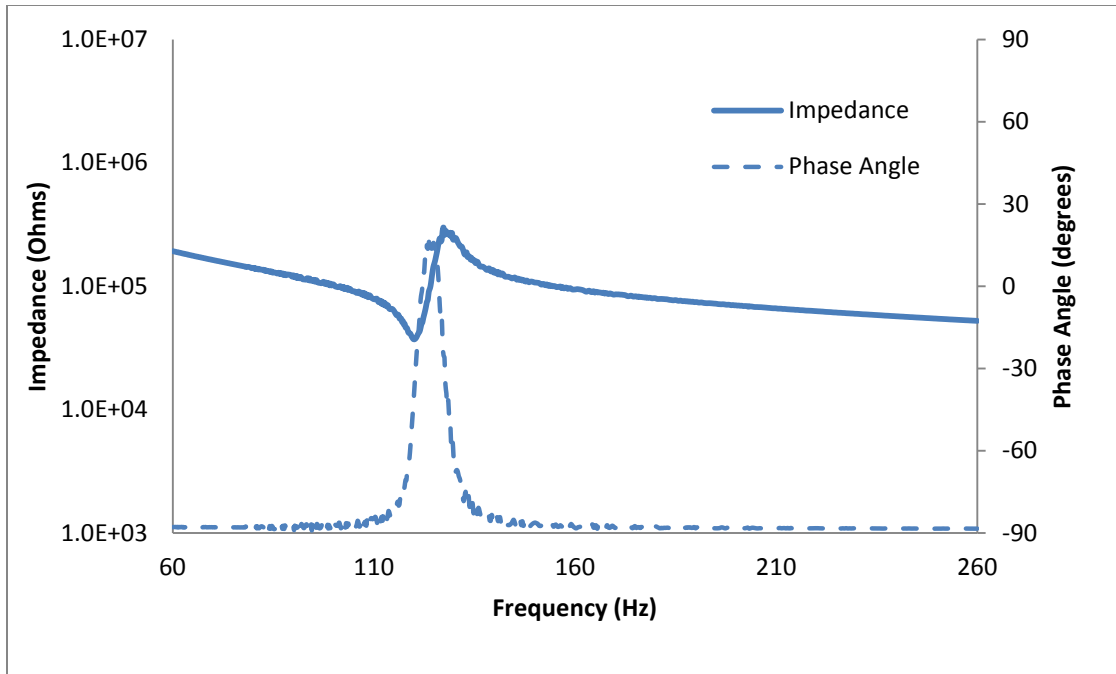


Figure 169: Impedance – Phase Angle for R70-1M (same as Figure 111)

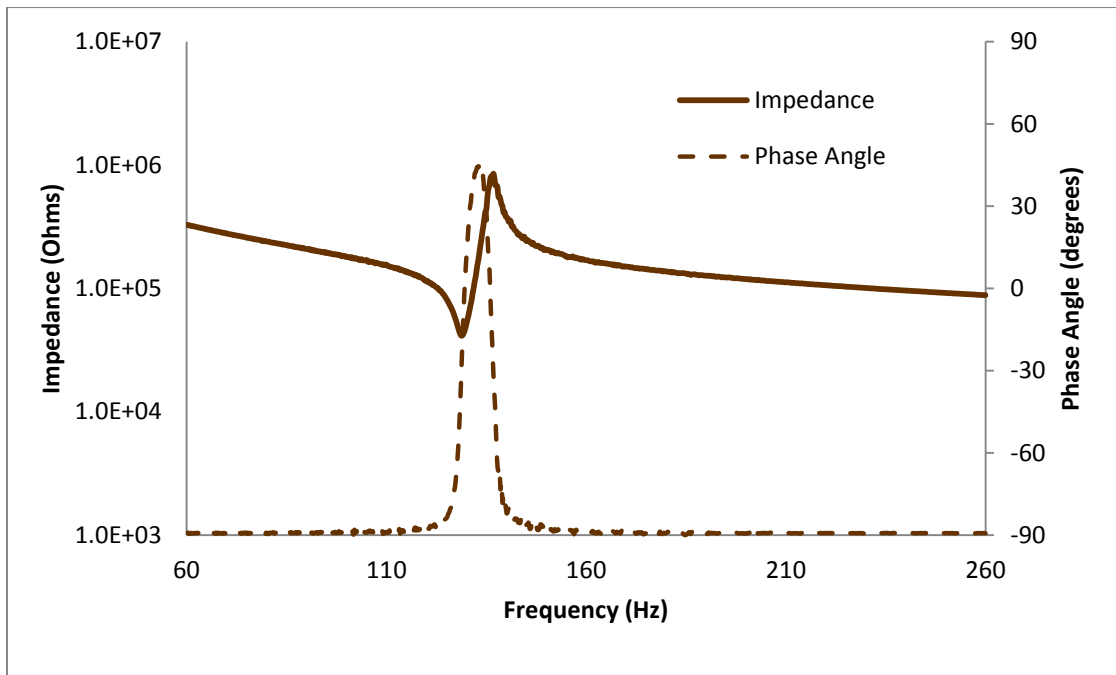


Figure 170: Impedance – Phase Angle for T35-1M-L

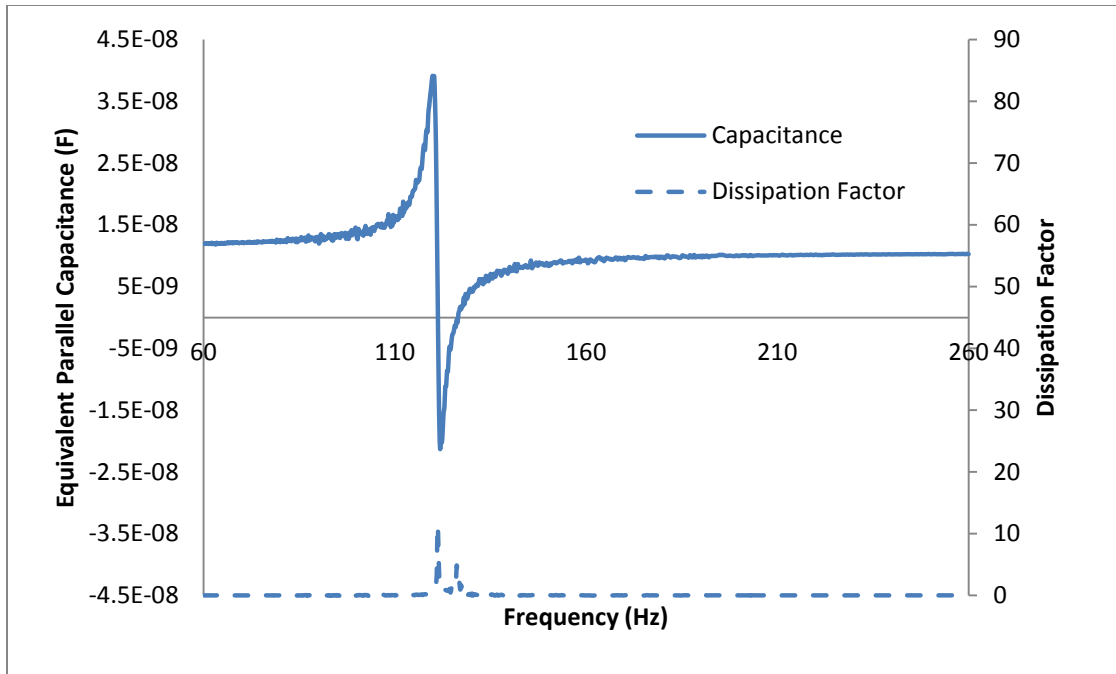


Figure 171: Capacitance – Dissipation Factor for R70-1M (same as Figure 114)

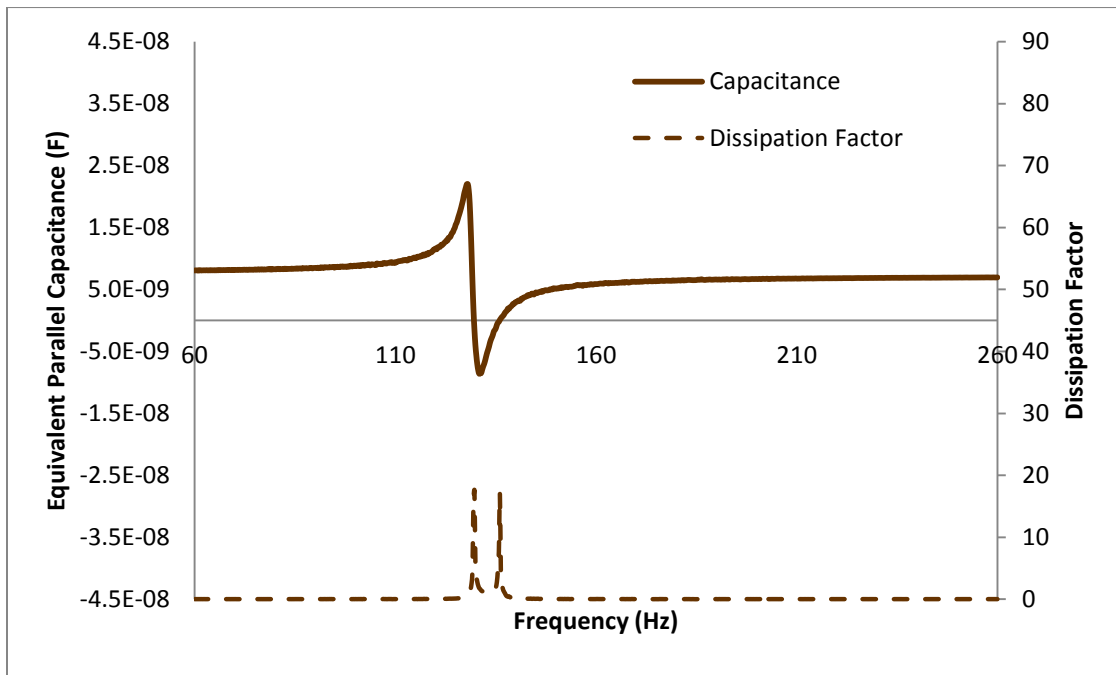


Figure 172: Capacitance – Dissipation factor for T35-1M-L

### 5.5.2: R140-1M vs. T70-1M

The next set of samples that is tested is a comparison of R140-1M which provided a short circuit resonance frequency of 159 Hz. The triangular counterpart to this sample originally was T140-1M, which had an altitude of 30.5 mm, and maintained a resonance frequency of about 115 Hz. Due to this large discrepancy, these two shapes did not provide viable comparisons. Hence the triangle being tested now is T70-1M-L, which is a triangular cut-out from the rectangular counterpart, with half the volume and the same length (21.5 mm), and same clamping width at the base (12.7 mm). Schematics of these samples are provided in Figure 173.

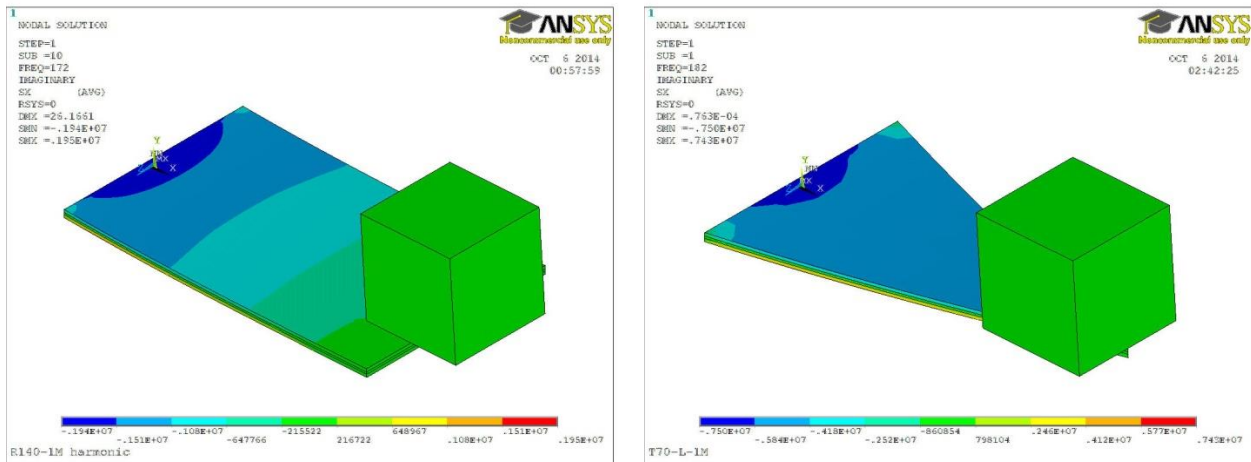


Figure 173: Schematic for T140-1M and T70-1M-L

As anticipated, with the matching dimensions of the two devices in terms of length/altitude, clamping width, and identical proof masses, the resonance frequencies of the two devices are found to be very similar to each other. While the resonance frequency of the T70-0M-L (in Chapter 4) device was twice as much as that of R70-0M, it is quite remarkable that these match with each other, as shown in Figure 174. The short circuit resonance frequency for T70-1M-L is found to be 162 Hz, which is much more comparable to R140-1M. This phenomena goes on to give an indication that the resonance frequency, which is directly proportional to the stiffness of the material, is dominated by the stiffness at the base in the case of cantilevers, provided the tip mass to beam ratio is large.

Figures 174 and 175 show that the electromechanical coupling coefficient in the case of the case of these two devices are quite similar to each other; where the  $k_{31}$  T70-1M-L is 0.34, and 0.32 for R140-1M. This is in trend with the previous section, where the triangular device with identical base width and altitude as its rectangular counterpart, but half the bimorph volume

provides similar electromechanical coupling coefficients. Therefore the tip mass to beam mass ratio in the triangular device is again doubled (3.64 for T70-1M-L; 1.82 for R140-1M).

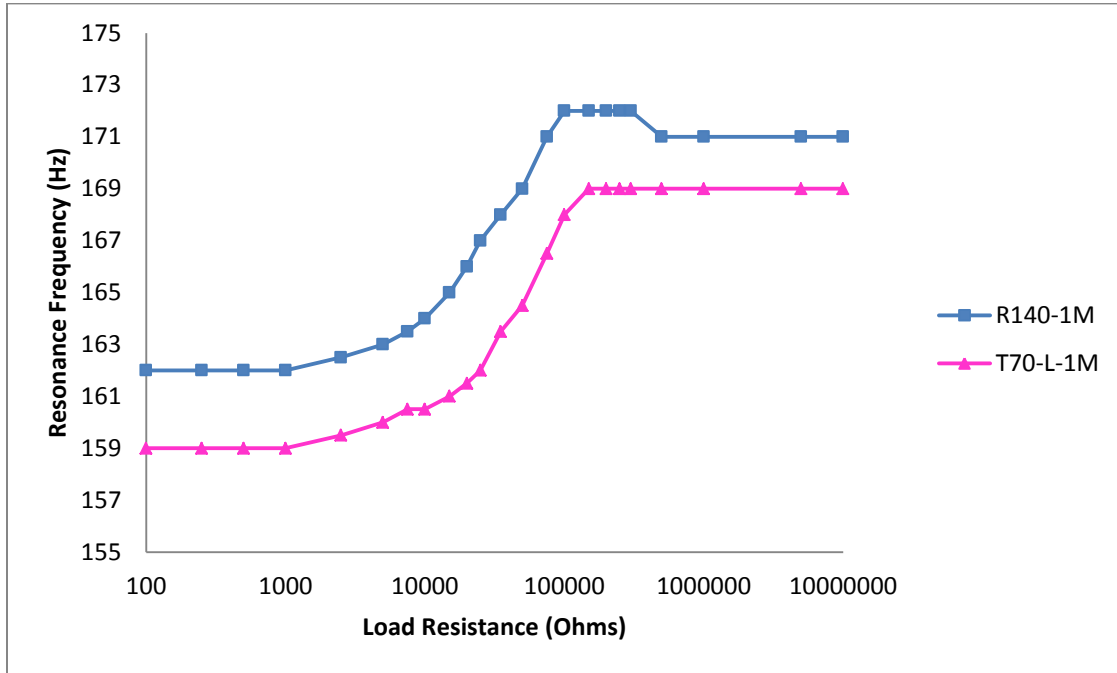


Figure 174: Resonance frequency vs. load resistance for R140-1M and T70-1M-L

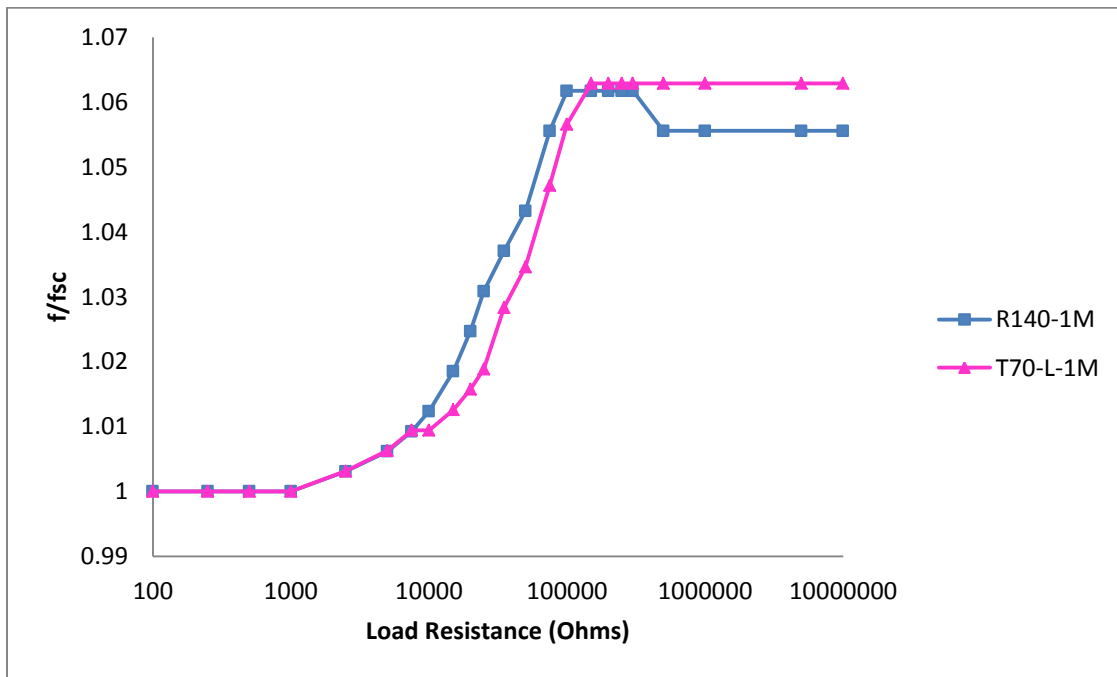


Figure 175: Short circuit normalized Resonance frequency vs. load resistance for R140-1M and T70-1M-L

The power generated by the two devices as a function of load resistance is shown in Figure 175. In this set of data, it can be seen that with the increased electromechanical coupling coefficients, and increased figure of merits, as presented in Table 27, two optimal load resistance occur. The maximum power generated by R140-1M occurs at optimal load resistance values of 15,000 and 200,000 ohms, about 88  $\mu$ W for both values. For the triangular cantilever, T70-1M-L, these values are observed to be 35,000 and 200,000 ohms, and the power in both these cases is also similar, to be about 55  $\mu$ W. Therefore, while the rectangular sample seems to provide a larger spread in terms of optimal load resistance values, the exact values for impedance matching are to be determined from impedance spectroscopy. The damping ratios for both these devices are also quite similar; hence the calculated  $k^2Q$  value for the triangular device is larger.

It is also once again important to observe the power density of the two devices due to the mismatch in volumes. The device volume for the 70 mm<sup>3</sup> triangle with the 2 gram proof mass is 0.326 cm<sup>3</sup>, and the 140 mm<sup>3</sup> rectangle is 0.395 cm<sup>3</sup>; hence both of these are quite close to each other. However, with the triangular device having half of the active volume, the power density between the two devices is quite similar. This is similar to the previous case, where the T35-1M-L and R70-1M samples were compared. The observation for the shift in the optimal load resistance for the triangular sample, under similar anticipated maximum stress is also observed, which is now a consistent trend. The deflection and stress analyses are presented in Figures 178 and 179.

Table 27: Power at optimal load resistance for R140-1M and T70-1M

	$R_{opt,1}(\Omega)$	P ( $\mu$ W)	$R_{opt,2}(\Omega)$	P ( $\mu$ W)	$\zeta$	$k_{31}$	$k^2Q$
R140-1M	15,000	88.34	200,000	88.75	0.00962	0.32	5.33
T70-1M-L	35,000	53.21	200,000	57.36	0.00923	0.34	6.22

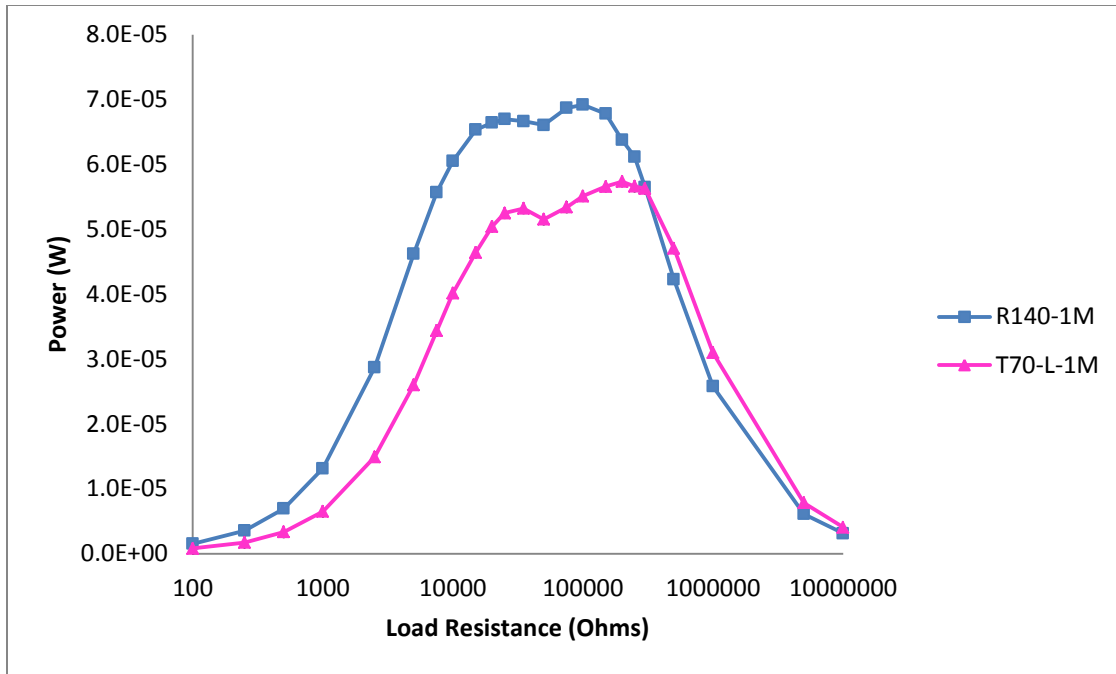


Figure 176: Power generated by R140-1M and T70-1M-L as a function of load resistance

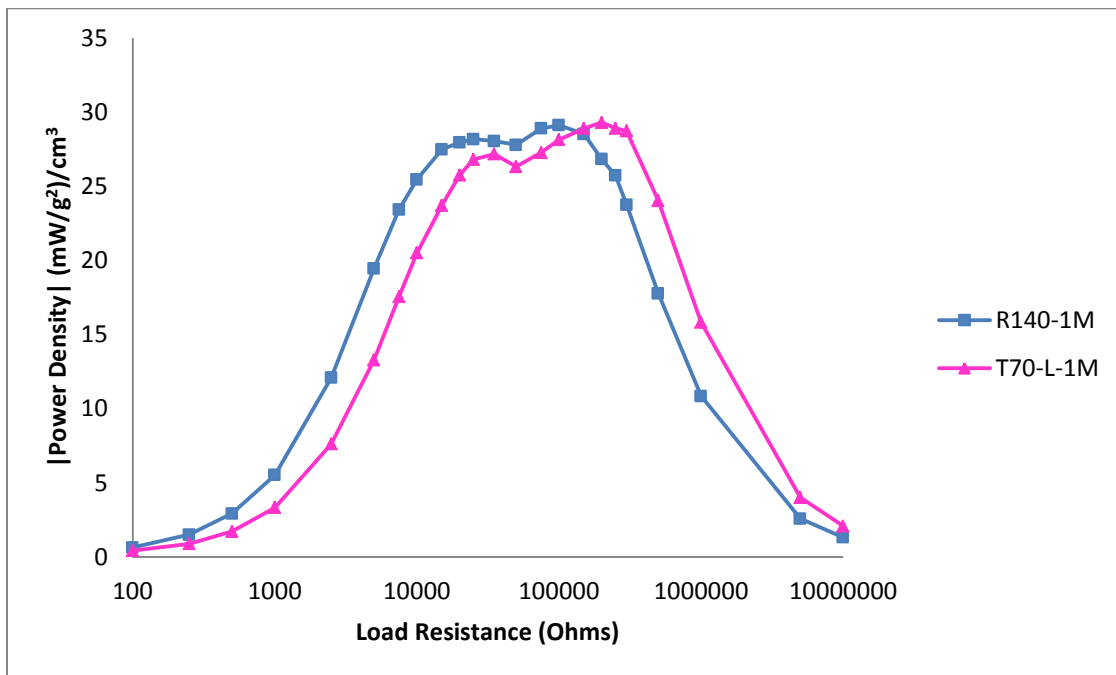


Figure 177: Power density for R140-1M and T70-1M-L as a function of load resistance

Figure 178, shows that the two devices operating at the same resonance frequency, and similar parameters result in the same deflection at the tip. The radius of curvature being more

pronounced is more apparent in the case of the triangular device. Overall, the deflection for the two devices is found to be about 69  $\mu\text{m}$ , expectedly lower than the devices presented in the previous case (R70-1M and T35-1M-L) due to the increased size. However, this deflection analysis emphasizes the importance of matching resonance frequency to compare the behavior of two structures for power generation. This is in spite of unequal volumes between the two devices, which can be normalized for power density, as shown.

In terms of the axial stresses generated in the two devices, even though the triangular device, T70-1M-L has half the bimorph volume, the maximum stress at the clamped end is still lower than the axial stress in R140-1M. The maximum stress for the rectangular device, R140-1M is found to be about 8.96 MPa, while the triangular device with half the volume has a maximum stress of 7.18 MPa. Both of these devices are resonating at about 160 Hz. Therefore, this shows that the triangular device, with its enhanced loading capacity is able to operate more reliably from a mechanical standpoint. Impedance characteristics are however affected, as observed in the power plots, and more clearly described using impedance spectroscopy results presented next.

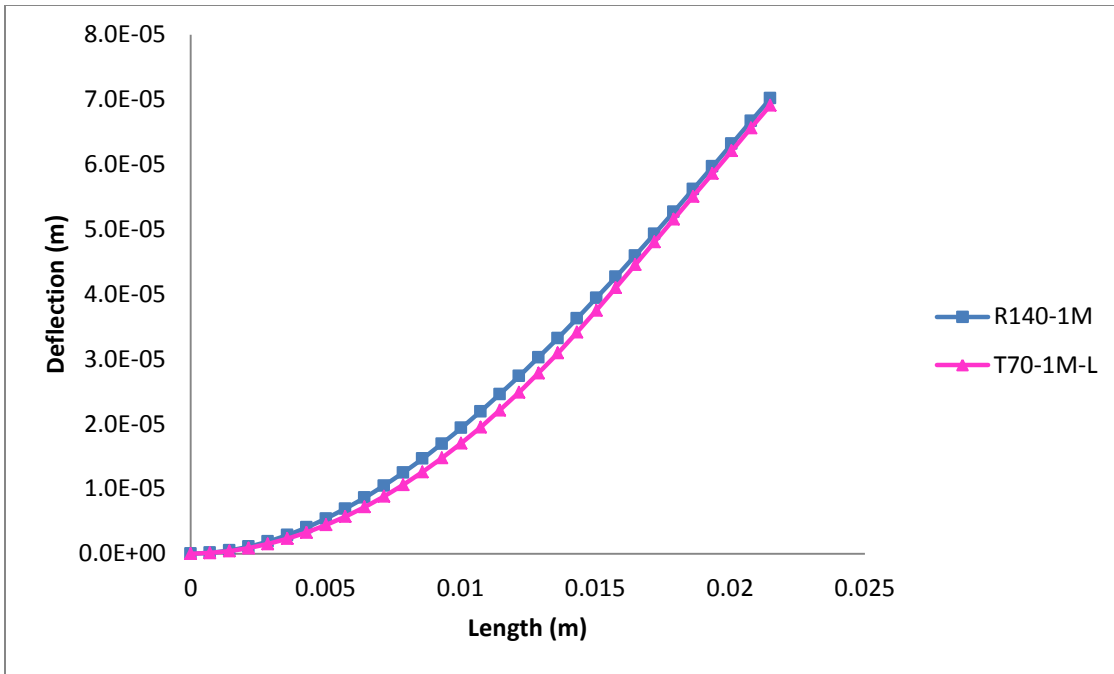


Figure 178: Longitudinal Deflection for R140-1M and T70-1M-L at resonance

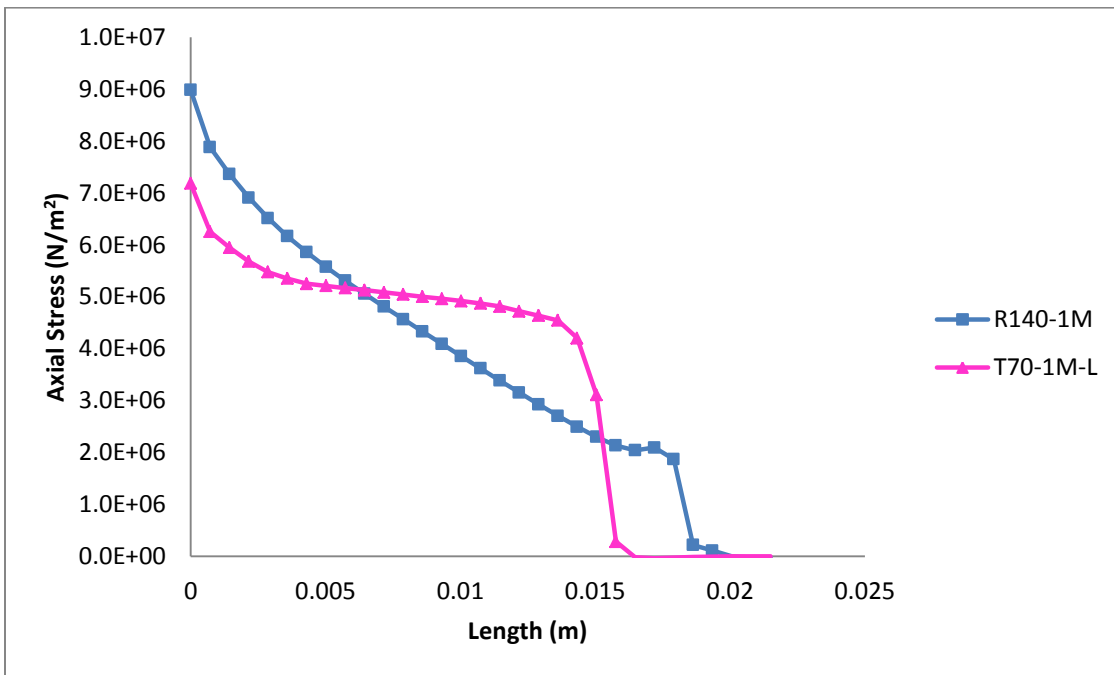


Figure 179: Axial Stress along the mid-span for R140-1M and T70-1M-L

The impedance analysis, which takes us back to the discussion of electromechanical coupling in the system, is presented in Figure 180 and Figure 181, and summarized in Table 28. The results here give a more accurate representation of the minimum and maximum impedance, which relate to the optimal load resistance. Here, it can be seen that as the two devices with unequal volumes are compared, the minimum impedance, which is found to be 9833 ohms R140-1M, is lower than 15,820 ohms for T70-1M. The maximum impedance, i.e. the impedance at the anti-resonance frequency is in much lower, in fact roughly half with a value of 227,071 ohms for R140-1M, as compared to 519,497 ohms for T70-1M-L. The larger spread between the maximum and minimum impedance, although similar difference between the resonance and anti-resonance frequency is an indication of higher coupling. However, the main parameter that is different between the two devices is the volume, and hence the resulting stress over the device.

Table 28: Impedance Analysis for R140-1M and T70-1M-L

Sample	$f_r$ (Hz)	Z (Ohms)	$f_a$ (Hz)	$ Z $ (Ohms)	Peak Phase <sup>o</sup>
R140-1M	168.1	9833	178.7	227,071	45
T70-1M-L	166	15,820	177	519,497	55

The capacitance of the two devices, presented in the Figure 182 and Figure 183 show a similar trend to the previous section again. The positive peak capacitance value for the triangular device is smaller, but not half of the rectangular device with half the volume. In fact, in the case of the negative capacitance peaks, the capacitance values in fact fall within 9 nF of each other. It is again difficult to compare these results with the previous set, due to changing resonance frequencies and tip mass to beam mass ratios. The bulk capacitance values however, are mainly size dependent.

Table 29: Capacitance peaks for R140-1M and T70-1M-L

Sample	Positive capacitance peak (nF)	Negative capacitance peak (nF)
R140-1M	68.13	-29.65
T70-1M-L	42.85	-21.30

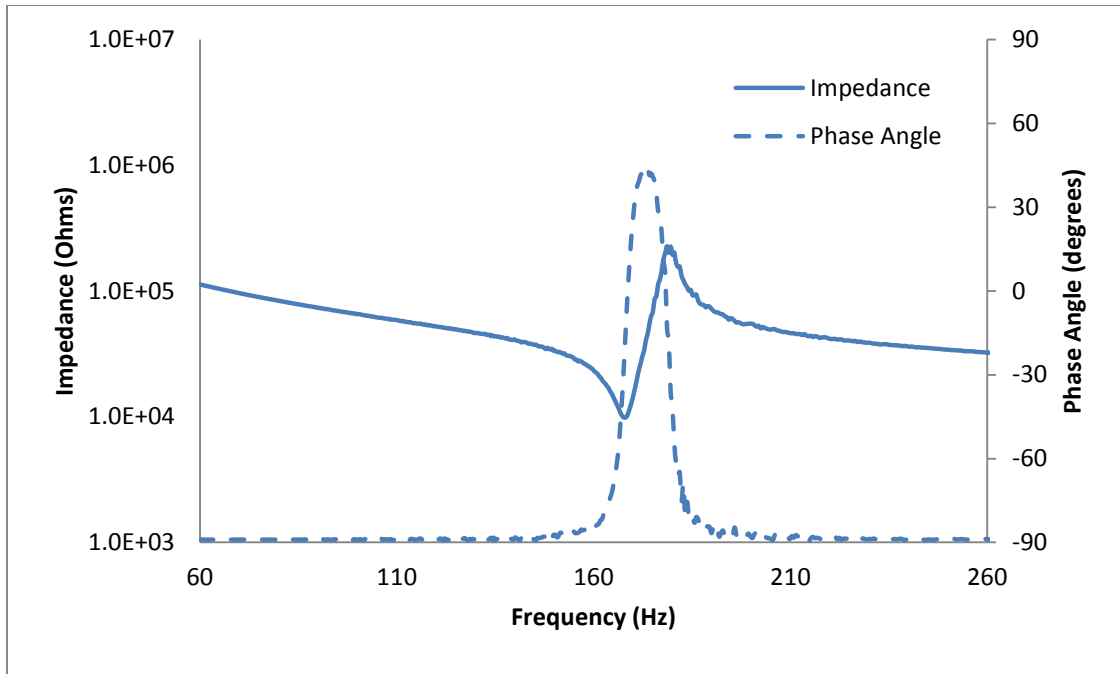


Figure 180: Impedance – Phase angle for R140-1M

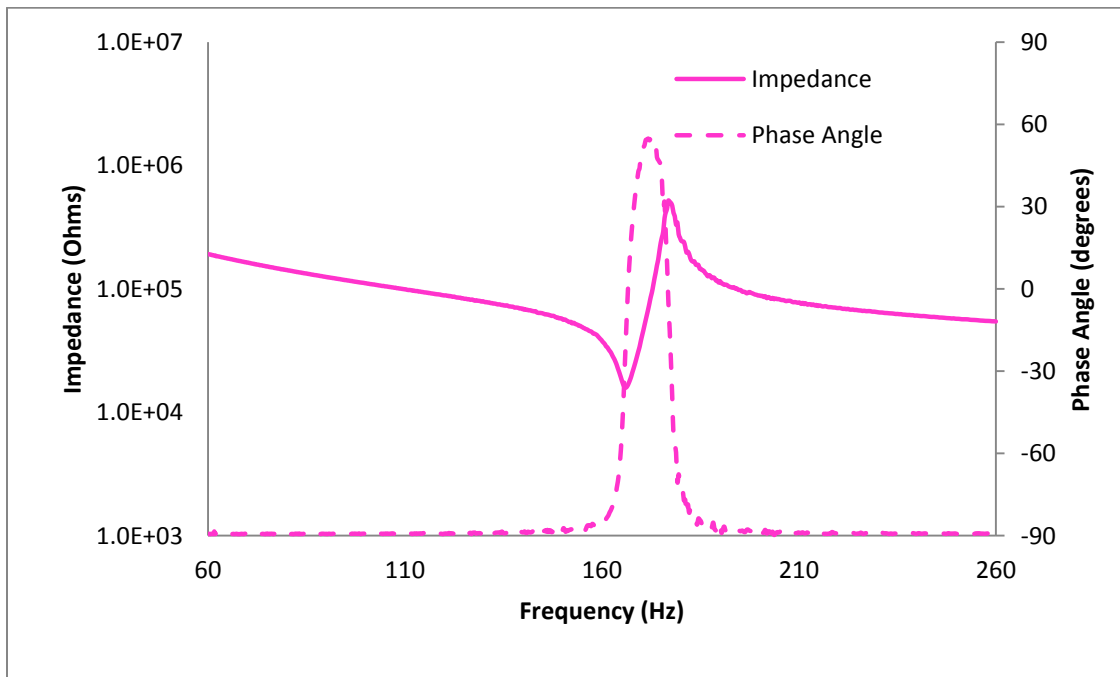


Figure 181: Impedance – Phase Angle for T70-1M-L

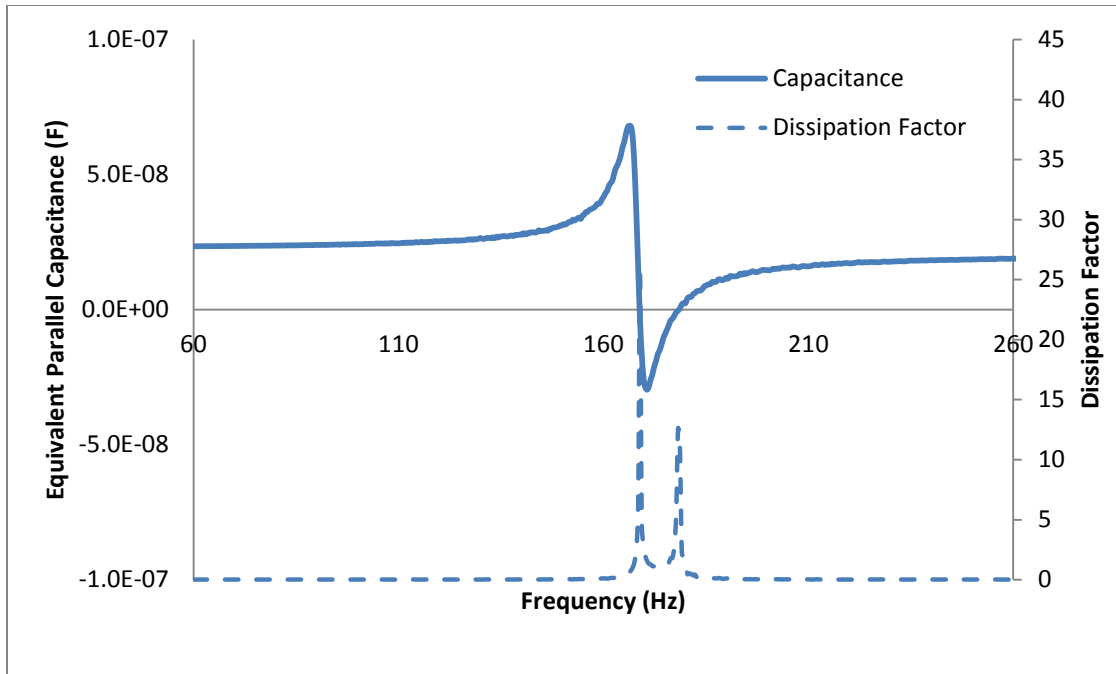


Figure 182: Capacitance – Dissipation for R140-1M

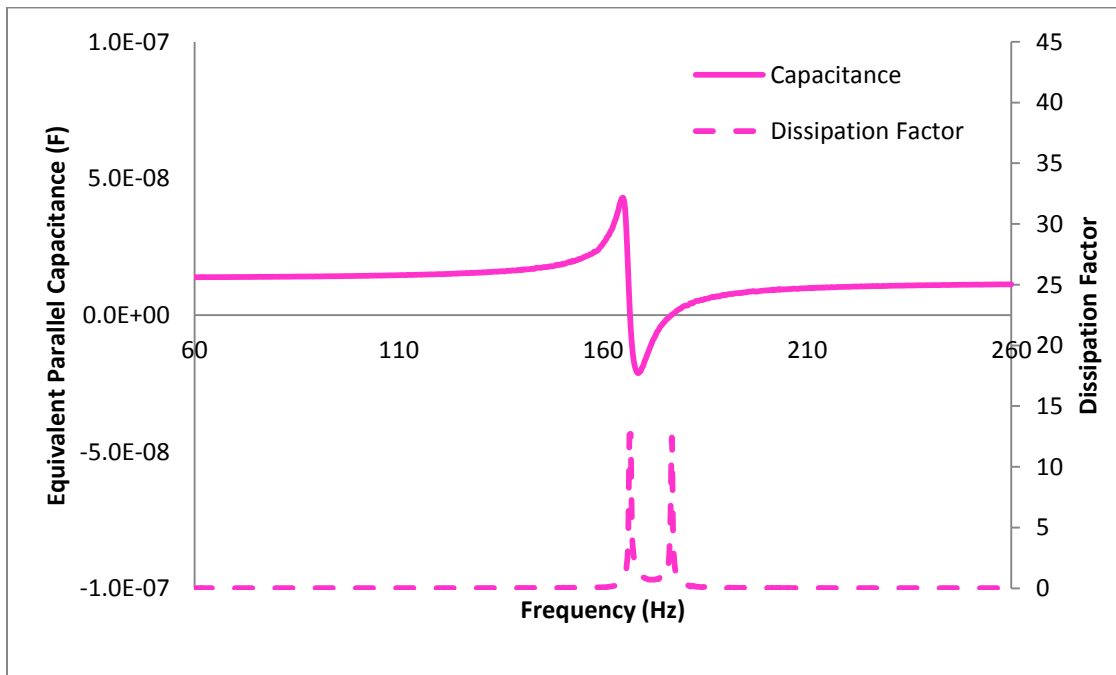


Figure 183: Capacitance – Dissipation Factor for T70-1M-L

### 5.5.3 Summary on constrained length devices

One of the major findings in this section is the dependence of resonance frequency on the shaped devices, as long as the tip mass to beam ratio is significant. In this section, when comparing two shapes, the clamping width and length (altitude for triangles) was kept the same, and the proof mass placed on the device, the resonance frequencies for the two devices was identical. This was quite unintuitive, due to the fact that without the proof mass, the resonance frequency of the triangular device in such circumstances is double as its rectangular counterpart. Therefore, as long as the tip mass to beam ratio is large, the simple analytical equation  $\omega = \sqrt{k/m}$  can be employed to predict the resonance frequency. In such cases, the clamping width, which affects the stiffness in the device greatly affects resonance frequency; hence indicating that the stiffness at the clamped cross-section is the one dominating the stiffness term in the analytical equation. Therefore, the two devices that were compared with unequal volumes (rectangle twice as large as triangle), and matching resonance frequencies.

With the volume in the triangular device being half as much as the rectangular device, the maximum stress values in the device were expected to match. This however was not the case, and attributed to the magnitude of maximum stress values, which are well below the maximum allowed stresses. However, with a higher amount of stress per unit volume in the triangular device, the electromechanical coupling coefficient matched that of the rectangular device. But with large mass tip to beam mass ratio, the damping ratios are large, which give smaller figure of merits.

Also, with the larger stresses in the triangular devices, the resonance frequency impedance were higher than the rectangular devices, a trend that was not observed in triangular devices when volumes matched. The impedance anti-resonance for triangular devices always remained larger than rectangular counterparts with half the volume.

It is quite difficult to consolidate data from this set in plots, due to the variability between the resonance frequency, and variability in size giving different tip mass to beam mass ratios. Moreover, an exact solution for the effective mass, or spring constant for a triangular bimorph is not known, which could otherwise have been used as an independent variable.

## 5.6 Damping Ratio as a function of load resistance

One of the biggest contributing factors towards the electromechanical coupling figure of merit  $k^2Q_m$  is the quality factor. This quality factor in common vibration literature is regarded as the inverse of the damping ratio. In the figure of merits that have been reported in this study, the quality factor used is the one calculated under open circuit conditions for each device. This is done because of the fact that the voltage signal under open circuit conditions is the largest; and as the load resistance tends to short circuit conditions, the voltage signal is very noisy and quite difficult to read. The results in this section justify the use of the open circuit damping ratio as a safe assumption for the mechanical quality factor.

While the literature uses the mechanical quality factor to describe the figure of merit, very few studies [28, 57] have focused on the effect of the load resistance on damping ratio. This section presents two sets of data on the effect of changing damping ratio with load resistance. The first set presented is for R104-1M and T104-1M, where the two devices were found to have pretty strong coupling with  $k^2Q_m > 5$ . The second set is from R70-2M and T70-2M, where the  $k^2Q_m$  figure of merit was approaching 2, the low coupling regime.

In both sets of data presented in Figure 184 and Figure 185, it is quite conclusive that the damping ratio does not remain constant with load resistance. The behavior presented shows an increase in the damping ratio with increase in load resistance up to a certain value, after which it diminishes. This phenomenon begs a comparison with the power generated from the device.

In the case of the 104 mm<sup>3</sup> devices with a 2 gram proof mass, it can be seen that the damping ratio increases up to 25,000 ohms, after which a small dip is found at 35,000 ohms, following which a small plateau exists. The damping ratio starts diminishing from 150,000 ohms. Comparing this with the data in Table 15, the two load resistance values mentioned are the ones where the optimal load resistance values were found for R70-1M. The plateau region is where the power generated remained flat. In the case of the triangular sample T104-1M, a small peak at 15,000 ohms is more evident, showing a damping ratio of about 0.02 ( $Q \approx 33$ ). This load resistance is precisely the same value for the first optimal load resistance in Figure 120. The second optimal load resistance was found at 250,000 ohms; interestingly where the damping ratio is again 0.02. The damping ratio shows a peak values at 75,000 and 100,000 ohms, which in the case of T104-1M triangles goes to about 0.032 ( $Q \approx 15$ ). Interestingly, these are the same load resistances where the dip in power is observed in Figure 120.

In the case of the 4 gram proof mass samples, as shown in Figure 185, it can be seen that the small peak followed by a large peak at intermediate load resistance values are still evident. The first peak for the R70-2M is observed at 15,000 ohms, and for the triangular device is observed at 10,000 ohms. Following these peaks, a small dip is observed, at 20,000 ohms for R70-2M, and 15,000 ohms for T70-2M. While two distinct optimal load resistance values for power were not discernable in Figure 149, it is worth comparing this region against the impedance minima for the two devices. The impedance at resonance frequency, although without an external load resistor in series with the bimorph showed peak values of 24,392 ohms and 16,325 ohms for R70-2M and T70-2M respectively from Table 22, which are in good correlation with the first peaks for the damping ratio. Therefore, the first peak damping ratio is related to the first optimal load resistance value.

The damping ratio at the first peak of 15,000 ohms for R70-2M is 0.025; and this particular damping ratio is found at 200,000 ohms. These are both locations where power is maximized in Figure 149.

However, for the relatively low coupling harvester, T70-2M, which had a  $k^2Q_m$  value of 2.7, the power was maximum at 100,000 ohms; precisely the location where the maximum damping ratio is found. Moreover, it can be seen that the damping ratio at this point is the largest, with a value of 0.043; corresponding to a low Q-factor of about 11.6.

Therefore, damping ratio has a noticeable dependency with load resistance. The damping ratio for triangular devices is found to be larger than rectangular counterparts. In the case of high coupling harvesters, the damping ratio at which power is maximized is not the largest, but higher than open or short circuit conditions. The highest damping ratio relates to the dip in the power curve in high coupling harvesters, whereas in low coupling harvesters, it is where the power is expected to be maximized.

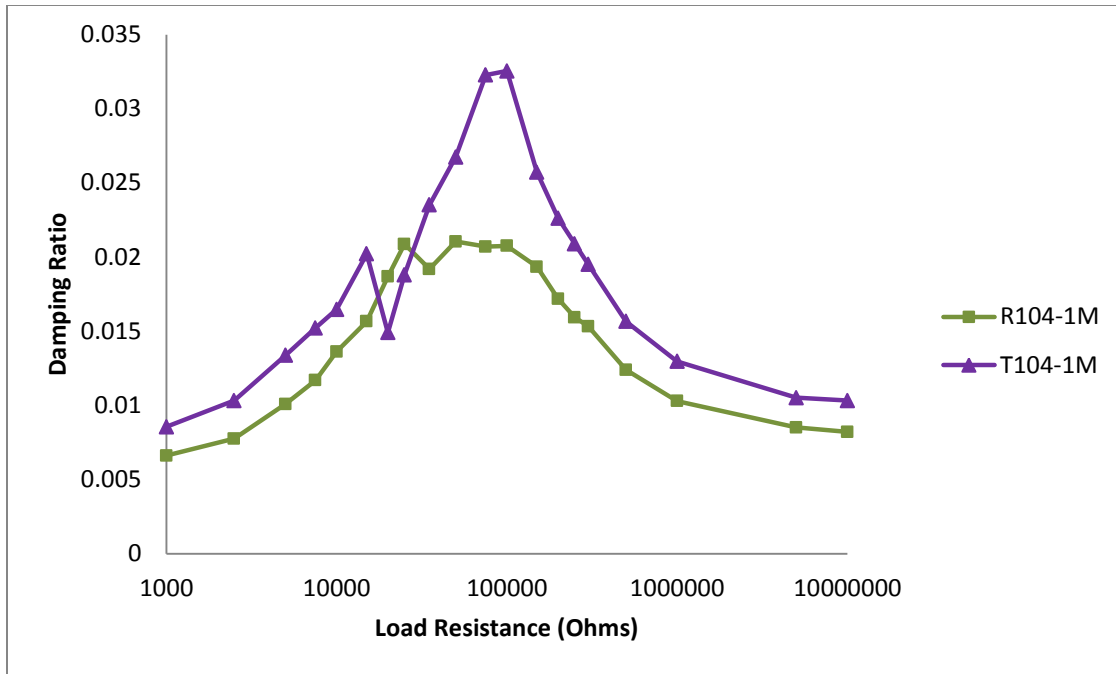


Figure 184: Damping ratio as a function of load resistance for 104 mm<sup>3</sup> devices with 2 grams proof mass

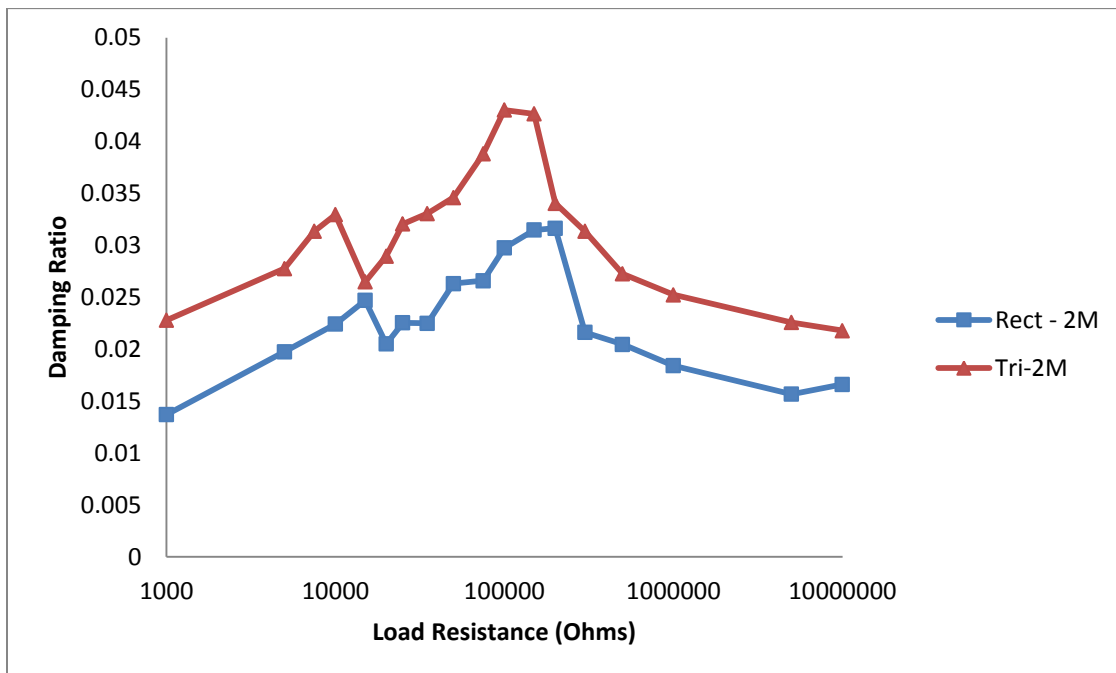


Figure 185: Damping ratio as a function of load resistance for 70 mm<sup>3</sup> devices with 4 grams proof mass

## CHAPTER 6: CONCLUSIONS & FUTURE WORK

In this study, the effect of changing geometry on cantilevered bimorphs has been explored. Cantilevered bimorphs of traditional rectangular geometry have a limitation, which is that the axial stress in the device under harmonic excitations is concentrated near the fixed end of the beam. The idea of linearizing strain by altering the geometry of the device, and producing more power has been presented in literature before. However, it was realized that in the dynamic mode, it is very important to compare devices at matching resonance frequencies to evaluate device characteristics. It was seen that managing the resonance frequency of two different shapes, with and without proof mass can be a difficult task to manage. This self-imposed constraint was attempted to be maintained throughout this study, with some success.

One of the aspects of changing geometry to enhance power output, with given constraints that is missing in literature is an exhaustive characterization of the material, especially with geometrical considerations. This was thoroughly performed by comparing power generated, the calculation of electromechanical coupling, impedance spectroscopy, and comparison of damping ratios. Several conclusions can be drawn from these studies, which are listed below:

- Changing the shape of the device from rectangular to triangular enhances the loading capacity of the device, hence making it stiffer (consistent with literature review).
- When rectangular and triangular counterparts with no proof mass are considered, the triangular bimorphs operate at very low axial stresses, providing more reliable operation. They however produce less power in such a scenario.
- When rectangular and triangular counterparts with proof masses are considered, triangles slightly produce greater power than rectangular bimorphs, provided the tip mass to beam ratio is significant. In this study, the smallest tip mass to beam mass ratio where the triangles outperformed rectangular counterparts was 3.6 (for example T70-1M).
- As rectangular and triangular devices with or without proof mass are compared, with each set having matching resonance frequency and volumes, the triangular devices show enhanced electromechanical coupling coefficients, which is quite significant for electrical parameters.

- With enhanced electromechanical coupling, the impedance at resonance is smaller, and impedance at anti-resonance is larger. Therefore, power can be more easily extracted at lower load resistance values from triangular devices, where the impedance minima are found.
- The triangular devices with larger electromechanical coupling also show larger capacitance peaks around resonance compared to rectangular counterparts, a phenomena that was observed very consistently. Therefore, triangular bimorphs are more efficient capacitors with larger positive capacitance peaks, and better conductors with larger (absolute value) negative capacitance peaks.
- The damping ratio for the triangular devices is usually larger than rectangular counterparts, especially when resonance frequencies match. With higher damping ratios at optimal load resistances, and smaller quality factors, a greater amount of power can be generated, and larger electromechanical coupling figure of merits are obtained.
- Also, with smaller quality factors, the frequency bandwidth at which appreciable power can be extracted is wider, making the devices more compliant, making them easier to tune for resonance frequency.
- Overall, triangular bimorphs, when compared to rectangular bimorphs with matching resonance frequency always operate with lower axial stresses, providing more reliable operation.

Therefore, triangular devices provide several advantages over rectangular counterparts. The only disadvantage is that with the added processes involved in cutting and producing requires more design work or finite element modeling to target devices for certain applications. However, with changing geometry as a function or size, it is quite difficult to manage the resonance frequency to compare devices. Due to the fact that most parameters in this study are frequency dependent, maintaining this becomes paramount.

From a future work perspective, an excellent study would be to study the effects of thickness of cantilevered bimorphs, and also the thickness ratio of the piezoelectric layers to the shim layer. However, due to the mismatch in elastic modulus and density between the shim and the piezoelectric layers, it would be difficult to compare devices with similar resonance frequencies. This would actually be quite difficult to constraint due to the fact that the resonance frequency in the generic formula is directly proportional to the stiffness, and the stiffness has a cubic proportionality with thickness. This would be a challenging but worthwhile study.

## BIBLIOGRAPHY

- [1] S. Roundy, P. K. Wright, and J. Rabaey, "A study of low level vibrations as a power source for wireless sensor nodes," *Computer Communications*, vol. 26, pp. 1131-1144, 2003.
- [2] H. A. Sodano, D. J. Inman, and G. Park, "A Review of Power Harvesting from Vibration Using Piezoelectric Materials," *The Shock and Vibration Digest*, vol. 36, pp. 197-205, 2004.
- [3] H. A. Sodano, D. J. Inman, and G. Park, "Comparison of Piezoelectric Energy Harvesting Devices for Recharging Batteries," *Journal of Intelligent Material Systems and Structures*, vol. 16, pp. 799-807, 2005.
- [4] R. Overfelt, B. Jones, S. Loo, R. Haney, A. Neer, J. Address, X. Yang, A. Zitova, B. Prorok, and J. Fergus, "Sensors and Prognostics to Mitigate Bleed Air Contamination Events," 2012.
- [5] S. J. Roundy, "Energy Scavenging for Wireless Sensor Nodes with a Focus on Vibration to Electricity Conversion," Mechanical Engineering, University of California, Berkeley, Berkeley, CA, 2003.
- [6] S. Roundy, P. K. Wright, and J. M. Rabaey, *Energy scavenging for wireless sensor networks: with special focus on vibrations*: Kluwer Academic Publishers, 2004.
- [7] K. A. Cook-Chennault, N. Thambi, and A. M. Sastry, "Powering MEMS portable devices—a review of non-regenerative and regenerative power supply systems with special emphasis on piezoelectric energy harvesting systems," *Smart Materials and Structures*, vol. 17, p. 043001, 2008.
- [8] E. K. Reilly, L. M. Miller, R. Fain, and P. Wright, "A study of ambient vibrations for piezoelectric energy conversion," in *Proc. PowerMEMS 2009*, 2009, pp. 312-315.
- [9] S. Priya, "Advances in energy harvesting using low profile piezoelectric transducers," *Journal of Electroceramics*, vol. 19, pp. 167-184, 2007.
- [10] N. S. Shenck and J. A. Paradiso, "Energy scavenging with shoe-mounted piezoelectrics," *Micro, IEEE*, vol. 21, pp. 30-42, 2001.
- [11] A. M. Karami and D. J. Inman, "Powering pacemakers from heartbeat vibrations using linear and nonlinear energy harvesters," *Applied Physics Letters*, vol. 100, pp. 042901-042901-4, 2012.
- [12] S. P. Beeby, M. J. Tudor, and N. M. White, "Energy harvesting vibration sources for microsystems applications," *Measurement Science and Technology*, vol. 17, pp. R175-R195, 2006.
- [13] C. B. Williams and R. B. Yates, "Analysis of a micro-electric generator for microsystems," *Sensors and Actuators A: Physical*, vol. 52, pp. 8-11, 1996.
- [14] A. Erturk and D. J. Inman, *Piezoelectric energy harvesting*: John Wiley & Sons, 2011.
- [15] S. R. Anton and H. A. Sodano, "A review of power harvesting using piezoelectric materials (2003–2006)," *Smart Materials and Structures*, vol. 16, p. R1, 2007.
- [16] A. Khaligh, P. Zeng, and C. Zheng, "Kinetic energy harvesting using piezoelectric and electromagnetic technologies—state of the art," *Industrial Electronics, IEEE Transactions on*, vol. 57, pp. 850-860, 2010.
- [17] H. Li, C. Tian, and Z. D. Deng, "Energy harvesting from low frequency applications using piezoelectric materials," *Applied Physics Reviews*, vol. 1, pp. -, 2014.

- [18] S. Roundy, E. S. Leland, J. Baker, E. Carleton, E. Reilly, E. Lai, B. Otis, J. M. Rabaey, P. K. Wright, and V. Sundararajan, "Improving power output for vibration-based energy scavengers," *Pervasive Computing, IEEE*, vol. 4, pp. 28-36, 2005.
- [19] Wikimedia. Available: <http://commons.wikimedia.org/wiki/File:Perovskite.svg#file>
- [20] F. Standards Committee of the IEEE Ultrasonics, and Frequency Control Society, "IEEE Standard on Piezoelectricity," in *ANSI/IEEE Std 176-1987*, ed. New York: IEEE, 1987.
- [21] T. O. Ikeda, *Fundamentals of piezoelectricity*. Oxford University Press, 1990.
- [22] D. Shen, "Piezoelectric Energy Harvesting for Low Frequency Vibration Applications," Ph.D, Materials Engineering, Auburn University, Auburn, AL, 2009.
- [23] S. Roundy and P. K. Wright, "A piezoelectric vibration based generator for wireless electronics," *Smart Materials and Structures*, vol. 13, pp. 1131-1142, 2004.
- [24] S. Roundy, "On the Effectiveness of Vibration-based Energy Harvesting," *Journal of Intelligent Material Systems and Structures*, vol. 16, pp. 809-823, 2005.
- [25] D. Isarakorn, D. Briand, P. Janphuang, A. Sambri, S. Gariglio, J. Triscone, F. Guy, J. Reiner, C. Ahn, and N. De Rooij, "The realization and performance of vibration energy harvesting MEMS devices based on an epitaxial piezoelectric thin film," *Smart Materials and Structures*, vol. 20, p. 025015, 2011.
- [26] A. Erturk, "Electromechanical Modeling of Piezoelectric Energy Harvesters," Doctor of Philosophy, Engineering Mechanics, Virginia Polytechnic Institute and State University, Blacksburg, VA, 2009.
- [27] M. Umeda, K. Nakamura, and S. Ueha, "Analysis of the transformation of mechanical impact energy to electric energy using piezoelectric vibrator," *Japanese Journal of Applied Physics*, vol. 35, pp. 3267-3273, 1996.
- [28] H. A. Sodano, G. Park, and D. J. Inman, "Estimation of Electric Charge Output for Piezoelectric energy harvesting," *Strain*, vol. 40, pp. 49-58, 2004.
- [29] A. Erturk and D. J. Inman, "A Distributed Parameter Electromechanical Model for Cantilevered Piezoelectric Energy Harvesters," *Journal of Vibration and Acoustics*, vol. 130, p. 041002, 2008.
- [30] A. Erturk and D. J. Inman, "An experimentally validated bimorph cantilever model for piezoelectric energy harvesting from base excitations," *Smart Materials and Structures*, vol. 18, p. 025009, 2009.
- [31] J. M. Dietl and E. Garcia, "Beam shape optimization for power harvesting," *Journal of Intelligent Material Systems and Structures*, vol. 21, pp. 633-646, 2010.
- [32] M. Rosa and C. D. M. Junior, "Modeling and Analysis of a Piezoelectric Energy Harvester with Varying Cross-Sectional Area," *Shock and Vibration*, vol. 2014, 2014.
- [33] P. Glynne-Jones, S. Beeby, and N. White, "Towards a piezoelectric vibration-powered microgenerator," in *IEE Proceedings - Science, Measurement and Technology*, 2001, pp. 68-72.
- [34] N. M. White, P. Glynne-Jones, and S. P. Beeby, "A novel thick-film piezoelectric micro-generator," *Smart Materials and Structures*, vol. 20, pp. 850-852, 2001.
- [35] M. I. Friswell and S. Adhikari, "Sensor shape design for piezoelectric cantilever beams to harvest vibration energy," *Journal of Applied Physics*, vol. 108, p. 014901, 2010.
- [36] L. Mateu and F. Moll, "Optimum Piezoelectric Bending Beam Structures for Energy Harvesting using Shoe Inserts," *Journal of Intelligent Material Systems and Structures*, vol. 16, pp. 835-845, 2005.

- [37] F. Goldschmidtboeing and P. Woias, "Characterization of different beam shapes for piezoelectric energy harvesting," *Journal of Micromechanics and Microengineering*, vol. 18, p. 104013, 2008.
- [38] J. H. Park, J. Kang, H. Ahn, S. B. Kim, D. Liu, and D. J. Kim, "Analysis of Stress distribution in piezoelectric MEMS energy harvester using shaped cantilever structure," *Ferroelectrics*, vol. 409, pp. 55-61, 2010.
- [39] D. Benasciutti, L. Moro, S. Zelenika, and E. Brusa, "Vibration energy scavenging via piezoelectric bimorphs of optimized shapes," *Microsystem Technologies*, vol. 16, pp. 657-668, 2009.
- [40] S. P. Matova, M. Renaud, M. Jambunathan, M. Goedbloed, and R. V. Schaijk, "Effect of length/width ratio of tapered beams on the performance of piezoelectric energy harvesters," *Smart Materials and Structures*, vol. 22, p. 075015, 2013.
- [41] J. Park, S. Lee, and B. M. Kwak, "Design optimization of piezoelectric energy harvester subject to tip excitation," *Journal of Mechanical Science and Technology*, vol. 26, pp. 137-143, 2012.
- [42] D. F. Berdy, P. Srisungsitthisunti, X. Xu, J. Rhoades, B. Jung, and D. Peroulis, "Compact low frequency meandered piezoelectric energy harvester," in *PowerMEMS*, Washington, DC, 2009, pp. 71-74.
- [43] M. A. Karami and D. J. Inman, "Analytical Modeling and Experimental Verification of the Vibrations of the Zigzag Microstructure for Energy Harvesting," *Journal of Vibration and Acoustics*, vol. 133, p. 011002, 2011.
- [44] S. Paquin and Y. St-Amant, "Improving the performance of a piezoelectric energy harvester using a variable thickness beam," *Smart Materials and Structures*, vol. 19, p. 105020, 2010.
- [45] Y. Shu and I. Lien, "Efficiency of energy conversion for a piezoelectric power harvesting system," *Journal of Micromechanics and Microengineering*, vol. 16, p. 2429, 2006.
- [46] Y. C. Shu and I. C. Lien, "Analysis of power output for piezoelectric energy harvesting systems," *Smart Materials and Structures*, vol. 15, pp. 1499-1512, 2006.
- [47] G. Frank, W. Martin, E. Christoph, and W. Peter, "Parameter identification for resonant piezoelectric energy harvesters in the low- and high-coupling regimes," *Journal of Micromechanics and Microengineering*, vol. 21, p. 045006, 2011.
- [48] A. Lei, R. Xu, L. M. Borregaard, M. Guizzetti, O. Hansen, and E. V. Thomsen, "Impedance Based Characterization of a High-Coupled Screen Printed PZT Thick Film Unimorph Energy Harvester," *Journal of Microelectromechanical Systems*, vol. 23, pp. 842-854, 2014.
- [49] N. Kong, D. S. Ha, A. Erturk, and D. J. Inman, "Resistive impedance matching circuit for piezoelectric energy harvesting," *Journal of Intelligent Material Systems and Structures*, 2010.
- [50] X. Xiong and S. O. Oyadiji, "Modal electromechanical optimization of cantilevered piezoelectric vibration energy harvesters by geometric variation," *Journal of Intelligent Material Systems and Structures*, p. 1045389X13502872, 2013.
- [51] Y. Yang and L. Tang, "Equivalent circuit modeling of piezoelectric energy harvesters," *Journal of Intelligent Material Systems and Structures*, vol. 20, pp. 2223-2235, 2009.
- [52] Z. Meiling, E. Worthington, and J. Njuguna, "Analyses of power output of piezoelectric energy-harvesting devices directly connected to a load resistor using a coupled

- piezoelectric-circuit finite element method," *Ultrasonics, Ferroelectrics and Frequency Control, IEEE Transactions on*, vol. 56, pp. 1309-1317, 2009.
- [53] Z. Meiling, E. Worthington, and A. Tiwari, "Design study of piezoelectric energy-harvesting devices for generation of higher electrical power using a coupled piezoelectric-circuit finite element method," *Ultrasonics, Ferroelectrics and Frequency Control, IEEE Transactions on*, vol. 57, pp. 427-437, 2010.
- [54] G. Takács and B. Roha-Ilkiv, *Model Predictive Vibration Control - Efficient Constrained MPC Vibration Control for Lightly Damped Mechanical Structures*: Springer, 2012.
- [55] S.-B. Kim, "Piezoelectric Cantilever for Mechanical Energy Harvesting," Ph.D, Mechanical Engineering, Auburn University, Auburn, AL, 2012.
- [56] B. S. Beck, "Negative capacitance shunting of piezoelectric patches for vibration control of continuous systems," 2012.
- [57] H. Huang, C. Zheng, X. Ruan, J. Zeng, L. Zheng, W. Chen, and G. Li, "Elastic and Electric Damping Effects on Piezoelectric Cantilever Energy Harvesting," *Ferroelectrics*, vol. 459, pp. 1-13, 2014.

## APPENDIX A: Coupled-Field Numerical Simulations

Numerical simulations using ANSYS have been performed in order to match experimental results, and use these simulations as a tool to evaluate power generation characteristics from devices of more complex geometry. In order to do so, a harmonic analysis is performed on a modeled rectangular bimorph in a multi-physics environment, as described in the methodology section. The rectangular bimorph has the same dimensions as mentioned for R70-0M, where length is 21.5 mm, width is 6.35 mm, and the overall thickness is 0.51 mm, but here three layers are modeled, where the piezoelectric layers are 0.19 mm and the brass layer is 0.13 mm in thickness respectively. The ANSYS model is able to calculate the transverse displacements at the free end as shown in Figures 186 and 187, and also the electric potential generated through the bimorph layers as shown in Figures 188 and 189.

It can be seen in Figures 188 and 189 that the value of the load resistance greatly influences the voltage generated in the device. It is observed that, increasing values of load resistances increase the amount of deflection in the device. This can be explained due to increased damping in the device with increasing values of load resistances. As the amount of electrical damping induced in the system increases, the device resonates at a lower frequency with a greater amplitude.

Moreover, as it was seen in the previous sections that there was an optimal load resistance for power generation. This effect may also be related to the large resonance frequency shift that is seen in Figures 68-71 where it is seen that at load resistance values of 25k ohms and below, the displacement and voltage plots show much lower resonance frequencies. The power generated here would be different, since these values may be close to the optimal load resistance of the device.

Figure 190 shows voltage generated by the device as a function of load resistances as calculated by ANSYS and compared with experimental data. The ANSYS plot mimics the behavior of the experimental data, but the values are quite far off from each other. This is once again attributed to the improper damping ratio that is prescribed in the ANSYS model, which utilized the equation  $\zeta_p = \frac{1}{2Q}$ , where Q is the quality factor of the device, which was given as 32 for PZT-5H by the manufacturer. The results from the impedance analyzer measurements suggest that this value changes when the devices are clamped as cantilevers. Therefore, the numerical model needs to be fine-tuned with proper damping ratios.

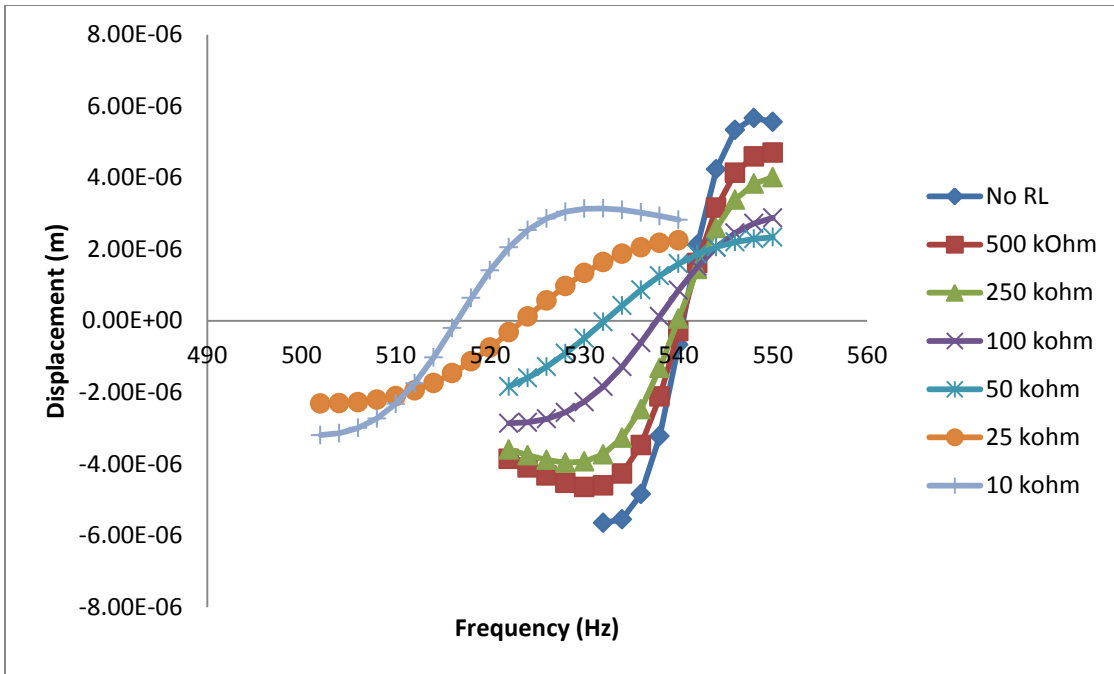


Figure 186: Real part of tip displacement for R70-0M at various load resistances

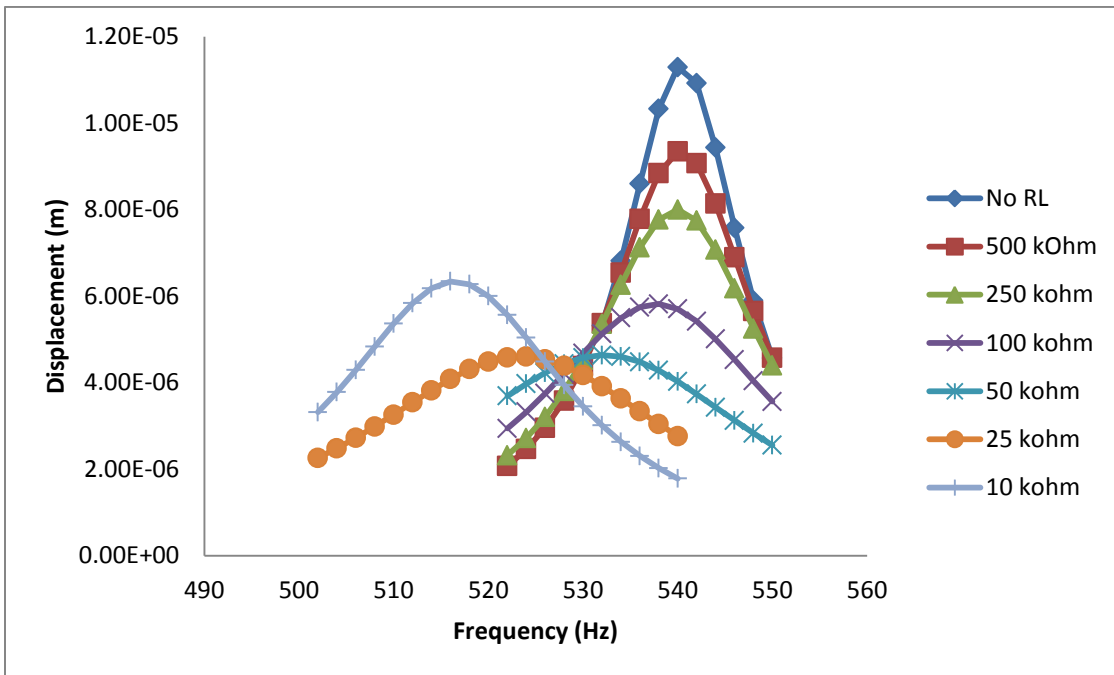


Figure 187: Imaginary part of tip displacement for R70-0M at various load resistances

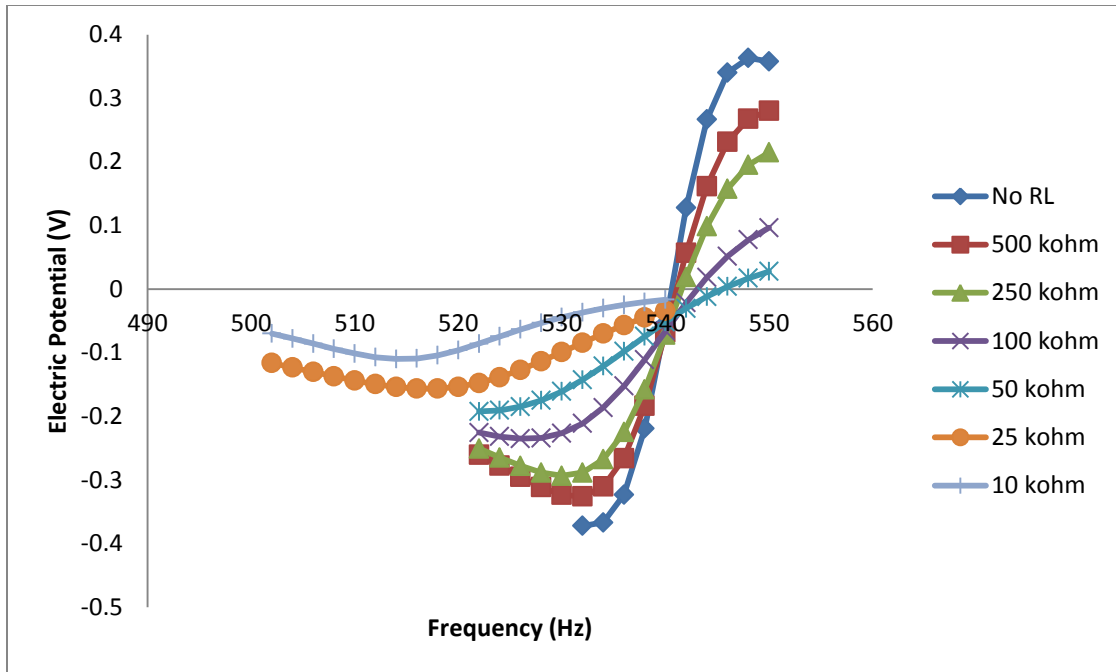


Figure 188: Real part of electric potential for R70-0M at various load resistances

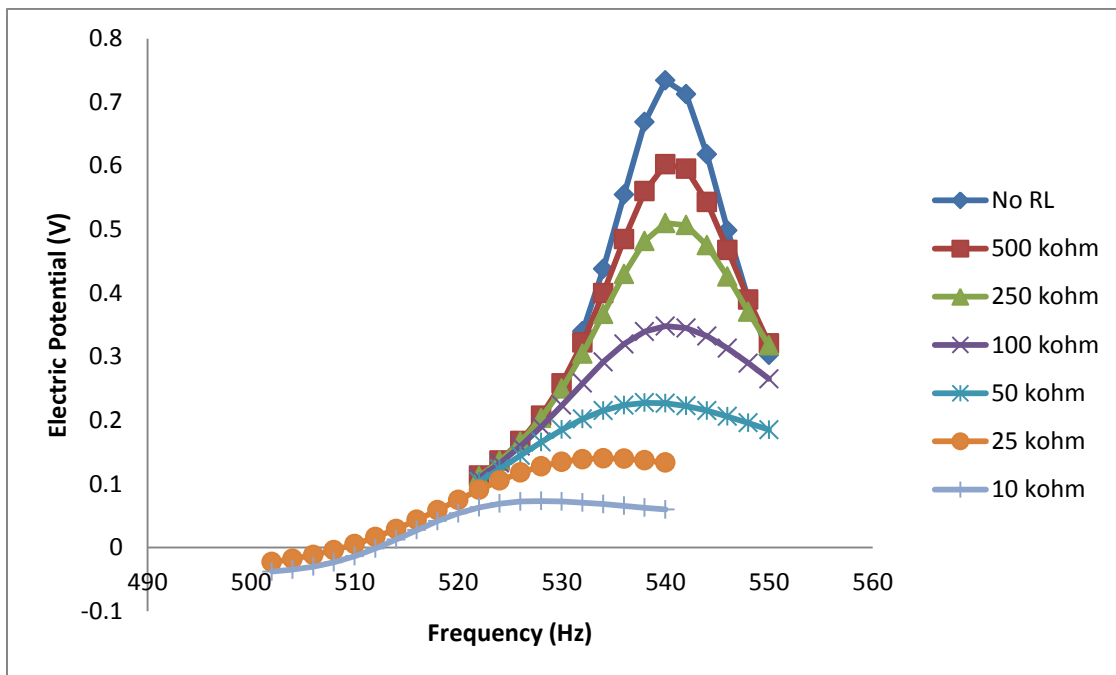


Figure 189: Imaginary part of electric potential for R70-0M at various load resistances

